

**Measurement of the CKM angle  $\phi_3$  from  
 $B^\pm \rightarrow D(K_S^0 \pi^+ \pi^- \pi^0) K^\pm$  decays and future  
prospects**

*A THESIS*

*submitted by*

**RESMI P K**

*for the award of the degree*

*of*

**DOCTOR OF PHILOSOPHY**



**DEPARTMENT OF PHYSICS  
INDIAN INSTITUTE OF TECHNOLOGY MADRAS.**

**November 2019**



*Dedicated to  
my Amma and Achhan*



# THESIS CERTIFICATE

This is to certify that the thesis titled **Measurement of the CKM angle  $\phi_3$  from  $B^\pm \rightarrow D(K_S^0 \pi^+ \pi^- \pi^0) K^\pm$  decays and future prospects**, submitted by **Resmi P K**, to the Indian Institute of Technology, Madras, for the award of the degree of **Doctor of Philosophy**, is a bonafide record of the research work done by her under my supervision. The contents of this thesis, in full or in parts, have not been submitted to any other Institute or University for the award of any degree or diploma.

**Prof. Jim Libby**  
Research Guide  
Professor  
Dept. of Physics  
IIT-Madras, 600 036

Place: Chennai

Date: 26 November 2019



## ACKNOWLEDGEMENTS

I take this opportunity with immense pleasure to acknowledge all the people without whose support this thesis would not have been possible. First of all, I would like to sincerely thank my supervisor Prof. Jim Libby for his guidance and support throughout my PhD period. I am really fortunate to have worked with him. I cannot thank him enough for motivating and patiently guiding me during the course of last five years. I also thank him for providing me an excellent opportunity to work with collaborators from different parts of the world. His Particle Physics course in my MSc led me through the details and helped in developing further interest in the subject.

I would like to acknowledge Prof. Guy Wilkinson and Dr. Sneha Malde from the University of Oxford for allowing me to visit the university and collaborate with them for my analysis with CLEO-c data. I am also indebted to Dr. Chris Thomas for providing me with technical help in the initial days of CLEO-c analysis. It was my pleasure to work with Dr. Karim Trabelsi from LAL, Orsay for the Belle and Belle II data analyses. I sincerely thank him for his constant encouragement and discussions. I am really amazed by his enthusiasm and sincerity and it was a privilege to have worked with him. I would like to express my gratitude to the Belle and Belle II Collaborations for allowing me to work at KEK and a special thanks to Prof. Yoshihide Sakai and Prof. Shoji Uno for providing me with local financial support for my visits.

I thank Dr. Gagan Mohanty from TIFR for providing me a good opportunity to participate in the SVD construction and characterization of Belle II. It was a great experience working alongside Mr. K. Kameshwara Rao and Mr. Sukant Mayekar on the SVD and I am grateful to them for their support during my stay at IPMU and KEK while working on the SVD. I also thank Dr. Takeo Higuchi from IPMU for providing me the financial support during my visit. I acknowledge all the members of Belle India Group who have encouraged and supported me during my PhD. The Belle Analysis Workshops, held every year, helped me to grasp different technical details on the analysis procedure and the physics discussions gave me a good knowledge of various experimental and theoretical aspects of Particle Physics.

The Department of Physics at IIT Madras has provided good infrastructure and resources which made this work possible. I would like to thank all the faculty members and staff for all their support. I thank my doctoral committee members Prof. D. Indumathi, Dr. Sunethra Ramanan and Dr. Prafulla Kumar Behera for their valuable comments and suggestions during the course of my PhD.

I am at a loss of words to thank Prasanth for being a supportive colleague and best friend; I am really lucky to have you as my life partner. I cannot thank you enough for all the technical help and stimulating Physics discussions. Thank you for being there for me always and taking care of me during difficult times. I sincerely thank my colleagues Minakshi, Jafar, Basith, Aleena, Rebin, Krishnakumar, Niharika and Anita for their support. I am grateful to all my friends for giving me a good atmosphere to live in the campus. I am greatly indebted to you, Maya, for being my best mate and sharing the same craziness as mine for the past seven years.

I would like to express my sincere gratitude towards my teachers at Sree Kerala Varma College, Thrissur and Sree Sarada Girls' HSS, Puranattukara for their constant support and encouragement. Without them, I would not have discovered my passion for Physics. A special thanks to my friends from school and college for their support.

I am deeply indebted to my parents Krishnankutty and Thankamma for their constant support and motivation throughout my life. Nothing can replace their selfless love. I would like to thank all my family members and relatives for their support. Above all, I am greatly thankful to the Almighty for all that I am now.

# ABSTRACT

We report the first model-independent measurement of the CKM unitarity triangle angle  $\phi_3$  using  $B^\pm \rightarrow D(K_S^0 \pi^+ \pi^- \pi^0) K^\pm$  decays, where  $D$  indicates either a  $D^0$  or  $\bar{D}^0$  meson. The five-dimensional phase space of the  $D$  decay is divided into independent regions called “bins”. The rates of  $B^-$  and  $B^+$  decays in  $i^{\text{th}}$  bin are expressed as

$$\Gamma_i^- = h \left( K_i + r_B^2 \bar{K}_i + 2\sqrt{K_i \bar{K}_i} (c_i x_- + s_i y_-) \right),$$

and

$$\Gamma_i^+ = h \left( \bar{K}_i + r_B^2 K_i + 2\sqrt{K_i \bar{K}_i} (c_i x_+ - s_i y_+) \right),$$

where  $x_\pm = r_B \cos(\delta_B \pm \phi_3)$  and  $y_\pm = r_B \sin(\delta_B \pm \phi_3)$ . The measurements of the strong-phase difference of the  $D \rightarrow K_S^0 \pi^+ \pi^- \pi^0$  amplitude,  $c_i$  and  $s_i$  parameters, are determined from CLEO-c data of  $0.8 \text{ fb}^{-1}$ . The parameters  $K_i$  and  $\bar{K}_i$ , the fraction of flavour-tagged  $D^0$  and  $\bar{D}^0$  events, are estimated from a sample of  $D^*$ -tagged  $D^0$  decays. We measure the  $x_\pm$  and  $y_\pm$  parameters from the full Belle data set of  $772 \times 10^6 \text{ } B\bar{B}$  events collected at the  $\Upsilon(4S)$  resonance, with the values of  $c_i$ ,  $s_i$ ,  $K_i$  and  $\bar{K}_i$  used as input. We obtain  $\phi_3 = (5.7_{-8.8}^{+10.2} \pm 3.5 \pm 5.7)^\circ$  and the suppressed amplitude ratio  $r_B = 0.323 \pm 0.147 \pm 0.023 \pm 0.051$ . Here the first uncertainty is statistical, the second is the experimental systematic, and the third is due to the precision of the strong-phase parameters measured from CLEO-c data. The 95% confidence interval on  $\phi_3$  is  $(-29.7, 109.5)^\circ$ , which is consistent with the current world average.

We present the expected sensitivity of this measurement at Belle II, a substantial upgrade of Belle. The construction and quality assurance of the vertex detector at Belle II and the first Physics results from the data collected in 2018 are also discussed.



# TABLE OF CONTENTS

<b>ACKNOWLEDGEMENTS</b>	<b>vi</b>
<b>ABSTRACT</b>	<b>viii</b>
<b>LIST OF TABLES</b>	<b>xiv</b>
<b>LIST OF FIGURES</b>	<b>xviii</b>
<b>1 Introduction</b>	<b>1</b>
1.1 Discrete symmetries . . . . .	2
1.2 CKM matrix . . . . .	5
1.3 The angle $\phi_3$ . . . . .	10
1.3.1 Methods to extract $\phi_3$ . . . . .	12
1.3.2 Model-independent method to extract $\phi_3$ . . . . .	14
1.4 Quantum-correlated $D$ mesons . . . . .	16
1.4.1 $CP$ -even fraction $F_+$ . . . . .	17
1.4.2 Strong phase difference parameters $c_i$ and $s_i$ . . . . .	19
1.5 $D \rightarrow K_S^0 \pi^+ \pi^- \pi^0$ decays . . . . .	20
<b>2 CLEO-c and Belle experiments</b>	<b>23</b>
2.1 Introduction . . . . .	23
2.2 CESR and CLEO-c detector . . . . .	23
2.2.1 CESR . . . . .	23
2.2.2 CLEO-c detector . . . . .	25
2.3 KEKB accelerator and Belle detector . . . . .	31
2.3.1 KEKB accelerator . . . . .	31
2.3.2 Belle detector . . . . .	34
<b>3 Quantum-correlated <math>D</math>-decay measurements at CLEO-c</b>	<b>49</b>
3.1 Introduction . . . . .	49

3.2	Data sample . . . . .	49
3.3	Event selection . . . . .	50
3.3.1	Selection of $K^\pm$ and $\pi^\pm$ candidates . . . . .	51
3.3.2	Selection of $\pi^0$ and $\eta$ candidates . . . . .	52
3.3.3	Selection of $K_S^0$ candidates . . . . .	53
3.3.4	Selection of $\eta'$ candidates . . . . .	54
3.3.5	Selection of $\omega$ candidates . . . . .	54
3.3.6	Selection of $D$ candidates . . . . .	57
3.3.7	Selection of events with $K_L^0$ candidates . . . . .	58
3.3.8	Selection of events with $\nu$ candidates . . . . .	60
3.3.9	Best-candidate selection . . . . .	61
3.4	Single-tagged yield estimation . . . . .	61
3.5	Double-tagged yield estimation . . . . .	66
3.6	Determination of $c_i$ and $s_i$ . . . . .	76
3.6.1	Systematic uncertainties . . . . .	83
3.7	Estimation of sensitivity to $\phi_3$ . . . . .	86
<b>4</b>	<b>Selection of <math>B^+ \rightarrow D(K_S^0\pi^+\pi^-\pi^0)h^+</math>, <math>h = K, \pi</math> and <math>D^{*+} \rightarrow D(K_S^0\pi^+\pi^-\pi^0)\pi^+</math> events at Belle</b>	<b>89</b>
4.1	Introduction . . . . .	89
4.2	Data sample . . . . .	89
4.3	Event selection . . . . .	90
4.3.1	Selection of $K^+$ and $\pi^+$ candidates . . . . .	91
4.3.2	Selection of $K_S^0$ candidates . . . . .	92
4.3.3	Selection of $\pi^0$ candidates . . . . .	93
4.3.4	Selection of $D$ candidates . . . . .	93
4.3.5	Selection of $B$ candidates . . . . .	94
4.3.6	Selection of $D^*$ candidates . . . . .	96
4.4	Background suppression . . . . .	98
4.4.1	Misreconstructed $\pi^0$ background . . . . .	98
4.4.2	Continuum background . . . . .	102
4.4.3	Background from $D^*$ events . . . . .	109
4.5	Multiplicity and best-candidate selection . . . . .	109

4.6	Efficiency and migration . . . . .	112
<b>5</b>	<b>Measurement of <math>\phi_3</math> at Belle</b>	<b>117</b>
5.1	Introduction . . . . .	117
5.2	Determination of $K_i$ and $\overline{K}_i$ . . . . .	117
5.3	Measurement of $x_{\pm}$ and $y_{\pm}$ . . . . .	126
5.3.1	Fit model for the $B^+ \rightarrow D\pi^+$ sample . . . . .	126
5.3.2	Data-MC comparison study . . . . .	133
5.3.3	Fit model for $B^+ \rightarrow DK^+$ sample . . . . .	136
5.3.4	Simultaneous fit to $B^+ \rightarrow D\pi^+$ and $B^+ \rightarrow DK^+$ samples . . . . .	141
5.3.5	Extraction of $x_{\pm}$ and $y_{\pm}$ parameters . . . . .	152
5.4	Systematic uncertainties . . . . .	158
5.5	Determination of $\phi_3$ , $r_B$ and $\delta_B$ . . . . .	162
5.6	Combination of $D \rightarrow K_S^0\pi^+\pi^-(\pi^0)$ results from Belle . . . . .	164
<b>6</b>	<b>Prospects at Belle II</b>	<b>167</b>
6.1	Belle II detector . . . . .	167
6.2	Silicon Vertex Detector at Belle II . . . . .	170
6.2.1	Components . . . . .	171
6.2.2	Construction . . . . .	173
6.2.3	Quality assurance . . . . .	174
6.3	Results from phase II . . . . .	180
<b>7</b>	<b>Conclusions</b>	<b>191</b>
<b>A</b>	<b>Measurement of <math>F_+</math></b>	<b>195</b>
A.0.1	$CP$ and quasi- $CP$ tags method . . . . .	196
A.0.2	$K_S^0\pi^+\pi^-$ and $K_L^0\pi^+\pi^-$ tags method . . . . .	197
A.0.3	$K_S^0\pi^+\pi^-\pi^0$ self-tags method and combined result . . . . .	199
<b>B</b>	<b>Fit projections in bins of <math>D^{*\pm} \rightarrow D\pi^{\pm}</math> sample</b>	<b>201</b>
<b>C</b>	<b>Fit projections in bins of <math>B^{\pm} \rightarrow Dh^{\pm}</math> sample</b>	<b>205</b>
<b>D</b>	<b>Results from pseudo-experiments</b>	<b>223</b>



# LIST OF TABLES

1.1	Properties of quarks and leptons in the SM. . . . .	2
1.2	Properties of force carrying bosons in the SM. . . . .	2
2.1	Data collected at or near different $\Upsilon$ resonances and their corresponding luminosity. . . . .	33
2.2	Different physics processes and their cross sections. Their respective trigger rates at a luminosity of $10^{34} \text{ cm}^{-2} \text{ s}^{-1}$ [58]. . . . .	45
3.1	Different tag modes used in the analysis. . . . .	50
3.2	$\Delta E$ selection for different $D$ decay modes. . . . .	57
3.3	Fit parameters for $m_{bc}$ signal component fit for $D^0 \rightarrow K_S^0 \pi^+ \pi^- \pi^0$ decays in MC. . . . .	63
3.4	Fit parameters for $m_{bc}$ background component fit for $D^0 \rightarrow K_S^0 \pi^+ \pi^- \pi^0$ decays in MC. Here, the fraction of Gaussian $f_G = 1 - f - f_{CB}$ . . . . .	64
3.5	The signal and sideband regions for fully reconstructed $D$ decays. . . . .	68
3.6	The signal yields of $D^0 \rightarrow K_S^0 \pi^+ \pi^- \pi^0$ decays tagged with different $D$ decay modes in data. . . . .	70
3.7	Signal region and sidebands for partially reconstructed final states having a $K_L^0$ or $\nu_e$ . The regions are defined on $m_{\text{miss}}^2$ and $U_{\text{miss}}$ distributions for $K_L^0$ modes and $K^\pm e^\mp \nu_e$ , respectively. . . . .	70
3.8	Signal yields for $D \rightarrow K_S^0 \pi^+ \pi^- \pi^0$ events tagged with decays involving a $K_L^0$ meson or a $\nu_e$ in data. . . . .	73
3.9	Specifications of the nine exclusive bins of $D \rightarrow K_S^0 \pi^+ \pi^- \pi^0$ phase space along with the fraction of flavour-tagged $D^0$ and $\bar{D}^0$ events in each of them. $m_L$ and $m_U$ are the lower and upper limits, respectively, of the invariant masses in each region. . . . .	78
3.10	The total yield in the signal region of $D \rightarrow K_S^0 \pi^+ \pi^- \pi^0$ decays tagged by $CP$ and quasi- $CP$ eigenstates in data. . . . .	78
3.11	Total yield in data for $K_S^0 \pi^+ \pi^- \pi^0$ decays tagged by $K_S^0 \pi^+ \pi^-$ events in the signal region. The rows represent the $K_S^0 \pi^+ \pi^- \pi^0$ phase space bins and columns show the tag side bins. . . . .	79
3.12	Total yield in data for $K_S^0 \pi^+ \pi^- \pi^0$ decays tagged by $K_L^0 \pi^+ \pi^-$ events in the signal region. The rows represent the $K_S^0 \pi^+ \pi^- \pi^0$ phase space bins and columns show the tag side bins. . . . .	79

3.13	Total yield in data for events in which, both the $D$ mesons decay into $K_S^0\pi^+\pi^-\pi^0$ final state, in the signal region. . . . .	80
3.14	The total yield of $D^0$ and $\overline{D^0}$ decays to $K_S^0\pi^+\pi^-\pi^0$ obtained from flavour tag mode $K^\pm e^\mp \nu_e$ in each bin for the signal region in data. . . . .	80
3.15	Reconstruction efficiency of $D \rightarrow K_S^0\pi^+\pi^-\pi^0$ events in each bin estimated from signal MC sample. The fractional five-dimensional volume of each bin is also given. . . . .	81
3.16	Migration matrix obtained from $D \rightarrow K_S^0\pi^+\pi^-\pi^0$ signal MC events. The rows and columns represent the reconstructed and true bins, respectively. . . . .	81
3.17	Fraction of flavour-tagged $D^0$ and $\overline{D^0}$ events in each bin. . . . .	82
3.18	Systematic uncertainties on $c_i$ values. . . . .	86
3.19	Systematic uncertainties on $s_i$ values. . . . .	86
3.20	Final results for $c_i$ and $s_i$ values. The uncertainties are statistical and systematic, respectively. The $s_i$ results marked by * in bins 3, 5 and 8 are derived from those in other bins, according to the constraints of Eqs. (3.34)–(3.36). . . . .	87
3.21	Statistical correlation coefficients between $c_i$ and $s_i$ values. . . . .	87
3.22	Systematic correlation coefficients between $c_i$ and $s_i$ values. . . . .	88
4.1	Optimized $E_\gamma$ thresholds for the photon candidates. . . . .	99
4.2	Input variables of NN ranked according to their significance ( $\sigma$ ). Here $\sigma$ is defined as the linear-correlation factor multiplied by $\sqrt{n}$ , where $n$ is the sample size. . . . .	107
4.3	Different BCS metrics with the corresponding efficiencies. Here $\chi^2(\pi^0)$ is the $\chi^2$ of the mass-vertex fit on $\pi^0$ . . . . .	110
4.4	Different contributions to $D \rightarrow K_S^0\pi^+\pi^-\pi^0$ final state used in signal MC generation [14]. . . . .	112
4.5	Efficiency of $B^\pm \rightarrow D(K_S^0\pi^+\pi^-\pi^0)\pi^\pm$ and $B^\pm \rightarrow D(K_S^0\pi^+\pi^-\pi^0)K^\pm$ samples in bins of $D$ phase space. . . . .	112
4.6	Efficiency in each bin of the $D$ phase space estimated from the $D^{*\pm} \rightarrow D(K_S^0\pi^+\pi^-\pi^0)\pi^\pm$ signal MC sample. . . . .	113
4.7	Migration matrix for $B^\pm \rightarrow D(K_S^0\pi^+\pi^-\pi^0)\pi^\pm$ sample estimated from signal MC. The rows correspond to the true bins and columns show the reconstructed bins. . . . .	116
4.8	Migration matrix for $B^\pm \rightarrow D(K_S^0\pi^+\pi^-\pi^0)K^\pm$ sample estimated from signal MC. The rows correspond to the true bins and columns show the reconstructed bins. . . . .	116

4.9	Migration matrix for $D^{*\pm} \rightarrow D(K_S^0\pi^+\pi^-\pi^0)\pi^\pm$ sample estimated from signal MC. The rows correspond to the true bins and columns show the reconstructed bins. . . . .	116
5.1	Yields obtained from two-dimensional fit in $D^{*\pm} \rightarrow D\pi^\pm$ generic MC sample. . . . .	123
5.2	Yields obtained from two-dimensional fit in data sample. The total as well as $D^0$ and $\bar{D}^0$ category yields are given. . . . .	124
5.3	$D^0$ and $\bar{D}^0$ yield in each bin of $D$ phase space along with $K_i$ and $\bar{K}_i$ values measured in $D^{*\pm} \rightarrow D\pi^\pm$ data sample. . . . .	125
5.4	Fit parameters for $\Delta E$ distribution of signal events in $B^+ \rightarrow D(K_S^0\pi^+\pi^-\pi^0)\pi^+$ signal MC sample. . . . .	127
5.5	Fit parameters for $\Delta E$ distribution of misreconstructed $\pi^0$ events in $B^+ \rightarrow D(K_S^0\pi^+\pi^-\pi^0)\pi^+$ signal MC sample. . . . .	130
5.6	Fit parameters for $\Delta E$ distribution of cross-feed peaking background events from $B^+ \rightarrow DK^+$ in $B^+ \rightarrow D(K_S^0\pi^+\pi^-\pi^0)\pi^+$ sample. . . . .	131
5.7	Fit parameters for $C'_{\text{NN}}$ distribution of signal component in $B^+ \rightarrow D(K_S^0\pi^+\pi^-\pi^0)\pi^+$ signal MC sample. . . . .	133
5.8	Fit parameters for $C'_{\text{NN}}$ distribution of background events in $B^+ \rightarrow D(K_S^0\pi^+\pi^-\pi^0)\pi^+$ generic MC sample. . . . .	133
5.9	Fit parameters for $\Delta E$ distribution of signal and continuum background events in $B^+ \rightarrow D(K_S^0\pi^+\pi^-\pi^0)K^+$ signal and generic MC samples, respectively. . . . .	138
5.10	Fit parameters for $\Delta E$ distribution of combinatorial $B\bar{B}$ events in $B^+ \rightarrow D(K_S^0\pi^+\pi^-\pi^0)K^+$ generic MC sample. . . . .	138
5.11	Fit parameters for $\Delta E$ distribution of cross-feed peaking background events from $B^+ \rightarrow D\pi^+$ in $B^+ \rightarrow D(K_S^0\pi^+\pi^-\pi^0)K^+$ sample. . . . .	139
5.12	Fit parameters for $C'_{\text{NN}}$ distribution of signal and background events in $B^+ \rightarrow D(K_S^0\pi^+\pi^-\pi^0)\pi^+$ signal and generic MC samples, respectively. . . . .	141
5.13	The PDFs used in the simultaneous fit of $B^+ \rightarrow D\pi^+$ and $B^+ \rightarrow DK^+$ decays along with the parameter information. . . . .	143
5.14	Residuals of yields in nine bins from simultaneous fit to five independent samples of generic MC. . . . .	147
5.15	Signal yields in bins obtained from the total two-dimensional simultaneous fit to the nine bins of $B^+ \rightarrow D\pi^+$ and $B^+ \rightarrow DK^+$ decays in generic MC sample with integrated luminosity equivalent to that of data. . . . .	147
5.16	PDF shape parameter values obtained from the total two-dimensional simultaneous fit to the nine bins of $B^+ \rightarrow D\pi^+$ and $B^+ \rightarrow DK^+$ generic MC sample with integrated luminosity equivalent to that of data. . . . .	149

5.17	Signal yield in nine $D$ phase space bin for $B^+ \rightarrow D\pi^+$ and $B^+ \rightarrow DK^+$ decays in data. . . . .	151
5.18	PDF shape parameter values obtained from the total two-dimensional simultaneous fit to the nine bins of $B^+ \rightarrow D\pi^+$ and $B^+ \rightarrow DK^+$ decays in data sample. . . . .	151
5.19	Mean and width of the pull distributions of $x_{\pm}$ and $y_{\pm}$ parameters from 250 pseudo-experiments. . . . .	155
5.20	$x_{\pm}$ and $y_{\pm}$ results from $B^{\pm} \rightarrow D\pi^{\pm}$ and $B^{\pm} \rightarrow DK^{\pm}$ decays in data. . . . .	156
5.21	Statistical correlation matrix for $(x_+, y_+, x_-, y_-)$ measured from the $B^{\pm} \rightarrow D\pi^{\pm}$ data sample . . . . .	157
5.22	Statistical correlation matrix for $(x_+, y_+, x_-, y_-)$ measured from the $B^{\pm} \rightarrow DK^{\pm}$ data sample . . . . .	158
5.23	Systematic uncertainties from various sources in $B^{\pm} \rightarrow D\pi^{\pm}$ and $B^{\pm} \rightarrow DK^{\pm}$ data samples. . . . .	161
5.24	$x_{\pm}$ and $y_{\pm}$ parameters from a combined fit to $B^{\pm} \rightarrow D\pi^{\pm}$ and $B^{\pm} \rightarrow DK^{\pm}$ data samples. The first uncertainty is statistical, the second is systematic, and the third is due to the uncertainty on the $c_i, s_i$ measurements. . . . .	162
5.25	$(\phi_3, \delta_B, r_B)$ obtained from the $B^{\pm} \rightarrow DK^{\pm}$ data sample. The first uncertainty is statistical, second is systematic and, the third one is due to the uncertainty on $c_i, s_i$ measurements. . . . .	163
5.26	Fraction of events in one, two, and three standard deviation regions of $x_{\pm}$ - $y_{\pm}$ plane from the simulated dataset. . . . .	164
6.1	DSSD specifications used in the SVD. . . . .	172
6.2	Typical CMM results for an L4 ladder. FW, CE and BW stands for forward, central and backward DSSDs. . . . .	175
6.3	Number of defective strips on $p$ - and $n$ -sides of a DSSD of an L4 ladder. . . . .	177
6.4	Selection criteria to reconstruct $D^*$ candidates in phase II data. . . . .	181
6.5	Resolution in MC and scale factor on that in data for Cabibbo-favoured $D$ final states in phase II data. . . . .	185
A.1	Background subtracted efficiency corrected yields of $D \rightarrow K_S^0\pi^+\pi^-\pi^0$ decays tagged with $K_S^0\pi^+\pi^-$ and $K_L^0\pi^+\pi^-$ modes in bins of the tagging decay. . . . .	198
A.2	$F_+$ results for the mode $K_S^0\pi^+\pi^-\pi^0$ from the tags $K_S^0\pi^+\pi^-$ and $K_L^0\pi^+\pi^-$ . The row $K_{S,L}^0\pi^+\pi^-$ indicates that the combined fit includes both the samples. The fit quality metric $\chi^2/DoF$ is also shown, where $DoF$ stands for the number of degrees of freedom. . . . .	198
A.3	$F_+$ results from different tag methods. . . . .	199

## LIST OF FIGURES

1.1	A $b \rightarrow u$ quark transition where the vertex factor is proportional to $V_{ub}$ .	6
1.2	Unitarity triangle in the $\bar{\rho} - \bar{\eta}$ plane [14]. . . . .	8
1.3	Experimental constraints of the unitarity triangle in $\bar{\rho} - \bar{\eta}$ plane [22].	9
1.4	Feynman diagrams for $B \rightarrow \bar{D}^{(*)} \mu \nu$ (left) and $B^0 - \bar{B}^0$ mixing (right) processes. . . . .	10
1.5	Experimental constraints of the unitarity triangle in $\bar{\rho} - \bar{\eta}$ plane coming from tree-level (top) and loop-level (bottom) processes [22]. . . . .	10
1.6	Colour-favoured (left) and colour-suppressed (right) $B^- \rightarrow DK^-$ processes. . . . .	11
1.7	Dalitz plot of $D \rightarrow K_S^0 \pi^+ \pi^-$ partitioned into different bins. The dashed line shows the symmetry axis, $s_{12} = m_{K_S^0 \pi^-}^2$ and $s_{13} = m_{K_S^0 \pi^+}^2$ [34].	15
1.8	One and two standard deviation contours in $\phi_3(\gamma) - r_B$ plane obtained from all the measurements using different $D$ final states [29]. . . . .	21
1.9	A Feynman diagram for the process $D^0 \rightarrow K_S^0 \pi^+ \pi^- \pi^0$ . . . . .	21
2.1	Schematic view of CESR with the accelerator units, along with the CLEO-c detector position [43]. . . . .	24
2.2	Cut-out view of the CLEO-c detector [44]. . . . .	25
2.3	Distribution of $ \vec{p} $ vs. $dE/dx$ for charged hadron tracks. [42]. . . . .	28
2.4	Cross section view of the RICH detector. The solid black arrow indicates the charged particle and the dashed arrows show the emitted light [41]. . . . .	29
2.5	Number of standard deviations between different particle hypotheses as a function of momentum obtained by the CLEO-c RICH detector [41].	30
2.6	Schematic of the KEKB accelerator complex [49]. . . . .	32
2.7	A schematic of cross-angle and crab crossings [55]. . . . .	33
2.8	Cross sections of various $\Upsilon$ resonances from $e^+e^-$ collisions [56]. . . . .	34
2.9	Schematic view of the Belle detector cross section [58]. . . . .	34
2.10	Schematic view of the SVD1 subsystem of Belle [60]. . . . .	36
2.11	Schematic view of the SVD2 subsystem of Belle [63]. . . . .	36

2.12	Resolution of the impact parameter measured by the SVD [58]. Here $p$ , $\beta$ and $\theta$ are the momentum, Lorentz boost factor and polar angle, respectively. . . . .	37
2.13	Schematic view of the CDC subsystem of Belle [64]. . . . .	38
2.14	$dE/dx$ measurements for various particle types as a function of momentum [58]. . . . .	39
2.15	Schematic view of the ACC subsystem of Belle [58]. . . . .	40
2.16	Kaon identification efficiency and pion fake rate from $D^{*+} \rightarrow D^0(K^-\pi^+)\pi^+$ decays using information from the ACC [58]. . . . .	40
2.17	Schematic view of the TOF modules and their dimensions [58]. . . . .	41
2.18	Mass distribution obtained from TOF measurements. The black points with error bars are the data points and histogram is the prediction from Monte Carlo simulations [66]. . . . .	42
2.19	Schematic view of the ECL subsystem of Belle [58]. . . . .	43
2.20	Energy resolution measured from Bhabha scattering in total (top left), barrel (top right), forward endcap (bottom left) and backward endcap (bottom right) regions of the ECL [58]. . . . .	44
2.21	An overview of the Belle trigger system [67]. . . . .	46
2.22	A schematic of the Belle DAQ system [58]. . . . .	47
3.1	Schematic diagram of a double-tagged event at CLEO-c. . . . .	51
3.2	$M_{\pi^0}$ distribution of MC simulated $D^0 \rightarrow K_S^0\pi^+\pi^-\pi^0$ single-tagged candidates after applying the selection criteria. . . . .	53
3.3	$M_\eta$ distribution of MC simulated $D^0 \rightarrow K_S^0\pi^+\pi^-\pi^0$ decays produced with $\overline{D}^0 \rightarrow K_S^0\eta$ decays. The vertical dotted lines indicate the signal region . . . . .	54
3.4	$M_{K_S^0}$ distribution of MC simulated $D^0 \rightarrow K_S^0\pi^+\pi^-\pi^0$ single-tagged candidates. The vertical dotted lines indicate the signal region . . . . .	55
3.5	$K_S^0$ flight significance distribution of MC simulated $D^0 \rightarrow K_S^0\pi^+\pi^-\pi^0$ single-tagged candidates. The red and blue solid lines indicate the signal and background components, respectively. The vertical dotted line indicates the selection criteria. . . . .	55
3.6	$M_{\eta'}$ distribution of MC simulated $D^0 \rightarrow K_S^0\pi^+\pi^-\pi^0$ decays tagged with $\overline{D}^0 \rightarrow K_S^0\eta'$ decays. The vertical dotted lines indicate the signal region . . . . .	56
3.7	$M_\omega$ distribution of MC simulated $D^0 \rightarrow K_S^0\pi^+\pi^-\pi^0$ decays tagged with $\overline{D}^0 \rightarrow K_L^0\omega$ decays. The vertical dotted lines indicate the signal region . . . . .	56
3.8	$\Delta E$ distribution for $D^0 \rightarrow K_S^0\pi^+\pi^-\pi^0$ single-tagged candidates in data. The vertical dotted lines indicate the signal region. . . . .	58

3.9	$m_{\text{miss}}^2$ distribution of MC simulated $D^0 \rightarrow K_S^0 \pi^+ \pi^- \pi^0$ decays tagged with $\overline{D^0} \rightarrow K_L^0 \pi^0$ decays. . . . .	59
3.10	$U_{\text{miss}}$ distribution of MC simulated $D^0 \rightarrow K_S^0 \pi^+ \pi^- \pi^0$ decays tagged with $\overline{D^0} \rightarrow K^\pm e^\mp \nu_e$ decays. . . . .	60
3.11	$m_{\text{bc}}$ distribution for the signal component of single-tagged $D^0 \rightarrow K_S^0 \pi^+ \pi^- \pi^0$ decays in MC fitted with the sum of an asymmetric Gaussian and two Gaussian functions. Blue solid curve represents the total fit and red, blue and green dashed curves are asymmetric Gaussian, narrow Gaussian and broad Gaussian function, respectively. . . . .	63
3.12	$m_{\text{bc}}$ distribution for the background component of single-tagged $D \rightarrow K_S^0 \pi^+ \pi^- \pi^0$ decays in MC with different contributions shown separately. Here, “bkg” stands for background. . . . .	64
3.13	$m_{\text{bc}}$ distribution for the background component of single-tagged $D^0 \rightarrow K_S^0 \pi^+ \pi^- \pi^0$ decays in MC fitted with the sum of an Argus, Crystal Ball and Gaussian PDFs. Blue solid curve represents the total fit and blue, red and green dashed curves are Argus, Crystal Ball and Gaussian PDF, respectively. . . . .	65
3.14	$m_{\text{bc}}$ distribution for single-tagged $D^0 \rightarrow K_S^0 \pi^+ \pi^- \pi^0$ decays in data. The black points are data, the solid blue curve is the total fit and the dashed red and blue curves are signal and background fit components, respectively. . . . .	65
3.15	$m_{\text{bc}}$ distributions for $D^0 \rightarrow K_S^0 \pi^+ \pi^- \pi^0$ decays tagged by $CP$ -even states (left) and $CP$ -odd states (right) both not involving a $K_L^0$ meson in data. The shaded histogram shows the estimated peaking background and the vertical dotted lines indicate the signal region. . . . .	66
3.16	$m_{\text{bc}}$ distribution for $D^0 \rightarrow K_S^0 \pi^+ \pi^- \pi^0$ decays tagged by $K_S^0 \pi^+ \pi^-$ events in data. The shaded histogram shows the estimated peaking background and the vertical dotted lines indicate the signal region. . . . .	67
3.17	Dalitz plot distribution for the tag $K_S^0 \pi^+ \pi^-$ against $D \rightarrow K_S^0 \pi^+ \pi^- \pi^0$ decays. The axis labels $m_\pm^2$ represents the invariant mass squares of $K_{S,L}^0 \pi^\pm$ pairs. . . . .	67
3.18	Division of the two dimensional $m_{\text{bc}}$ plane distribution. The red square box indicates the signal region and the remaining boxes show the various sideband regions that are used to determine the combinatorial background contribution. . . . .	68
3.19	Two dimensional $m_{\text{bc}}$ plane distribution for $D^0 \rightarrow K_S^0 \pi^+ \pi^- \pi^0$ tagged with $\overline{D^0} \rightarrow K_L^0 \pi^0$ decays. The red square box indicates the signal region and the remaining boxes show the various sideband regions that are used to determine the combinatorial background contribution. . . . .	69
3.20	$m_{\text{miss}}^2$ distribution for background events of $D^0 \rightarrow K_S^0 \pi^+ \pi^- \pi^0$ decays tagged by $\overline{D^0} \rightarrow K_L^0 \pi^0$ decays in MC sample. Here “PBkg sig” refers to peaking background in signal-side decay of $D^0 \rightarrow K_S^0 \pi^+ \pi^- \pi^0$ and “Comb bkg” refers to combinatorial background. . . . .	72

3.21	$m_{\text{miss}}^2$ distribution for background events of $D^0 \rightarrow K_S^0 \pi^+ \pi^- \pi^0$ decays tagged by $\overline{D^0} \rightarrow K_L^0 \omega$ decays in MC sample. Here “PBkg sig” refers to peaking background in signal-side decay of $D^0 \rightarrow K_S^0 \pi^+ \pi^- \pi^0$ and “Comb bkg” refers to combinatorial background. . . . .	73
3.22	$m_{\text{miss}}^2$ distribution for background events of $D^0 \rightarrow K_S^0 \pi^+ \pi^- \pi^0$ decays tagged by $\overline{D^0} \rightarrow K_L^0 \pi^+ \pi^-$ decays in MC sample. Here “PBkg sig” refers to peaking background in signal-side decay of $D^0 \rightarrow K_S^0 \pi^+ \pi^- \pi^0$ and “Comb bkg” refers to combinatorial background. . . . .	74
3.23	$U_{\text{miss}}$ distribution for background events of $D^0 \rightarrow K_S^0 \pi^+ \pi^- \pi^0$ decays tagged by $\overline{D^0} \rightarrow K^\pm e^\mp \nu_e$ , decays in MC sample. Here, “bkg” refers to background. . . . .	74
3.24	$m_{\text{miss}}^2$ distributions for $D \rightarrow K_S^0 \pi^+ \pi^- \pi^0$ decays tagged by $CP$ -even states involving a $K_L^0$ meson (left) and $K_L^0 \pi^+ \pi^-$ (right). The shaded histogram shows the estimated peaking background and the vertical dotted lines indicate the signal region. . . . .	75
3.25	$U_{\text{miss}}$ distribution for $K^\pm e^\mp \nu_e$ tag. The shaded histogram shows the estimated peaking background and the vertical dotted lines indicate the signal region. . . . .	75
3.26	Dalitz plot distributions for the tag $K_L^0 \pi^+ \pi^-$ against $D \rightarrow K_S^0 \pi^+ \pi^- \pi^0$ decays. The axis labels $m_\pm^2$ represents the invariant mass squares of $K_{S,L}^0 \pi^\pm$ pairs. . . . .	76
3.27	Invariant mass distributions for $\pi^+ \pi^- \pi^0$ (top left), $K_S^0 \pi^-$ (top right), $\pi^+ \pi^0$ (bottom left) and $K_S^0 \pi^0$ (bottom right) of $D \rightarrow K_S^0 \pi^+ \pi^- \pi^0$ decays tagged by $K^\pm e^\mp \nu$ . Candidates from the pervious bins are removed sequentially in the order given in Table 3.9. The vertical dotted lines indicate the selected mass windows for the $\omega$ , $K^*$ and $\rho$ resonances, respectively. . . . .	77
3.28	$\pi^+ \pi^- \pi^0$ invariant mass fitted with a double Gaussian and polynomial PDFs in MC sample. Blue solid curve represents the total fit and red and blue dashed curves are double Gaussian and polynomial functions, respectively. . . . .	85
3.29	$\pi^+ \pi^- \pi^0$ invariant mass fitted with a double Gaussian and polynomial PDFs in data sample. Blue solid curve represents the total fit and red and blue dashed curves are double Gaussian and polynomial functions, respectively. . . . .	85
3.30	$c_i$ and $s_i$ values in each bin. The black and red error bars represent statistical and systematic uncertainties, respectively. . . . .	88
4.1	$L(K/\pi)$ distributions for charged pion and kaon tracks in the signal MC sample. . . . .	91
4.2	$M_{K_S^0}$ distribution after applying the selection criteria in $B^+ \rightarrow D(K_S^0 \pi^+ \pi^- \pi^0) K^+$ signal MC sample. . . . .	92

4.3	$M_{\pi^0}$ distribution in $B^+ \rightarrow D(K_S^0\pi^+\pi^-\pi^0)K^+$ signal MC sample. The vertical dotted lines indicate the selected region. . . . .	93
4.4	$M_D$ distribution in $B^+ \rightarrow D(K_S^0\pi^+\pi^-\pi^0)K^+$ signal MC sample. The vertical dotted lines indicate the selected region. . . . .	94
4.5	$M_{bc}$ (left) and $\Delta E$ (right) distributions in $B^+ \rightarrow D(K_S^0\pi^+\pi^-\pi^0)K^+$ signal MC sample. The vertical dotted line indicates the selected region in $M_{bc}$ . . . . .	95
4.6	$M_{bc}$ (left) and $\Delta E$ (right) distributions in $B^+ \rightarrow D(K_S^0\pi^+\pi^-\pi^0)K^+$ generic background MC sample. The vertical dotted line indicates the selected region in $M_{bc}$ . . . . .	95
4.7	$\Delta E$ distribution in the $B^+ \rightarrow D(K_S^0\pi^+\pi^-\pi^0)K^+$ signal MC sample before applying any kinematic or vertex constraints (left) and after applying mass-vertex constraints on $K_S^0$ , $\pi^0$ and $D$ and vertex constraint on $B^+$ (right). Black points with error bar are signal MC sample and blue solid curve represent the total fit. $\sigma_{CB}$ is the resolution of the core Crystal Ball function shown by the red dotted curve. The double Gaussian is shown by the blue dotted curve. . . . .	96
4.8	Slow pion momentum distribution in the $D^{*+} \rightarrow D(K_S^0\pi^+\pi^-\pi^0)\pi^+$ signal MC sample. . . . .	97
4.9	$M_D$ (left) and $\Delta M$ (right) distributions in $D^{*+} \rightarrow D(K_S^0\pi^+\pi^-\pi^0)\pi_{\text{slow}}^+$ signal MC sample. . . . .	97
4.10	$p_D$ distribution in the lab frame for (blue) $D^{*+}$ and (red) $B^+ \rightarrow Dh^+$ signal MC samples. The vertical dotted line indicates the selected region. . . . .	98
4.11	$S/\sqrt{S+B}$ and efficiency distributions after the two dimensional optimization of the photon energy requirements in the MC sample for events with both the photons coming from barrel region of the ECL. The black point shows the optimized requirement. . . . .	100
4.12	$S/\sqrt{S+B}$ and efficiency distributions after the two dimensional optimization of the photon energy requirements in the MC sample for events with one photon coming from FWD endcap and the other from barrel regions of the ECL. The black point shows the optimized requirement. . . . .	100
4.13	$S/\sqrt{S+B}$ and efficiency distributions after the two dimensional optimization of the photon energy requirements in the MC sample for events with both one photon coming from barrel and the other from BWD endcap regions of the ECL. The black point shows the optimized requirement. . . . .	101
4.14	$S/\sqrt{S+B}$ and efficiency distributions after the two dimensional optimization of the photon energy requirements in the MC sample for events with both the photons coming from FWD endcap region of the ECL. The black point shows the optimized requirement. . . . .	101

4.15	$\pi^+\pi^-\pi^0$ invariant mass distribution with $p_{\pi^0} > 0.3$ GeV/c and with optimized $E_\gamma$ threshold criteria in $B^+ \rightarrow D(K_S^0\omega(\pi^+\pi^-\pi^0))K^+$ signal MC sample (left) and the $S/\sqrt{S+B}$ distribution with different $p_{\pi^0}$ selection criteria . . . . .	102
4.16	The event topology of $e^+e^- \rightarrow \Upsilon(4S) \rightarrow B\bar{B}$ (left) and $e^+e^- \rightarrow q\bar{q}$ (right) events. . . . .	103
4.17	Directions of momenta of particles $i$ and $j$ in an event and the angle between them, $\theta_{ij}$ . . . . .	103
4.18	Distribution of the likelihood ratio formed from the Fisher discriminants in MC sample. The red and blue histograms show $B\bar{B}$ and $q\bar{q}$ events, respectively. . . . .	104
4.19	$ \cos\theta_B $ (left) and $ \cos\theta_T $ (right) distributions in MC sample. The red and blue histograms show $B\bar{B}$ and $q\bar{q}$ events, respectively. . . . .	105
4.20	$\Delta z$ ( top left), $ qr $ (top right), $\Delta Q$ (bottom left) and $Q_B Q_K$ (bottom right) distributions in MC sample. The red and blue histograms show $B\bar{B}$ and $q\bar{q}$ events, respectively. . . . .	106
4.21	$\cos\theta_D^B$ distribution in MC sample. The red and blue histograms show $B\bar{B}$ and $q\bar{q}$ events, respectively. . . . .	107
4.22	$C_{NN}$ (left) and $C'_{NN}$ (right) distributions in the MC samples. The red and blue histograms show $B\bar{B}$ and $q\bar{q}$ events, respectively. . . . .	108
4.23	ROC curve demonstrating the signal efficiency <i>vs.</i> background rejection of the NN. The performance of the LR is also shown in red solid line. . . . .	108
4.24	The $\Delta M$ distribution in $B^+ \rightarrow D(K_S^0\pi^+\pi^-\pi^0)K^+$ generic MC sample. The range is zoomed in near to 0.145 GeV/c. . . . .	109
4.25	$B^+$ (left) and $D^{*+}$ (right) candidate multiplicities after applying all the selection criteria in $B^+ \rightarrow D(K_S^0\pi^+\pi^-\pi^0)K^+$ and $D^{*+} \rightarrow D(K_S^0\pi^+\pi^-\pi^0)\pi^+$ signal MC samples, respectively. . . . .	110
4.26	$M_{bc}$ (left) and $M_D$ (right) distributions in $B^+ \rightarrow D(K_S^0\pi^+\pi^-\pi^0)K^+$ signal MC sample. Black points with error bar are data and blue solid line is the fit model. . . . .	111
4.27	$M_{\pi^0}$ distribution in $B^+ \rightarrow D(K_S^0\pi^+\pi^-\pi^0)K^+$ signal MC sample. Black points with error bar are data and blue solid line is the fit model. . . . .	111
4.28	Ratio of $D^*$ and $B$ efficiencies across the nine $D$ phase space bins. . . . .	113
4.29	$\pi^+\pi^-\pi^0$ invariant mass distribution in $B^+ \rightarrow D(K_S^0\pi^+\pi^-\pi^0)\pi^+$ generic MC (left) and data (right) samples. Black points with error bars show the data and blue solid curve is the fit model. . . . .	114
4.30	$\pi^+\pi^-\pi^0$ invariant mass distribution in $D^{*+} \rightarrow D(K_S^0\pi^+\pi^-\pi^0)\pi^+$ generic MC (left) and data (right) samples. Black points with error bars show the data and blue solid curve is the fit model. . . . .	115

5.1	One-dimensional fit distributions of $M_D$ (left) and $\Delta M$ (right) signal component in $D^{*\pm} \rightarrow D\pi^\pm$ generic MC sample. Black points with error bars indicate data and the solid blue curve is the total fit. The pull between the fit and the data is shown below the distributions. The red and blue dotted lines in $M_D$ projection represent Crystal Ball and double Gaussian PDFs, respectively. In $\Delta M$ projection, blue, red and green dotted lines indicate double Gaussian, asymmetric Gaussian and Gaussian PDFs, respectively. . . . .	118
5.2	$\Delta M$ distribution of misreconstructed $\pi^0$ events in $D^{*\pm} \rightarrow D\pi^\pm$ generic MC sample. Black points with error bars indicate data and the solid blue curve is the total fit. The blue and red dotted lines show the two Gaussian PDFs. . . . .	119
5.3	One-dimensional fit distributions of $M_D$ (left) and $\Delta M$ (right) combinatorial component in $D^{*\pm} \rightarrow D\pi^\pm$ generic MC sample. Black points with error bars indicate data and the solid blue curve is the total fit. The pull between the fit and the data is shown below the distributions. The red and blue dotted lines in $\Delta M$ projection represent the peaking component and threshold function PDF, respectively. . . . .	120
5.4	The resolution of $\Delta M$ in different $M_D$ regions determined from $D^{*\pm} \rightarrow D\pi^\pm$ generic MC sample. . . . .	121
5.5	Projections of $M_D$ (left) and $\Delta M$ (right) from a two-dimensional fit to the signal component in $D^{*\pm} \rightarrow D\pi^\pm$ generic MC sample. Black points with error bars indicate data and the solid blue curve is the total fit. The pull between the fit and the data is shown below the distributions. . . . .	122
5.6	Projections of $M_D$ (left) and $\Delta M$ (right) from a two-dimensional fit to the random-slow-pion background component in $D^{*\pm} \rightarrow D\pi^\pm$ generic MC sample. Black points with error bars indicate data and the solid blue curve is the total fit. The pull between the fit and the data is shown below the distributions. . . . .	122
5.7	Signal-enhanced fit projections of $M_D$ (left) and $\Delta M$ (right) distributions from $D^{*\pm} \rightarrow D\pi^\pm$ generic MC sample. The black points with error bars are the data and the solid blue curve shows the total fit. The dotted red, blue and magenta curves represent the signal, combinatorial and random-slow-pion backgrounds respectively. The pull between the fit and the data is shown below the distributions. . . . .	123
5.8	Signal-enhanced fit projections of $M_D$ (left) and $\Delta M$ (right) distributions from data. The black points with error bars are the data and the solid blue curve shows the total fit. The dotted red, blue and magenta curves represent the signal, combinatorial and random-slow-pion backgrounds respectively. The pull between the fit and the data is shown below the distributions. . . . .	124

5.9	Signal-enhanced fit projections of $M_D$ (left) and $\Delta M$ (right) distributions from data in bin 1. The black points with error bars are the data and the solid blue curve shows the total fit. The dotted red, blue and magenta curves represent the signal, combinatorial and random-slow-pion backgrounds respectively. The pull between the fit and the data is shown below the distributions. . . . .	125
5.10	One-dimensional fit to the $\Delta E$ distributions of signal component in $B^+ \rightarrow D(K_S^0 \pi^+ \pi^- \pi^0) \pi^+$ signal MC sample. Black points with error bars indicate data and the solid blue curve is the total fit. The pull between the fit and the data is shown below the distributions. The red and blue dotted curves in represent Crystal Ball and double Gaussian PDFs, respectively. . . . .	127
5.11	One-dimensional fit to the $\Delta E$ distribution of continuum background events in $B^+ \rightarrow D(K_S^0 \pi^+ \pi^- \pi^0) \pi^+$ generic MC sample. Black points with error bars indicate data and the solid blue curve is the total fit. The pull between the fit and the data is shown below the distributions. . . . .	128
5.12	$\Delta E$ distribution of combinatorial $B\bar{B}$ background events in $B^+ \rightarrow D(K_S^0 \pi^+ \pi^- \pi^0) \pi^+$ generic MC sample. Different possible contributions are separately shown as stacked histograms. The vertical lines show the signal region. . . . .	129
5.13	$\Delta E$ distribution of misreconstructed $\pi^0$ events in $B^+ \rightarrow D(K_S^0 \pi^+ \pi^- \pi^0) \pi^+$ signal MC sample fitted with a Crystal Ball PDF. Black points with error bars indicate data and the solid blue curve is the total fit. The pull between the fit and the data is shown below the distributions. . . . .	129
5.14	One-dimensional fit to the $\Delta E$ distribution of combinatorial $B\bar{B}$ background events in $B^+ \rightarrow D(K_S^0 \pi^+ \pi^- \pi^0) \pi^+$ generic MC sample. Black points with error bars indicate data and the solid blue curve is the total fit. The pull between the fit and the data is shown below the distributions. The dotted magenta and red curves indicate the exponential and Crystal Ball PDFs, respectively. . . . .	130
5.15	One-dimensional fit to the $\Delta E$ distribution of cross-feed peaking background events from $B^+ \rightarrow DK^+$ in $B^+ \rightarrow D(K_S^0 \pi^+ \pi^- \pi^0) \pi^+$ sample. Black points with error bars indicate data and the solid blue curve is the total fit. The pull between the fit and the data is shown below the distributions. The dotted red, magenta and green curves indicate the three Gaussian PDFs. . . . .	131
5.16	One-dimensional fit to the $C'_{\text{NN}}$ distributions of signal (left) and cross-feed peaking background (right) events from $B^+ \rightarrow D(K_S^0 \pi^+ \pi^- \pi^0) \pi^+$ signal MC sample. The black points with error bars are the data and the solid blue curve shows the total fit. The dotted red and green curves represent the Gaussian and asymmetric Gaussian PDFs, respectively. The dotted magenta curve shows the $C'_{\text{NN}}$ signal PDF overlayed on the cross-feed peaking background model. The pull between the fit and the data is shown below the distributions. . . . .	132

5.17	One-dimensional fit to the $C'_{\text{NN}}$ distributions of continuum (left) and combinatorial $B\bar{B}$ background (right) events from $B^+ \rightarrow D(K_S^0\pi^+\pi^-\pi^0)\pi^+$ generic MC sample. The black points with error bars are the data and the solid blue curve shows the total fit. The dotted red and green curves represent the two Gaussian PDFs. The pull between the fit and the data is shown below the distributions. . . . .	132
5.18	$B^+$ candidate multiplicities in $B^+ \rightarrow D(K_S^0\pi^+\pi^-\pi^0)\pi^+$ generic MC and data samples with equal integrated luminosities after applying all the selection criteria mentioned in Chapter 4. . . . .	134
5.19	$\Delta E$ (left) and $C'_{\text{NN}}$ distributions in $B^+ \rightarrow D(K_S^0\pi^+\pi^-\pi^0)\pi^+$ generic MC sample before and after the best-candidate selection. . . . .	134
5.20	$\Delta E$ distribution in $B^+ \rightarrow D(K_S^0\pi^+\pi^-\pi^0)\pi^+$ generic MC and data samples with equal integrated luminosities. . . . .	135
5.21	$C'_{\text{NN}}$ distributions in signal (left) and higher sideband (right) regions of $\Delta E$ in $B^+ \rightarrow D(K_S^0\pi^+\pi^-\pi^0)\pi^+$ generic MC and data samples. . . . .	136
5.22	LR of KSFW moments (left) and $\Delta z$ (right) distributions in higher $\Delta E$ sideband region in $B^+ \rightarrow D(K_S^0\pi^+\pi^-\pi^0)\pi^+$ generic MC and data samples. . . . .	136
5.23	One-dimensional fit to the $\Delta E$ distributions of signal (left) and continuum background (right) events in $B^+ \rightarrow D(K_S^0\pi^+\pi^-\pi^0)K^+$ signal and generic MC samples, respectively. Black points with error bars indicate data and the solid blue curve is the total fit. The pull between the fit and the data is shown below the distributions. The red and blue dotted curves in represent Crystal Ball and double Gaussian PDFs, respectively. . . . .	137
5.24	One-dimensional fit to the $\Delta E$ distribution of combinatorial $B\bar{B}$ background events in $B^+ \rightarrow D(K_S^0\pi^+\pi^-\pi^0)K^+$ generic MC sample. Black points with error bars indicate data and the solid blue curve is the total fit. The pull between the fit and the data is shown below the distributions. The dotted blue, green and red curves indicate the Chebyshev polynomial, exponential function and Crystal Ball PDF, respectively. . . . .	138
5.25	One-dimensional fit to the $\Delta E$ distribution of cross-feed peaking background events from $B^+ \rightarrow D\pi^+$ decays in $B^+ \rightarrow D(K_S^0\pi^+\pi^-\pi^0)K^+$ sample. Black points with error bars indicate data and the solid blue curve is the total fit. The pull between the fit and the data is shown below the distributions. The dotted magenta, blue and red curves indicate the Gaussian PDFs. . . . .	139
5.26	One-dimensional fit to the $C'_{\text{NN}}$ distributions of signal (left) and cross-feed peaking background (right) events from $B^+ \rightarrow D(K_S^0\pi^+\pi^-\pi^0)K^+$ signal MC sample. The black points with error bars are the data and the solid blue curve shows the total fit. The dotted red and green curves represent the Gaussian and asymmetric Gaussian PDFs, respectively. The dotted magenta curve shows the $C'_{\text{NN}}$ signal PDF overlaid on the cross-feed peaking background model. The pull between the fit and the data is shown below the distributions. . . . .	140

5.27	One-dimensional fit to the $C'_{\text{NN}}$ distributions of continuum (left) and combinatorial $B\bar{B}$ background (right) events from $B^+ \rightarrow D(K_S^0\pi^+\pi^-\pi^0)K^+$ generic MC sample. The black points with error bars are the data and the solid blue curve shows the total fit. The dotted red and green curves represent the two Gaussian PDFs. The pull between the fit and the data is shown below the distributions. . . . .	140
5.28	Two-dimensional distributions between $\Delta E$ and $C'_{\text{NN}}$ of signal (left), continuum (middle) and combinatorial $B\bar{B}$ background (right) events from $B^+ \rightarrow D(K_S^0\pi^+\pi^-\pi^0)\pi^+$ generic MC sample. . . . .	142
5.29	$\Delta E$ distribution of signal events in $B^+ \rightarrow D\pi^+$ (left) and $B^+ \rightarrow DK^+$ decays in each bin as well as in the integrated $D$ phase space in signal MC sample. . . . .	144
5.30	$\Delta E$ distribution of continuum background events in $B^+ \rightarrow D\pi^+$ (left) and $B^+ \rightarrow DK^+$ decays in each bin as well as in the integrated $D$ phase space in generic MC sample. . . . .	144
5.31	$\Delta E$ distribution of combinatorial $B\bar{B}$ background events in $B^+ \rightarrow D\pi^+$ (left) and $B^+ \rightarrow DK^+$ decays in each bin as well as in the integrated $D$ phase space in generic MC sample. . . . .	145
5.32	$C'_{\text{NN}}$ distribution of signal events in $B^+ \rightarrow D\pi^+$ (left) and $B^+ \rightarrow DK^+$ decays in each bin as well as in the integrated $D$ phase space in signal MC sample. . . . .	145
5.33	$C'_{\text{NN}}$ distribution of continuum background events in $B^+ \rightarrow D\pi^+$ (left) and $B^+ \rightarrow DK^+$ decays in each bin as well as in the integrated $D$ phase space in generic MC sample. . . . .	146
5.34	$C'_{\text{NN}}$ distribution of combinatorial $B\bar{B}$ background events in $B^+ \rightarrow D\pi^+$ (left) and $B^+ \rightarrow DK^+$ decays in each bin as well as in the integrated $D$ phase space in generic MC sample. . . . .	146
5.35	Signal-enhanced projections of $\Delta E$ (left) and $C'_{\text{NN}}$ (right) distributions of $B^\pm \rightarrow D(K_S^0\pi^+\pi^-\pi^0)\pi^\pm$ decays in bin 1 from a two-dimensional simultaneous fit to $B^\pm \rightarrow D\pi^\pm$ and $B^\pm \rightarrow DK^\pm$ events in generic MC sample with integrated luminosity equivalent to that of data. The black points with error bars are the data and the solid blue curve is the total fit. The dotted red, blue, magenta, and green curves represent the signal, continuum, random $B\bar{B}$ backgrounds and cross-feed peaking background components, respectively. The pull between the fit and the data is shown below the distributions. . . . .	148
5.36	Signal-enhanced projections of $\Delta E$ (left) and $C'_{\text{NN}}$ (right) distributions of $B^\pm \rightarrow D(K_S^0\pi^+\pi^-\pi^0)K^\pm$ decays in bin 1 from a two-dimensional simultaneous fit to $B^\pm \rightarrow D\pi^\pm$ and $B^\pm \rightarrow DK^\pm$ events in generic MC sample with integrated luminosity equivalent to that of data. The black points with error bars are the data and the solid blue curve is the total fit. The dotted red, blue, magenta, and green curves represent the signal, continuum, random $B\bar{B}$ backgrounds and cross-feed peaking background components, respectively. The pull between the fit and the data is shown below the distributions. . . . .	148

5.37	Signal-enhanced projections of $\Delta E$ (left) and $C'_{\text{NN}}$ (right) distributions of $B^\pm \rightarrow D(K_S^0 \pi^+ \pi^- \pi^0) \pi^\pm$ decays in bin 1 from a two-dimensional simultaneous fit to $B^\pm \rightarrow D\pi^\pm$ and $B^\pm \rightarrow DK^\pm$ events in data. The black points with error bars are the data and the solid blue curve is the total fit. The dotted red, blue, magenta, and green curves represent the signal, continuum, random $B\bar{B}$ backgrounds and cross-feed peaking background components, respectively. The pull between the fit and the data is shown below the distributions. . . . .	150
5.38	Signal-enhanced projections of $\Delta E$ (left) and $C'_{\text{NN}}$ (right) distributions of $B^\pm \rightarrow D(K_S^0 \pi^+ \pi^- \pi^0) K^\pm$ decays in bin 1 from a two-dimensional simultaneous fit to $B^\pm \rightarrow D\pi^\pm$ and $B^\pm \rightarrow DK^\pm$ events in data. The black points with error bars are the data and the solid blue curve is the total fit. The dotted red, blue, magenta, and green curves represent the signal, continuum, random $B\bar{B}$ backgrounds and cross-feed peaking background components, respectively. The pull between the fit and the data is shown below the distributions. . . . .	150
5.39	$x_+$ (left) and $y_+$ (right) results for $B^+ \rightarrow D\pi^+$ decays in five independent generic MC samples. . . . .	152
5.40	$x_-$ (left) and $y_-$ (right) results for $B^- \rightarrow D\pi^-$ decays in five independent generic MC samples. . . . .	152
5.41	$x_+$ (left) and $y_+$ (right) results for $B^+ \rightarrow DK^+$ decays in five independent generic MC samples. . . . .	153
5.42	$x_-$ (left) and $y_-$ (right) results for $B^- \rightarrow DK^-$ decays in five independent generic MC samples. . . . .	153
5.43	One (solid line), two (dashed line), and three (dotted line) standard deviation likelihood contours for the $(x_\pm, y_\pm)$ parameters for $B^\pm \rightarrow D\pi^\pm$ (left) and $B^\pm \rightarrow DK^\pm$ (right) decays in generic MC sample. The point marks the best fit value. . . . .	154
5.44	Measured and expected yields in bins for $B^+ \rightarrow D\pi^+$ (left) and $B^- \rightarrow D\pi^-$ (right) decays in generic MC sample. The data points with error bars are the measured yields and the solid histogram is the expected yield from the best fit $(x_\pm, y_\pm)$ parameter values. . . . .	154
5.45	Measured and expected yields in bins for $B^+ \rightarrow DK^+$ (left) and $B^- \rightarrow DK^-$ (right) decays in generic MC sample. The data points with error bars are the measured yields and the solid histogram is the expected yield from the best fit $(x_\pm, y_\pm)$ parameter values. . . . .	155
5.46	One (solid line), two (dashed line), and three (dotted line) standard deviation likelihood contours for the $(x_\pm, y_\pm)$ parameters for $B^\pm \rightarrow D\pi^\pm$ (left) and $B^\pm \rightarrow DK^\pm$ (right) decays in data. The point marks the best fit value and the cross marks the expected value from the world average values of $\phi_3$ , $r_B^{DK}$ , and $\delta_B^{DK}$ [29]. . . . .	156

5.47	Measured and expected yields in bins for $B^+ \rightarrow D\pi^+$ (left) and $B^- \rightarrow D\pi^-$ (right) data samples. The data points with error bars are the measured yields and the solid histogram is the expected yield from the best fit $(x_{\pm}, y_{\pm})$ parameter values. . . . .	156
5.48	Measured and expected yields in bins for $B^+ \rightarrow DK^+$ (left) and $B^- \rightarrow DK^-$ (right) data samples. The data points with error bars are the measured yields and the solid histogram is the expected yield from the best fit $(x_{\pm}, y_{\pm})$ parameter values. . . . .	157
5.49	$x_+^{D\pi}$ (left) and $y_+^{D\pi}$ (right) results for different input values in 250 pseudo experiment sets each. . . . .	159
5.50	$x_-^{D\pi}$ (left) and $y_-^{D\pi}$ (right) results for different input values in 250 pseudo experiment sets each. . . . .	159
5.51	$x_+^{DK}$ (left) and $y_+^{DK}$ (right) results for different input values in 250 pseudo experiment sets each. . . . .	160
5.52	$x_-^{DK}$ (left) and $y_-^{DK}$ (right) results for different input values in 250 pseudo experiment sets each. . . . .	160
5.53	Projection of the statistical confidence intervals in the $\phi_3 - r_B$ (left) and $\phi_3 - \delta_B$ (right) planes. The black, red, and blue contours represent the one, two, and three standard deviation regions, respectively. The crosses show the positions of the world-average values [29]. . . . .	163
5.54	$x_+ - y_+$ (left) and $x_- - y_-$ (right) results obtained from a set of 400 pseudo-experiments. The likelihood contours from data are included for comparison. . . . .	164
5.55	Distribution of p-value for $\phi_3$ from multibody $D$ final states at Belle, which is shown by the solid blue curve. The results from $B \rightarrow DK^{(*)}$ decays with $D \rightarrow K_S^0\pi^+\pi^-$ are shown by the solid green curve and the $D \rightarrow K_S^0\pi^+\pi^-\pi^0$ final states are shown by the solid brown curve [78, 94]. . . . .	165
5.56	Projections of the confidence intervals in the $\phi_3 - r_B$ plane from multibody $D$ final states at Belle, which is shown by the blue intervals. The results from $B \rightarrow DK^{(*)}$ decays with $D \rightarrow K_S^0\pi^+\pi^-$ are shown by the green intervals and the $D \rightarrow K_S^0\pi^+\pi^-\pi^0$ final states are shown by the brown intervals. The solid and dashed curves correspond to one and two standard deviation contours, respectively [78, 94]. . . . .	165
6.1	Schematic view of SuperKEKB accelerator units along with the Belle II detector position [96]. . . . .	168
6.2	Schematic view of the beam crossing at the interaction region of Belle (left) and Belle II (right). The spread of the $z$ vertex distribution is expected to be 1 cm and 0.05 cm at Belle and Belle II, respectively [97].	168
6.3	Schematic view of the Belle II detector [98]. . . . .	169
6.4	A cross-section view of the Belle II SVD [99]. . . . .	170

6.5	Schematic configuration of the Belle II SVD showing the different sensor geometries and the number of readout chips [95]. . . . .	171
6.6	Rectangular (left) and trapezoidal (right) sensors. . . . .	171
6.7	Image of the APV25 readout chip showing the features and bond pads (left); four APV25 readout chips mounted on a hybrid (right). . . . .	172
6.8	Origami chip-on-sensor concept where the readout from the other side of the DSSD is wrapped around using flexible circuits and connected to APV25 chips in a single line on the DSSD. . . . .	173
6.9	Thickness of the glue dispensed by the robotic arm. . . . .	174
6.10	Pull strength measured for 97 samples of wire-bonds. . . . .	174
6.11	A completed layer 4 ladder. . . . .	175
6.12	Ladder coordinate frame for L4. . . . .	175
6.13	Plot of a forward DSSD in L4 from CMM data. . . . .	176
6.14	Signal <i>vs.</i> time plot for three different channels of a readout chip. . . . .	176
6.15	Signal <i>vs.</i> time plot for an “open” channel of a readout chip. The red curve shows the “open” channel and green curve shows its adjacent one. . . . .	177
6.16	Signal <i>vs.</i> time plot for two adjacent “short” channels of a readout chip. The red and green curves show the “short” channels and blue curve represents a good channel. . . . .	177
6.17	I-V characteristics for an L4 DSSD. . . . .	178
6.18	Particle response to a source scan of <i>p</i> -side of a DSSD in an L4 ladder. . . . .	178
6.19	Particle response to a source scan of <i>n</i> -side of a DSSD in an L4 ladder. . . . .	178
6.20	One half-shell of SVD mounted to the final structure. . . . .	179
6.21	Full SVD mounted to the final structure. . . . .	179
6.22	First cosmic track seen in the full SVD on July 17, 2018. . . . .	180
6.23	$R_2$ distribution in phase II data along with MC predictions. . . . .	181
6.24	$M(K^-\pi^+)$ distribution of $D^{*+} \rightarrow D^0(K^-\pi^+)\pi^+$ decays in phase II data. . . . .	182
6.25	$\Delta M$ distribution of $D^{*+} \rightarrow D^0(K^-\pi^+)\pi^+$ decays in phase II data. . . . .	182
6.26	$M(K^-\pi^+\pi^0)$ distribution of $D^{*+} \rightarrow D^0(K^-\pi^+\pi^0)\pi^+$ decays in phase II data. . . . .	183
6.27	$\Delta M$ distribution of $D^{*+} \rightarrow D^0(K^-\pi^+\pi^0)\pi^+$ decays in phase II data. . . . .	183
6.28	$M(K^-\pi^+\pi^-\pi^+)$ distribution of $D^{*+} \rightarrow D^0(K^-\pi^+\pi^-\pi^+)\pi^+$ decays in phase II data. . . . .	184

6.29	$\Delta M$ distribution of $D^{*+} \rightarrow D^0(K^-\pi^+\pi^-\pi^+)\pi^+$ decays in phase II data. . . . .	184
6.30	$M(K^-K^+)$ distribution of $D^{*+} \rightarrow D^0(K^-K^+)\pi^+$ decays in phase II data. . . . .	185
6.31	$\Delta M$ distribution of $D^{*+} \rightarrow D^0(K^-K^+)\pi^+$ decays in phase II data.	185
6.32	$M(K_S^0\pi^+\pi^-)$ distribution of $D^{*+} \rightarrow D^0(K_S^0\pi^+\pi^-)\pi^+$ decays in phase II data. . . . .	186
6.33	$\Delta M$ distribution of $D^{*+} \rightarrow D^0(K_S^0\pi^+\pi^-)\pi^+$ decays in phase II data.	186
6.34	$M(K_S^0\pi^+\pi^-\pi^0)$ distribution of $D^{*+} \rightarrow D^0(K_S^0\pi^+\pi^-\pi^0)\pi^+$ decays in phase II data. . . . .	187
6.35	$\Delta M$ distribution of $D^{*+} \rightarrow D^0(K_S^0\pi^+\pi^-\pi^0)\pi^+$ decays in phase II data.	187
6.36	$\Delta E$ distribution of various $B$ decay modes in phase II data. . . . .	188
6.37	$M_{bc}$ distribution of various $B$ decay modes in phase II data. . . . .	188
6.38	Signal-enhanced projections of $\Delta E$ distribution of $B$ events without (left) and with (right) a $\pi^0$ in the final state in phase II data. The black points with error bars show data and solid blue curve indicate the total fit. The dotted red and blue curves show signal and background components, respectively. . . . .	189
6.39	Signal-enhanced projection of $M_{bc}$ distribution of $B$ events in phase II data. The black points with error bars show data and solid blue curve indicate the total fit. The dotted red and blue curves show signal and background components, respectively. . . . .	189
7.1	Projection of instantaneous and integrated luminosities at Super KEKB as function of time [96]. . . . .	192
7.2	$\phi_3$ sensitivity with $50 \text{ ab}^{-1}$ Belle II sample. . . . .	193
7.3	Projection of $\phi_3$ sensitivity from all possible $B \rightarrow D^{(*)}K^{(*)}$ final states at Belle II [108]. . . . .	193
A.1	$N^+$ values for the $CP$ -odd modes (left) and $N^-$ values for the $CP$ -even modes (right). The yellow region shows the average value. The horizontal black and red error bars show the statistical and the total uncertainty, respectively. . . . .	196
A.2	Predicted and measured yields for $K_S^0\pi^+\pi^-$ (left) and $K_L^0\pi^+\pi^-$ (right) in each bin obtained from the combined fit of both the modes. The histogram shows the predicted values from the fit, points show the measured values, the dashed line corresponds to $F_+ = 0$ and the dotted line shows $F_+ = 1$ . . . . .	199
B.1	Signal-enhanced fit projections of $M_D$ (left) and $\Delta M$ (right) distributions from data in bin 2. . . . .	201

B.2	Signal-enhanced fit projections of $M_D$ (left) and $\Delta M$ (right) distributions from data in bin 3. . . . .	201
B.3	Signal-enhanced fit projections of $M_D$ (left) and $\Delta M$ (right) distributions from data in bin 4. . . . .	202
B.4	Signal-enhanced fit projections of $M_D$ (left) and $\Delta M$ (right) distributions from data in bin 5. . . . .	202
B.5	Signal-enhanced fit projections of $M_D$ (left) and $\Delta M$ (right) distributions from data in bin 6. . . . .	203
B.6	Signal-enhanced fit projections of $M_D$ (left) and $\Delta M$ (right) distributions from data in bin 7. . . . .	203
B.7	Signal-enhanced fit projections of $M_D$ (left) and $\Delta M$ (right) distributions from data in bin 8. . . . .	204
B.8	Signal-enhanced fit projections of $M_D$ (left) and $\Delta M$ (right) distributions from data in bin 9. . . . .	204
C.1	Signal-enhanced projections of $\Delta E$ (left) and $C'_{\text{NN}}$ (right) distributions of $B^\pm \rightarrow D(K_S^0\pi^+\pi^-\pi^0)\pi^\pm$ decays in bin 2 from a two-dimensional simultaneous fit to $B^\pm \rightarrow D\pi^\pm$ and $B^\pm \rightarrow DK^\pm$ events in generic MC sample with integrated luminosity equivalent to that of data. . . . .	206
C.2	Signal-enhanced projections of $\Delta E$ (left) and $C'_{\text{NN}}$ (right) distributions of $B^\pm \rightarrow D(K_S^0\pi^+\pi^-\pi^0)K^\pm$ decays in bin 2 from a two-dimensional simultaneous fit to $B^\pm \rightarrow D\pi^\pm$ and $B^\pm \rightarrow DK^\pm$ events in generic MC sample with integrated luminosity equivalent to that of data. . . . .	206
C.3	Signal-enhanced projections of $\Delta E$ (left) and $C'_{\text{NN}}$ (right) distributions of $B^\pm \rightarrow D(K_S^0\pi^+\pi^-\pi^0)\pi^\pm$ decays in bin 3 from a two-dimensional simultaneous fit to $B^\pm \rightarrow D\pi^\pm$ and $B^\pm \rightarrow DK^\pm$ events in generic MC sample with integrated luminosity equivalent to that of data. . . . .	207
C.4	Signal-enhanced projections of $\Delta E$ (left) and $C'_{\text{NN}}$ (right) distributions of $B^\pm \rightarrow D(K_S^0\pi^+\pi^-\pi^0)K^\pm$ decays in bin 3 from a two-dimensional simultaneous fit to $B^\pm \rightarrow D\pi^\pm$ and $B^\pm \rightarrow DK^\pm$ events in generic MC sample with integrated luminosity equivalent to that of data. . . . .	207
C.5	Signal-enhanced projections of $\Delta E$ (left) and $C'_{\text{NN}}$ (right) distributions of $B^\pm \rightarrow D(K_S^0\pi^+\pi^-\pi^0)\pi^\pm$ decays in bin 4 from a two-dimensional simultaneous fit to $B^\pm \rightarrow D\pi^\pm$ and $B^\pm \rightarrow DK^\pm$ events in generic MC sample with integrated luminosity equivalent to that of data. . . . .	208
C.6	Signal-enhanced projections of $\Delta E$ (left) and $C'_{\text{NN}}$ (right) distributions of $B^\pm \rightarrow D(K_S^0\pi^+\pi^-\pi^0)K^\pm$ decays in bin 4 from a two-dimensional simultaneous fit to $B^\pm \rightarrow D\pi^\pm$ and $B^\pm \rightarrow DK^\pm$ events in generic MC sample with integrated luminosity equivalent to that of data. . . . .	208
C.7	Signal-enhanced projections of $\Delta E$ (left) and $C'_{\text{NN}}$ (right) distributions of $B^\pm \rightarrow D(K_S^0\pi^+\pi^-\pi^0)\pi^\pm$ decays in bin 5 from a two-dimensional simultaneous fit to $B^\pm \rightarrow D\pi^\pm$ and $B^\pm \rightarrow DK^\pm$ events in generic MC sample with integrated luminosity equivalent to that of data. . . . .	209

C.8	Signal-enhanced projections of $\Delta E$ (left) and $C'_{\text{NN}}$ (right) distributions of $B^\pm \rightarrow D(K_S^0\pi^+\pi^-\pi^0)K^\pm$ decays in bin 5 from a two-dimensional simultaneous fit to $B^\pm \rightarrow D\pi^\pm$ and $B^\pm \rightarrow DK^\pm$ events in generic MC sample with integrated luminosity equivalent to that of data. . . . .	209
C.9	Signal-enhanced projections of $\Delta E$ (left) and $C'_{\text{NN}}$ (right) distributions of $B^\pm \rightarrow D(K_S^0\pi^+\pi^-\pi^0)\pi^\pm$ decays in bin 6 from a two-dimensional simultaneous fit to $B^\pm \rightarrow D\pi^\pm$ and $B^\pm \rightarrow DK^\pm$ events in generic MC sample with integrated luminosity equivalent to that of data. . . . .	210
C.10	Signal-enhanced projections of $\Delta E$ (left) and $C'_{\text{NN}}$ (right) distributions of $B^\pm \rightarrow D(K_S^0\pi^+\pi^-\pi^0)K^\pm$ decays in bin 6 from a two-dimensional simultaneous fit to $B^\pm \rightarrow D\pi^\pm$ and $B^\pm \rightarrow DK^\pm$ events in generic MC sample with integrated luminosity equivalent to that of data. . . . .	210
C.11	Signal-enhanced projections of $\Delta E$ (left) and $C'_{\text{NN}}$ (right) distributions of $B^\pm \rightarrow D(K_S^0\pi^+\pi^-\pi^0)\pi^\pm$ decays in bin 7 from a two-dimensional simultaneous fit to $B^\pm \rightarrow D\pi^\pm$ and $B^\pm \rightarrow DK^\pm$ events in generic MC sample with integrated luminosity equivalent to that of data. . . . .	211
C.12	Signal-enhanced projections of $\Delta E$ (left) and $C'_{\text{NN}}$ (right) distributions of $B^\pm \rightarrow D(K_S^0\pi^+\pi^-\pi^0)K^\pm$ decays in bin 7 from a two-dimensional simultaneous fit to $B^\pm \rightarrow D\pi^\pm$ and $B^\pm \rightarrow DK^\pm$ events in generic MC sample with integrated luminosity equivalent to that of data. . . . .	211
C.13	Signal-enhanced projections of $\Delta E$ (left) and $C'_{\text{NN}}$ (right) distributions of $B^\pm \rightarrow D(K_S^0\pi^+\pi^-\pi^0)\pi^\pm$ decays in bin 8 from a two-dimensional simultaneous fit to $B^\pm \rightarrow D\pi^\pm$ and $B^\pm \rightarrow DK^\pm$ events in generic MC sample with integrated luminosity equivalent to that of data. . . . .	212
C.14	Signal-enhanced projections of $\Delta E$ (left) and $C'_{\text{NN}}$ (right) distributions of $B^\pm \rightarrow D(K_S^0\pi^+\pi^-\pi^0)K^\pm$ decays in bin 8 from a two-dimensional simultaneous fit to $B^\pm \rightarrow D\pi^\pm$ and $B^\pm \rightarrow DK^\pm$ events in generic MC sample with integrated luminosity equivalent to that of data. . . . .	212
C.15	Signal-enhanced projections of $\Delta E$ (left) and $C'_{\text{NN}}$ (right) distributions of $B^\pm \rightarrow D(K_S^0\pi^+\pi^-\pi^0)\pi^\pm$ decays in bin 9 from a two-dimensional simultaneous fit to $B^\pm \rightarrow D\pi^\pm$ and $B^\pm \rightarrow DK^\pm$ events in generic MC sample with integrated luminosity equivalent to that of data. . . . .	213
C.16	Signal-enhanced projections of $\Delta E$ (left) and $C'_{\text{NN}}$ (right) distributions of $B^\pm \rightarrow D(K_S^0\pi^+\pi^-\pi^0)K^\pm$ decays in bin 9 from a two-dimensional simultaneous fit to $B^\pm \rightarrow D\pi^\pm$ and $B^\pm \rightarrow DK^\pm$ events in generic MC sample with integrated luminosity equivalent to that of data. . . . .	213
C.17	Signal-enhanced projections of $\Delta E$ (left) and $C'_{\text{NN}}$ (right) distributions of $B^\pm \rightarrow D(K_S^0\pi^+\pi^-\pi^0)\pi^\pm$ decays in bin 2 from a two-dimensional simultaneous fit to $B^\pm \rightarrow D\pi^\pm$ and $B^\pm \rightarrow DK^\pm$ events in data. . .	214
C.18	Signal-enhanced projections of $\Delta E$ (left) and $C'_{\text{NN}}$ (right) distributions of $B^\pm \rightarrow D(K_S^0\pi^+\pi^-\pi^0)K^\pm$ decays in bin 2 from a two-dimensional simultaneous fit to $B^\pm \rightarrow D\pi^\pm$ and $B^\pm \rightarrow DK^\pm$ events in data. . .	214



D.1	The pull (left), error (middle) and parameter distributions (right) for $x_+^{D\pi}$ from 250 pseudo-experiments. The solid blue curve represents the Gaussian fit to the pull distribution. The error obtained from MC sample fit is marked in blue arrow. . . . .	223
D.2	The pull (left), error (middle) and parameter distributions (right) for $y_+^{D\pi}$ from 250 pseudo-experiments. The solid blue curve represents the Gaussian fit to the pull distribution. The error obtained from MC sample fit is marked in blue arrow. . . . .	223
D.3	The pull (left), error (middle) and parameter distributions (right) for $x_-^{D\pi}$ from 250 pseudo-experiments. The solid blue curve represents the Gaussian fit to the pull distribution. The error obtained from MC sample fit is marked in blue arrow. . . . .	224
D.4	The pull (left), error (middle) and parameter distributions (right) for $y_-^{D\pi}$ from 250 pseudo-experiments. The solid blue curve represents the Gaussian fit to the pull distribution. The error obtained from MC sample fit is marked in blue arrow. . . . .	224
D.5	The pull (left), error (middle) and parameter distributions (right) for $x_+^{DK}$ from 250 pseudo-experiments. The solid blue curve represents the Gaussian fit to the pull distribution. The error obtained from MC sample fit is marked in blue arrow. . . . .	224
D.6	The pull (left), error (middle) and parameter distributions (right) for $y_+^{DK}$ from 250 pseudo-experiments. The solid blue curve represents the Gaussian fit to the pull distribution. The error obtained from MC sample fit is marked in blue arrow. . . . .	225
D.7	The pull (left), error (middle) and parameter distributions (right) for $x_-^{DK}$ from 250 pseudo-experiments. The solid blue curve represents the Gaussian fit to the pull distribution. The error obtained from MC sample fit is marked in blue arrow. . . . .	225
D.8	The pull (left), error (middle) and parameter distributions (right) for $y_-^{DK}$ from 250 pseudo-experiments. The solid blue curve represents the Gaussian fit to the pull distribution. The error obtained from MC sample fit is marked in blue arrow. . . . .	225



# CHAPTER 1

## Introduction

Particle physicists have been acquiring knowledge about the building blocks of the Universe and the forces that hold them together at ever decreasing scales for over 120 years, since it was established that atoms are divisible with the discovery of the electron in 1897. Then Rutherford confirmed the presence of a positively charged centre in an atom, the nucleus. It was again shown that nucleus also has discrete components, the protons and neutrons. Now, we know that even these are not fundamental in nature, but made up of quarks.

The Standard Model (SM) of particle physics encompasses the fundamental building blocks of matter, the quarks and leptons [1, 2, 3]. They are fermions with spin  $\frac{1}{2}$  and their properties are summarized in Table 1.1. The SM also accommodates three out of the four fundamental interactions between them, the strong, electromagnetic and weak interactions, while leaving out the gravitational force. The strong interaction binds the quarks together to form mesons and baryons and is mediated by gluons. The electromagnetic interaction is mediated by photons and it is about 1000 times weaker than the strong interaction. Since photons are electrically neutral, there is no self-coupling between them, unlike gluons, which couple to themselves due to the colour charge they carry. The weak interaction is mediated by  $W^\pm$  and  $Z^0$  bosons, which is  $10^{-13}$  times weaker than the electromagnetic interaction. These force carrying bosons have spin 1 and their other properties are given in Table 1.2. The SM picture is complete with the recent discovery of Higgs boson in 2014 [4, 5]. This scalar boson is responsible for providing mass to the fundamental particles via spontaneous symmetry breaking [6, 7]. The mass of Higgs boson is found to be  $125.09 \pm 0.24 \text{ GeV}/c^2$ .

This thesis describes measurements related to the violation of the discrete symmetry of the combined operation of the charge conjugation and parity operators ( $CP$ ) within the SM. The remainder of this Chapter introduces discrete symmetries, including  $CP$  violation, in Sec. 1.1 and the Cabibbo-Kobayashi-Maskawa (CKM) matrix, which provides the SM explanation of  $CP$  violation, in Sec. 1.2. Section 1.3 discusses the

Type	Particle	Mass (MeV/ $c^2$ )	Charge ( $e$ )
Quark	up ( $u$ )	$2.2^{+0.6}_{-0.4}$	$+\frac{2}{3}$
	down ( $d$ )	$4.7^{+0.5}_{-0.4}$	$-\frac{1}{3}$
	strange ( $s$ )	$96^{+8}_{-4}$	$-\frac{1}{3}$
	charm ( $c$ )	$1275 \pm 30$	$+\frac{2}{3}$
	bottom ( $b$ )	$4180^{+40}_{-30}$	$-\frac{1}{3}$
	top ( $t$ )	$173210 \pm 874$	$+\frac{2}{3}$
Lepton	electron ( $e$ )	$0.511 \pm 0.000$	$-1$
	electron neutrino ( $\nu_e$ )	$< 2 \times 10^{-6}$	$0$
	muon ( $\mu$ )	$106.658 \pm 0.000$	$-1$
	muon neutrino ( $\nu_\mu$ )	$< 0.19$	$0$
	tauon ( $\tau$ )	$1776.86 \pm 0.12$	$-1$
	tauon neutrino ( $\nu_\tau$ )	$< 18.2$	$0$

Table 1.1: Properties of quarks and leptons in the SM.

Boson	Interaction	Mass (GeV/ $c^2$ )	Charge ( $e$ )
gluon ( $g$ )	strong	$0$	$0$
Photon ( $\gamma$ )	electromagnetic	$< 10^{-24}$	$0$
$W^\pm$	weak	$80.385 \pm 0.015$	$\pm 1$
$Z^0$	weak	$91.188 \pm 0.002$	$0$

Table 1.2: Properties of force carrying bosons in the SM.

unitarity triangle angle  $\phi_3$  in detail, along with the different estimation methods. The extraction of strong-phase differences across  $D$  meson phase space, which serves as input to the model-independent determination of  $\phi_3$ , is explained in Sec. 1.4. The Chapter concludes with a discussion on the signal mode chosen,  $D \rightarrow K_S^0 \pi^+ \pi^- \pi^0$ , in Sec. 1.5.

## 1.1 Discrete symmetries

There are certain discrete symmetries in nature like parity ( $P$ ), charge conjugation ( $C$ ) and time reversal ( $T$ ), that are useful for interpreting the dynamics of particle interactions. Symmetries lead to conservation laws in physics as per Noether's theorem [8]. For example, time, translational or rotational invariances result in conservation of energy, linear momentum and angular momentum, respectively.

The  $P$  operator inverts the spatial coordinates of a particle without altering any other quantum numbers. Furthermore, there is an intrinsic parity associated with fermions,

having values  $+1$  for fermions and  $-1$  for antifermions. So a meson which is a combination of a quark and an antiquark with no relative angular momentum between the quark and antiquark will have an intrinsic parity of  $-1$  due to the multiplicative nature of the  $P$  quantum number. The  $P$  symmetry is conserved in strong and electromagnetic interactions, but maximally violated in weak interactions [9, 10]. If  $P$  acts on a left-handed  $\nu$ , then it becomes a right-handed  $\nu$ , which is non-existent in the SM (if we assume the  $\nu$  mass is zero). This is an artefact of the “V–A” form of weak interaction current, where V is a vector and A is an axial vector [1, 2, 3]. The strong and electromagnetic interaction currents are purely of “V” type, so there is no distinction in the interaction for particles of different handedness.

When a  $C$  operation is performed on a particle, the sign of its internal quantum numbers such as baryon number, lepton number, and charge will be inverted. However, the handedness of the particle remains unchanged. The handedness can be defined in terms of the helicity, which is the projection of the spin of a particle in the direction of its momentum. In the ultra-relativistic limit, when the energy of a particle is very much greater than its mass, the helicity and handedness are equivalent. If the spin is oriented in the same direction as the momentum, then the particle is right-handed and if the orientation is opposite to that of momentum, then the particle is left-handed. The  $C$  symmetry is also conserved in strong and electromagnetic interactions, but maximally violated in the weak interaction [9, 10]. When  $C$  operates on a left-handed  $\nu$ , it becomes a left-handed  $\bar{\nu}$ , which does not exist in the SM (if we assume the  $\nu$  mass is zero).

The combined operation of  $C$  and  $P$  would convert a particle into its antiparticle. For example, a left-handed  $\nu$  will become a right-handed  $\bar{\nu}$  when acted upon by the  $CP$  operator. It was believed that the  $CP$  symmetry was conserved in weak interactions until 1964 when  $CP$  violation was observed in  $K^0 - \bar{K}^0$  oscillations [11]. The oscillation proceeds as a second-order weak process mediated by the “up”-type quarks  $u$ ,  $c$  and  $t$ . The states  $K^0$  and  $\bar{K}^0$  are not  $CP$  eigenstates because  $CP|K^0\rangle = |\bar{K}^0\rangle$ . But  $CP$  eigenstates can be constructed from linear combinations of these states as

$$|K_S^0\rangle = \left( p|K^0\rangle + q|\bar{K}^0\rangle \right), \quad (1.1)$$

$$|K_L^0\rangle = \left( p|K^0\rangle - q|\bar{K}^0\rangle \right), \quad (1.2)$$

such that they are  $CP$  even and odd eigenstates, respectively. Here,  $|p|^2 + |q|^2 = 1$ .

If  $CP$  were to be conserved, the  $K_S^0$  would decay to a two-pion final state and  $K_L^0$  to a three-pion final state. The two- and three-pion final states are  $CP$  even and odd, respectively because of their intrinsic parity. But experimental observations showed that the  $K_L^0$  meson also decayed to the two-pion final state, thus violating  $CP$  symmetry. The branching fraction of  $K_L^0 \rightarrow \pi^+\pi^-$  was found to be  $(2.0 \pm 0.4) \times 10^{-3}$  [11].

There are three types of  $CP$  violation observed in hadronic weak decays: (i) direct, (ii) in mixing and (iii) interference between mixing and decay. Direct  $CP$  violation is observed when the amplitudes of a decay and its  $CP$  conjugate process have different magnitudes. For example,  $CP$  asymmetry is observed in the  $CP$  conjugate decays  $B^+ \rightarrow DK^+$  and  $B^- \rightarrow DK^-$ , which is the main topic of this thesis.  $CP$  violation in mixing or indirect  $CP$  violation is observed in neutral meson systems like in Eq. (1.1) and (1.2), when the condition  $|p/q| = 1$  is not satisfied. This is measured in neutral meson decays, where the flavour of the meson could be identified. When a neutral meson decays to a final state  $f$ , there are two possible ways: either direct decay to  $f$  or oscillate to the antimeson and decays to the same state  $f$ . There will be interference between these processes when  $f$  is a  $CP$  eigenstate. One can define

$$\lambda_f = \left(\frac{q}{p}\right) \left(\frac{\overline{A}_f}{A_f}\right), \quad (1.3)$$

where  $A_f$  and  $\overline{A}_f$  are the amplitudes of meson and antimeson decays.  $CP$  violation is observed when the imaginary part of  $\lambda_f$  is nonzero. The  $CP$ -asymmetry in the decay  $B^0 \rightarrow J/\psi K_S^0$  is an example of this this type of  $CP$  violation [12].

The  $T$  operation inverts the temporal coordinates of a particle. It is found that the behaviour of the interactions remain the same under the combined operation of  $C$ ,  $P$  and  $T$ . This is known as the  $CPT$  theorem and it ensures that the particles and their antiparticles have the same mass and lifetime [13]. This symmetry is essential in quantum field theory and can be proved using causality and Lorentz invariance. Several experiments have confirmed that the  $CPT$  symmetry is intact in all particle interactions, for example see Sec. 77 of Ref. [14].

Earlier it was thought that the observation of  $CP$  violation could explain the matter abundance in the universe. The conditions proposed by Andrei Sakharov in 1967 [15] for the existence of a matter-dominated universe are

1. at least one process violates baryon number,
2.  $C$  and  $CP$  symmetry violation and
3. interaction out of thermal equilibrium.

So there were efforts underway to explain the  $CP$  violation within the SM framework.

## 1.2 CKM matrix

The suppression of processes where the strangeness quantum number is not conserved was explained by Nicola Cabibbo in 1963, as a mixing between  $d$  and  $s$  quarks [16]. The mixing angle is called the Cabibbo angle ( $\theta_C$ ) and it determines the probability of the  $d$  and  $s$  quarks decaying into  $u$  quarks. The weak eigenstate is formed from the mass eigenstates as

$$d' = \cos \theta_C d + \sin \theta_C s, \quad (1.4)$$

and this  $d'$  state is interacting with the  $u$  quark and  $W$  boson.

Later Glashow, Iliopoulos and Maiani extended this idea to four quarks by predicting the existence of another “up”-type quark, the charm ( $c$ ) [17]. The  $c$  quark was predicted to couple with the weak eigenstate

$$s' = -\sin \theta_C d + \cos \theta_C s. \quad (1.5)$$

Thus the suppression of flavour-changing neutral current interactions were explained in the decay  $K_L^0 \rightarrow \mu^+ \mu^-$  with the introduction of  $c$  quark. The experimental observation of  $J/\psi$  meson, a  $c\bar{c}$  bound state, in 1974 confirmed the GIM mechanism [18].

Then a third generation of quarks, the top ( $t$ ) and bottom ( $b$ ), was proposed by Kobayashi and Maskawa [19]. Thus the mixing between the mass and weak eigenstates is described by a  $3 \times 3$  mixing matrix known as the Cabibbo-Kobayashi-Maskawa (CKM) matrix. This is represented as

$$\begin{pmatrix} d' \\ s' \\ b' \end{pmatrix} = \begin{pmatrix} V_{ud} & V_{us} & V_{ub} \\ V_{cd} & V_{cs} & V_{cb} \\ V_{td} & V_{ts} & V_{tb} \end{pmatrix} \begin{pmatrix} d \\ s \\ b \end{pmatrix}, \quad (1.6)$$

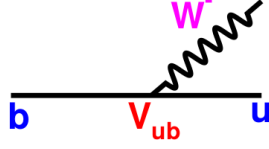


Figure 1.1: A  $b \rightarrow u$  quark transition where the vertex factor is proportional to  $V_{ub}$ .

where  $d$ ,  $s$ , and  $b$  are the quark mass eigenstates and  $d'$ ,  $s'$ , and  $b'$  are their weak eigenstates. Each element  $V_{ij}$  signifies the strength of the corresponding quark transition. An example is given in Fig. 1.1.

In general a  $3 \times 3$  complex matrix will be described by 18 parameters. The CKM matrix is unitary in nature, which removes nine parameters due to the constraint that  $V^\dagger V = I$ , where  $I$  is the identity matrix. This results in three mixing angles and six complex phases. Five out of the six phases can be removed by re-phasing the quark fields. Hence the matrix can be formed from three Euler angles and one complex phase. The presence of the complex phase naturally explains the  $CP$  violation in the SM. If we define  $\cos \theta_{ij} = c_{ij}$  and  $\sin \theta_{ij} = s_{ij}$ , where  $\theta_{ij}$  is the mixing angle between the quarks  $i$  and  $j$ , then the CKM matrix can be written in the following way,

$$\begin{pmatrix} 1 & 0 & 0 \\ 0 & c_{23} & s_{23} \\ 0 & -s_{23} & c_{23} \end{pmatrix} \times \begin{pmatrix} c_{13} & 0 & s_{13}e^{-i\delta_{13}} \\ 0 & 1 & 0 \\ -s_{13}e^{-i\delta_{13}} & 0 & c_{13} \end{pmatrix} \times \begin{pmatrix} c_{12} & s_{12} & 0 \\ -s_{12} & c_{12} & 0 \\ 0 & 0 & 1 \end{pmatrix} \quad (1.7)$$

$$= \begin{pmatrix} c_{12}c_{13} & s_{12}c_{13} & s_{13}e^{-i\delta_{13}} \\ -s_{12}c_{23} - c_{12}s_{23}s_{13}e^{-i\delta_{13}} & c_{12}c_{23} - s_{12}s_{23}s_{13}e^{-i\delta_{13}} & s_{23}c_{13} \\ s_{12}s_{23} - c_{12}c_{23}s_{13}e^{-i\delta_{13}} & -c_{12}s_{23} - s_{12}c_{23}e^{-i\delta_{13}} & c_{23}c_{13} \end{pmatrix}, \quad (1.8)$$

where  $\delta_{13}$  is the complex phase and  $\theta_{12}$  is equivalent to the Cabibbo angle. When a  $CP$  operation is performed, the complex phase inverts its sign and the symmetry is violated. The diagonal entries of the matrix are approximately one while the off-diagonal entries are close to zero. This is a clear indication that the quark transition is favoured within the same generation.

A more convenient parametrisation of the CKM matrix is the Wolfenstein parametrization [20], named after its proposer Lincoln Wolfenstein. In this parametrization

the CKM matrix is written as

$$V = \begin{pmatrix} 1 - \lambda^2/2 & \lambda & A\lambda^3(\rho - i\eta) \\ -\lambda & 1 - \lambda^2/2 & A\lambda^2 \\ A\lambda^3(1 - \rho - i\eta) & -A\lambda^2 & 1 \end{pmatrix} + \mathcal{O}(\lambda^4), \quad (1.9)$$

where  $\lambda$ ,  $A$ ,  $\rho$  and  $\eta$  are independent real parameters of the same order. The parameter  $\lambda$  is equivalent to  $\sin \theta_{12} \equiv \sin \theta_C \simeq 0.22$ . The farther one goes from the diagonal elements, the higher the order of the dependence on  $\lambda$ , which implies that the strength of the interaction decreases. This parametrisation is commonly used for studying the interactions of  $B$  mesons. A non-zero value of  $\eta$  would signify the complex phase in  $V_{ub}$  and  $V_{td}$  that is the source of  $CP$  violation in the SM.

We can write the relations among the elements of the matrix as

$$\sum_{j=d,s,b} V_{ij} V_{kj}^* = \delta_{ik}, \quad (1.10)$$

where  $i$  and  $k$  are  $u, c, t$ . The six expressions for which the righthand side of Eq. (1.10) are zero give the following relations among the elements of the CKM matrix

$$V_{ud}^* V_{cd} + V_{us}^* V_{cs} + V_{ub}^* V_{cb} = 0 \quad (1.11)$$

$$V_{ud}^* V_{td} + V_{us}^* V_{ts} + V_{ub}^* V_{tb} = 0 \quad (1.12)$$

$$V_{cd}^* V_{td} + V_{cs}^* V_{ts} + V_{cb}^* V_{tb} = 0 \quad (1.13)$$

$$V_{ud} V_{us}^* + V_{cd} V_{cs}^* + V_{td} V_{ts}^* = 0 \quad (1.14)$$

$$V_{ud} V_{ub}^* + V_{cd} V_{cb}^* + V_{td} V_{tb}^* = 0 \quad (1.15)$$

$$V_{us} V_{ub}^* + V_{cs} V_{cb}^* + V_{ts} V_{tb}^* = 0. \quad (1.16)$$

These can be visualised as triangles in a complex plane with sides  $V_{ij} V_{kj}^*$ . Each of them has the same area, which is a measure of the amount of  $CP$  violation in the SM [21]. The unitarity triangle formed from Eq. (1.15) is more significant because its sides are of similar length,  $\mathcal{O}(\lambda^3)$ , and all the angles can be measured from decays of  $B$  mesons. Conventionally, the base of the triangle along the real axis is normalized to 1 and two new parameters  $\bar{\rho} = \rho(1 - \frac{\lambda^2}{2} + \dots)$  and  $\bar{\eta} = \eta(1 - \frac{\lambda^2}{2} + \dots)$  are introduced. The unitarity triangle in the  $\bar{\rho} - \bar{\eta}$  plane is shown in Fig. 1.2.

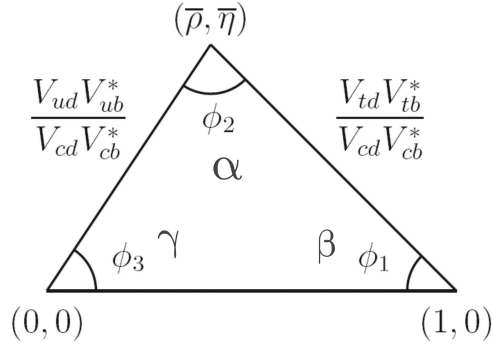


Figure 1.2: Unitarity triangle in the  $\bar{\rho} - \bar{\eta}$  plane [14].

The three angles are defined as

$$\phi_1 \equiv \beta = \arg \left( \frac{-V_{cd}V_{cb}^*}{V_{td}V_{tb}^*} \right), \quad (1.17)$$

$$\phi_2 \equiv \alpha = \arg \left( \frac{-V_{td}V_{tb}^*}{V_{ud}V_{ub}^*} \right), \quad (1.18)$$

$$\phi_3 \equiv \gamma = \arg \left( \frac{-V_{ud}V_{ub}^*}{V_{cd}V_{cb}^*} \right). \quad (1.19)$$

They have been measured in various  $B$  decay modes by independent experiments. The SM description of  $CP$  violation can be tested by analysing these measurements and checking if the apex of the triangle coincides, as expected in the SM, among the various measurements. The current experimental status of these parameters are summarized in Fig. 1.3.

The measurement of  $\sin(2\phi_1)$  from  $B \rightarrow J/\psi K_S^0$  decays was performed by the  $B$ -factory experiments Belle and BABAR [23, 24]. This was the first observation of  $CP$  violation in  $B$  meson decays and confirmed the Kobayashi and Maskawa mechanism of  $CP$  violation; this led to them being awarded the Nobel Prize in 2008.

The  $CP$  violation present in the SM is not sufficient to explain the observed matter-antimatter asymmetry in the universe [25, 26, 27]. This indicates that there is some new physics beyond the SM (BSM) that generates the matter-antimatter asymmetry. A precise determination of  $CP$  violating observables allows a test for BSM effects. Such tests can be done by comparing measurements that have differing sensitivity to BSM effects. There are first-order and second-order weak processes indicated by tree-level

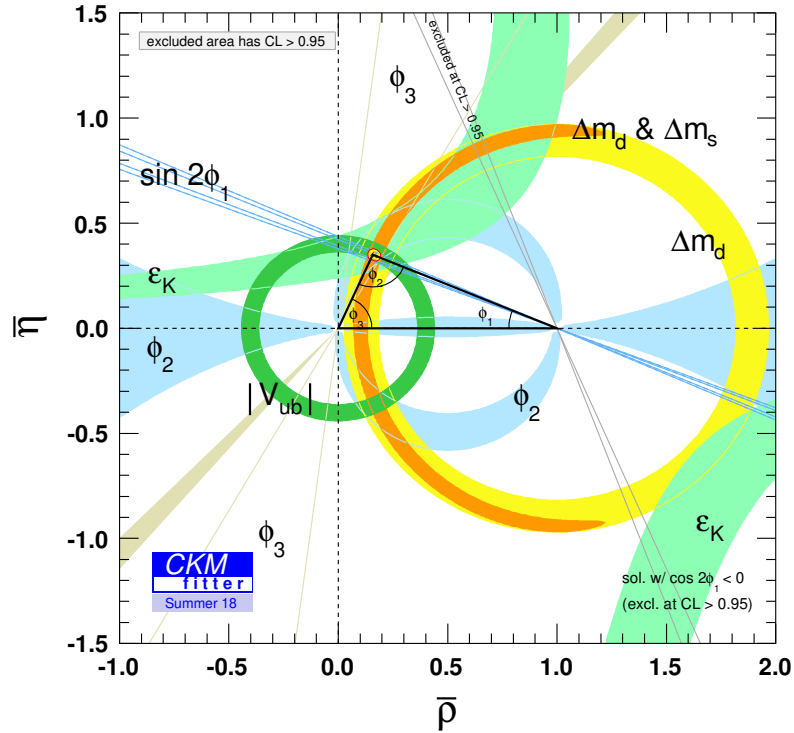


Figure 1.3: Experimental constraints of the unitarity triangle in  $\bar{\rho} - \bar{\eta}$  plane [22].

and loop-level diagrams, respectively. In tree-level processes, it is easy to assign momentum to outgoing particles based on conservation laws. Loop-level processes need integration over all possible values of momenta. An example of tree-level process is the decay of  $B$  meson into a semileptonic final state of  $B \rightarrow \bar{D}^{(*)} \mu \nu$ . The  $B^0 - \bar{B}^0$  mixing is a loop-level process. The Feynman diagrams for these two processes are shown in Fig. 1.4. If we categorize the measurements shown in Fig 1.3 into those coming from first-order weak processes (tree-level) and second-order weak processes (loop-level), there are two separate triangles as given in Fig. 1.5. The particle interactions in BSM scenarios will affect the loop-level processes and hence any disagreement in the position of the apex of the triangle in both the cases would indicate possible new-physics effects. It is evident from Fig. 1.5 that the uncertainty associated with the apex position is not comparable in both the cases. This motivates efforts to reduce the experimental uncertainty in tree-level processes.

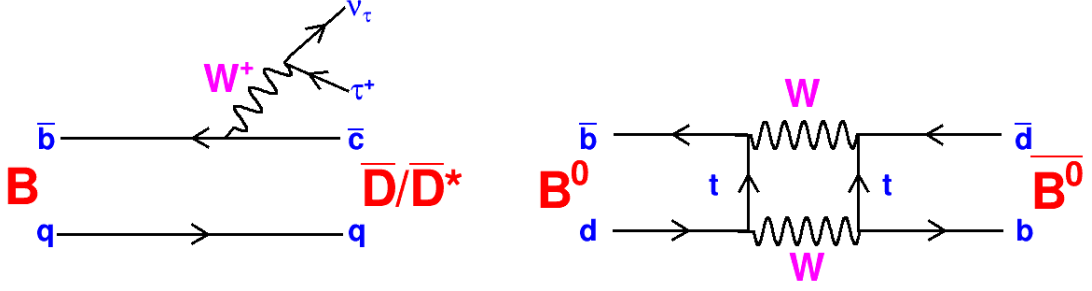


Figure 1.4: Feynman diagrams for  $B \rightarrow \bar{D}^{(*)} \mu \nu$  (left) and  $B^0 - \bar{B}^0$  mixing (right) processes.

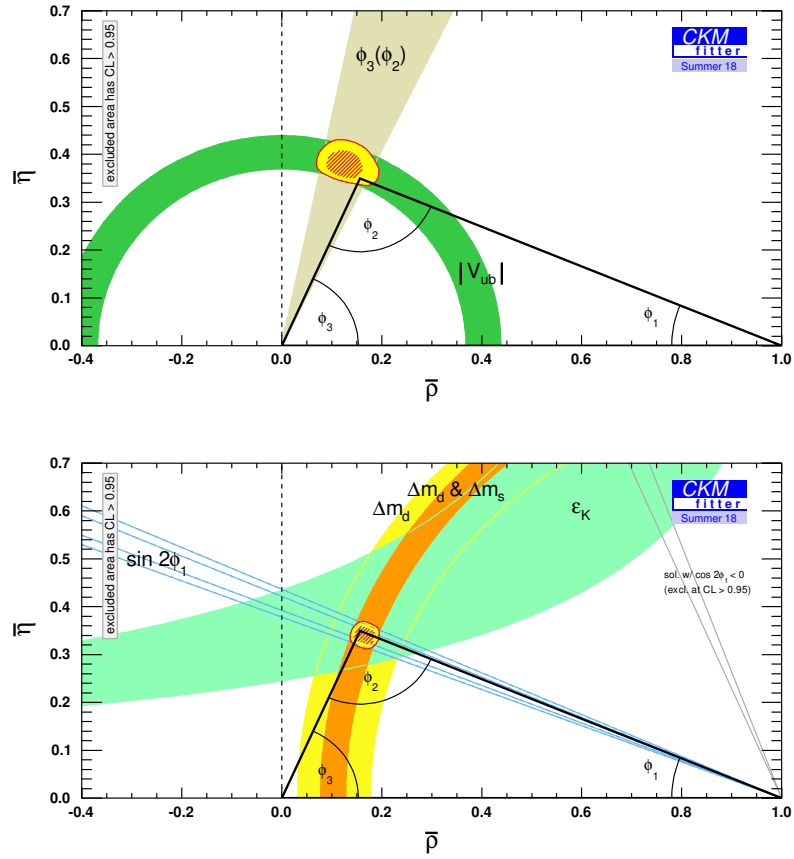


Figure 1.5: Experimental constraints of the unitarity triangle in  $\bar{\rho} - \bar{\eta}$  plane coming from tree-level (top) and loop-level (bottom) processes [22].

### 1.3 The angle $\phi_3$

The experimental uncertainty on the angle  $\phi_3$  is larger than the other parameters that constrain the tree- and loop-level Unitarity Triangles, as is clearly noticeable from Fig. 1.5. It is the only angle accessible via tree-level processes and its measurement is an important test of the SM. The theoretical uncertainty on a  $\phi_3$  measurement is negligible [ $\sigma_{\phi_3}/\phi_3 \sim \mathcal{O}(10^{-7})$ ] [28]. The current best  $\phi_3$  measurement of  $\phi_3$ , combining all

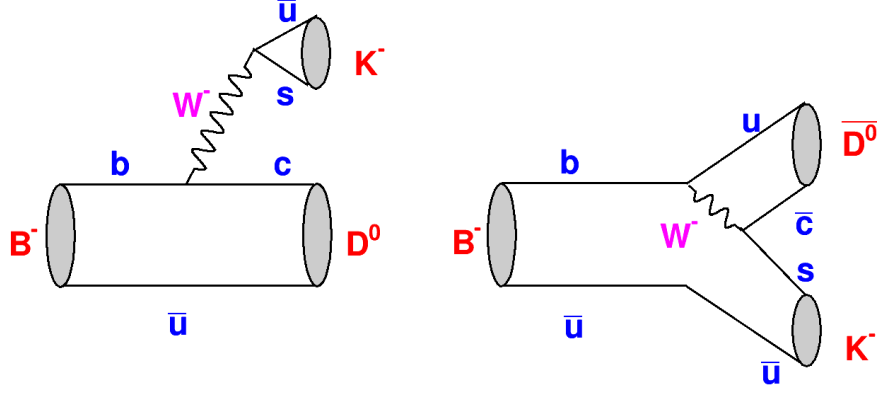


Figure 1.6: Colour-favoured (left) and colour-suppressed (right)  $B^- \rightarrow DK^-$  processes.

the results from different experiments, is  $(73.5^{+4.2}_{-5.1})^\circ$  [29]. This large uncertainty is due to the small branching fractions of the decays sensitive to  $\phi_3$ . The value of  $\phi_3$  estimated indirectly from other parameters of the unitarity triangle is  $(65.3^{+1.0}_{-2.5})^\circ$  [29]. Any disagreement between these results could also imply that there is new physics. But a comparison would be meaningful only if the associated uncertainties are comparable. Thus an improved measurement of  $\phi_3$  is essential for testing the SM description of  $CP$  violation.

The measurement of  $\phi_3$  is possible when there is interference between the transitions  $\bar{b} \rightarrow \bar{c}u\bar{s}$  and  $\bar{b} \rightarrow \bar{u}c\bar{s}$ , which is the case in the decay  $B^+ \rightarrow DK^+$ , where  $D$  is a neutral charm meson decaying to a common final state for both  $D^0$  and  $\bar{D}^0$  decays.<sup>1</sup> This is due to the dependence of the colour-suppressed decay on the CKM element  $V_{ub}$ . The Feynman diagrams for the colour-favoured  $B^- \rightarrow D^0K^-$  and colour-suppressed  $B^- \rightarrow \bar{D}^0K^-$  decays are shown in Fig. 1.6.

If the amplitude for the colour-favoured decay is  $A_{\text{fav}} = A$ , then the colour-suppressed one can be written as  $A_{\text{sup}} = Ar_B e^{i(\delta_B - \phi_3)}$ , where  $\delta_B$  and  $\phi_3$  are the strong phase and weak phase differences between the decay processes, respectively, and

$$r_B = \frac{|A_{\text{sup}}|}{|A_{\text{fav}}|}. \quad (1.20)$$

The value of  $r_B$  is approximately given as

$$r_B = \frac{|V_{ub}||V_{cs}|}{|V_{us}||V_{cb}|} \times \frac{1}{3} \approx 0.1, \quad (1.21)$$

<sup>1</sup>Charge-conjugation is implied here and elsewhere in this thesis, unless otherwise specified.

where the factor  $\frac{1}{3}$  accounts for the colour suppression.

### 1.3.1 Methods to extract $\phi_3$

There are different methods to extract  $\phi_3$  from  $B^+ \rightarrow DK^+$  decays that are classified according to the  $D$  meson final state. If the  $D$  final state is a  $CP$  eigenstate such as  $K^+K^-$ ,  $\pi^+\pi^-$ ,  $K_S^0\pi^0$ , then the method described in Ref. [30] is employed. The parameters sensitive to  $\phi_3$  can be extracted by taking a ratio between the  $CP$  eigenstates and Cabibbo-favoured decay rates, and a measurement of  $CP$  asymmetries. The observables are

$$\begin{aligned} R_{CP}^\pm &= \frac{\Gamma(B^- \rightarrow D_{CP\pm}K^-) + \Gamma(B^+ \rightarrow D_{CP\pm}K^+)}{\Gamma(B^- \rightarrow D^0K^-) + \Gamma(B^+ \rightarrow \overline{D^0}K^+)} \\ &= 1 + r_B^2 \pm 2r_B\delta_B \cos \phi_3, \end{aligned} \quad (1.22)$$

and

$$\begin{aligned} A_{CP}^\pm &= \frac{\Gamma(B^- \rightarrow D_{CP\pm}K^-) - \Gamma(B^+ \rightarrow D_{CP\pm}K^+)}{\Gamma(B^- \rightarrow D_{CP\pm}K^-) + \Gamma(B^+ \rightarrow D_{CP\pm}K^+)} \\ &= \pm 2r_B \sin \delta_B \sin \phi_3 / R_{CP}^\pm, \end{aligned} \quad (1.23)$$

where  $\Gamma$  is the partial decay rate and  $D_{CP\pm}$  indicate a  $CP$ -even (+) or  $CP$ -odd (−) eigenstate. If the  $D$  final state is a multibody decay, then additional input of the fractional  $CP$ -content  $F_+$  [31] is needed. The interference terms, which are the ones that depend on  $\phi_3$ , will be scaled by a factor  $(2F_+ - 1)$ . The sensitivity of these observables to the  $CP$  violation is limited because of the small value of  $r_B$ . There is an inherent eight-fold ambiguity on  $\phi_3$  from these observables.

If the  $D$  final state is any doubly-Cabibbo-suppressed states such as  $K^+X^-$ , where  $X^-$  can be  $\pi^-$ ,  $\pi^-\pi^0$ ,  $\pi^-\pi^-\pi^+$ , then the method presented in Ref. [32] can be used to extract  $\phi_3$ . The  $\phi_3$  sensitive parameters are defined as

$$\begin{aligned} R_{ADS} &= \frac{\Gamma(B^- \rightarrow [K^+X^-]_D K^-) + \Gamma(B^+ \rightarrow [K^-X^+]_D K^+)}{\Gamma(B^- \rightarrow [K^-X^+]_D K^-) + \Gamma(B^+ \rightarrow [K^+X^-]_D K^+)} \\ &= r_B^2 + r_D^2 + 2r_B r_D \cos(\delta_B + \delta_D) \cos \phi_3, \end{aligned} \quad (1.24)$$

and the  $CP$  asymmetry

$$\begin{aligned}
A_{\text{ADS}} &= \frac{\Gamma(B^- \rightarrow [K^+ X^-]_D K^-) - \Gamma(B^+ \rightarrow [K^- X^+]_D K^+)}{\Gamma(B^- \rightarrow [K^+ X^-]_D K^-) + \Gamma(B^+ \rightarrow [K^- X^+]_D K^+)} \\
&= 2r_B r_D \sin(\delta_B \delta_D) \sin \phi_3 / R_{\text{ADS}}.
\end{aligned} \tag{1.25}$$

Here,  $r_D$  and  $\delta_D$  are the ratio of the amplitudes of the suppressed and favoured  $D$  decays, and the  $D$  strong phase, respectively. For multibody  $D$  decays, additional input, the coherence factor  $\kappa$  [33], is needed, which multiplies the interference terms in the observables. It is not possible to extract  $\phi_3$ ,  $r_B$  and  $\delta_B$  from a single decay mode because there are less number of parameters than the unknowns. However, combining the results from these decay modes makes the extraction of  $\phi_3$  feasible.

If the  $D$  meson decays to a multibody self-conjugate final state like  $K_S^0 \pi^+ \pi^-$ ,  $K_S^0 K^+ K^-$ , or  $K_S^0 \pi^+ \pi^- \pi^0$ , there are regions in their phase space, that behave like GLW or ADS type modes, depending on the resonance contributions, making them more sensitive to  $\phi_3$ . The  $\phi_3$  extraction can be performed via two methods: model-dependent and model-independent. The model-dependent method requires that the distribution of events over the  $D$  phase space be fit to a model of the amplitudes corresponding to the intermediate resonances and partial waves that are assumed to be contributing to the decay; the model assumptions lead to a difficult to determine systematic uncertainty that could potentially limit the precision of the  $\phi_3$  measurement. The model-independent method requires that measurements of  $CP$  violating asymmetries are made in independent regions, which we refer to as bins, of the  $D$  phase space [34, 35]. The binning reduces the statistical precision compared to the model-dependent method, but the uncertainty related to the model assumptions is removed by using measurements of the average strong phase differences within the bins.

The statistical uncertainty on  $\phi_3$  measurements could be reduced by adding more and more  $D$  final states. This in practice means the addition of more three and four-body  $D$  final states. We develop the model-independent approach for a four-body  $D$  final state  $D^0 \rightarrow K_S^0 \pi^+ \pi^- \pi^0$  in the current analysis.

### 1.3.2 Model-independent method to extract $\phi_3$

The amplitude of  $B^+ \rightarrow DK^+$ ,  $D \rightarrow f$ , where  $f$  is a multibody self-conjugate final state, can be written as

$$A_B(\vec{x}) = \bar{A}(\vec{x}) + r_B e^{i(\delta_B + \phi_3)} A(\vec{x}), \quad (1.26)$$

where  $A$  is the amplitude of  $D^0 \rightarrow f$ ,  $\bar{A}$  is that of  $\bar{D}^0 \rightarrow f$  at a point in  $D$  phase space  $\vec{x}$ . The probability density for events in the  $D$ -decay phase space can be written as the square of the amplitude as

$$\begin{aligned} P_B &= |A_B|^2 = |\bar{A} + r_B e^{i(\delta_B + \phi_3)} A|^2 \\ &= |\bar{A}|^2 + r_B^2 |A|^2 + r_B (\bar{A}^* A e^{i(\delta_B + \phi_3)} + \bar{A} A^* e^{-i(\delta_B + \phi_3)}). \end{aligned} \quad (1.27)$$

Note that

$$\bar{A}^* A = |\bar{A}| |A| e^{i(\delta_D - \delta_{\bar{D}})} = |\bar{A}| |A| e^{i\Delta\delta_D}, \quad (1.28)$$

where  $\delta_D$  and  $\delta_{\bar{D}}$  are the strong phases for  $D^0 \rightarrow f$  and  $\bar{D}^0 \rightarrow f$  decays, respectively. With this, the last term of Eq. 1.27 becomes

$$\begin{aligned} \bar{A}^* A e^{i(\delta_B + \phi_3)} + \bar{A} A^* e^{-i(\delta_B + \phi_3)} &= |\bar{A}| |A| (e^{i\Delta\delta_D} e^{i(\delta_B + \phi_3)} + e^{-i\Delta\delta_D} e^{-i(\delta_B + \phi_3)}) \\ &= 2|\bar{A}| |A| (\cos(\Delta\delta_D + (\delta_B + \phi_3))) \\ &= 2|\bar{A}| |A| (\cos \Delta\delta_D \cos(\delta_B + \phi_3) \\ &\quad - \sin \Delta\delta_D \sin(\delta_B + \phi_3)) \end{aligned} \quad (1.29)$$

Thus, Eq. 1.27 becomes

$$\begin{aligned} P_B &= |\bar{A}|^2 + r_B^2 |A|^2 + 2r_B |\bar{A}| |A| (\cos \Delta\delta_D \cos(\delta_B + \phi_3) - \sin \Delta\delta_D \sin(\delta_B + \phi_3)) \\ &= |\bar{A}|^2 + r_B^2 |A|^2 + 2\sqrt{P\bar{P}}(x_+ C - y_+ S), \end{aligned} \quad (1.30)$$

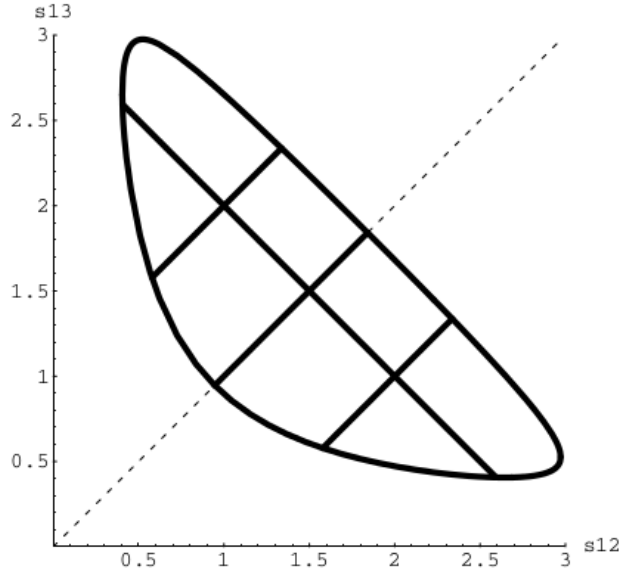


Figure 1.7: Dalitz plot of  $D \rightarrow K_S^0 \pi^+ \pi^-$  partitioned into different bins. The dashed line shows the symmetry axis,  $s_{12} = m_{K_S^0 \pi^-}^2$  and  $s_{13} = m_{K_S^0 \pi^+}^2$  [34].

where  $\bar{P} = |\bar{A}|^2$ ,  $x_+ = r_B \cos(\delta_B + \phi_3)$ ,  $y_+ = r_B \sin(\delta_B + \phi_3)$ ,  $C = \cos \Delta\delta_D$  and  $S = \sin \Delta\delta_D$ . For the charge-conjugate mode,  $B^- \rightarrow DK^-$ , the density is given by

$$\begin{aligned} P_{\bar{B}} &= |A|^2 + r_B^2 |\bar{A}|^2 + 2r_B |\bar{A}| |A| (\cos \Delta\delta_D \cos(\delta_B - \phi_3) - \sin \Delta\delta_D \sin(\delta_B - \phi_3)) \\ &= |A|^2 + r_B^2 |\bar{A}|^2 + 2\sqrt{P\bar{P}}(x_- C - y_- S), \end{aligned} \quad (1.31)$$

where,  $x_- = r_B \cos(\delta_B - \phi_3)$ ,  $y_- = r_B \sin(\delta_B - \phi_3)$ .

The  $D$  phase space is divided to different bins illustrated in Fig. 1.7. The partial decay rate in each bin of the  $D$  phase space for  $B^-$  and  $B^+$  decays can be written as

$$\Gamma_i^- = h \left( K_i + r_B^2 \bar{K}_i + 2\sqrt{K_i \bar{K}_i} (c_i x_- + s_i y_-) \right), \quad (1.32)$$

$$\Gamma_i^+ = h \left( \bar{K}_i + r_B^2 K_i + 2\sqrt{K_i \bar{K}_i} (c_i x_+ - s_i y_+) \right), \quad (1.33)$$

respectively, where  $i$  represents a particular region of the  $D$  decay phase space. Here,  $K_i$  and  $\bar{K}_i$  are the fraction of flavour-tagged  $D^0$  and  $\bar{D}^0$  events in each bin and  $h$  is the normalization factor. The  $K_i$  and  $\bar{K}_i$  parameters are defined as

$$K_i \propto \int_{\mathcal{D}_i} |A|^2 d\mathcal{D}, \quad (1.34)$$

and

$$\overline{K}_i \propto \int_{\mathcal{D}_i} |\overline{A}|^2 d\mathcal{D}, \quad (1.35)$$

where  $\mathcal{D}_i$  is the  $i^{\text{th}}$  bin region over which the integration is performed and  $\mathcal{D}$  is the phase space volume. A sample of  $D^*$ -tagged  $D^0$  decays can be used to determine  $K_i$  and  $\overline{K}_i$ . The  $c_i$  and  $s_i$  parameters are the amplitude-weighted averages of the functions  $C$  and  $S$  averaged over the bin region. For example,  $c_i$  parameter is defined as

$$c_i = \frac{\int_{\mathcal{D}_i} |A| |\overline{A}| C d\mathcal{D}}{\sqrt{\int_{\mathcal{D}_i} |A|^2 d\mathcal{D} \int_{\mathcal{D}_i} |\overline{A}|^2 d\mathcal{D}}}, \quad (1.36)$$

Similar definition exists for  $s_i$  with  $C$  being substituted by  $S$ . If the number of bins  $N \geq 3$  (6 observables from  $B^+$  and  $B^-$  decays), then it is possible to extract  $x_+$ ,  $y_+$ ,  $x_-$ ,  $y_-$  and  $h$  from a single decay mode with  $c_i$ ,  $s_i$ ,  $K_i$  and  $\overline{K}_i$  as external inputs. Then, one can determine  $r_B$ ,  $\delta_B$  and  $\phi_3$  from  $x_{\pm}$  and  $y_{\pm}$  values. The process of determining the  $c_i$  and  $s_i$  parameters, as well as the  $F_+$  parameter, to perform these measurements is described in the following section.

## 1.4 Quantum-correlated $D$ mesons

The measurements of  $c_i$  and  $s_i$  parameters, as well as  $CP$ -content, can be performed at a charm factory, where the  $e^+e^-$  collisions occur at the centre-of-mass energy corresponding to  $\psi(3770)$  meson. The  $\psi(3770)$  immediately decays to a  $D$  meson pair at threshold, *i.e.* without any other accompanying particles. These  $D$  meson pairs are produced in a  $P$ -wave state because the  $\psi(3770)$  is a vector meson, hence the wave function for the decay is antisymmetric. The amplitude of a  $D$  meson decaying into a self-conjugate state can be written as  $A(D^0 \rightarrow f) \equiv |A|e^{i\delta_D}$ . Then the branching fraction for the decay can be expressed as

$$\mathcal{B}(f) = \int_{\mathcal{D}_i} |A(D^0 \rightarrow f)|^2 d\mathcal{D}, \quad (1.37)$$

where  $\mathcal{D}$  represents the entire phase space. As before we can define the strong-phase difference between  $D^0$  and  $\overline{D}^0$  as  $\Delta\delta_D = \delta_D - \delta_{\overline{D}}$ . In Sec. 1.4.1 we describe the dependence of various rates of correlated  $D^0\overline{D}^0$  decay on the value of  $F_+$ . In Sec. 1.4.2, the

relations between the  $D^0\overline{D}^0$  decay rates and parameter values of  $c_i$  and  $s_i$  are discussed.

### 1.4.1 $CP$ -even fraction $F_+$

If we consider the  $CP$  eigenstates to be

$$|D_{CP\pm}\rangle = \frac{|D^0\rangle \pm |\overline{D}^0\rangle}{\sqrt{2}}, \quad (1.38)$$

then  $F_+$  of an inclusive decay  $D^0 \rightarrow f$  can be defined as

$$\begin{aligned} F_+^f &= \frac{\int_{\mathcal{D}} |\langle f|D_{CP+}\rangle|^2 d\mathcal{D}}{\int_{\mathcal{D}} |\langle f|D_{CP+}\rangle|^2 + |\langle f|D_{CP-}\rangle|^2 d\mathcal{D}} \\ &= \frac{\int_{\mathcal{D}} |A|^2 + |\overline{A}|^2 + 2|A||\overline{A}| \cos \Delta\delta_D d\mathcal{D}}{\int_{\mathcal{D}} 2(|A|^2 + |\overline{A}|^2) d\mathcal{D}} \\ &= \frac{1}{2} \left[ 1 + \frac{1}{\mathcal{B}(f)} \int_{\mathcal{D}} |A||\overline{A}| \cos \Delta\delta_D d\mathcal{D} \right]. \end{aligned} \quad (1.39)$$

We can show that the rate of quantum-correlated  $D^0\overline{D}^0$  pair decay is sensitive to  $F_+$  by considering one of the  $D$  mesons decaying into  $f$  at point  $\mathcal{D}$  and the other one to  $g$  at point  $\mathcal{D}'$ .  $A(D_1 \rightarrow f) \equiv |A_1|e^{i\delta_{D1}}$  and  $A(D_2 \rightarrow g) \equiv |A_2|e^{i\delta_{D2}}$ . The antisymmetric wave function for the inclusive decay can be written as

$$A(f|g) = \frac{1}{\sqrt{2}} (|A_1|e^{i\delta_{D1}}|\overline{A}_2|e^{i\delta_{\overline{D}2}} - |\overline{A}_1|e^{i\delta_{\overline{D}1}}|A_2|e^{i\delta_{D2}}), \quad (1.40)$$

which leads to the probability

$$\begin{aligned} \mathcal{P}(f|g) &\propto [ |A_1|^2|\overline{A}_2|^2 + |\overline{A}_1|^2|A_2|^2 \\ &\quad - 2|A_1||\overline{A}_2||\overline{A}_1||A_2|(\cos \Delta\delta_{D1} \cos \Delta\delta_{D2} + \sin \Delta\delta_{D1} \sin \Delta\delta_{D2}) ]. \end{aligned} \quad (1.41)$$

It is possible to write the double-tagged yield, where we specify the decays of both the  $D$  mesons, either in the integrated phase space or in different regions of phase space

as

$$\begin{aligned}
M(f|g) &= \int_{\mathcal{D}} \int_{\mathcal{D}'} \mathcal{P}(f|g) d\mathcal{D} d\mathcal{D}' \\
&= \int_{\mathcal{D}} |A_1|^2 d\mathcal{D} \int_{\mathcal{D}'} |\overline{A_2}|^2 d\mathcal{D}' + \int_{\mathcal{D}} |\overline{A_1}|^2 d\mathcal{D} \int_{\mathcal{D}'} |A_2|^2 d\mathcal{D}' - \\
&\quad \int_{\mathcal{D}} |A_1| |\overline{A_1}| \cos \Delta\delta_{D_1} d\mathcal{D} \int_{\mathcal{D}'} |A_2| |\overline{A_2}| \cos \Delta\delta_{D_2} d\mathcal{D}' - \\
&\quad \int_{\mathcal{D}} |A_1| |\overline{A_1}| \sin \Delta\delta_{D_1} d\mathcal{D} \int_{\mathcal{D}'} |A_2| |\overline{A_2}| \sin \Delta\delta_{D_2} d\mathcal{D}'. \tag{1.42}
\end{aligned}$$

If  $f$  or  $g$  is a  $CP$  eigenstate, the last term in Eq. (1.42) is zero because  $\Delta\delta_{D_{1,2}} = 0$  or  $\pi$ . So the double-tagged yield becomes

$$M(f|g) = \mathcal{N} \mathcal{B}(f) \mathcal{B}(g) \left[ 1 - (2F_+^f - 1)(2F_+^g - 1) \right], \tag{1.43}$$

when Eqs. (1.37) and (1.39) are substituted into Eq. (1.42). Here  $\mathcal{N}$  is the overall normalization factor. The term  $(2F_+ - 1)$  represents the  $CP$  eigenvalue  $\lambda_{CP}$  depending on whether they are  $CP$ -even ( $F_+ = 1$ ) or  $CP$ -odd ( $F_+ = 0$ ). Then it is evident that there is two-fold enhancement in the yield if  $f$  and  $g$  have opposite  $CP$  eigenvalue whereas yield becomes zero if  $f$  and  $g$  have the same  $CP$  eigenvalue. We can rewrite Eq. (1.43) as

$$M(f|g) = \mathcal{N} \mathcal{B}(f) \mathcal{B}(g) \left[ 1 - \lambda_{CP}^g (2F_+^f - 1) \right]. \tag{1.44}$$

The  $g$  mode can be self-conjugate modes like  $K_S^0 \pi^+ \pi^-$  or  $K_L^0 \pi^+ \pi^-$ . If  $g$  is a multibody state, then its phase space could be divided into bins. The decay probability in  $i^{\text{th}}$  bin of  $g$  while integrating over the full phase space of  $f$  is

$$\mathcal{P}(f|g_i) \propto \int_{\mathcal{D}_i} \left( |A_2|^2 + |\overline{A_2}|^2 - (2F_+^f - 1) |A_2| |\overline{A_2}| \cos \Delta\delta_{D_2} \right) d\mathcal{D}_i, \tag{1.45}$$

where  $\mathcal{D}_i$  indicates the phase space of bin  $i$ . The double-tagged yield in each bin can be written as

$$\begin{aligned}
M_i(f|K_{S,L}^0 \pi^+ \pi^-) &= h_{K_{S,L}^0 \pi^+ \pi^-} \left[ K_i^{K_{S,L}^0 \pi^+ \pi^-} + K_{-i}^{K_{S,L}^0 \pi^+ \pi^-} \right. \\
&\quad \left. - 2c_i \sqrt{K_i^{K_{S,L}^0 \pi^+ \pi^-} K_{-i}^{K_{S,L}^0 \pi^+ \pi^-}} (2F_+^f - 1) \right], \tag{1.46}
\end{aligned}$$

where  $K_i^{K_{S,L}^0 \pi^+ \pi^-}$  and  $K_{-i}^{K_{S,L}^0 \pi^+ \pi^-}$  are the fraction of flavour-tagged  $D^0$  and  $\overline{D^0}$  decays,  $c_i$  is the cosine of the strong phase difference for  $K_{S,L}^0 \pi^+ \pi^-$  and  $h_{K_{S,L}^0 \pi^+ \pi^-}$  is the nor-

malization factor. With these,  $F_+^f$  can be determined if the double-tagged yields in each bin are measured.

The events where both the  $D$  mesons decay to the same final state  $f$  also provide information about  $F_+$ . The double-tagged yield in that case is given by

$$M(f|f) = \mathcal{N}\mathcal{B}(f)^2 4F_+(1 - F_+). \quad (1.47)$$

#### 1.4.2 Strong phase difference parameters $c_i$ and $s_i$

The quantum-correlation means that the decays of  $D \rightarrow K_S^0 \pi^+ \pi^- \pi^0$  recoiling against  $CP$  and quasi- $CP$  eigenstates and other self-conjugate states as tag modes provide direct sensitivity to measure  $c_i$  and  $s_i$  when the rates are measured in bins of the  $D \rightarrow K_S^0 \pi^+ \pi^- \pi^0$  phase space. The double-tagged yields for a  $CP$  tag  $g$  in bins of the decay phase space of  $f$  can be written by integrating Eq. (1.41) as

$$\begin{aligned} M_i(f|CP\pm) &= \int_{\mathcal{D}_i} \left( |A|^2 + |\bar{A}|^2 \mp 2\sqrt{|A|^2|\bar{A}|^2} \cos \Delta\delta_D \right) d\mathcal{D} \\ &= h_{CP} \left[ K_i + \bar{K}_i \mp 2\sqrt{K_i\bar{K}_i} c_i \right], \end{aligned} \quad (1.48)$$

where  $h_{CP}$  is the normalization constant. For a quasi- $CP$  tag, the  $c_i$  sensitive term is scaled by  $(2F_+ - 1)$  rather than 1.

For the self-conjugate final state  $K_S^0 \pi^+ \pi^-$  [36, 37], Eq. (1.41) is modified to give the double-tagged yield as

$$\begin{aligned} M_{i\pm j}(f|K_S^0 \pi^+ \pi^-) &= h_{K_S^0 \pi^+ \pi^-} [K_i K_{\mp j}^{K_S^0 \pi^+ \pi^-} + \bar{K}_i K_{\pm j}^{K_S^0 \pi^+ \pi^-} \\ &\quad - 2\sqrt{K_i K_{\pm j}^{K_S^0 \pi^+ \pi^-} \bar{K}_i K_{\mp j}^{K_S^0 \pi^+ \pi^-}} (c_i c_j^{K_S^0 \pi^+ \pi^-} + s_i s_j^{K_S^0 \pi^+ \pi^-})], \end{aligned} \quad (1.49)$$

where  $j$  is a particular region of the decay phase space of  $K_S^0 \pi^+ \pi^-$ . Similarly for

$K_L^0 \pi^+ \pi^-$ ,

$$M_{i\pm j}(f|K_L^0 \pi^+ \pi^-) = h_{K_L^0 \pi^+ \pi^-} [K_i K_{\mp j}^{K_L^0 \pi^+ \pi^-} + \overline{K_i} K_{\pm j}^{K_L^0 \pi^+ \pi^-} + 2\sqrt{K_i K_{\pm j}^{K_L^0 \pi^+ \pi^-} \overline{K_i} K_{\mp j}^{K_L^0 \pi^+ \pi^-}} (c_i c_j^{K_L^0 \pi^+ \pi^-} + s_i s_j^{K_L^0 \pi^+ \pi^-})]. \quad (1.50)$$

In Eqs. (1.49) and (1.50),  $h_{K_S^0 \pi^+ \pi^-}$  and  $h_{K_L^0 \pi^+ \pi^-}$  are the normalization constants, respectively. If both the  $D$  meson decays are the same, then

$$M_{ij}(f|f) = h_f \left[ K_i \overline{K_j} + \overline{K_i} K_j - 2\sqrt{K_i \overline{K_j} \overline{K_i} K_j} (c_i c_j + s_i s_j) \right], \quad (1.51)$$

where  $h_f$  is the normalization constant.

## 1.5 $D \rightarrow K_S^0 \pi^+ \pi^- \pi^0$ decays

Currently the most precise measurement of  $\phi_3$  [38] exploits the self-conjugate final state  $D \rightarrow K_S^0 \pi^+ \pi^-$  where the  $CP$  asymmetry in different regions of the  $D$  Dalitz plot is measured to determine  $\phi_3$  [34, 35] (see Fig. 1.8). Given the success of such analyses in determining  $\phi_3$ , other self-conjugate final states can be studied in a similar fashion to improve the determination of  $\phi_3$ . The decay  $D \rightarrow K_S^0 \pi^+ \pi^- \pi^0$  is a suitable addition because it has a branching fraction of 5.2% [14], which is large compared to that of other multibody final states. This is in part due to its Cabibbo-favoured nature and many possible intermediate resonances. A Feynman diagram for this  $D$  decay is given in Fig. 1.9.

The decay occurs through many intermediate resonances, such as  $K_S^0 \omega$  ( $CP$  eigenstates) and  $K^{*\pm} \rho^\mp$  (VV states) that lead to variations of the strong phase difference over the phase space, which is required to extract  $\phi_3$  from a single final state, as described in Sec. 1.3. However, a significant complication is that the four-body final state requires a binning of the five-dimensional  $D$  phase space rather than a two-dimensional Dalitz plot for the three-body case.

In this thesis the first measurements of  $\phi_3$  from using  $B^+ \rightarrow D(K_S^0 \pi^+ \pi^- \pi^0) K^+$  as well as the strong-phase parameters required are presented. The strong-phase measurements and  $CP$ -content estimation have been performed using a data sample consisting

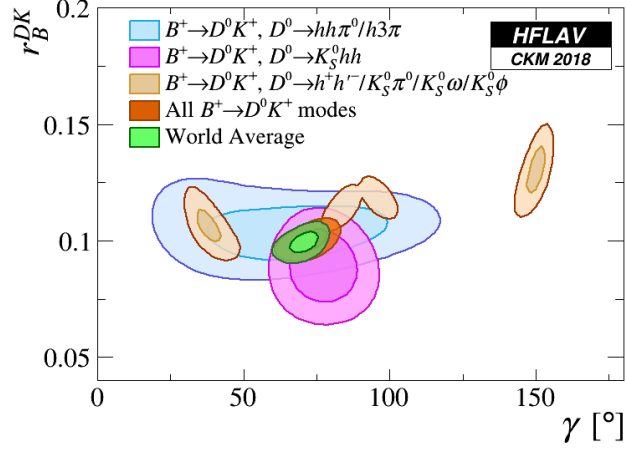


Figure 1.8: One and two standard deviation contours in  $\phi_3(\gamma)$ - $r_B$  plane obtained from all the measurements using different  $D$  final states [29].

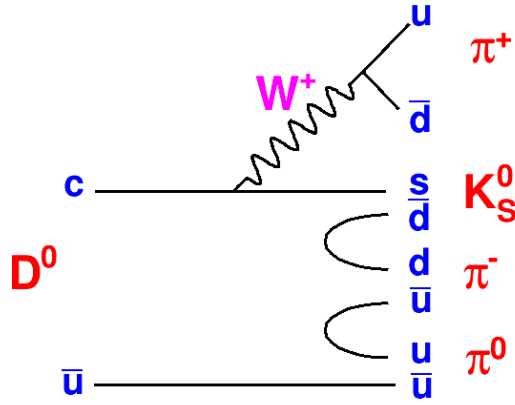


Figure 1.9: A Feynman diagram for the process  $D^0 \rightarrow K_S^0 \pi^+ \pi^- \pi^0$ .

of  $D\bar{D}$  pairs coming from the  $\psi(3770)$  resonance collected by the CLEO-c detector at the CESR  $e^+e^-$  collider. The  $\phi_3$  measurement is performed with an  $e^+e^-$  collision data sample collected at centre-of-mass energy corresponding to the  $\Upsilon(4S)$  resonance by the Belle detector at the KEKB collider. The remainder of this thesis is organized as follows: Chapter 2 gives a detailed description of the experimental set-up. The measurements using the  $D\bar{D}$  pairs at CLEO-c are described in Chapter 3. Chapters 4 and 5 give the event selection criteria and signal extraction followed by estimation of  $\phi_3$  from Belle data, respectively. The Belle II detector is a substantial upgrade of Belle and the construction and quality assurance of the silicon vertex detectors are discussed in Chapter 6 along with a brief description of the significant upgrades to all the sub-detector systems. The data analysis performed with the data collected by the initial physics run of Belle II is also summarized in Chapter 6, then Chapter 7 provides the conclusions and outlook.



# CHAPTER 2

## CLEO-c and Belle experiments

### 2.1 Introduction

This thesis is based on the measurements performed on the data collected by three experiments, CLEO-c, Belle and Belle II. The strong-phase difference parameters,  $c_i$  and  $s_i$ , of  $D \rightarrow K_S^0 \pi^+ \pi^- \pi^0$  decays are measured from the quantum-correlated  $D$  meson pairs produced at CLEO-c. Then the CKM angle  $\phi_3$  is extracted from  $B^\pm \rightarrow DK^\pm$  decays at Belle with the same  $D$  final state. An overview of these two detectors and their associated accelerators are described in the following sections. The salient features of Belle II, a significant upgrade of Belle, will be described in Chapter 6.

### 2.2 CESR and CLEO-c detector

The CLEO-c detector [39, 40, 41, 42] is the last in a series of detectors starting from the 1970s, located at Cornell University, New York, USA. The particle collisions are produced at the Cornell Electron Storage Ring (CESR), a symmetric-energy electron-positron collider. The earlier CLEO detector versions operated at (or near) the  $\Upsilon(4S)$  resonance. With the competition that came from the larger statistics samples collected by the  $B$  factories, such as Belle, CESR reduced its operational energy to be at charm threshold. The corresponding detector revision is CLEO-c.

#### 2.2.1 CESR

A schematic view of the CESR accelerator complex is shown in Fig. 2.1. The electrons and positrons are accelerated to the desired energy in three steps, using a linear accelerator (LINAC), a synchrotron and CESR storage ring. The LINAC is 30 m in length and the total CESR circumference is 768 m.

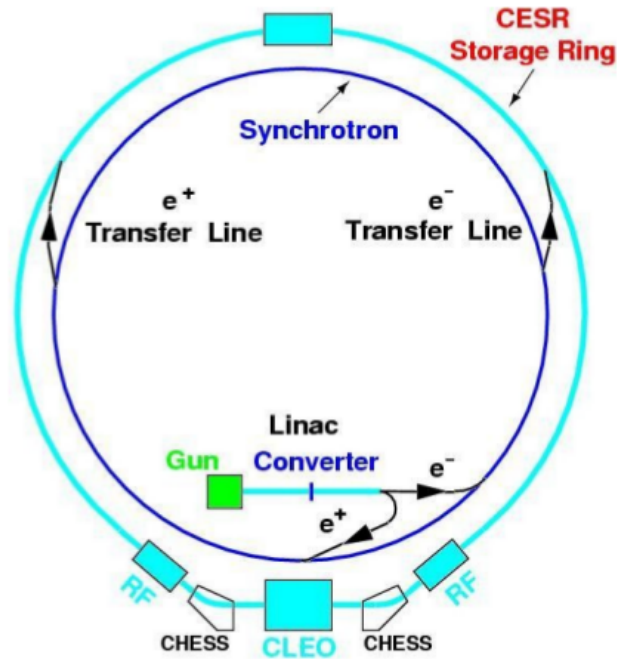


Figure 2.1: Schematic view of CESR with the accelerator units, along with the CLEO-c detector position [43].

Electrons are produced in the LINAC with a 120 kV electron gun. They are accelerated up to 300 MeV with the help of 500 MHz radio frequency (RF) cavities. Particle showers, including positrons, are created when the electrons are incident upon a tungsten target inserted into the beam. The positrons are captured using a magnetic field and then accelerated to 160 MeV. The electrons and positrons are then transferred to the synchrotron via two separate lines.

The synchrotron brings the particles from the LINAC to CESR energies. They are then injected into the CESR ring using kicker magnets. Dipole magnets are used to control the beam direction in the synchrotron and CESR. A series of quadrupole magnets are used for focusing the beam. The quadrupole magnets are convergent in one plane, but divergent in the other and hence a combination of them is required to accomplish focusing in both the planes. The chromatic effects, due to the beam energy spread, result in different focal points for particles, which are corrected using sextupole magnets. A sextupole magnet can focus particles that are far from the axis as it is designed to have a magnetic field that varies quadratically with the radial distance.

Around 1 cm long bunches are formed in CESR from the injected particles. They are further grouped into *trains* with three to five bunches in each, separated by 14 ns.

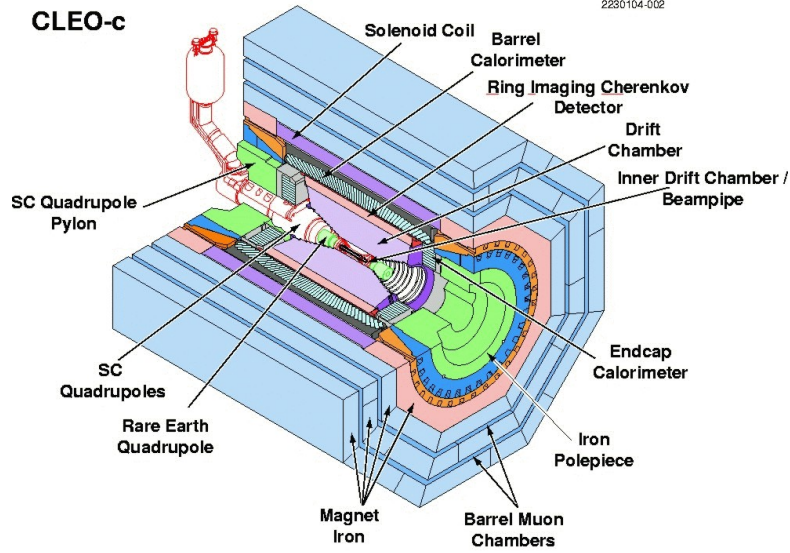


Figure 2.2: Cut-out view of the CLEO-c detector [44].

The ring consists of eight to nine trains separated by 240 ns. The particles collide at the interaction point (IP) in bunches. Electrostatic separators, located close to the IP, exerted kicks to the electron and positron beams in the horizontal direction to collide at the IP.

The centre-of-mass energy of the electron-positron system is approximately 4 GeV for the charm factory. The instantaneous luminosity is

$$L \propto f \frac{N_B n_{e^-} n_{e^+}}{4\pi\sigma_x\sigma_y}, \quad (2.1)$$

where  $N_B$  is the total number of bunches,  $f$  is the revolution frequency,  $n_{e^-}$  and  $n_{e^+}$  are the number of electrons and positrons in each bunch and  $\sigma_x$  and  $\sigma_y$  are the transverse beam sizes in the horizontal and vertical directions. CESR achieved an instantaneous luminosity of  $10^{31} \text{ cm}^{-2}\text{s}^{-1}$  in the CLEO-c era.

### 2.2.2 CLEO-c detector

The CLEO-c detector surrounds the interaction region of CESR with an approximate coverage of 93% of the  $4\pi$  solid angle. It is a general purpose detector with various sub-detector systems in different layers to measure the kinematic properties of the detected particles and distinguish between them. A schematic view of the detector cross section is shown in Fig. 2.2.

The innermost part is a drift chamber that tracks the charged particles and measures their ionization energy loss. The Ring Imaging Cherenkov (RICH) detector acts as the particle identification system. A crystal calorimeter measures the electromagnetic showers. All of these subsystems are kept in a 1 T superconducting magnetic field. The outermost layer is the barrel muon chamber. The following subsections describe these sub-detector systems in detail, along with the trigger and data-acquisition (DAQ) systems.

## **Drift chamber**

The drift chamber is the tracking system of CLEO-c, devised to determine the trajectories of charged particles as well as measure their momentum and energy loss. It has two concentric cylindrical regions, the inner drift chamber (ZD) and the outer drift chamber (DR). Together, they cover 93% of the total  $4\pi$  solid angle. The ZD is situated between the radii of 5.3 cm and 10.5 cm, whereas the DR is between 12 cm and 82 cm. The 1 T magnetic field makes the charged-particle trajectories curve in the  $x - y$  plane. The coordinate system is defined by taking the direction of the positron as the  $z$  axis and the  $y$  axis vertically upwards, hence the  $x$  axis points outwards from the centre of the CESR ring.

The drift chamber is filled with a gaseous mixture of helium and propane in 3:2 ratio. The detecting elements in both the ZD and the DR are square cells with each of them having a sense wire surrounded by eight parallel field wires. The sense wires are made from gold-plated tungsten and the field wires from gold-plated aluminium; they have radii of 20  $\mu\text{m}$  and 110  $\mu\text{m}$ , respectively. These wires are at a potential difference of 2.1 kV in the ZD and 1.9 kV in the DR. There are 300 sense wires in total arranged in six layers, parallel to the  $z$  axis, in the ZD. The DR consists of 16 layers of sense wires in its inner axial section and 31 layers in its outer stereo section, all parallel to the  $z$  axis. Segmented cathode pads are attached to the outer radial wall of the DR to constrain the track parameters and improve the spatial resolution in the  $z$  direction.

The charged particles, while passing through the drift chamber, ionise the gas inside, thus liberating electrons. These electrons drift towards the sense wires because of the presence of electric field. The time of charge deposition on the sense wires is utilized to determine the trajectory of the particle. The electrons cause further ionisa-

tion as they accelerate towards the wire and an avalanche is produced. The distance of closest approach of the particle to the sense wire is determined by recording the time at which the avalanche occurred. The signals from all the cells are combined to form the trajectory of the particle using a Kalman filter [45] algorithm, which determines the best-fit trajectory of the particle after accounting for the energy loss. The momentum resolution for charged particles at normal incidence is about 0.4%. The position resolution of the total tracking system is about  $100 \mu\text{m}$  and the momentum resolution is about 0.6% for tracks having  $1 \text{ GeV}/c$  momentum.

The drift chamber is used to distinguish between different particle species by measuring the energy loss per unit length  $dE/dx$  of a charged particle in the gaseous medium. This is obtained from the pulse height of the avalanche. The Bethe-Bloch formula [46, 47, 48] describes the relation between the energy loss and the velocity of a particle. This is then combined with the particle momentum ( $|\vec{p}|$ ) to obtain its mass by comparing the measurement with expectations from the electron, muon, pion, kaon and proton mass values, which in turn distinguish different types of charged particles.

The distribution of  $|\vec{p}|$  vs.  $dE/dx$  for charged hadron tracks is shown in Fig. 2.3; the bands due to different hadrons are clearly visible. It is possible to form a likelihood based on the number of standard deviations between the measured values and expected values for a particular class of particles. This method works well for particles with momenta  $\leq 0.7 \text{ GeV}/c$ .

### **Ring Imaging Cherenkov (RICH) detector**

The Ring Imaging Cherenkov (RICH) detector acts as a particle identification system. It operates on the basic principle that a charged particle travelling faster than the speed of light in a medium emits a Cherenkov light cone. This is detected as a ring of hits using photosensitive materials. The opening angle of the light cone ( $\theta_C$ ) depends on the refractive index of the medium ( $n$ ) as

$$\cos \theta_C = \frac{c}{nv} \quad (2.2)$$

$$= \frac{1}{n} \sqrt{1 + \left( \frac{mc}{|\vec{p}|} \right)^2}, \quad (2.3)$$

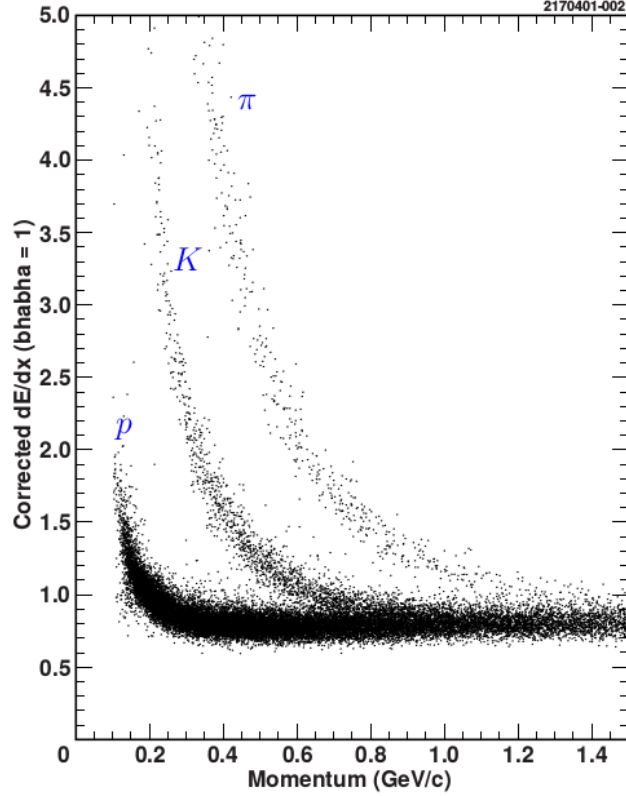


Figure 2.3: Distribution of  $|\vec{p}|$  vs.  $dE/dx$  for charged hadron tracks. [42].

where  $v$  is velocity,  $m$  is the mass and  $|\vec{p}|$  is the momentum of the particle. The velocity of the particle can be obtained from the radius of the Cherenkov ring, which combined with the momentum measurement, helps to infer the mass of the particle. A cross section view of the RICH detector is shown in Fig. 2.4.

The maximum opening angle of the light cone is  $48^\circ$  with 1 cm thick Lithium Fluoride (LiF) crystals having a refractive index of 1.5 covering the inner surface of RICH. The majority of the photons are in the ultraviolet (UV) region. The possible total internal reflections near normal incidence are reduced with a sawtooth pattern for the crystals. The Cherenkov photons are passed through a  $N_2$  expansion gap of around 16 cm so that the ring would be large enough to be measurable. Then they go through a  $CaF_2$  window, which is UV transparent, into a gaseous mixture of methane and triethylamine. The Cherenkov photon avalanches ionize the gas to produce photo electrons. Multiwire proportional chambers are used to amplify these photoelectrons and they are detected by cathode pads.

A likelihood is formed for a Cherenkov ring from a particular type of particle by considering the photons that are within five standard deviations of the expected ring

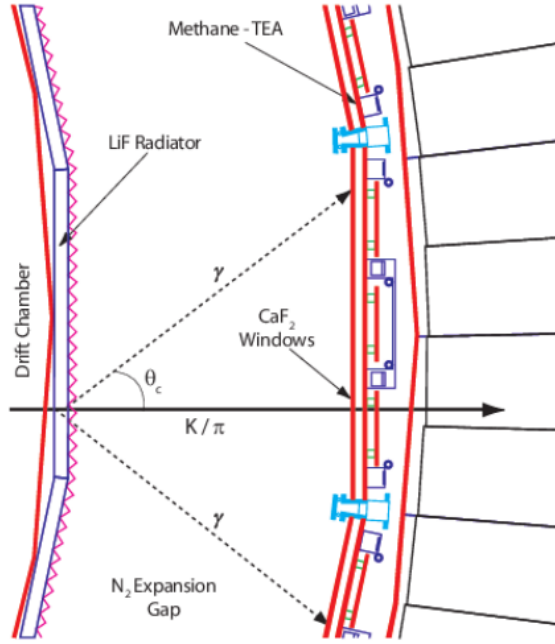


Figure 2.4: Cross section view of the RICH detector. The solid black arrow indicates the charged particle and the dashed arrows show the emitted light [41].

size of that species. Number of standard deviations between different particle types are shown as a function of momentum in Fig. 2.5.

The kaon identification efficiency achieved by the RICH is 87% with a pion fake rate of 0.2% at a momentum value of 0.9 GeV/c. The information from the RICH is combined with the  $dE/dx$  measurement from the drift chamber to form an overall likelihood for particle identification. The RICH works better in the high momentum range whereas the drift chamber is effective in the low momentum region, so the detectors complement each other. In the analysis presented in this thesis, charged particles (mainly kaons and pions) in the momentum range 0.1–1.0 GeV/c are encountered. So they can be distinguished efficiently by the drift chamber and RICH measurements.

## Calorimeter

The electromagnetic calorimeter is composed of 7800 scintillating crystals that cover about 93% of the  $4\pi$  solid angle. This sub-detector is designed to measure the energy of showers produced by electromagnetic interactions. The crystals are made of CsI doped with 0.1% thallium (Tl); the dimensions of the crystals are 5 cm × 5 cm × 30 cm. The CsI crystals are doped with Tl to shift the wavelength of the emitted photons into the visible spectrum so that the photodiodes can detect them efficiently. The Tl doping also

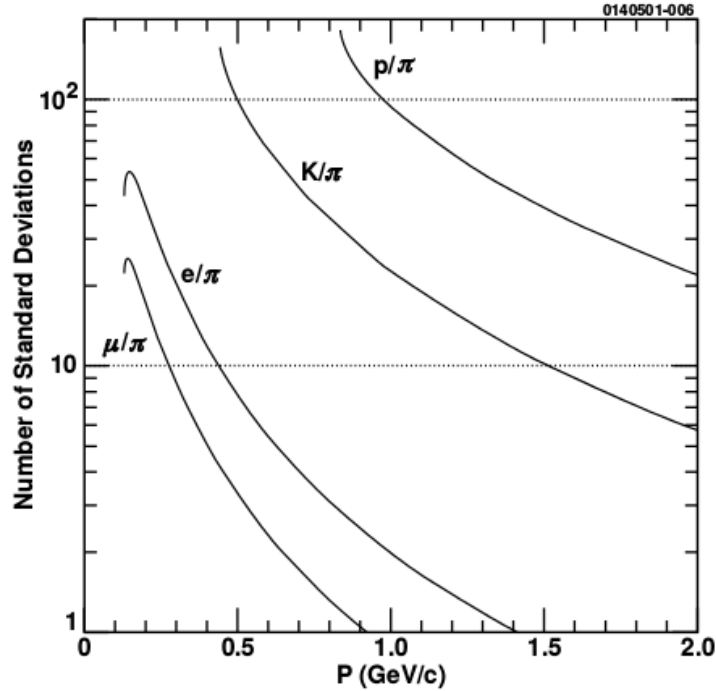


Figure 2.5: Number of standard deviations between different particle hypotheses as a function of momentum obtained by the CLEO-c RICH detector [41].

increases the light output significantly.

The crystals are located in the barrel and the two endcap regions. They are arranged in such a way that the probability of the particles travelling in a gap between the crystals is minimised. Each crystal has four photodiodes to detect the scintillation light. The photon and electron energy deposits are relatively narrow. Photons are distinguished by looking at showers that are not associated with a track. Most of the energy deposited by a shower in a crystal is contained within that or its immediate neighbours since the Molière radius of CsI is 3.8 cm.

The calorimeter material can have hadronic interactions with the particles, which produce showers. But the secondary particles travel a significant distance before depositing the energy. These spillover shower candidates are isolated at the reconstruction stage by applying appropriate selection criteria on the shower energy and direction. The energy resolution of the calorimeter is about 5% for a photon energy of 100 MeV.

## **Muon chamber**

The outermost part of the CLEO-c detector is a muon chamber covering 85% of the  $4\pi$  solid angle. There are anode wires interleaved with iron layers in the chamber. The analysis described in this thesis does not include muons in the final state of any decay channel and hence we do not use any information from the muon chambers.

## **Trigger and data acquisition**

The  $e^+e^-$  collisions produce a lot of events out of which only a few are of interest. The trigger system is designed to select these events of interest while rejecting the others. The selected events are stored by the data acquisition (DAQ) system.

The information from the DR and calorimeter are used in the trigger by partially reconstructing each event. This is used to determine the presence of tracks and showers in an event. A set of conditions are imposed on these partially reconstructed objects to select events of interest and discard others. In addition to this, there is a random trigger that accepts events arbitrarily at the rate of 1 kHz. The DAQ stores an event, that passes the trigger conditions, in  $30 \mu\text{s}$  and records events at 500 Hz.

## **2.3 KEKB accelerator and Belle detector**

The search for possibilities to test the Kobayashi-Maskawa mechanism of  $CP$  violation lead to the concept of the  $B$  factory experiments, of which the Belle experiment is one. It is located at the High Energy Accelerator Research Organisation (KEK) in Tsukuba, Japan. The  $e^+$  and  $e^-$  bunches collide in the KEKB storage ring approximately 3 km in circumference. The beam energies are tuned in such a way that  $\Upsilon(4S)$  mesons are produced, which in turn decay into a pair of  $B$  mesons. The Belle detector sits at the interaction point of KEKB.

### **2.3.1 KEKB accelerator**

A schematic of the KEKB accelerator complex is given in Fig. 2.6. KEKB is an asymmetric-energy  $e^+e^-$  collider [49]. Electrons and positrons are accelerated and

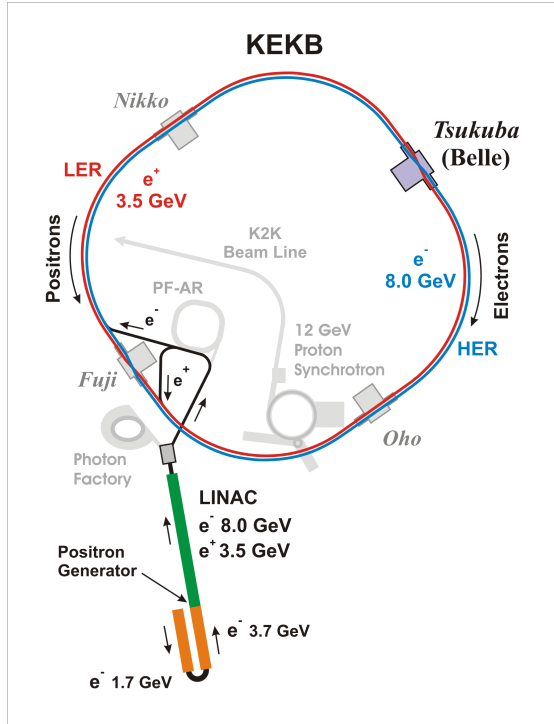


Figure 2.6: Schematic of the KEKB accelerator complex [49].

stored in two separate storage rings; a high energy ring (HER) for electron beams having energy 8 GeV and a low energy ring (LER) for positron beams with energy 3.5 GeV. The Lorentz boost created by the asymmetric-energy collisions aid the time-dependent  $CP$  violation measurements in  $B$  meson decays.

The LER and HER are located 11 m below the ground in a tunnel that was earlier utilized for the TRISTAN experiment [50] in the 1980s. A LINAC is used to accelerate the electron beams. A tungsten target material is placed in their path and hence some of the electron beams hit the target producing a shower of particles including positrons. Positrons are then isolated with the help of a magnetic field. The electron and positron beams are then injected into the storage rings. The LER and HER can store currents up to 2.6 A and 1.1 A, respectively; they use an RF of 508.9 MHz to accelerate the beams [51]. The beams are made to circulate in precise paths with the help of dipole, quadrupole and sextupole magnets in a similar manner to CESR as described in Sec. 2.2.1.

The electron and positron beams collide at the IP in Tsukuba Hall. There is a crossing angle of  $\pm 11$  mrad between the bunches at the time of collision [52]. This crossing angle makes the interaction region free from any parasitic collisions due to multiple bunches. Also it eliminates the need for any separation-bend magnets, which

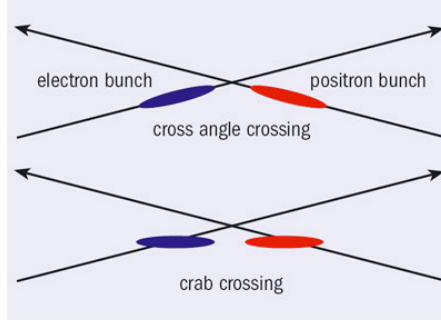


Figure 2.7: A schematic of cross-angle and crab crossings [55].

Data type	$\sqrt{s}$ (GeV)	Luminosity ( $\text{fb}^{-1}$ )
$\Upsilon(4S)$ resonance	10.58	711
$\Upsilon(4S)$ off-resonance	10.52	89
$\Upsilon(5S)$ resonance	10.86	121
$\Upsilon(5S)$ scan	$10.58 < E_{\text{CM}} < 11.02$ ( $E_{\text{CM}} \neq M_{\Upsilon(5S)}$ )	7
$\Upsilon(3S)$ resonance & off-resonance	10.35 & 10.32	2
$\Upsilon(2S)$ resonance & off-resonance	10.02 & 9.99	28
$\Upsilon(1S)$ resonance & off-resonance	9.46 & 9.43	8
Total		966

Table 2.1: Data collected at or near different  $\Upsilon$  resonances and their corresponding luminosity.

significantly reduces the beam-related background level. The maximum luminosity is achieved when the beams collide head on and hence two superconducting crab cavities [53, 54] are used to kick the bunches into horizontal plane. A transverse RF in the crab cavities allows the bunches to rotate and collide with maximum overlap at the IP. This is illustrated in Fig. 2.7.

The collisions happen at different centre-of-mass energies ( $\sqrt{s}$ ) corresponding to various  $\Upsilon$  resonances. The majority of the data (74%) is collected at the  $\Upsilon(4S)$  resonance. The data collected at or near different  $\Upsilon$  resonances are given in Table 2.1. The cross section in the  $\Upsilon$  resonance region is shown in Fig. 2.8. The highest instantaneous luminosity achieved by KEKB is  $2.11 \times 10^{34} \text{ cm}^{-2}\text{s}^{-1}$ , which is a world record [57]. The total integrated luminosity is approximately  $1 \text{ ab}^{-1}$  at the end of the physics running in 2010.

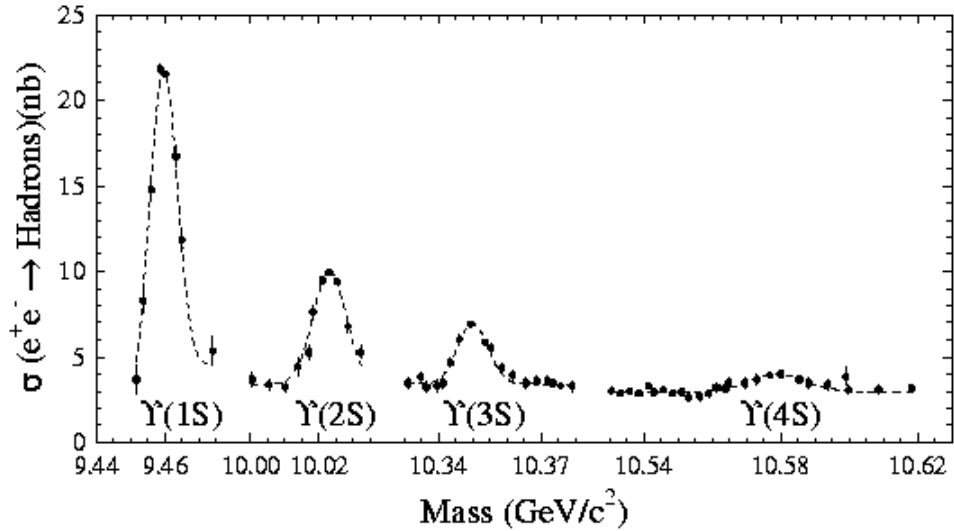


Figure 2.8: Cross sections of various  $\Upsilon$  resonances from  $e^+e^-$  collisions [56].

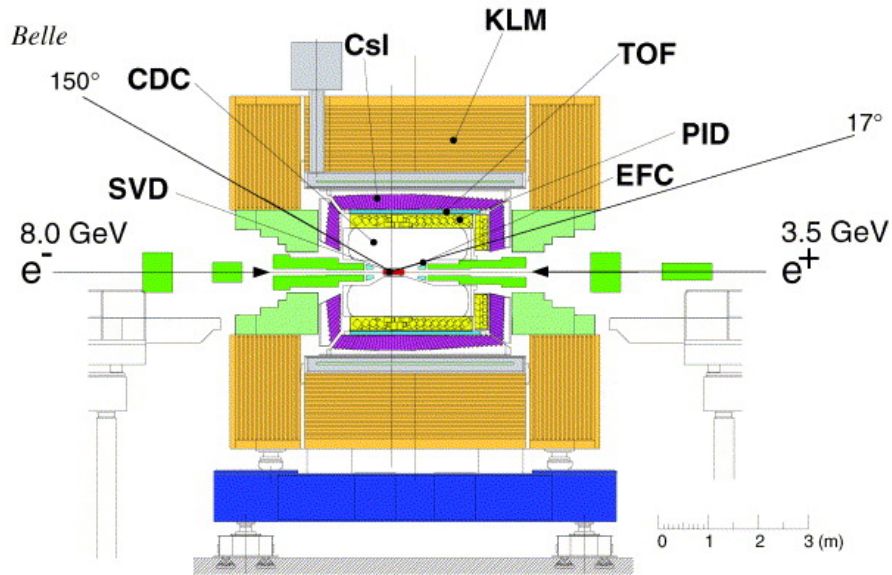


Figure 2.9: Schematic view of the Belle detector cross section [58].

### 2.3.2 Belle detector

The Belle detector [58, 59] surrounds the interaction region of the electron and positron beams. It is a layered general purpose detector with different subsystems dedicated to various aspects of the event reconstruction. A schematic view of the detector cross section is given in Fig. 2.9.

The innermost part is a Silicon Vertex Detector (SVD) system, which precisely determines the decay vertices of particles and obtains trajectories of charged particles. A Central Drift Chamber (CDC) surrounds the SVD completing the tracking system. The CDC also helps in distinguishing various particle types via  $dE/dx$  measurements.

The Aerogel Cherenkov Counter (ACC) and Time-of-Flight (TOF) counter subsystems aim to separate the particle species efficiently. A lot of kaons and pions are produced at Belle from the decay of primary particles and they behave identically at high momentum. So the particle identification system comprising the CDC, ACC and TOF detectors is essential in distinguishing them efficiently. A crystal calorimeter surrounds the particle identification system and it measures the energy deposited by electromagnetic interactions. The whole detector is located in a 1.5 T magnetic field produced by a superconducting solenoid. The outermost part is the  $K_L^0$  and muon detection system (KLM).

The IP region should have minimum material surrounding it to minimize multiple scattering before the charged particle is detected. So the IP region is surrounded by cylindrical pipes made of beryllium (Be), which is the lightest stable element on the earth. Therefore, Be induces minimal multiple scattering as the average angle of deflection is proportional to the atomic number. The beam pipe is 0.5 mm thick which corresponds to only 0.3% of a radiation length. The coordinate system is defined with the origin at the position of IP. The  $z$  direction is defined as the  $e^+$  beam direction and,  $x$  and  $y$  directions point outward from the centre of KEKB ring horizontally and vertically, respectively.

The following subsections describe the sub-detector systems in detail.

### **Silicon Vertex Detector (SVD)**

The SVD is the tracking system surrounding the beam pipe; it provides precise determination of the decay vertices of particles like the  $B$  and  $D$  mesons. This vertexing capacity is essential for time-dependent  $CP$  violation measurements such as those of  $B^0 \rightarrow J/\psi K_S^0$ . The average separation between the decay vertices of  $B$  and  $\bar{B}$  mesons is 200  $\mu\text{m}$ . The resolution of the vertex separation measurement by the SVD along the  $z$  direction is 100  $\mu\text{m}$ . The vertex resolution is affected by the multiple-Coulomb scattering as most of the particles produced at Belle are of momenta 1 GeV/ $c$  or less. This effect is minimized by placing the SVD as close to the IP as possible. The supporting structure used for the SVD is of low mass and the accompanying electronics are placed outside the tracking volume to keep the material budget low.

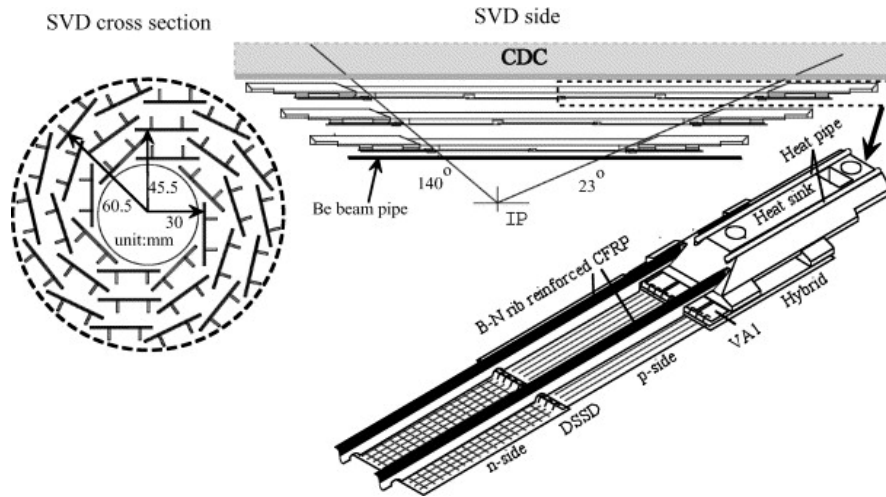


Figure 2.10: Schematic view of the SVD1 subsystem of Belle [60].

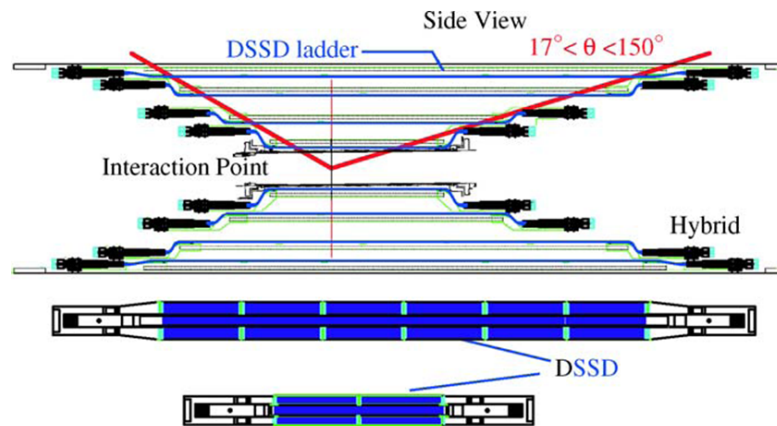


Figure 2.11: Schematic view of the SVD2 subsystem of Belle [63].

The SVD is a tracking detector to obtain the trajectories of charged particles. Their path is helical in shape due to the presence of the uniform magnetic field, with its axis in the direction of the magnetic field. It is possible that some low momentum particles do not reach the drift chamber and get curved back into the SVD. The tracking provided by the SVD is crucial in such cases. There are two types of SVD sub-detectors used in Belle: a three layer SVD1 until summer 2003 and a four layer SVD2 till the end of data taking in 2010.

The schematic of SVD1 is shown in Fig. 2.10. There are three layers made of double-sided silicon strip detectors (DSSD) that cover 86% of the  $4\pi$  solid angle. These

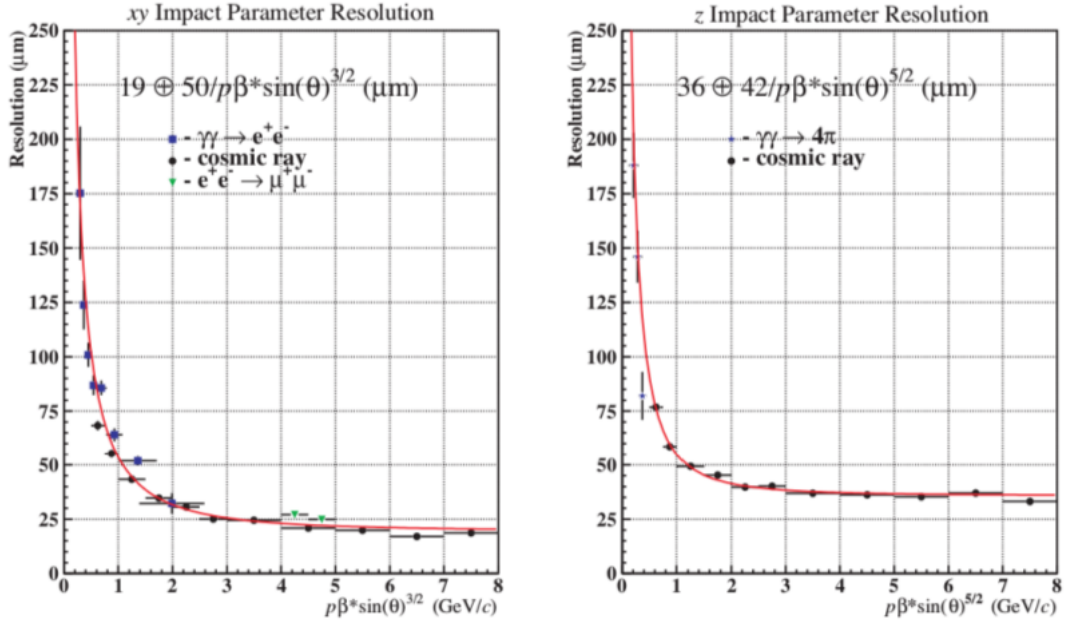


Figure 2.12: Resolution of the impact parameter measured by the SVD [58]. Here  $p$ ,  $\beta$  and  $\theta$  are the momentum, Lorentz boost factor and polar angle, respectively.

layers are located at radii of 30.0 mm, 45.5 mm and 60.5 mm, respectively. Each DSSD has 1280 sensor strips and 640 readout pads on either sides. There are a total of 102 DSSDs used that each have a size of  $57.5 \times 33.5 \text{ mm}^2$ . The  $z$ -strip pitch is 42 mm and  $\phi$ -strip pitch is 25 mm. The readout system is based on the VA1 integrated circuit [61, 62].

SVD2 replaced the previous version in 2003 because SVD1 was damaged by synchrotron radiation. A schematic of SVD2 is given in Fig. 2.11. SVD2 covers 92% of the  $4\pi$  solid angle and has four layers. The measured impact parameter resolution is given in Fig. 2.12 as a function of momentum. The performance of SVD2 is found to be better than SVD1 due to the presence of an extra layer of DSSDs that results in more coverage.

The reconstruction of a  $K_S^0$  meson from a pair of charged pions requires information from the SVD; they often decay within the SVD as their average decay length is about the same as the radius of the last layer (less than 6 cm). So the hits from the charged pions in the SVD are essential for efficient reconstruction. Another instance where SVD information is crucial is the detection of charged pions in the decay  $D^{*\pm} \rightarrow D\pi^\pm$ , where the pion is produced with low momentum. The track multiplicity of these pion tracks are reduced with the help of SVD hit information.

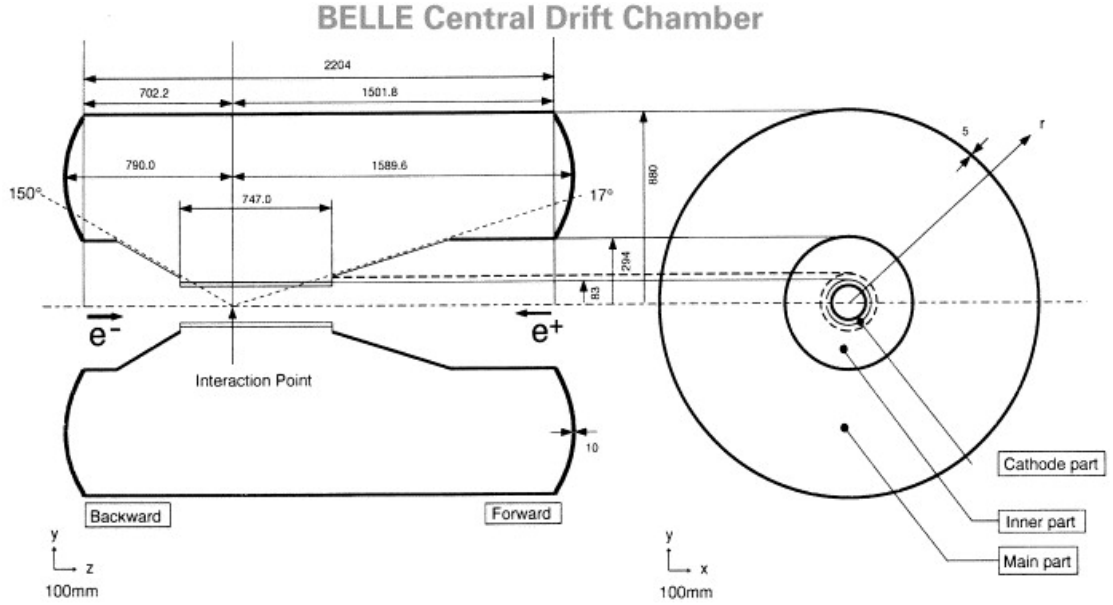


Figure 2.13: Schematic view of the CDC subsystem of Belle [64].

### Central Drift Chamber (CDC)

The CDC is a gaseous detector [64], which together with the SVD, forms the tracking system of the Belle experiment. Equal amounts of He and C<sub>2</sub>H<sub>6</sub> fill the detector volume, which ensures minimal multiple scattering. Charged particles, while travelling through the gaseous medium, interact with the molecules and ionize them. A tracking algorithm enables the reconstruction of this path from the hits in the CDC. A schematic of the CDC is given in Fig. 2.13.

The CDC is an asymmetric detector with an angular coverage of  $17^\circ \leq \theta \leq 150^\circ$ , where  $\theta$  is the polar angle. The inner and outer radii are 103.5 mm and 874.0 mm, respectively. The inner part has a conical shape to have no intrusion from the accelerator components and also to maximize the acceptance. There are 50 cylindrical layers in total and the spatial resolution is of about approximately 130  $\mu\text{m}$ . Each layer contain between three and six axial or small-angle-stereo layers, and three cathode strip layers. There are 8400 drift cells in the CDC, each consisting of a sense wire surrounded by eight parallel field wires. The momentum resolution is  $\sigma_{p_t}/p_t \sim 0.5\% \sqrt{1 + p_t^2}$ , where  $p_t$  is the momentum in the transverse direction, for charged particles with  $p_t > 100 \text{ MeV}/c$ .

The CDC is also designed to measure the rate of energy loss ( $dE/dx$ ) of a charged particle as described in Sec. 2.2.2. The  $dE/dx$  measurement for various particle types

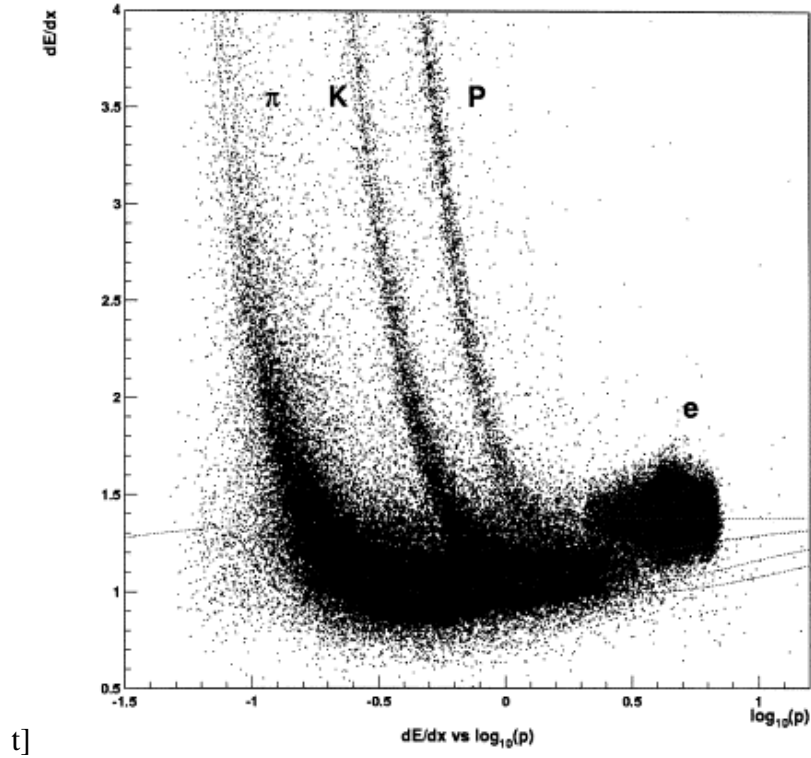


Figure 2.14:  $dE/dx$  measurements for various particle types as a function of momentum [58].

as a function of momentum is shown in Fig. 2.14. The  $dE/dx$  measurement provides good separation between various particle species at momentum values  $\leq 0.8$  GeV/c. It is essential for the efficient separation of kaons and pions for the analysis presented in this thesis.

### Aerogel Cherenkov Counter (ACC)

The ACC [55, 65] is a dedicated system for identifying different particle types. It works well in the momentum range 0.5–4 GeV/c. It extends the particle identification capabilities to momenta beyond that which can be measured by the CDC. The basic working principle is the production of Cherenkov radiation as mentioned earlier in the case of RICH detector at CLEO-c in Sec. 2.2.2. A threshold ACC is used at Belle, *i.e.* the refractive index of the medium is selected such that the pions emit Cherenkov radiation and kaons do not. The kaons and pions are distinguished by measuring the difference in the corresponding Cherenkov photon yields.

A schematic of the ACC subsystem is shown in Fig. 2.15. There are 960 modules in total that are segmented into 60 cells in the  $\phi$  direction, as the barrel part, and 228

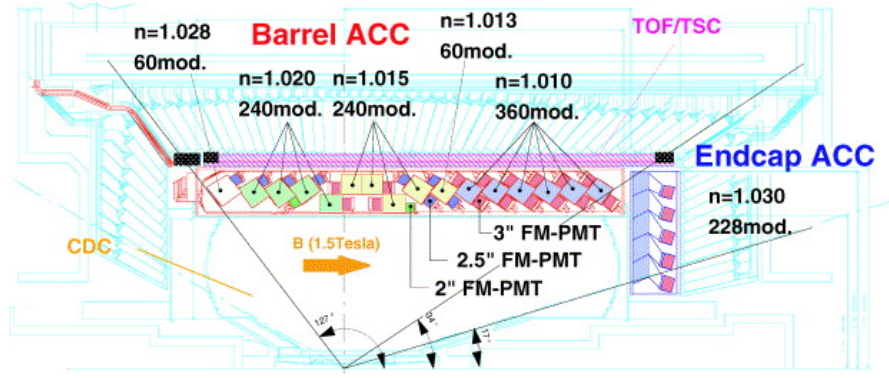


Figure 2.15: Schematic view of the ACC subsystem of Belle [58].

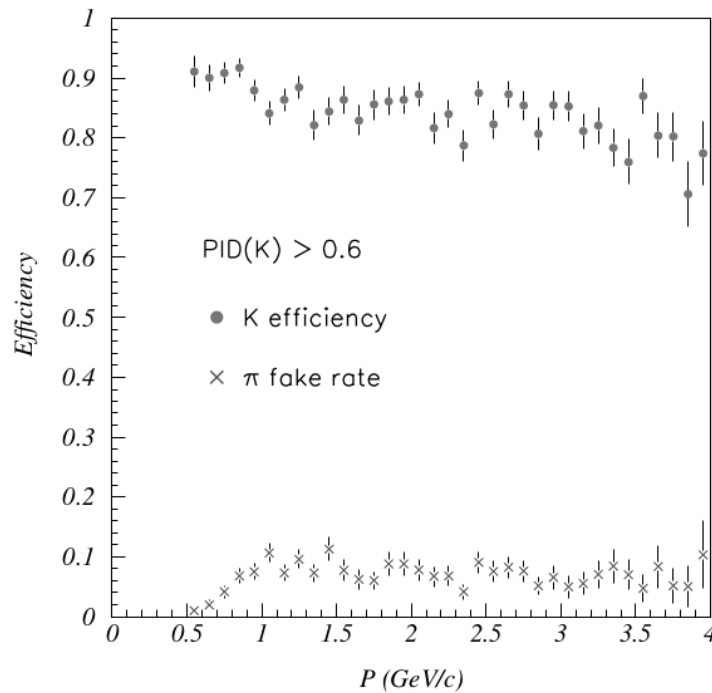


Figure 2.16: Kaon identification efficiency and pion fake rate from  $D^{*+} \rightarrow D^0(K^-\pi^+)\pi^+$  decays using information from the ACC [58].

modules in five concentric layers, in the forward endcap part. A single ACC cell has dimensions  $12 \times 12 \times 12 \text{ cm}^3$  and is made of aluminum with silica aerogel tiles enclosed in it. There are photo-multiplier tubes in each cell to detect the Cherenkov photons. They are specially designed to work in a magnetic field of 1.5 T. The refractive index of the aerogel in each cell is selected in the range (1.010–1.028) according to the momentum distribution of particles at their polar angle position to give optimal separation between kaons and pions. The polar angle coverage of the ACC is  $17^\circ \leq \theta \leq 127^\circ$ . The barrel and forward endcap regions of the ACC works well in the momentum ranges 1.0–3.6 GeV/c and 0.7–2.4 GeV/c, respectively.

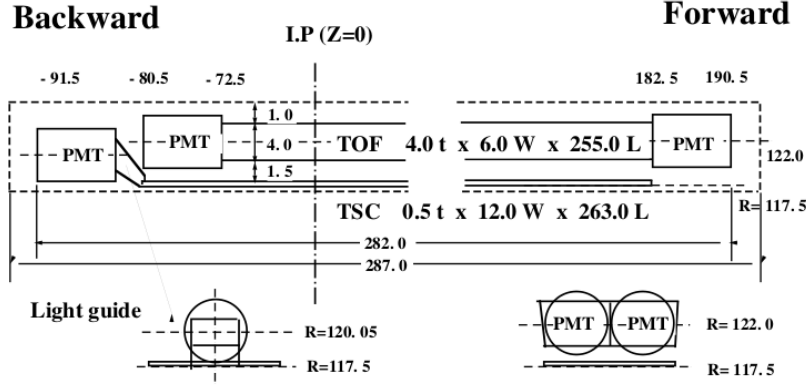


Figure 2.17: Schematic view of the TOF modules and their dimensions [58].

The performance of the ACC while distinguishing between kaons and pions is illustrated in Fig. 2.16. The decays  $D^{*+} \rightarrow D^0(K^-\pi^+)\pi^+$ , where the charges of the pion and kaon ( $D$  daughters) are fixed by the charge of the pion from the  $D^{*+}$ , are used to estimate the performance of the ACC. The kaon identification efficiency is greater than 80% with less than 10% chance of it being identified as a pion.

### Time Of Flight (TOF) counter

The third component of the particle identification system at Belle is the TOF sub-detector [65]. It distinguishes different particles with momenta less than 1.2 GeV/c. Particles with a minimum transverse momentum of 0.28 GeV/c reach the TOF. It provides fast-timing signals with a resolution of 100 ps that are also used in the Belle trigger system.

The TOF system is an array of plastic scintillators, that have 128 TOF counters and 64 trigger scintillation counters (TSC) in total. One module is comprised of two trapezoidal shaped TOF counters and one TSC counter with a radial gap of 1.5 cm between them. The gap ensures that the TOF counters are protected from any electrons and positrons created in the TSC layer. There are 64 such modules in the system that is located at a radius of 1.2 m from the IP. The TOF system covers the polar angle region  $34^\circ < \theta < 120^\circ$ . The TOF modules and their dimensions are shown in Fig. 2.17.

Scintillation counters excite molecules that then radiate to generate photons and photomultiplier tubes are used to detect them. The desired time resolution is achieved with various design strategies: a fast scintillator with an attenuation length longer than

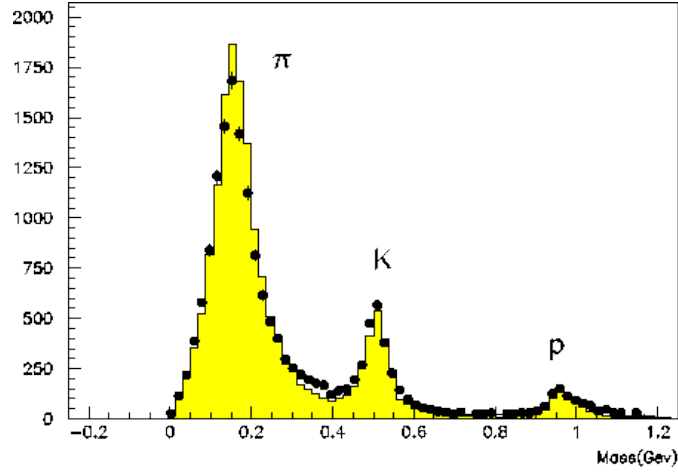


Figure 2.18: Mass distribution obtained from TOF measurements. The black points with error bars are the data points and histogram is the prediction from Monte Carlo simulations [66].

2 m is used; the time dispersion of scintillation photons is minimized by eliminating light guides; and the phototubes have a large area photocathode to maximize the photon collection efficiency.

The TOF measures the time interval between the  $e^+e^-$  collision and the time at which a charged particle hits the TOF system. The average time to travel between the IP and TOF counters is 3 ns. The time resolution of the TOF is good enough to measure this time interval. Different particle types are identified by the difference in the time of flight, which can be written as

$$t = \frac{l}{c\beta} = \frac{l}{c} \sqrt{1 + c^2 \left( \frac{m}{|\vec{p}|} \right)^2}, \quad (2.4)$$

where  $l$ ,  $\beta$ ,  $m$  and  $|\vec{p}|$  are the path length, velocity, mass and momentum of the particle, respectively. The TOF is capable of measuring the relevant time differences between particle hypotheses. The  $t$  measurement along with the given  $l$  and  $|\vec{p}|$  are used to extract the mass of the particle and thus the particle species. The mass distributions obtained for various particle types are shown in Fig. 2.18.

An overall likelihood is formed by combining the measurements of CDC, ACC and TOF subsystems and this is used to identify the particle type at the reconstruction level. The analysis presented here uses this likelihood to separate between charged kaons and pions.

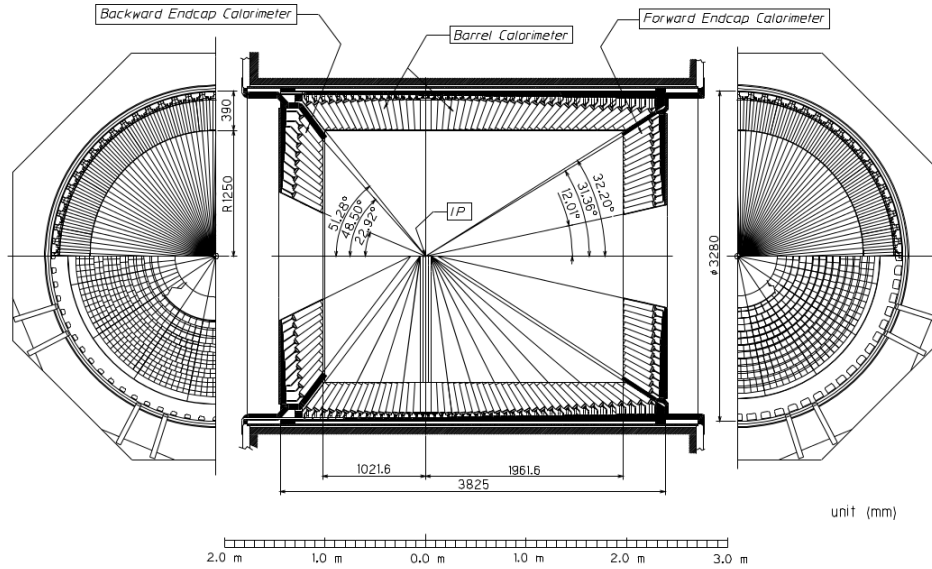


Figure 2.19: Schematic view of the ECL subsystem of Belle [58].

### Electromagnetic Calorimeter (ECL)

The ECL surrounds the particle identification system of Belle. It is used to measure the energy of electromagnetic showers produced by electrons, positrons and photons. It has high efficiency and excellent resolution. When an electron or a photon is incident on a thick absorber, it loses all its energy by bremsstrahlung and  $e^+e^-$  pair production, respectively. This shower propagates longitudinally and the characteristic scale of this process is the radiation length of the absorber. The photons and  $e^\pm$  are distinguished by combining the shower energy measurement with the tracking information. An energy cluster that is not associated with any tracks would be a photon candidate, if there is an associated track, then it is more likely to be from an  $e^+$  or  $e^-$  candidate.

The ECL is made up of a highly segmented array of thallium doped CsI crystals. Silicon photodiodes are used as readout units. The CsI(Tl) crystals ensure large photon yield along with mechanical stability. Weak hygroscopicity and moderate price are the other reasons for this choice of the crystals. The crystals emit photons at a rate proportional to the energy loss of the incident particle. A schematic of the ECL is shown in Fig. 2.19. The barrel region is 3.0 m in length with an inner radius of 1.25 m. The forward and backward endcap sections are located at  $z = 2.0$  m and  $-1.0$  m, respectively from the IP. A small tilt of  $1.3^\circ$  in  $\theta$  and  $\phi$  directions is imposed in the barrel region to avoid any photons escaping through the gap between the crystals. The total coverage of the ECL is about 91% of the  $4\pi$  solid angle with  $17^\circ < \theta < 150^\circ$ . The forward

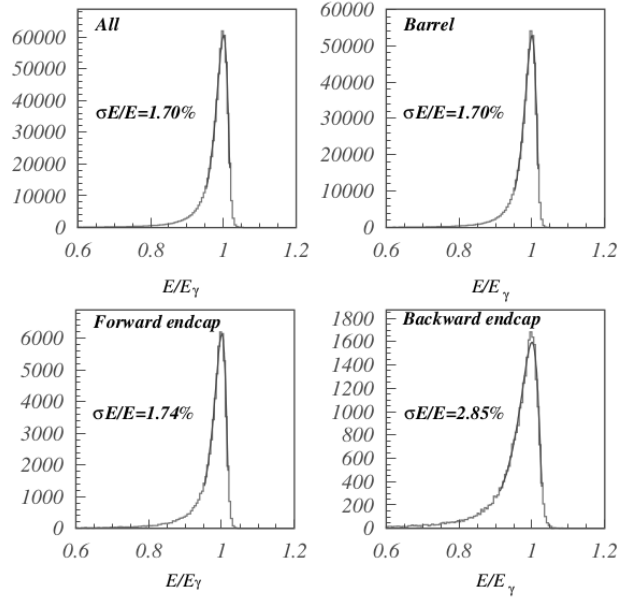


Figure 2.20: Energy resolution measured from Bhabha scattering in total (top left), barrel (top right), forward endcap (bottom left) and backward endcap (bottom right) regions of the ECL [58].

endcap, barrel and backward endcap regions of the ECL are defined in the polar angle ranges  $(12.4^\circ, 31.4^\circ)$ ,  $(32.2^\circ, 128.7^\circ)$  and  $(130.7^\circ, 155.1^\circ)$ , respectively. There are 8736 crystals in total.

The energy calibration of the ECL is performed with Bhabha and  $e^+e^- \rightarrow \gamma\gamma$  events. The energy resolution is found to be 1.70%, 1.74% and 2.85% for the barrel, forward endcap and backward endcap regions, respectively. The energy resolution from the Bhabha events are given in Fig. 2.20. The diphoton invariant mass resolutions is achieved to be  $4.9 \text{ MeV}/c^2$  for  $\pi^0$  and less than  $10 \text{ MeV}/c^2$  for  $\eta$ .

All the subsystems of Belle described so far, are placed in a magnetic field of 1.5 T provided by a superconducting solenoid in a cylindrical volume of dimensions 4.4 m in length and 3.4 m in diameter. The coil is surrounded by a multi-layered iron structure that serves as the return path of the magnetic flux. It also acts as the absorber material for KLM sub-detector.

### $K_L^0$ and muon detector (KLM)

The KLM is the outermost subsystem of Belle. It is designed to identify  $K_L^0$  mesons and muons that travel a sufficient distance in the detector volume and reach the outermost

Particle interaction	Cross section (nb)	Rate (Hz)
$\Upsilon(4S) \rightarrow B\bar{B}$	1.2	12
$e^+e^- \rightarrow q\bar{q}(q = u, d, s, c)$	2.8	28
$e^+e^- \rightarrow \mu^+\mu^-/\tau^+\tau^-$	1.6	16
$e^+e^- \rightarrow e^+e^-$ (Bhabha scattering) ( $\theta_{\text{lab}} > 17^\circ$ )	44	4.4
$e^+e^- \rightarrow \gamma\gamma$ ( $\theta_{\text{lab}} > 17^\circ$ )	2.4	0.24
Two photon events ( $\theta_{\text{lab}} > 17^\circ$ & $p_T \geq 0.1$ GeV/c)	$\approx 15$	$\approx 35$

Table 2.2: Different physics processes and their cross sections. Their respective trigger rates at a luminosity of  $10^{34}$  cm<sup>-2</sup> s<sup>-1</sup> [58].

part. It is made of resistive plate counters (RPC) sandwiched between iron plates. Iron plates act as the active medium for the particle to interact and the RPCs detect the signal from these interactions. RPCs are made of two parallel plate glass electrodes having bulk resistivity  $> 10^{10}$   $\Omega$  cm separated by a gas mixture of 62% CH<sub>2</sub>FCF<sub>3</sub>, 30% Ar and 8% C<sub>4</sub>H<sub>10</sub>. The analysis presented here, does not use any information from the KLM subsystem to reconstruct the final states of interest.

### Trigger system

The  $e^+e^-$  collisions produce a variety of events and particles. To record all events, it would require a lot of storage space and the bandwidth of the data acquisition (DAQ) system would be saturated. This is avoided by using a triggering system, which selects only the events of interest. An efficient trigger system identifies different event types quickly and selects only those events that are needed for analyses. The selection criteria are defined based on the information from the Belle sub-detector systems. The triggering rate for different processes at an instantaneous luminosity of  $10^{34}$  cm<sup>-2</sup> s<sup>-1</sup> is given in Table 2.2. The trigger rates for Bhabha and  $\gamma\gamma$  events are pre-scaled by a factor of  $10^{-2}$  because of their large cross section.

The physics processes of interest have a trigger rate of 100 Hz in total. Simulation studies show that the beam-related backgrounds have an expected rate of around 100 Hz. So the total rate is expected to be 200 Hz. The Belle trigger system is designed to operate up to 500 Hz and is robust against high beam background levels.

The Belle trigger system schematic is shown in Fig. 2.21. The trigger system has two stages: Level 1 (L1) and Level 3 (L3). L1 trigger is built based on the information

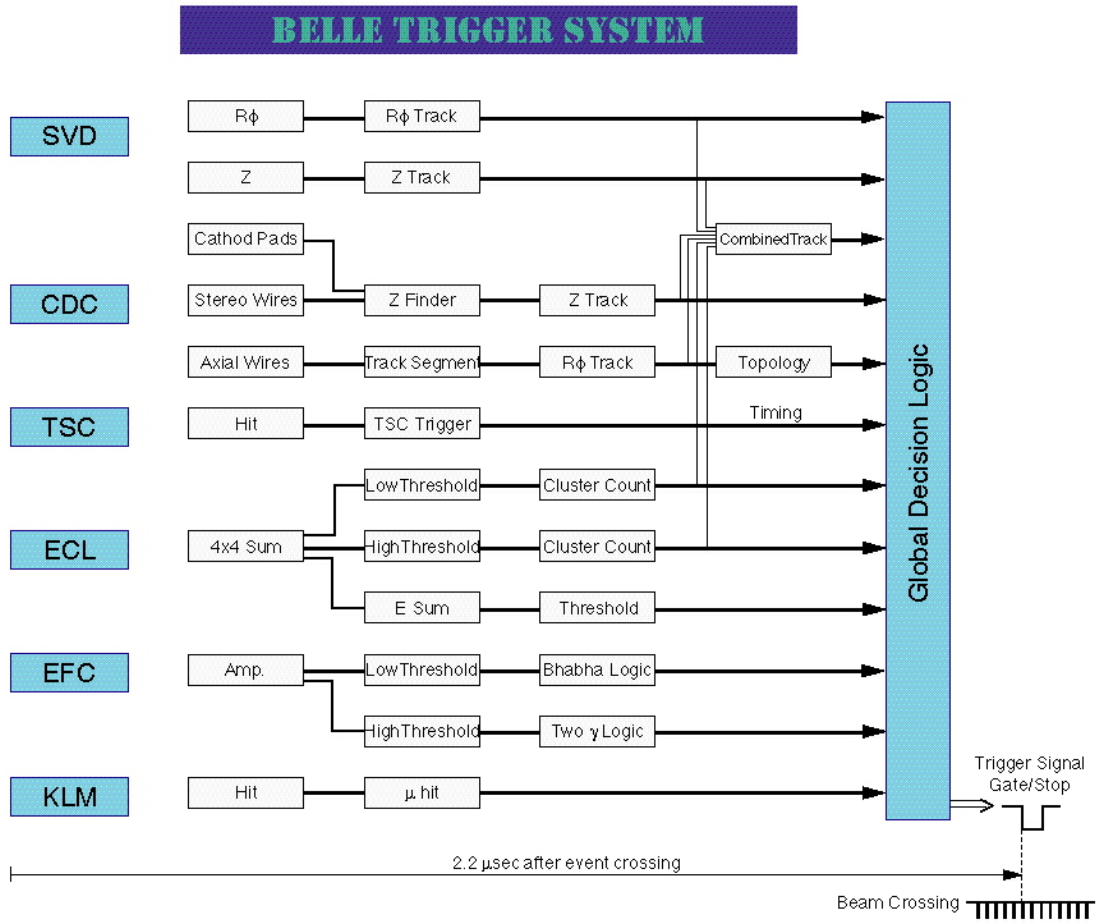


Figure 2.21: An overview of the Belle trigger system [67].

from the sub-detectors, whereas L3 is a software trigger implemented online in the computer farm. The CDC, ACC and TOF subsystems provide a track trigger for L1. The energy trigger is obtained from the ECL based on the energy deposition in the CsI(Tl) crystals. These are processed in parallel and then transferred to the central triggering system, the Global Decision Logic (GDL), which characterizes different event types. The L1 trigger system has an efficiency of more than 98% for hadronic events, which are of interest in this thesis.

The L3 trigger has the raw data information from the sub-detectors. First the L3 trigger algorithm checks if the event is already classified at L1 level. If not, then L3 performs a fast reconstruction and rejects events having no track with an impact parameter  $|z| < 5$  cm and an energy less than 3 GeV deposited in the ECL. Thus a large amount of beam related backgrounds are rejected. The efficiency of the L3 trigger is 98% for hadronic and  $\tau$ -pair events.

## Data Acquisition system (DAQ)

The DAQ can record data up to 500 Hz and the typical event size is 30 kB with a maximum data transfer rate of 15 MB/s. A schematic of the DAQ system is shown in Fig. 2.22. The data obtained from the sub-detectors are in the form of analog pulses proportional to the energy deposited in them. These analog pulses are converted to digital by time-to-digital converters (TDC). A charge-to-time (Q-to-T) technique is adopted to read out signals from all the sub-detectors except SVD and KLM. The SVD uses flash analog-to-digital converter instead of TDCs. When the GDL receives a trigger signal, the event-builder combines the data from each sub-detector into a single event. Thus the detector-by-detector parallel data streams are converted into event-by-event data. The output of the event-builder is then transferred to the online computer farm through the L3 trigger. The data quality is continuously monitored by the data quality monitor in the online computer farm. In the end, the data is passed on to the mass-storage system at the KEK computing facility by optical fibre.

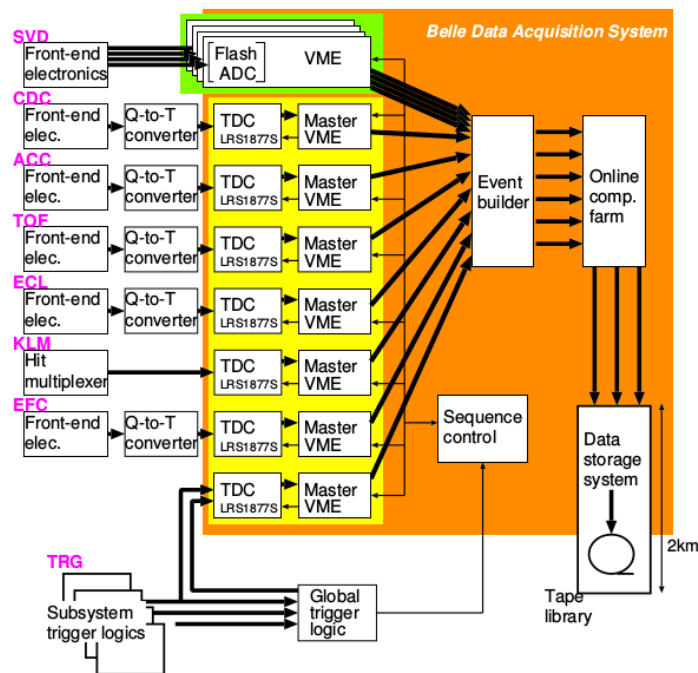


Figure 2.22: A schematic of the Belle DAQ system [58].



# CHAPTER 3

## Quantum-correlated $D$ -decay measurements at CLEO-c

### 3.1 Introduction

This chapter describes the reconstruction of  $D \rightarrow K_S^0 \pi^+ \pi^- \pi^0$  decays tagged with a variety of  $D$  final states at CLEO-c. These quantum-correlated  $D$  decays are exploited to estimate the  $CP$ -content and the strong-phase difference between  $D^0$  and  $\bar{D}^0$  in localized regions of  $D$  phase space.

The double-tagged yields for the signal mode produced along with a set of other  $D$  final state are measured. The single-tagged yield,  $S$ , where only one of the  $D$  meson decays is specified, is needed to normalize the double-tagged yields while estimating the parameters of interest. This is given by

$$S(g) = \mathcal{N}\mathcal{B}(g), \quad (3.1)$$

for a final state  $g$ , where  $\mathcal{B}$  is the branching fraction of  $D \rightarrow g$  and  $\mathcal{N}$  is the normalization factor. This normalization by the single-tagged yield reduces the dependence of the measurement on the reconstruction efficiency.

The remainder of this Chapter is structured as followed. In Sec. 3.2 the data and Monte Carlo (MC) samples used are described. The event selection criteria of different final-state particles are given in Sec. 3.3. Sections 3.4 and 3.5 explain the single-tagged and double-tagged yield estimations, respectively. The measurement of strong-phase parameters is presented in Sec. 3.6, followed by the sensitivity of these measurements to the determination of  $\phi_3$  in Sec. 3.7.

### 3.2 Data sample

A data sample consisting of  $D\bar{D}$  pairs coming from the  $\psi(3770)$  resonance collected by the CLEO-c detector at the CESR symmetric  $e^+e^-$  collider is used. This sample

Type	Modes
<i>CP</i> -even	$K^+K^-, \pi^+\pi^-, K_S^0\pi^0\pi^0, K_L^0\omega, K_L^0\pi^0$
<i>CP</i> -odd	$K_S^0\pi^0, K_S^0\eta, K_S^0\eta'$
Mixed <i>CP</i>	$\pi^+\pi^-\pi^0, K_S^0\pi^+\pi^-, K_L^0\pi^+\pi^-$
Flavour	$K^\pm e^\mp \nu_e$

Table 3.1: Different tag modes used in the analysis.

corresponds to an integrated luminosity of  $0.82 \text{ fb}^{-1}$  and approximately three million  $D\bar{D}$  pairs. Both the  $D$  mesons are reconstructed so that the quantum-correlated rates can be determined. There are no accompanying fragmentation particles because the decay of  $\psi(3770)$  to  $D\bar{D}$  happens at the kinematic threshold for their production. The clean environment of  $e^+e^-$  collisions ensures that any possible  $D$  final state can be reconstructed precisely. This also allows the reconstruction of final states where one particle escapes detection like a  $\nu$  or a  $K_L^0$  meson. The four momentum of this particle can be inferred from the four momentum of the detected particles and the known beam energy.

Monte Carlo (MC) simulations of signal events are used to estimate selection efficiencies. Generic samples of  $D\bar{D}$  MC events having twenty times the integrated luminosity of the data set are used to determine the background contributions. The `EvtGen` [68] package is used to generate the decays and the detector response is modelled with `Geant` [69]. The final-state radiation associated with charged particles is simulated with `PHOTOS` [70].

### 3.3 Event selection

One of the  $D$  mesons is reconstructed in the final state of interest,  $K_S^0\pi^+\pi^-\pi^0$ , and the other to one of the different tag states given in Table 3.1. The decay modes are reconstructed in the CLEO-c software framework via custom C++ codes. All tracks and showers associated with both the  $D$  mesons are reconstructed. The selection is done in multiple stages. A set of loose selection criteria are applied when the data is centrally produced; this is also known as skimming or preselection. This reduces the data size significantly. A typical event size is 25 kB. Then additional requirements are placed to optimize the signal efficiency, while rejecting most of the background events.

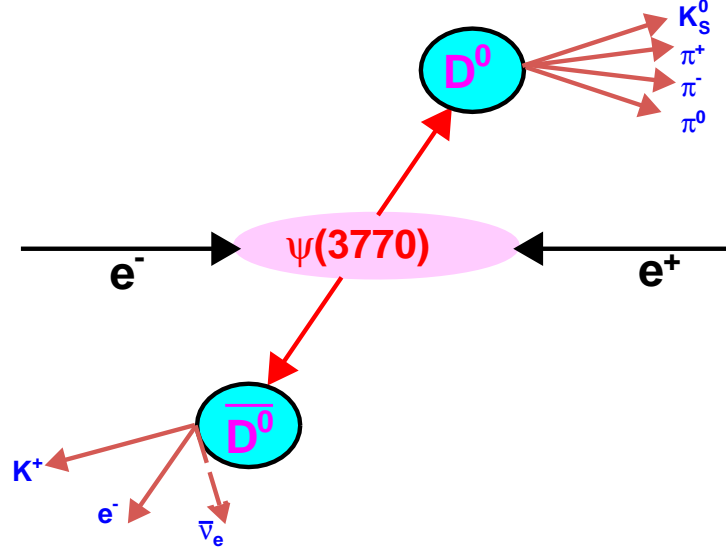


Figure 3.1: Schematic diagram of a double-tagged event at CLEO-c.

In a double-tagged event, both the  $D$  mesons are reconstructed; one to the signal mode and the other to any of the tag modes as illustrated in Fig. 3.1. If only one of the  $D$  mesons is reconstructed, then the event is referred to as single-tagged. The final state particles of interest are  $K^\pm, \pi^\pm, \gamma$  and  $e^\pm$ ; they get directly detected by various sub-detectors as described in Chapter 2. The parent particles like  $\pi^0, \eta, \eta', K_S^0$  and  $D$  are then reconstructed from them. The selection criteria for each of these particle types are described in the following subsections.

### 3.3.1 Selection of $K^\pm$ and $\pi^\pm$ candidates

Each charged track ( $K^\pm$  or  $\pi^\pm$ ) is required to have momentum in the range 50 MeV/ $c$  to 2 GeV/ $c$ . The impact parameter, the distance of closest approach to the interaction point of a reconstructed track, is evaluated in the  $z$  direction and in the  $x - y$  plane denoted as  $z_0$  and  $d_0$ , respectively. The selection criteria on these impact parameters ensures that the signal candidates originate from the IP and beam-induced background are rejected. Events with  $|z_0| < 5.0$  cm and  $|d_0| < 0.5$  cm are selected for further analysis.

As described in Chapter 2, the charged tracks are made from the hits obtained in the tracking system with the help of a Kalman filter algorithm [45]. Good tracks are selected based on the quality of the fit with a criteria that the fit converges. The track is required to lie in the region  $|\cos \theta| < 0.93$ , where  $\theta$  is the angle between the track

and the beam axis. This criterion helps in removing background from noise hits close to the beam pipe. The hit fraction of a track is defined as the ratio of the number of hits recorded in the tracking system to the number of expected hits given the momentum and trajectory of the track; this quantity is required to be at least 0.5 for a good track.

The collection of good charged tracks needs to be separated into kaons and pions. The particle identification (PID) information from the Drift Chamber and RICH sub-detector systems are used for this purpose. The energy loss  $dE/dx$  of one particular track is required to be less than three standard deviations away from that expected for the chosen mass hypothesis, provided the track momentum is known. The information from RICH is used if  $|\cos \theta| \leq 0.83$ , track momentum greater than 0.7 GeV/c and there are at least three Cherenkov photons detected. Thus the tracks reaching the RICH will have sufficient momentum to be above the Cherenkov threshold. A combined log likelihood is formed from  $dE/dx$  and RICH information that is used to distinguish between a pion and a kaon.

### 3.3.2 Selection of $\pi^0$ and $\eta$ candidates

The neutral  $\pi^0$  and  $\eta$  mesons are identified from their decay to a pair of photons. The photon energy is measured in the electromagnetic calorimeter and the reconstructed invariant mass of the diphoton candidate is required to be less than 1 GeV/ $c^2$  at the preselection level. The magnitude of the pull mass of the candidate should be less than three, where the pull mass is defined as

$$m_p = \frac{M - m_0}{\sigma_m}, \quad (3.2)$$

with  $M$  as the measured  $\pi^0/\eta$  mass,  $m_0$  the nominal mass [14] and  $\sigma_m$  the uncertainty on the measured mass.

The photon showers in the ECL are required to be well isolated by placing an additional shower-quality requirement. The ratio of the energy deposited by each shower in a  $3 \times 3$  grid of ECL cells around the shower to that in  $5 \times 5$  grid of cells must be equal to 1. This variable is represented as  $E_9/E_{25}$ . A vertex fit is performed and if the fit converges the candidate is retained. The  $M_{\pi^0}$  distribution of MC simulated  $D^0 \rightarrow K_S^0 \pi^+ \pi^- \pi^0$  single-tagged candidates after applying the selection criteria is

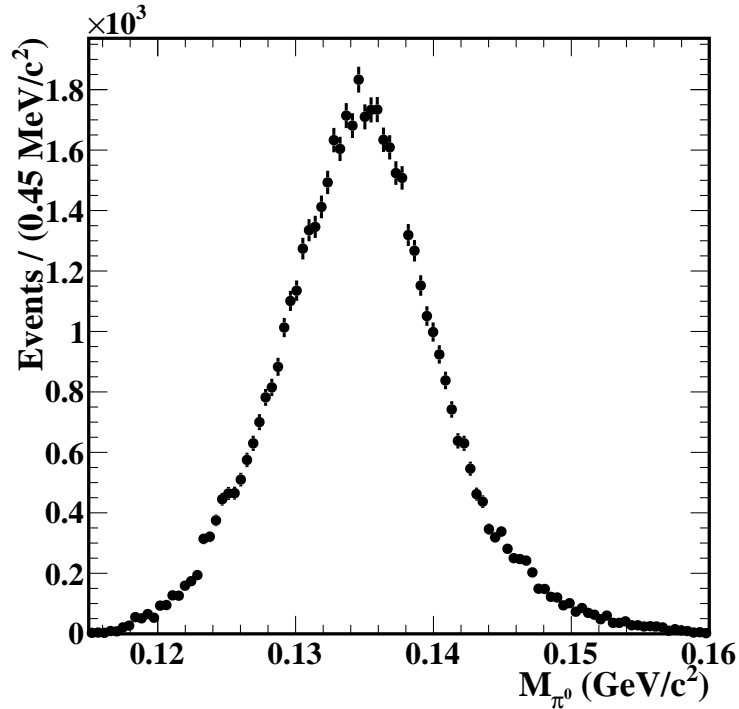


Figure 3.2:  $M_{\pi^0}$  distribution of MC simulated  $D^0 \rightarrow K_S^0 \pi^+ \pi^- \pi^0$  single-tagged candidates after applying the selection criteria.

shown in Fig. 3.2. A mass-constrained fit is performed on the photon pair to the neutral-meson candidate and the fit is required to converge.

The  $\eta$  meson candidates with the diphoton invariant mass in the range (0.506, 0.590)  $\text{GeV}/c^2$  are retained for further analysis. This reduces any background from  $\pi^0 \rightarrow \gamma\gamma$  decays and showers due to hadronic interactions. The  $M_\eta$  distribution of MC simulated signal decays produced with  $\overline{D}^0 \rightarrow K_S^0 \eta$  decays is given in Fig. 3.3.

### 3.3.3 Selection of $K_S^0$ candidates

Two oppositely charged pion tracks are combined to reconstruct a  $K_S^0$  meson candidates. The invariant mass of the pion pair must be at most 30  $\text{MeV}/c^2$  away from the nominal  $K_S^0$  mass [14]. The pion tracks are constrained to a common vertex point and this vertex fit is required to converge.

In addition, each  $K_S^0$  candidate after the vertex fit is required to lie within  $\pm 7.5 \text{ MeV}/c^2$  of its nominal mass [14] as illustrated in Fig. 3.4. Usually,  $K_S^0$  mesons traverse through some portion of the detector before decaying to a pair of pions. So it is required that the three dimensional flight significance should be at least 2.0, which is defined as the

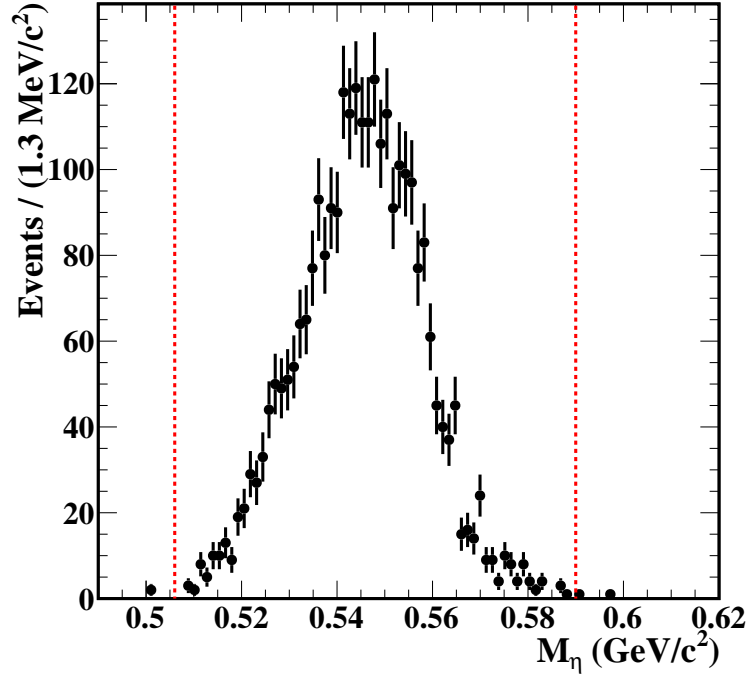


Figure 3.3:  $M_\eta$  distribution of MC simulated  $D^0 \rightarrow K_S^0 \pi^+ \pi^- \pi^0$  decays produced with  $\overline{D}^0 \rightarrow K_S^0 \eta$  decays. The vertical dotted lines indicate the signal region

distance from the IP to the  $K_S^0$  decay vertex divided by the associated uncertainty. An example of the flight-significance distribution is shown in Fig. 3.5.

### 3.3.4 Selection of $\eta'$ candidates

The  $\eta'$  meson candidates are reconstructed from two oppositely charged pions and an  $\eta$ . All the  $\eta'$  candidates must have an invariant mass within  $\pm 10 \text{ MeV}/c^2$  of the nominal mass [14] at skim level selection. A vertex fit is performed to the decay vertex, which is required to converge. The candidates with invariant mass in the range (0.950, 0.964)  $\text{GeV}/c^2$  are kept for further analysis. The mass distribution is shown in Fig. 3.6.

### 3.3.5 Selection of $\omega$ candidates

The  $\omega$  meson candidates are formed from two oppositely charged pions and a  $\pi^0$ . The invariant mass of the three pions should be between (0.762, 0.802)  $\text{GeV}/c^2$ . The invariant mass distribution is shown in Fig. 3.7. In addition, a vertex fit is done to ensure that the daughters originate from a common decay vertex and the fit is required to converge.

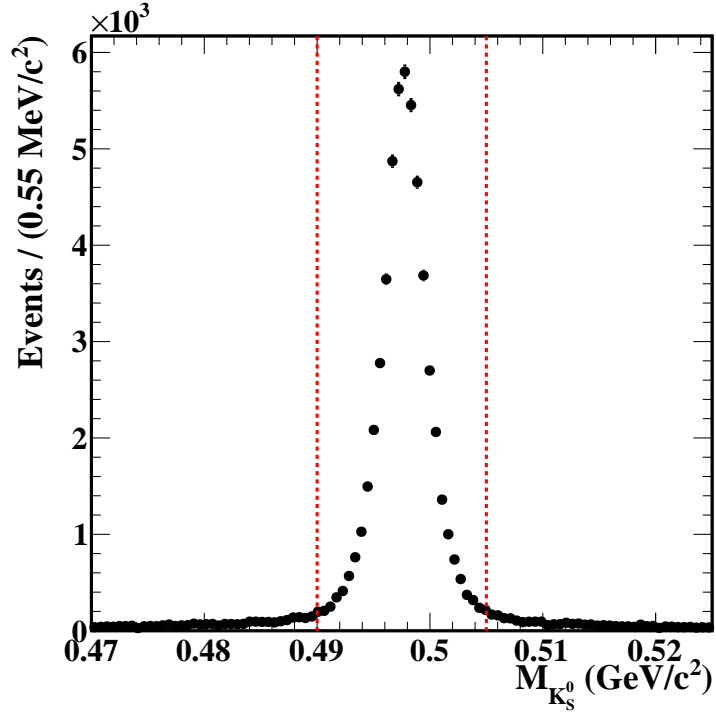


Figure 3.4:  $M_{K_S^0}$  distribution of MC simulated  $D^0 \rightarrow K_S^0 \pi^+ \pi^- \pi^0$  single-tagged candidates. The vertical dotted lines indicate the signal region

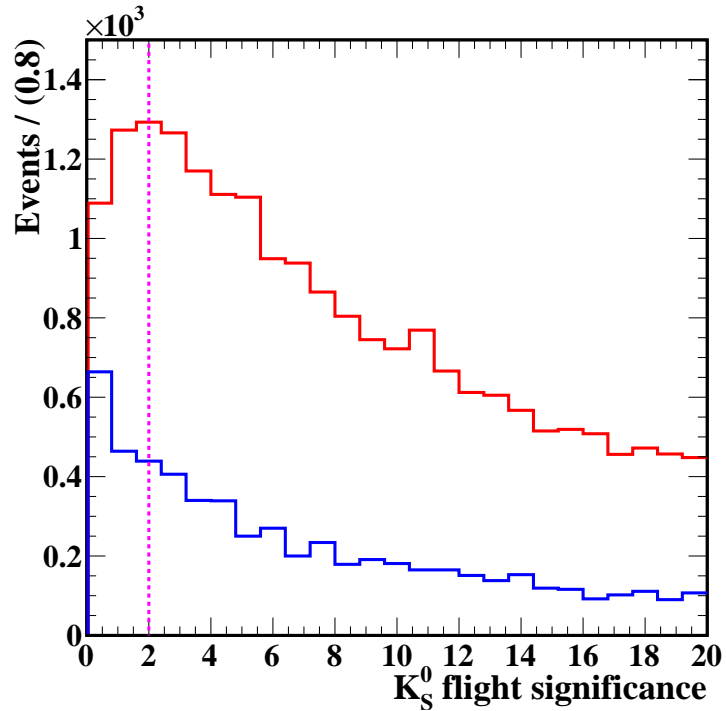


Figure 3.5:  $K_S^0$  flight significance distribution of MC simulated  $D^0 \rightarrow K_S^0 \pi^+ \pi^- \pi^0$  single-tagged candidates. The red and blue solid lines indicate the signal and background components, respectively. The vertical dotted line indicates the selection criteria.

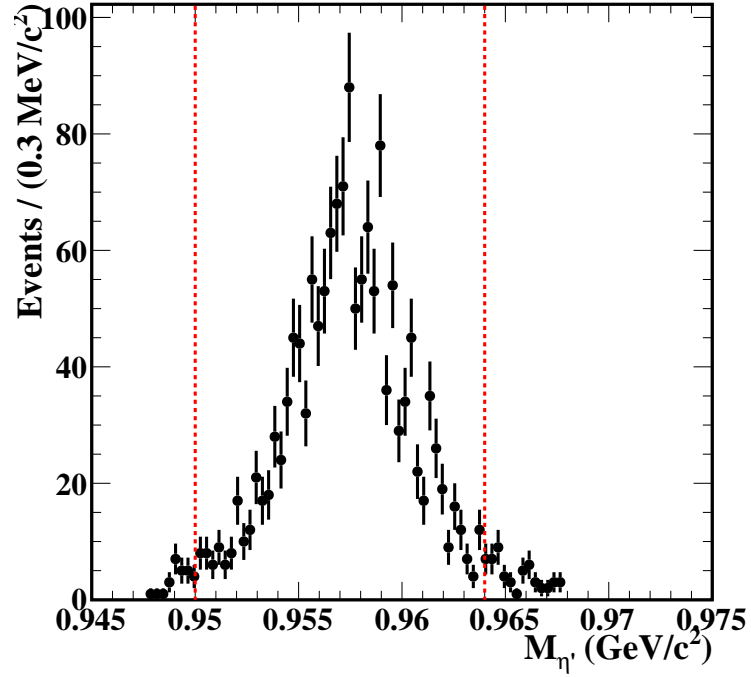


Figure 3.6:  $M_{\eta'}$  distribution of MC simulated  $D^0 \rightarrow K_S^0 \pi^+ \pi^- \pi^0$  decays tagged with  $\overline{D^0} \rightarrow K_S^0 \eta'$  decays. The vertical dotted lines indicate the signal region

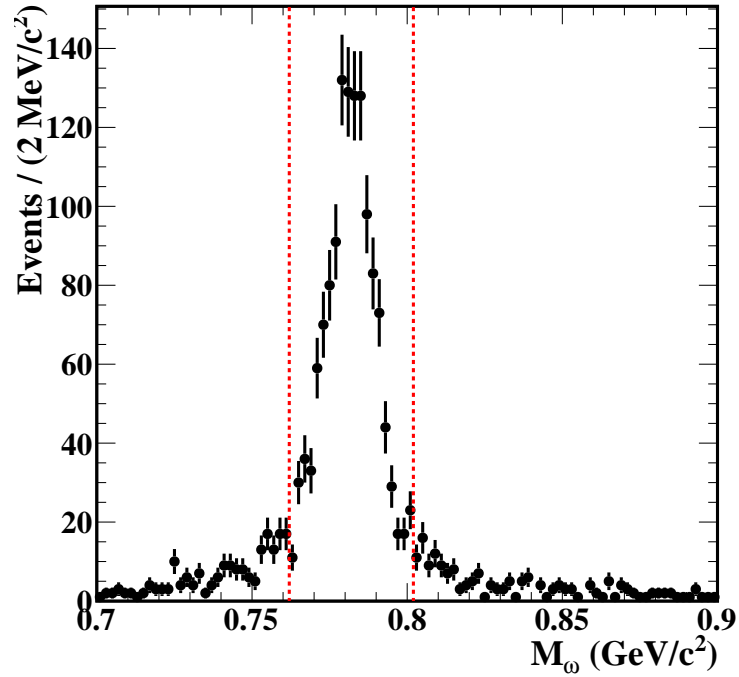


Figure 3.7:  $M_{\omega}$  distribution of MC simulated  $D^0 \rightarrow K_S^0 \pi^+ \pi^- \pi^0$  decays tagged with  $\overline{D^0} \rightarrow K_L^0 \omega$  decays. The vertical dotted lines indicate the signal region

Mode	$\Delta E_{\min}$ (GeV)	$\Delta E_{\max}$ (GeV)
$K^+K^-$	-0.020	0.020
$\pi^+\pi^-$	-0.030	0.020
$K_S^0\pi^0\pi^0$	-0.055	0.045
$K_S^0\pi^0$	-0.071	0.045
$K_S^0\eta$	-0.055	0.035
$K_S^0\eta'$	-0.030	0.020
$\pi^+\pi^-\pi^0$	-0.030	0.030
$K_S^0\pi^+\pi^-$	-0.020	0.020
$K_S^0\pi^+\pi^-\pi^0$	-0.025	0.025

Table 3.2:  $\Delta E$  selection for different  $D$  decay modes.

### 3.3.6 Selection of $D$ candidates

Various final state particles are combined to reconstruct a  $D$  meson. Two kinematic variables are used to identify the correctly reconstructed candidates, beam-constrained mass ( $m_{bc}$ ) and the beam-energy difference ( $\Delta E$ ), which are defined as

$$m_{bc} = c^{-2} \sqrt{E_{\text{beam}}^2 - |\vec{\mathbf{p}}_D|^2 c^2} \quad (3.3)$$

$$\Delta E = E_D - E_{\text{beam}}, \quad (3.4)$$

where  $E_{\text{beam}}$  is the beam energy and  $\vec{\mathbf{p}}_D$  and  $E_D$  are the summed momenta and energy of the  $D$  daughter particles, respectively. For a correctly reconstructed  $D$  meson,  $m_{bc}$  and  $\Delta E$  peak at the nominal  $D$  mass [14] and zero, respectively. The selection criteria  $1.83 < m_{bc} < 1.89 \text{ GeV}/c^2$  is applied on all  $D$  decay modes, whereas different requirements are placed on  $\Delta E$  for various modes as given in Table 3.2. The  $\Delta E$  selection criteria are the same as earlier CLEO-c analyses [31], except for the  $K_S^0\pi^+\pi^-\pi^0$  final state. The selected  $\Delta E$  range corresponds to approximately three times the experimental resolution. Figure 3.8 shows the  $\Delta E$  distribution for single-tagged  $D^0 \rightarrow K_S^0\pi^+\pi^-\pi^0$  candidates.

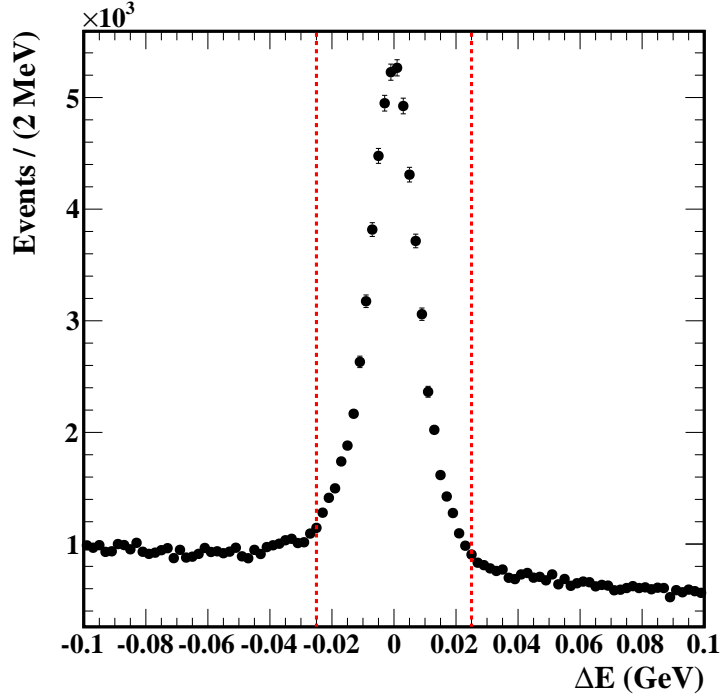


Figure 3.8:  $\Delta E$  distribution for  $D^0 \rightarrow K_S^0 \pi^+ \pi^- \pi^0$  single-tagged candidates in data. The vertical dotted lines indicate the signal region.

### 3.3.7 Selection of events with $K_L^0$ candidates

Usually a  $K_L^0$  meson will decay outside the CLEO-c detector due to its long lifetime compared to the  $K_S^0$ , hence no signature of a  $K_L^0$  decay can be measured. Still, it is possible to reconstruct decay modes involving a  $K_L^0$  because of the good  $4\pi$  solid-angle coverage of the detector. Four-momentum conservation is utilised when all the remaining particles in the final state are detected. A missing-mass squared ( $m_{\text{miss}}^2$ ) technique [71] is used to reconstruct those events. The  $m_{\text{miss}}^2$  is

$$m_{\text{miss}}^2 = E_{\text{miss}}^2 c^{-4} - |\vec{\mathbf{p}}_{\text{miss}}|^2 c^{-2}, \quad (3.5)$$

where  $E_{\text{miss}}$  is the missing energy and  $|\vec{\mathbf{p}}_{\text{miss}}|$  is the magnitude of the missing three-momentum in the event. The missing energy in the case of  $\overline{D}^0 \rightarrow K_L^0 X$  is calculated as  $E_{\text{miss}} = E_{\text{total}} - E_{\text{signal}} - E_X$  and similarly the missing momentum using the conservation principles. Here  $E_{\text{signal}}$  and  $E_X$  are the energy of signal decay  $D \rightarrow K_S^0 \pi^+ \pi^- \pi^0$  and  $X$  from the other  $D$  meson, respectively.  $E_{\text{total}}$  is the total energy of the event, which is equivalent to twice the beam energy. For a correctly reconstructed event,  $m_{\text{miss}}^2$  peaks near the square of the  $K_L^0$  mass [14]. The distribution is shown in Fig. 3.9.

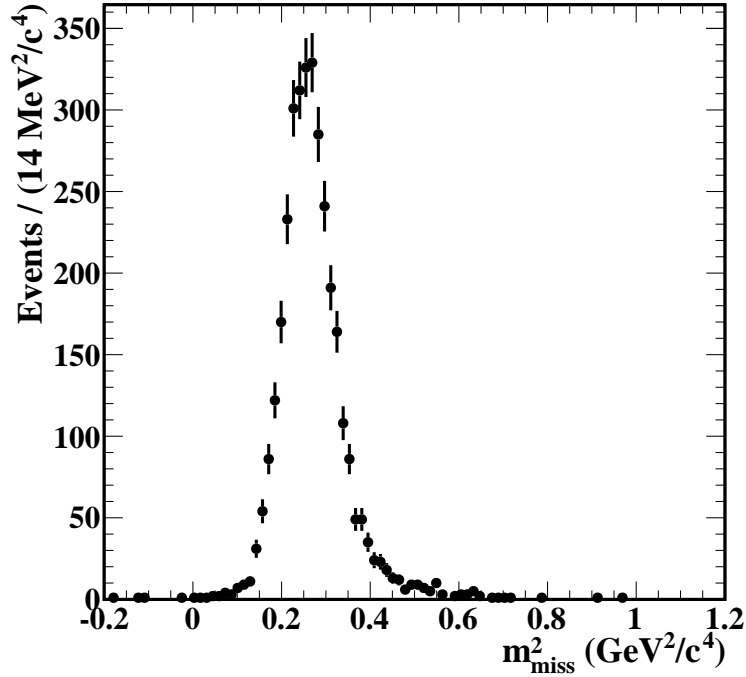


Figure 3.9:  $m_{\text{miss}}^2$  distribution of MC simulated  $D^0 \rightarrow K_S^0 \pi^+ \pi^- \pi^0$  decays tagged with  $D^0 \rightarrow K_L^0 \pi^0$  decays.

The calorimeter showers that are not directly linked to the final states are studied and a selection is applied to find out if they originate from a  $K_L^0$  candidate. Two variables are used for this purpose: the energy of the shower  $E_s$  and the angle  $\alpha$  between the shower and the missing momentum in the event. The selection is applied on  $(E_s, \cos \alpha)$  plane. Events that satisfy

$$-1.0 \leq \cos \alpha < 0.9 \text{ and } E_s < 0.1 \text{ GeV} \quad (3.6)$$

or

$$0.9 \leq \cos \alpha < 0.98 \text{ and } E_s < (2.5 \cos \alpha - 2.15) \text{ GeV}. \quad (3.7)$$

are selected for the following analysis stages [72].

The particular decay modes of interest are  $K_L^0 \pi^0$ ,  $K_L^0 \omega$  and  $K_L^0 \pi^+ \pi^-$ . In addition, some tag-specific selection criteria are applied. In the case of  $K_L^0 \pi^0$ , events with only one  $\pi^0$  are selected and there should be no tracks from the  $D$  meson. The momentum of the  $\pi^0$  is required to be between 0.75 and 1.00 GeV/c. These criteria reduce the backgrounds further. For the  $K_L^0 \omega$  mode, it is required that there is only one  $\pi^0$  and no  $\eta$  in the final state along with the two pion tracks. The  $\pi^0$  momentum should lie in the

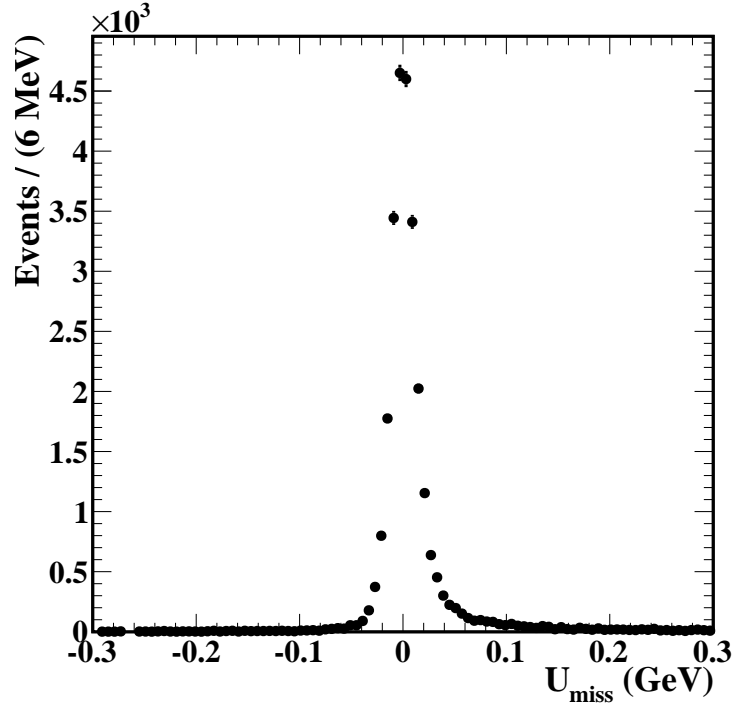


Figure 3.10:  $U_{\text{miss}}$  distribution of MC simulated  $D^0 \rightarrow K_S^0 \pi^+ \pi^- \pi^0$  decays tagged with  $D^0 \rightarrow K^\pm e^\mp \nu_e$  decays.

range (0.15, 0.60) GeV/c. There must be two pion tracks in  $K_L^0 \pi^+ \pi^-$  final state and no  $\pi^0$  or  $\eta$  should be found.

### 3.3.8 Selection of events with $\nu$ candidates

Neutrinos have negligible probability to interact with the detector mass. The four-momentum conservation becomes key when all the other particles in the final state are detected at CLEO-c. Since neutrinos are massless within the SM, the energy-momentum relation is modified to  $E = |\vec{p}|c$ . So semileptonic decays involving a neutrino are reconstructed by considering the quantity

$$U_{\text{miss}} = E_{\text{miss}} - c|\vec{p}_{\text{miss}}|, \quad (3.8)$$

where  $E_{\text{miss}}$  is the missing energy and  $|\vec{p}_{\text{miss}}|$  is the magnitude of the missing three momentum in the event. The  $U_{\text{miss}}$  distribution peaks near zero for a correctly reconstructed event. Our mode of interest is  $K^\pm e^\mp \nu_e$ , where two tracks are required in an event and there should not be any  $\pi^0$  or  $\eta$  candidates. The  $U_{\text{miss}}$  distribution is given in Fig. 3.10.

### 3.3.9 Best-candidate selection

Reconstructed events might consist of more than one  $D$  meson candidate due to other combinations of the final-state particles satisfying the selection criteria. From these multiple candidates, the one that best matches the final-state hypothesis is selected to avoid double counting of events. We refer to this as the best-candidate selection. The discriminating metric is

$$\delta = \left| \frac{m_{bc}(S) + m_{bc}(T)}{2} - m_D \right|, \quad (3.9)$$

where  $m_{bc}(S)$  and  $m_{bc}(T)$  are the beam constrained masses of signal side and tag side respectively and  $m_D$  is the nominal mass of  $D$  meson. When there is a missing particle in the final state, the metric reduces to

$$\delta = |m_{bc}(S) - m_D|. \quad (3.10)$$

The case is the same for a single-tagged event.

The average number of candidates per event ranges from 1.5 to 3.7 for the different tag modes. The efficiency of this best-candidate selection (BCS) is defined as

$$\epsilon = \frac{\text{No of true signal candidates selected by the BCS}}{\text{No of events with a true signal having multiplicity} > 1}, \quad (3.11)$$

and it is greater than or equal to 83% for all the tag modes used in the analysis.

## 3.4 Single-tagged yield estimation

The single-tagged yields, which are needed for normalization while estimating the parameters of interest, for the  $CP$  and quasi- $CP$  modes are taken from Ref. [31] as the selection criteria applied are the same. The single-tagged yield for  $D^0 \rightarrow K_S^0 \pi^+ \pi^- \pi^0$  is obtained from a maximum likelihood fit to the  $m_{bc}$  distribution. The fit is done using the RooFit software package [73] for modelling and fitting different data sets. In the maximum likelihood fit, the parameters in the probability density function (PDF) are estimated by varying them until the likelihood reaches the global minimum and the best

fit to data is obtained. The likelihood function for  $n$  measurements of a parameter  $x$  is given by

$$L(x_1, x_2, x_3 \dots x_n) = \prod_{i=1}^n P(x_i, x_0), \quad (3.12)$$

where  $P(x_i, x_0)$  is the PDF describing the data points and  $x_0$  is the parameter to be estimated. If there is more than one type of event in the data sample, the likelihood is modified as

$$L(x_1, x_2, x_3 \dots x_n) = \prod_{i=1}^n \sum_{j=1}^m f_j P_j(x_i, x_0), \quad (3.13)$$

where  $f_j$  is the fraction of events in  $j^{\text{th}}$  component and  $m$  is the total number of components. During the calculation, it is preferred to use  $\ln(L)$ , instead of the likelihood itself, as this makes computations involving large numbers easy. Moreover,  $\ln(L)$  is efficient in estimating the uncertainties. So Eq. 3.13 is now given as

$$\ln L(x_i) = \sum_{i=1}^n \left[ \sum_{j=1}^m f_j P_j(x_i, x_0) \right] - \sum_{j=1}^m f_j. \quad (3.14)$$

The likelihood is maximum for the estimator  $\hat{x}_0$  when

$$\left. \frac{d \ln L}{d x_0} \right|_{x_0 = \hat{x}_0} = 0. \quad (3.15)$$

Since RooFit minimizes a function, rather than maximizing it,  $-\ln L$  is used.

There are signal and combinatorial background components present in the sample. The combinatorial background originates from the random combinations of the final state particles. These components are modelled separately in MC to obtain a suitable PDF for each of them. The signal component is modelled with an asymmetric Gaussian and a sum of two Gaussian functions with a common mean. The signal peaks at the nominal  $D$  mass [14]. The fitted distribution is shown in Fig. 3.11 and the parameter values obtained are given in Table 3.3.

The background component is studied in MC and the different contributions are shown in Fig. 3.12. The distribution is fitted with Argus [74], Crystal Ball [75] and Gaussian PDFs. The Argus PDF is of the form

$$f_{\text{ARGUS}}(x) = x \left( 1 - \left( \frac{x}{m} \right)^2 \right)^{\frac{1}{2}} \exp \left[ a \left( 1 - \left( \frac{x}{m} \right)^2 \right) \right], \quad (3.16)$$

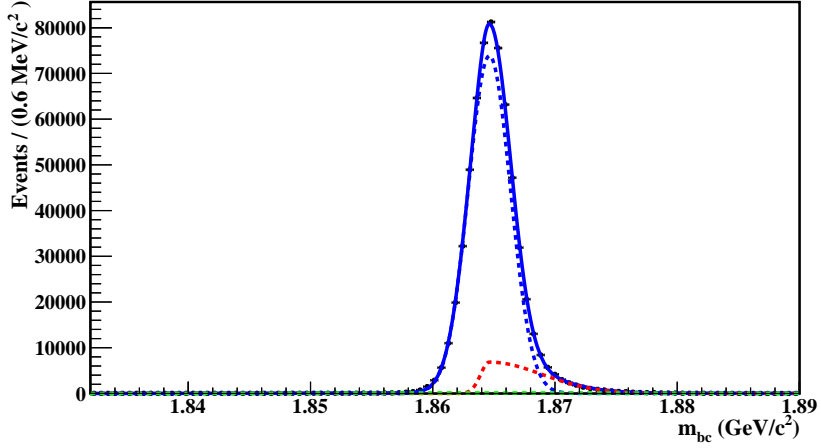


Figure 3.11:  $m_{bc}$  distribution for the signal component of single-tagged  $D^0 \rightarrow K_S^0 \pi^+ \pi^- \pi^0$  decays in MC fitted with the sum of an asymmetric Gaussian and two Gaussian functions. Blue solid curve represents the total fit and red, blue and green dashed curves are asymmetric Gaussian, narrow Gaussian and broad Gaussian function, respectively.

Parameter	Description	Value
$\mu$	signal mean	$(1864.6 \pm 0.4) \text{ MeV}/c^2$
$\sigma_L$	left $\sigma$ of asymmetric Gaussian	$(71.8 \pm 0.4) \text{ MeV}/c^2$
$\sigma_R$	right $\sigma$ of asymmetric Gaussian	$(432.3 \pm 2.6) \text{ MeV}/c^2$
$\sigma_1$	$\sigma$ of first Gaussian	$(172.5 \pm 0.2) \text{ MeV}/c^2$
$\sigma_2$	$\sigma$ of second Gaussian	$(1268.0 \pm 22.0) \text{ MeV}/c^2$
$f_{G1}$	fraction of first Gaussian	$0.881 \pm 0.017$
$f_{G2}$	fraction of second Gaussian	$0.020 \pm 0.003$

Table 3.3: Fit parameters for  $m_{bc}$  signal component fit for  $D^0 \rightarrow K_S^0 \pi^+ \pi^- \pi^0$  decays in MC.

where  $m$  is the endpoint and  $a$  is the shape parameter. The value of  $m$  is fixed to  $1.8864 \text{ GeV}/c^2$ . The Crystal Ball PDF is given by

$$f_{CB}(x) = \frac{\left(\frac{n_{CB}}{|\alpha_{CB}|}\right)^{n_{CB}} e^{-\frac{1}{2}\alpha_{CB}^2}}{\left(\frac{n_{CB}}{|\alpha_{CB}|} - |\alpha_{CB}| - \left(\frac{x-\mu}{\sigma_{CB}}\right)\right)^{n_{CB}} \Big|_{x < -|\alpha_{CB}|} \exp\left(-\frac{1}{2}\left(\frac{x-\mu}{\sigma_{CB}}\right)^2\right) \Big|_{x > -|\alpha_{CB}|} ; \quad (3.17)$$

where  $\mu$ ,  $\sigma_{CB}$ ,  $\alpha_{CB}$  and  $n_{CB}$  are the shape parameters. The Argus PDF models the flat background that drops sharply at the threshold set by the beam energy of the accelerator.

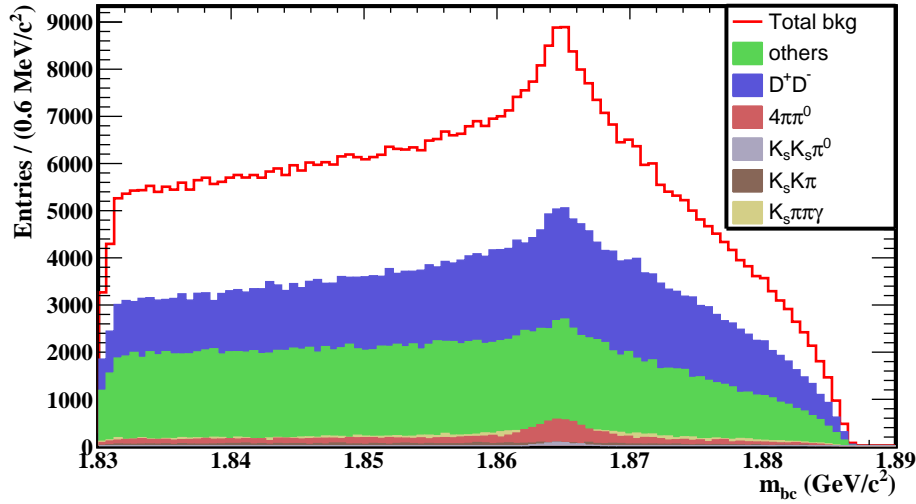


Figure 3.12:  $m_{bc}$  distribution for the background component of single-tagged  $D \rightarrow K_S^0 \pi^+ \pi^- \pi^0$  decays in MC with different contributions shown separately. Here, “bkg” stands for background.

Parameter	Description	Value
$a$	Argus parameter	$-10.59 \pm 0.24$
$\mu$	mean of Gaussian and Crystal Ball	$(1864.9 \pm 4.6) \text{ MeV}/c^2$
$\sigma_{CB}$	$\sigma$ of Crystal Ball	$(7.3 \pm 0.1) \text{ MeV}/c^2$
$\alpha_{CB}$	Crystal Ball parameter	$0.59 \pm 0.04$
$n_{CB}$	Crystal Ball parameter	$8.40 \pm 3.70$
$\sigma$	$\sigma$ of Gaussian	$(1.4 \pm 0.1) \text{ MeV}/c^2$
$f$	fraction of Argus	$0.789 \pm 0.007$
$f_{CB}$	fraction of Crystal Ball	$0.193 \pm 0.007$

Table 3.4: Fit parameters for  $m_{bc}$  background component fit for  $D^0 \rightarrow K_S^0 \pi^+ \pi^- \pi^0$  decays in MC. Here, the fraction of Gaussian  $f_G = 1 - f - f_{CB}$ .

The latter two PDFs in the background fit are for the small peaking component arising from  $D^0 \rightarrow \pi^+ \pi^- \pi^+ \pi^- \pi^0$  and  $D^0 \rightarrow K_S^0 K_S^0 \pi^0$  decays. The fitted distribution is shown in Fig. 3.13. The shape parameters are summarized in Table 3.4.

An extended maximum likelihood fit is performed with these PDFs to get the signal yield in the data sample. The  $m_{bc}$  distribution fitted in data is shown in Fig. 3.14. The signal yield obtained is  $54,949 \pm 781$ , where the uncertainty is statistical only.

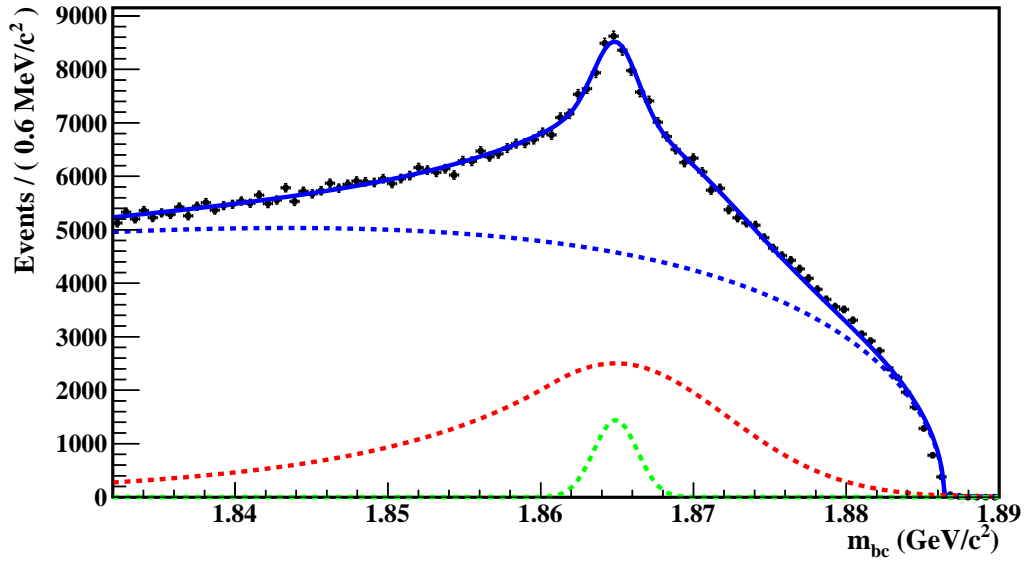


Figure 3.13:  $m_{bc}$  distribution for the background component of single-tagged  $D^0 \rightarrow K_S^0 \pi^+ \pi^- \pi^0$  decays in MC fitted with the sum of an Argus, Crystal Ball and Gaussian PDFs. Blue solid curve represents the total fit and blue, red and green dashed curves are Argus, Crystal Ball and Gaussian PDF, respectively.

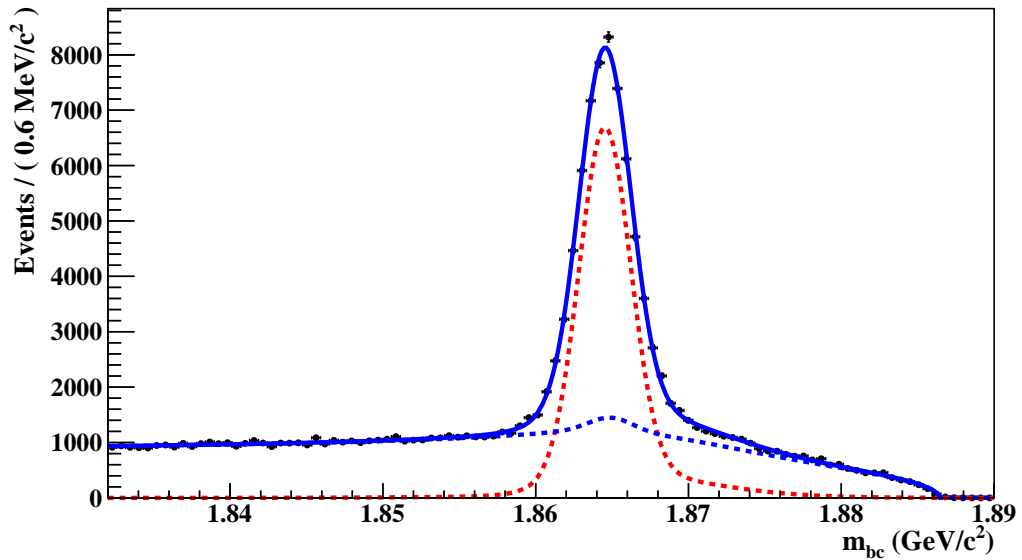


Figure 3.14:  $m_{bc}$  distribution for single-tagged  $D^0 \rightarrow K_S^0 \pi^+ \pi^- \pi^0$  decays in data. The black points are data, the solid blue curve is the total fit and the dashed red and blue curves are signal and background fit components, respectively.

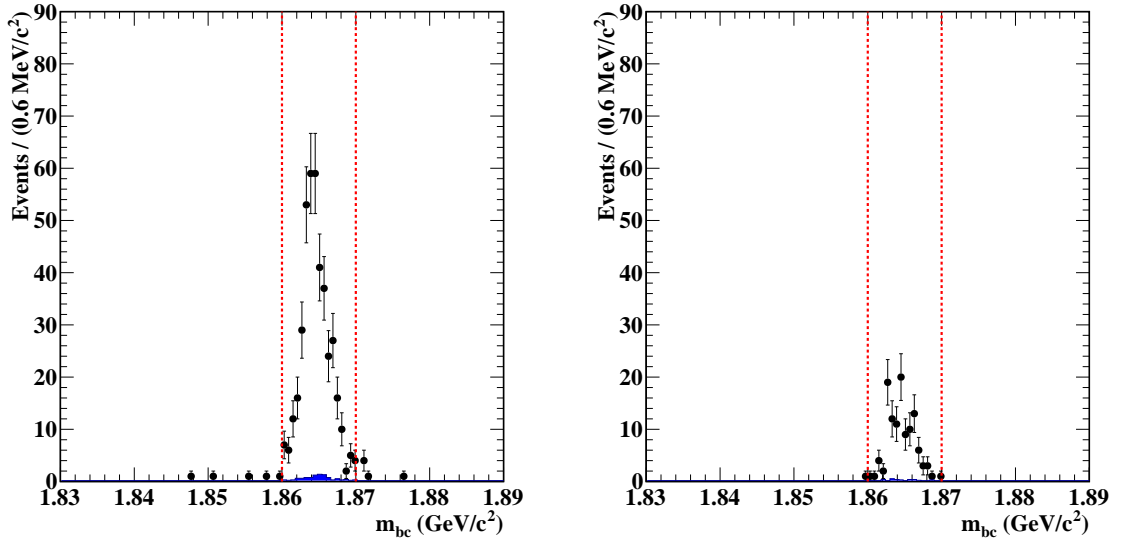


Figure 3.15:  $m_{bc}$  distributions for  $D^0 \rightarrow K_S^0 \pi^+ \pi^- \pi^0$  decays tagged by  $CP$ -even states (left) and  $CP$ -odd states (right) both not involving a  $K_L^0$  meson in data. The shaded histogram shows the estimated peaking background and the vertical dotted lines indicate the signal region.

### 3.5 Double-tagged yield estimation

Hadronic modes without a  $K_L^0$  in the final state are fully reconstructed, *i.e.* both the  $D$  mesons in an event are correctly identified, using the kinematic variables (see Sec. 3.3.6). A kinematic fit is performed to constrain the final-state particles to the  $D$  meson invariant mass. This fit improves the momentum resolution of the  $D$  daughter particles. The double-tagged yield is calculated by counting the events in the signal and sideband regions of  $m_{bc}$ . The peaking backgrounds in both the  $D$  decays are estimated from MC simulations.

Double-tagged events containing two  $K_S^0 \pi^+ \pi^- \pi^0$  decays are also reconstructed in a similar fashion. The  $m_{bc}$  distributions for  $D \rightarrow K_S^0 \pi^+ \pi^- \pi^0$  decays tagged with  $CP$  eigenstates, not involving a  $K_L^0$ , are shown in Fig. 3.15. There is an enhancement in the number of events in the signal region for tag modes that are  $CP$ -even eigenstates. The  $m_{bc}$  distribution for  $K_S^0 \pi^+ \pi^-$  tagged events is shown in Fig. 3.16. The tag-side Dalitz plot distribution for  $K_S^0 \pi^+ \pi^-$  is shown in Fig. 3.17.

The two-dimensional  $m_{bc}$  plane in an event is divided into four different background regions A, B, C and D along with the signal region S as shown in Fig. 3.18. The signal region is identified as the region where both the  $D$  mesons are correctly reconstructed.

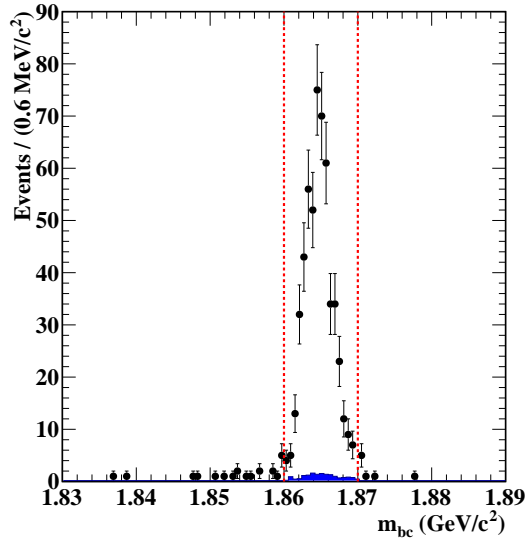


Figure 3.16:  $m_{bc}$  distribution for  $D^0 \rightarrow K_S^0 \pi^+ \pi^- \pi^0$  decays tagged by  $K_S^0 \pi^+ \pi^-$  events in data. The shaded histogram shows the estimated peaking background and the vertical dotted lines indicate the signal region.

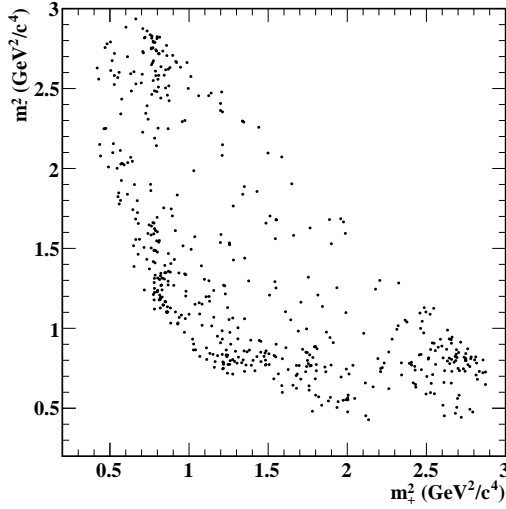


Figure 3.17: Dalitz plot distribution for the tag  $K_S^0 \pi^+ \pi^-$  against  $D \rightarrow K_S^0 \pi^+ \pi^- \pi^0$  decays. The axis labels  $m_{\pm}^2$  represents the invariant mass squares of  $K_{S,L}^0 \pi^{\pm}$  pairs.

Signal, as well as the backgrounds that mimic the final state of the signal, peak in the S region. The background originates from misreconstructed events on the lower end of the  $m_{bc}$  distribution and are flat in shape. The regions A and B correspond to the events in which only one of the  $D$  mesons is correctly reconstructed. Regions C and D contain combinatorial events, in which the particle tracks are swapped, and flat background from non  $D\bar{D}$  sources, respectively. The C and D regions are distinguished by having an additional requirement on  $\delta m_{bc} = |m_{bc}(D_1) - m_{bc}(D_2)|$ , where  $D_1$  and  $D_2$  are the

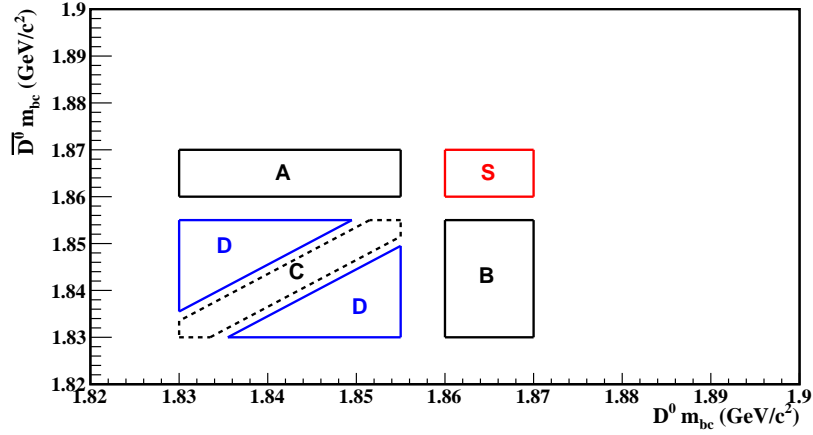


Figure 3.18: Division of the two dimensional  $m_{bc}$  plane distribution. The red square box indicates the signal region and the remaining boxes show the various sideband regions that are used to determine the combinatorial background contribution.

Region	$m_{bc}(D_1)$ (GeV/c <sup>2</sup> )		$m_{bc}(D_2)$ (GeV/c <sup>2</sup> )		additional requirement
	Minimum	Maximum	Minimum	Maximum	
S	1.860	1.870	1.860	1.870	-
A	1.830	1.855	1.860	1.870	-
B	1.860	1.870	1.830	1.855	-
C	1.830	1.855	1.830	1.855	$\delta m_{bc} \leq 0.0035$ GeV/c <sup>2</sup>
D	1.830	1.855	1.830	1.855	$\delta m_{bc} \geq 0.0055$ GeV/c <sup>2</sup>

Table 3.5: The signal and sideband regions for fully reconstructed  $D$  decays.

two  $D$  mesons in an event. The boundaries of each region are summarized in Table 3.5.

The flat background from the sideband is calculated as,

$$N_{\text{flat}} = \frac{R_S}{R_D} D + \sum_{i=A,B,C} \frac{R_S}{R_i} \left( i - \frac{R_i}{R_D} D \right), \quad (3.18)$$

where  $A$ ,  $B$ ,  $C$  and  $D$  are the entries in the corresponding regions and  $R_i$  is the area of the  $i^{\text{th}}$  region in the  $m_{bc}$  plane. The peaking background  $N_{\text{peak}}$  for each decay mode is obtained by studying the MC and identifying different contributions. The estimated background from MC is then scaled to the luminosity of data. Therefore, the signal yield

$$Y = S - N_{\text{flat}} - N_{\text{peak}}, \quad (3.19)$$

where  $S$  is the number of entries in the signal box of the data sample. The two-

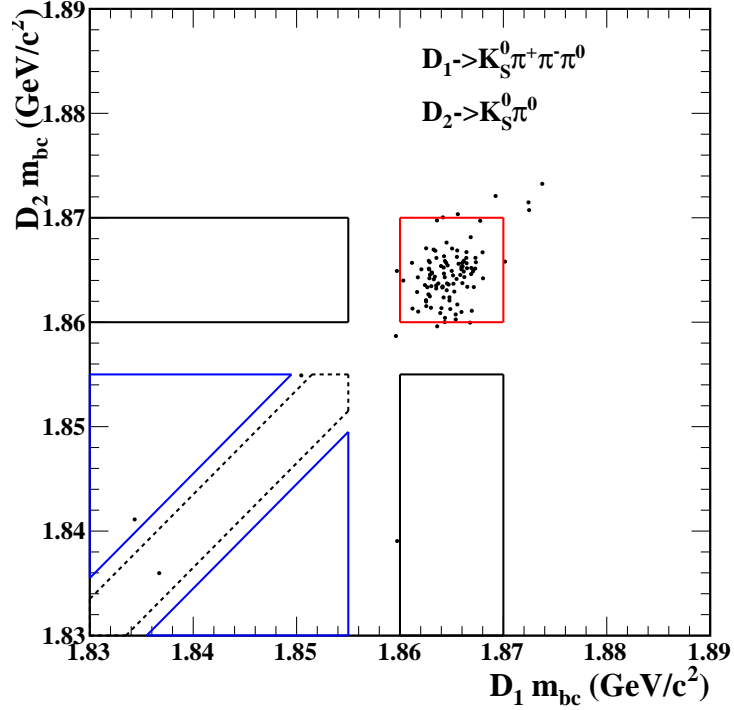


Figure 3.19: Two dimensional  $m_{bc}$  plane distribution for  $D^0 \rightarrow K_S^0 \pi^+ \pi^- \pi^0$  tagged with  $\overline{D^0} \rightarrow K_S^0 \pi^0$  decays. The red square box indicates the signal region and the remaining boxes show the various sideband regions that are used to determine the combinatorial background contribution.

dimensional  $m_{bc}$  distribution for  $K_S^0 \pi^+ \pi^- \pi^0$  tagged with  $K_S^0 \pi^0$  decays is shown in Fig. 3.19. The signal yields obtained for the various tag modes are given in Table 3.6.

A  $K_S^0$  veto is applied for the final state  $\pi^+ \pi^- \pi^0$  to eliminate  $K_S^0(\pi^+ \pi^-) \pi^0$  background events. Still there is a small contamination of  $K_S^0 \pi^0$  events as a peaking background for this tag mode. Since the preliminary calculations show that  $F_+^{K_S^0 \pi^+ \pi^- \pi^0} \approx 0.25 \pm 0.02$ ,  $K_S^0 \pi^0$  decays of the other  $D$  would be suppressed as it is a  $CP$ -odd eigenstate due to the quantum correlation. This introduces a correction factor to the estimated peaking background from MC, where all events are generated with  $F_+ = 0.5$ . In general the double-tagged yield can be written as

$$M(K_S^0 \pi^+ \pi^- \pi^0 | K_S^0 \pi^0) = \alpha \left[ (1 - F_+^{K_S^0 \pi^+ \pi^- \pi^0}) F_+^{K_S^0 \pi^0} + (1 - F_+^{K_S^0 \pi^0}) F_+^{K_S^0 \pi^+ \pi^- \pi^0} \right], \quad (3.20)$$

where  $\alpha$  is a normalization factor (see Eq. (1.43)). The yield is equal to  $0.5\alpha$  when

$$F_+^{K_S^0 \pi^+ \pi^- \pi^0} = F_+^{K_S^0 \pi^0} = 0.5$$

Type	Tag	S	$N_{\text{flat}}$	$N_{\text{peak}}$	Yield	Efficiency (%)
<i>CP</i> -even	$K^+K^-$	202	1.2	0.1	$201 \pm 14$	$9.95 \pm 0.13$
	$\pi^+\pi^-$	92	0.0	0.6	$91 \pm 10$	$12.54 \pm 0.15$
	$K_S^0\pi^0\pi^0$	113	3.1	3.6	$106 \pm 11$	$2.78 \pm 0.07$
<i>CP</i> -odd	$K_S^0\pi^0$	96	0.1	2.0	$94 \pm 10$	$5.03 \pm 0.10$
	$K_S^0\eta$	13	0.8	0.6	$12 \pm 4$	$5.14 \pm 0.10$
	$K_S^0\eta'$	7	0.0	0.0	$7 \pm 3$	$2.63 \pm 0.07$
Mixed <i>CP</i>	$\pi^+\pi^-\pi^0$	454	19.2	6.1	$429 \pm 22$	$6.67 \pm 0.11$
	$K_S^0\pi^+\pi^-$	530	17.6	7.7	$505 \pm 23$	$5.77 \pm 0.10$
	$K_S^0\pi^+\pi^-\pi^0$	201	19.2	5.4	$176 \pm 15$	$2.68 \pm 0.07$

Table 3.6: The signal yields of  $D^0 \rightarrow K_S^0\pi^+\pi^-\pi^0$  decays tagged with different  $D$  decay modes in data.

Variable	Tag	Low sideband		Signal region		High sideband	
		Min	Max	Min	Max	Min	Max
$m_{\text{miss}}^2$ (GeV $^2/c^4$ )	$K_L^0\pi^0$	-0.10	0.10	0.10	0.50	0.60	1.00
	$K_L^0\omega$	0.00	0.10	0.15	0.35	0.40	1.20
	$K_L\pi^+\pi^-$	0.10	0.15	0.20	0.30	0.60	1.10
$U_{\text{miss}}$ (GeV)	$K^\pm e^\mp \nu_e$	-0.30	-0.05	-0.05	0.05	0.05	0.30

Table 3.7: Signal region and sidebands for partially reconstructed final states having a  $K_L^0$  or  $\nu_e$ . The regions are defined on  $m_{\text{miss}}^2$  and  $U_{\text{miss}}$  distributions for  $K_L^0$  modes and  $K^\pm e^\mp \nu_e$ , respectively.

as in the MC, but in reality,  $F_+^{K_S^0\pi^0} = 0$  and  $F_+^{K_S^0\pi^+\pi^-\pi^0} = 0.25$  (see Appendix A) which leads to

$$M(K_S^0\pi^+\pi^-\pi^0|K_S^0\pi^0) = 0.25\alpha. \quad (3.21)$$

Therefore a correction factor of 0.5 is applied to the number of  $K_S^0\pi^0$  events reconstructed against  $K_S^0\pi^+\pi^-\pi^0$  decays in MC, when the peaking background is estimated. The uncertainty on  $F_+^{K_S^0\pi^+\pi^-\pi^0}$  is propagated through the expression and included in the statistical uncertainty of the yield.

The double-tagged yields for modes with a  $K_L^0$  meson or a  $\nu_e$  in the final state are estimated from the signal and sideband regions of the  $m_{\text{miss}}^2$  and  $U_{\text{miss}}$  distributions, respectively. The low sideband (L), signal (S) and high sideband (H) regions are defined for each mode and are given in Table 3.7. The peaking background contributions are identified from MC.

For the  $K_L^0\pi^0$  tag mode,  $K_S^0\pi^0$  and  $\eta\pi^0$  final states are identified to be peaking in the S region,  $K^*\pi^0$  and  $K_L^0\pi^0\pi^0$  are peaking in the H region and  $\pi^0\pi^0$  events in the L region. All other background events are considered in  $B_{\text{else}}$  category. Then the total yields in the three mass windows can be written as

$$S = Y_{K_L^0\pi^0} + B_{\text{peak}}^S + \delta B_{\text{peak}}^L + \gamma B_{\text{else}}, \quad (3.22)$$

$$L = B_{\text{peak}}^L + \alpha Y_{K_L^0\pi^0}, \quad (3.23)$$

$$H = B_{\text{else}} + B_{\text{peak}}^H + \beta Y_{K_L^0\pi^0}, \quad (3.24)$$

where  $Y_{K_L^0\pi^0}$  is the yield of  $K_L^0\pi^0$ -tagged events and  $B_{\text{peak}}^j$  is the peaking background contribution in region  $j$ . The parameters  $\alpha$ ,  $\beta$ ,  $\delta$  and  $\gamma$  are the ratio of MC yields given as

$$\alpha = \frac{\text{MC signal in L}}{\text{MC signal in S}}, \quad \beta = \frac{\text{MC signal in H}}{\text{MC signal in S}}, \quad (3.25)$$

$$\delta = \frac{\text{MC } \pi^0\pi^0 \text{ in S}}{\text{MC } \pi^0\pi^0 \text{ in L}}, \quad \gamma = \frac{\text{MC } B_{\text{else}} \text{ in S}}{\text{MC } B_{\text{else}} \text{ in H}}. \quad (3.26)$$

Eliminating  $B_{\text{peak}}^L$  and  $B_{\text{else}}$  from Eq. (3.22) using Eqs. (3.23) and (3.24), we can write  $Y_{K_L^0\pi^0}$  as

$$Y_{K_L^0\pi^0} = \frac{(S - B_{\text{peak}}^S) - \delta L - \gamma(H - B_{\text{peak}}^H)}{1 - \alpha\delta - \beta\gamma}. \quad (3.27)$$

The quantum-correlation correction is applied to the peaking component due to  $K_S^0\pi^0$  using the same method as applied to  $\pi^+\pi^-\pi^0$  tag. The background classification in the signal and sideband regions from MC simulated events are shown in Fig. 3.20.

In the case of the  $K_L^0\omega$  tag mode, there are negligible number of events in the L region and hence the expression for the yield becomes

$$Y_{K_L^0\omega} = \frac{(S - B_{\text{peak}}^S) - \gamma(H - B_{\text{peak}}^H)}{1 - \beta\gamma}. \quad (3.28)$$

For this mode  $K_S^0\omega$ ,  $K_L^0\pi^+\pi^-\pi^0$  and  $K_S^0\pi^+\pi^-\pi^0$  are a peaking background in the S region and  $Ka_1$  and  $K_L^0\pi^+\pi^-\pi^0\pi^0$  are peaking in the H region. Other decays do not peak so they fall into the  $B_{\text{else}}$  category. The different background contributions in the signal and sideband regions from MC simulated events are shown in Fig. 3.21.

For the  $K_L^0\pi^+\pi^-$  tag mode, the expression is the same as that for the  $K_L^0\pi^0$ . For

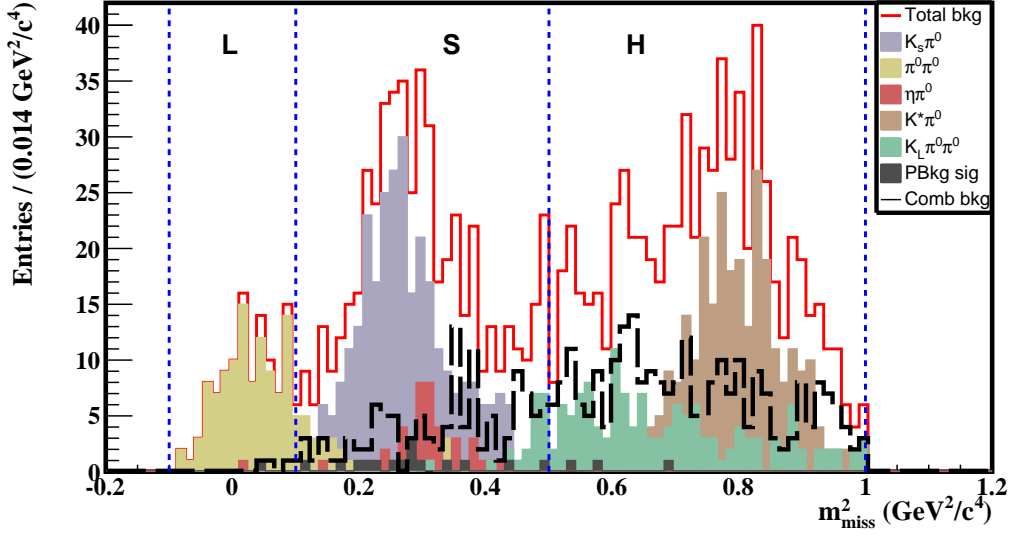


Figure 3.20:  $m_{\text{miss}}^2$  distribution for background events of  $D^0 \rightarrow K_S^0 \pi^+ \pi^- \pi^0$  decays tagged by  $\overline{D}^0 \rightarrow K_L^0 \pi^0$  decays in MC sample. Here ‘‘PBkg sig’’ refers to peaking background in signal-side decay of  $D^0 \rightarrow K_S^0 \pi^+ \pi^- \pi^0$  and ‘‘Comb bkg’’ refers to combinatorial background.

this mode,  $K_S^0 \pi^+ \pi^-$ ,  $K_S^0 K_S^0$ ,  $K_S^0 \eta$  and  $\eta \pi^+ \pi^-$  events peak in the S region,  $K^{*0} \pi^+ \pi^-$ ,  $K_L^0 \pi^+ \pi^- \pi^0 \pi^0$ ,  $K_L^0 l$ ,  $K_S^0 \pi^+ \pi^- \pi^0$  and  $K_L^0 \pi^+ \pi^- \pi^0$  peak in the H region and  $\pi^+ \pi^- \pi^0$  peaks in the L region. Other modes come in the  $B_{\text{else}}$  category. MC simulated events classifying the different background contributions in the signal and sideband regions are shown in Fig. 3.22.

The decay mode  $K^\pm e^\mp \nu$  is used as a flavour-tag *i.e.* to identify the flavour of the  $D$  meson. The double-tagged yield in this case, obtained by analysing the  $U_{\text{miss}}$  distribution, can be written as

$$Y_{K^\pm e^\mp \nu} = \frac{S - B_{\text{peak}}^S}{1 - \beta\gamma}. \quad (3.29)$$

We leave out the events in L and H regions because there is no component of S peaking in them. The component peaking in S region is due to  $K^{*\pm} e^\mp \nu$  decays. Different background components from MC simulated events are shown in Fig. 3.23. The estimated signal yields are summarized in Table 3.8.

The  $m_{\text{miss}}^2$  distributions for  $D \rightarrow K_S^0 \pi^+ \pi^- \pi^0$  decays tagged by  $CP$ -even states involving a  $K_L^0$  meson and  $K_L^0 \pi^+ \pi^-$  along with the  $U_{\text{miss}}$  distribution for  $K^\pm e^\mp \nu_e$  tag in data are shown in Fig. 3.24 and 3.25, respectively. The tag-side Dalitz plot distribution for  $K_L^0 \pi^+ \pi^-$  is shown in Fig. 3.26. These results are used to calculate the  $CP$ -content  $F_+$ , which is documented in Appendix A.

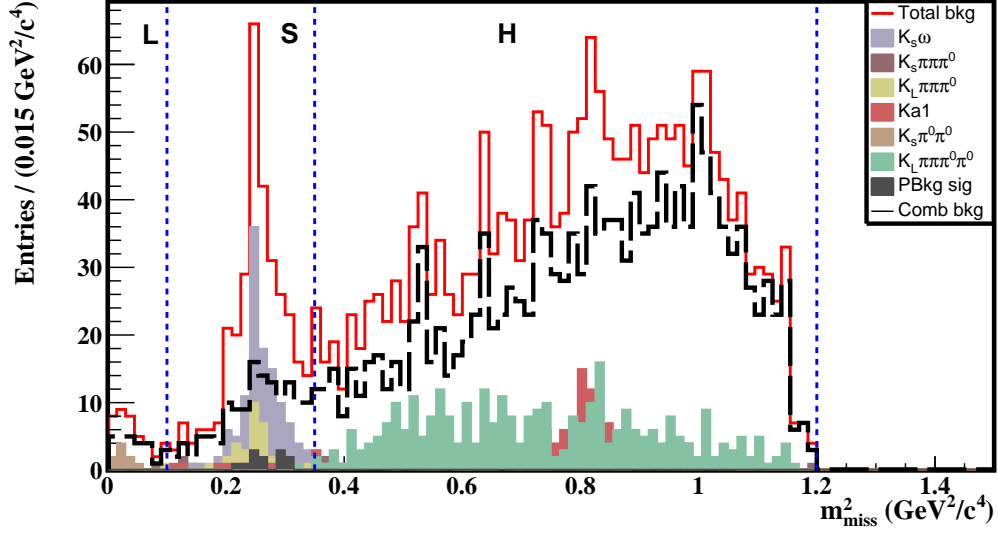


Figure 3.21:  $m_{\text{miss}}^2$  distribution for background events of  $D^0 \rightarrow K_S^0 \pi^+ \pi^- \pi^0$  decays tagged by  $\overline{D^0} \rightarrow K_L^0 \omega$  decays in MC sample. Here “PBkg sig” refers to peaking background in signal-side decay of  $D^0 \rightarrow K_S^0 \pi^+ \pi^- \pi^0$  and “Comb bkg” refers to combinatorial background.

Tag	S	$N_{\text{peak}}^S$	Yield	Efficiency (%)
$K_L^0 \pi^0$	381	11	$357 \pm 20$	$7.82 \pm 0.12$
$K_L^0 \omega$	186	13	$162 \pm 14$	$2.64 \pm 0.08$
$K_L^0 \pi^+ \pi^-$	1324	40	$864 \pm 46$	$13.07 \pm 0.15$
$K^\pm e^\mp \nu_e$	1040	9	$1010 \pm 32$	$10.63 \pm 0.06$

Table 3.8: Signal yields for  $D \rightarrow K_S^0 \pi^+ \pi^- \pi^0$  events tagged with decays involving a  $K_L^0$  meson or a  $\nu_e$  in data.

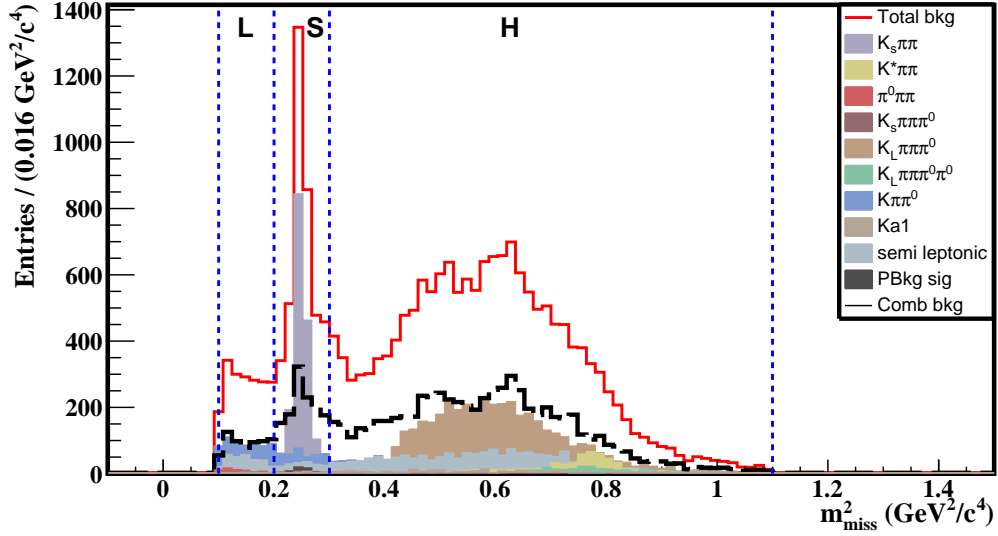


Figure 3.22:  $m_{\text{miss}}^2$  distribution for background events of  $D^0 \rightarrow K_S^0 \pi^+ \pi^- \pi^0$  decays tagged by  $\overline{D}^0 \rightarrow K_L^0 \pi^+ \pi^-$  decays in MC sample. Here “PBkg sig” refers to peaking background in signal-side decay of  $D^0 \rightarrow K_S^0 \pi^+ \pi^- \pi^0$  and “Comb bkg” refers to combinatorial background.

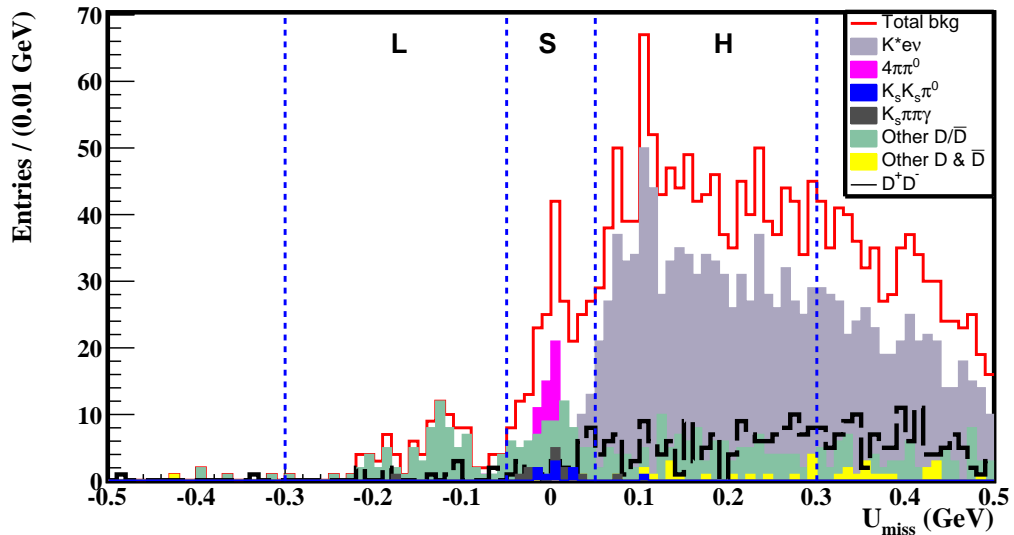


Figure 3.23:  $U_{\text{miss}}$  distribution for background events of  $D^0 \rightarrow K_S^0 \pi^+ \pi^- \pi^0$  decays tagged by  $\overline{D}^0 \rightarrow K^\pm e^\mp \nu_e$ , decays in MC sample. Here, “bkg” refers to background.

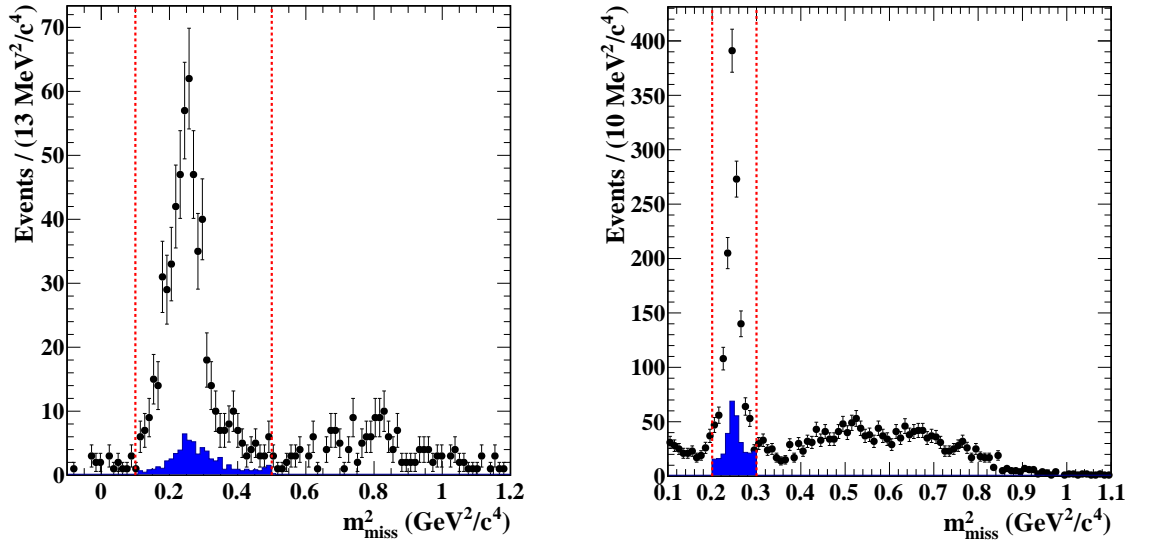


Figure 3.24:  $m_{\text{miss}}^2$  distributions for  $D \rightarrow K_S^0 \pi^+ \pi^- \pi^0$  decays tagged by  $CP$ -even states involving a  $K_L^0$  meson (left) and  $K_L^0 \pi^+ \pi^-$  (right). The shaded histogram shows the estimated peaking background and the vertical dotted lines indicate the signal region.

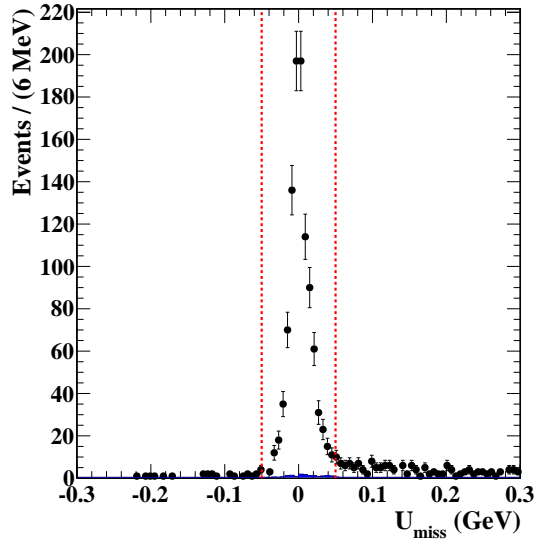


Figure 3.25:  $U_{\text{miss}}$  distribution for  $K^\pm e^\mp \nu_e$  tag. The shaded histogram shows the estimated peaking background and the vertical dotted lines indicate the signal region.

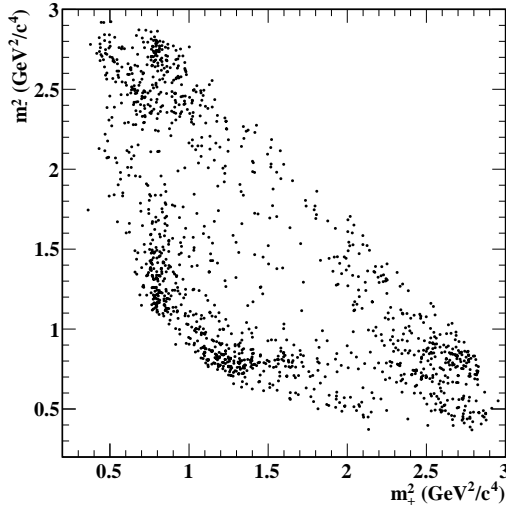


Figure 3.26: Dalitz plot distributions for the tag  $K_L^0 \pi^+ \pi^-$  against  $D \rightarrow K_S^0 \pi^+ \pi^- \pi^0$  decays. The axis labels  $m_{\pm}^2$  represents the invariant mass squares of  $K_{S,L}^0 \pi^{\pm}$  pairs.

### 3.6 Determination of $c_i$ and $s_i$

The  $c_i$  and  $s_i$  values are extracted by looking at the same  $D \rightarrow K_S^0 \pi^+ \pi^- \pi^0$  data divided into bins of phase space. The decay phase space is five-dimensional, hence there is no trivial symmetry to define the bins as in the case for three-body decays [34, 35]. Furthermore, a proper optimization is impossible due to the lack of an amplitude model. Therefore, a nine-bin scheme is defined around the most significant intermediate resonances, such as the  $\omega$ ,  $K^*$  and  $\rho$ . The kinematic regions of the bins are given in Table 3.9 and the relevant kinematic distributions are shown in Fig. 3.27 for data tagged by  $D^0 \rightarrow K^- e^+ \nu_e$  decays. The bins are exclusive and the criteria are applied sequentially in the order of the bin number. We also note that increasing the number of bins, which would result in better sensitivity to  $\phi_3$ , led to instabilities in the fit due to the large number of null bins. MC studies showed that robust results are obtained for the nine bins chosen.

The total yield in data is obtained in the signal region. The background contributions are estimated from MC simulated events. These are done in the same way as in the case of integrated  $D$  phase space as described in Sec. 3.5. The total yield in data for  $CP$  and quasi- $CP$  tag modes are shown in Table 3.10. Similarly the double-tagged yields for  $K_{S,L}^0 \pi^+ \pi^-$  tag modes for each of the  $9 \times 16$  bins are obtained in data. They are shown in Table 3.11 and 3.12, respectively. As the binning scheme for the signal mode

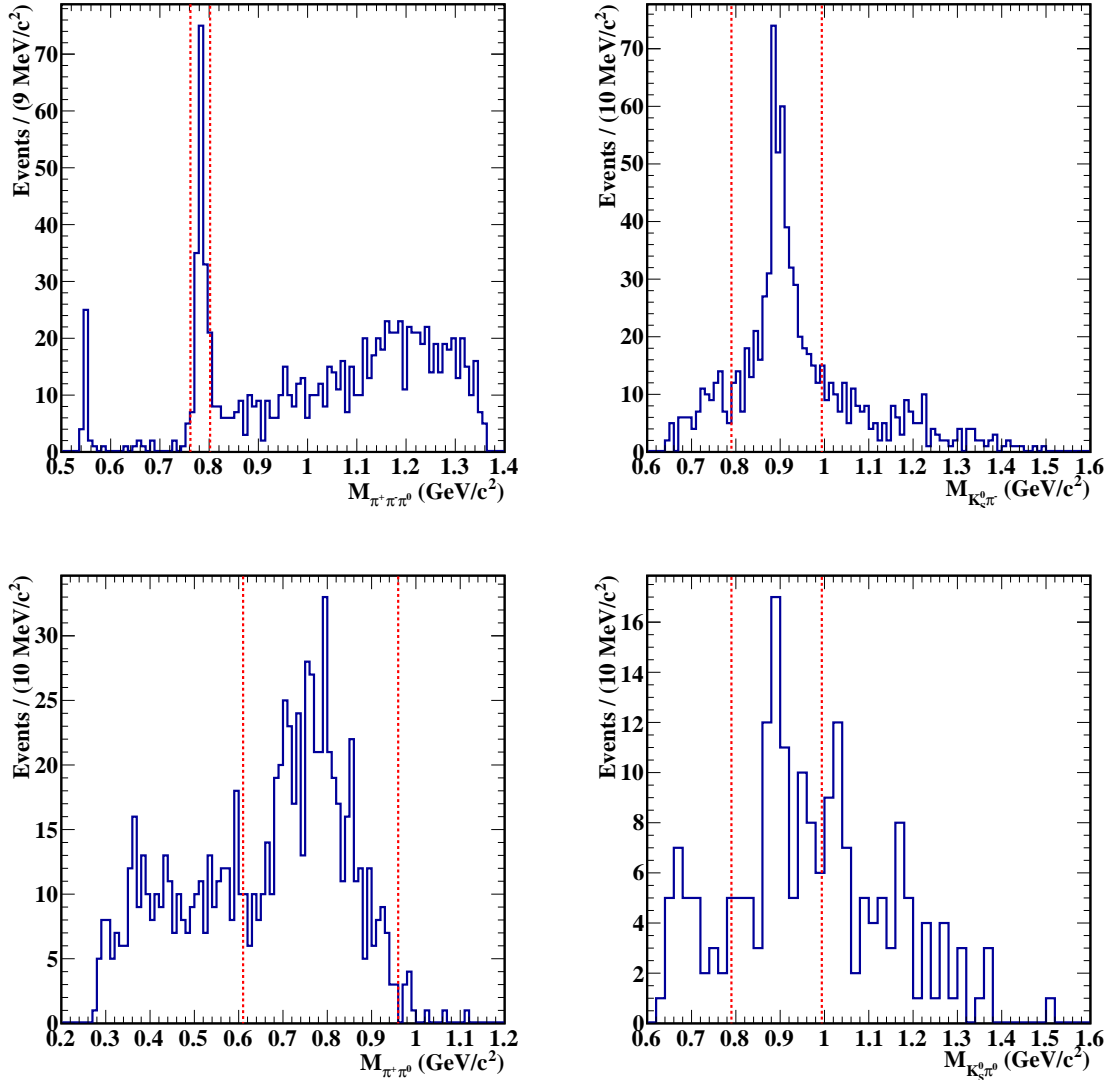


Figure 3.27: Invariant mass distributions for  $\pi^+\pi^-\pi^0$  (top left),  $K_S^0\pi^-$  (top right),  $\pi^+\pi^0$  (bottom left) and  $K_S^0\pi^0$  (bottom right) of  $D \rightarrow K_S^0\pi^+\pi^-\pi^0$  decays tagged by  $K^\pm e^\mp \nu$ . Candidates from the previous bins are removed sequentially in the order given in Table 3.9. The vertical dotted lines indicate the selected mass windows for the  $\omega$ ,  $K^*$  and  $\rho$  resonances, respectively.

is not symmetric, it is no longer possible to exploit the symmetry of the tagging decay. Therefore, there are sixteen bins in the tag-side and nine bins in the signal-side. There are a few bins with negative yields observed for  $K_L^0\pi^+\pi^-$  tagged events. All negative yields in bins are changed to zero. The yields of the remaining bins with positive yields are redistributed so that the total number of events remains the same. Monte Carlo studies showed that this procedure did not significantly bias the values of  $c_i$  and  $s_i$  and has been used in other analyses with CLEO-c data[76]. The double-tagged yield for events in which, both the  $D$  mesons decay into  $K_S^0\pi^+\pi^-\pi^0$  final state, are obtained in data. The yields in the signal region are given in Table 3.13 for each of the  $9 \times 9$  bins.

Bin	Bin region	$m_L$ (GeV/c <sup>2</sup> )	$m_U$ (GeV/c <sup>2</sup> )
1	$m_{\pi^+\pi^-\pi^0} \approx m_\omega$	0.762	0.802
2	$m_{K_S^0\pi^-} \approx m_{K^{*-}}$ & $m_{\pi^+\pi^0} \approx m_{\rho^+}$	0.790 0.610	0.994 0.960
3	$m_{K_S^0\pi^+} \approx m_{K^{*+}}$ & $m_{\pi^-\pi^0} \approx m_{\rho^-}$	0.790 0.610	0.994 0.960
4	$m_{K_S^0\pi^-} \approx m_{K^{*-}}$	0.790	0.994
5	$m_{K_S^0\pi^+} \approx m_{K^{*+}}$	0.790	0.994
6	$m_{K_S^0\pi^0} \approx m_{K^{*0}}$	0.790	0.994
7	$m_{\pi^+\pi^0} \approx m_{\rho^+}$	0.610	0.960
8	$m_{\pi^-\pi^0} \approx m_{\rho^-}$	0.610	0.960
9	Remainder	-	-

Table 3.9: Specifications of the nine exclusive bins of  $D \rightarrow K_S^0\pi^+\pi^-\pi^0$  phase space along with the fraction of flavour-tagged  $D^0$  and  $\overline{D}^0$  events in each of them.  $m_L$  and  $m_U$  are the lower and upper limits, respectively, of the invariant masses in each region.

Bin	$K^+K^-$	$\pi^+\pi^-$	$K_S^0\pi^0\pi^0$	$K_L^0\pi^0$	$K_L^0\omega$	$K_S^0\pi^0$	$K_S^0\eta$	$K_S^0\eta'$	$\pi^+\pi^-\pi^0$
1	50	24	16	75	53	1	0	0	95
2	47	28	34	106	45	43	5	1	108
3	39	17	27	82	37	26	5	3	88
4	10	9	9	26	12	2	0	0	36
5	14	2	5	23	8	4	1	1	38
6	18	5	6	28	15	11	2	2	27
7	14	3	10	18	6	4	0	0	30
8	7	1	2	13	3	3	0	0	12
9	3	3	4	10	7	2	0	0	20

Table 3.10: The total yield in the signal region of  $D \rightarrow K_S^0\pi^+\pi^-\pi^0$  decays tagged by  $CP$  and quasi- $CP$  eigenstates in data.

The double-tagged yields with the semileptonic tag  $K^\pm e^\mp \nu_e$  identify the flavour of the  $D$  meson unambiguously, allowing us to determine the parameters  $K_i$  and  $\overline{K}_i$  in each bin. If the tag side final state has  $K^-$  and  $e^+$ , then it indicates that the mother particle is a  $D^0$  meson, which in turn confirms that the flavour of the other  $D$  meson, which decays into our signal state of interest, is  $\overline{D}^0$  and vice-versa. The raw yields in nine bins are given in Table 3.14. Unlike the analysis to determine  $c_i$  and  $s_i$  in  $D^0 \rightarrow K_S^0\pi^+\pi^-$  decay [77], we do not use  $K^\pm X\pi^\mp$ ,  $K^\pm\pi^\mp\pi^0$  or  $K^\pm\pi^\mp\pi^\pm\pi^\mp$  as flavour tags because the corrections from the Cabibbo-favoured and doubly-Cabibbo-suppressed amplitudes cannot be calculated in the absence of an amplitude model for  $D \rightarrow K_S^0\pi^+\pi^-\pi^0$ .

		$K_S^0\pi^+\pi^-$															
Bin	-8	-7	-6	-5	-4	-3	-2	-1	1	2	3	4	5	6	7	8	
1	5	9	2	0	0	4	6	15	19	4	5	2	0	2	4	9	
2	16	10	6	9	0	5	6	23	19	9	4	3	7	5	8	10	
3	5	3	2	4	1	4	3	15	19	11	7	1	8	4	6	18	
4	6	3	0	1	1	3	3	10	5	4	0	0	1	2	2	0	
5	5	2	1	3	1	2	2	8	4	4	5	0	1	1	4	3	
6	7	4	1	1	1	1	0	4	6	0	4	0	1	3	1	3	
7	4	2	0	1	0	3	3	8	7	1	0	0	1	0	1	4	
8	0	0	1	1	0	2	0	3	3	2	0	0	0	1	1	3	
9	1	1	1	0	0	0	0	1	3	0	1	0	0	0	0	2	

Table 3.11: Total yield in data for  $K_S^0\pi^+\pi^-\pi^0$  decays tagged by  $K_S^0\pi^+\pi^-$  events in the signal region. The rows represent the  $K_S^0\pi^+\pi^-\pi^0$  phase space bins and columns show the tag side bins.

		$K_L^0\pi^+\pi^-$															
Bin	-8	-7	-6	-5	-4	-3	-2	-1	1	2	3	4	5	6	7	8	
1	14	10	8	17	13	6	6	17	16	6	5	5	24	7	19	12	
2	30	34	18	22	16	19	21	54	33	19	19	10	20	10	20	22	
3	16	9	4	24	13	7	11	26	43	16	20	5	21	20	28	28	
4	12	12	8	6	2	3	6	9	14	4	3	5	9	5	4	6	
5	2	5	2	9	7	5	5	11	13	7	5	1	8	8	8	7	
6	10	7	1	4	0	8	4	11	17	2	5	1	10	6	10	6	
7	2	4	6	4	1	1	4	10	8	3	4	3	10	4	6	3	
8	0	0	2	2	0	0	2	5	6	1	1	3	6	4	3	0	
9	5	2	8	4	3	0	4	8	9	0	1	2	2	3	4	5	

Table 3.12: Total yield in data for  $K_S^0\pi^+\pi^-\pi^0$  decays tagged by  $K_L^0\pi^+\pi^-$  events in the signal region. The rows represent the  $K_S^0\pi^+\pi^-\pi^0$  phase space bins and columns show the tag side bins.

$K_S^0 \pi^+ \pi^- \pi^0$									
Bin	1	2	3	4	5	6	7	8	9
1	1	6	6	0	0	2	0	0	0
2	12	18	22	3	2	2	1	2	3
3	8	13	5	3	3	8	4	0	2
4	1	4	3	2	2	3	1	0	0
5	1	5	1	1	0	0	1	0	0
6	2	4	6	2	1	1	0	1	2
7	0	7	4	0	0	1	0	0	0
8	1	0	3	0	0	3	0	0	0
9	0	6	3	1	0	1	1	0	0

Table 3.13: Total yield in data for events in which, both the  $D$  mesons decay into  $K_S^0 \pi^+ \pi^- \pi^0$  final state, in the signal region.

Bin	Yield	
	$D^0 \rightarrow K_S^0 \pi^+ \pi^- \pi^0$	$\overline{D}^0 \rightarrow K_S^0 \pi^+ \pi^- \pi^0$
1	89	76
2	197	101
3	51	167
4	41	28
5	32	38
6	33	50
7	25	26
8	13	13
9	15	21

Table 3.14: The total yield of  $D^0$  and  $\overline{D}^0$  decays to  $K_S^0 \pi^+ \pi^- \pi^0$  obtained from flavour tag mode  $K^\pm e^\mp \nu_e$  in each bin for the signal region in data.

Bin	Efficiency (%)	Fraction of $\mathcal{D}$
1	$15.0 \pm 0.5$	0.027
2	$17.3 \pm 0.2$	0.209
3	$18.5 \pm 0.2$	0.164
4	$16.9 \pm 0.2$	0.122
5	$17.3 \pm 0.2$	0.103
6	$16.7 \pm 0.2$	0.143
7	$16.6 \pm 0.3$	0.078
8	$16.2 \pm 0.3$	0.052
9	$13.7 \pm 0.2$	0.102

Table 3.15: Reconstruction efficiency of  $D \rightarrow K_S^0 \pi^+ \pi^- \pi^0$  events in each bin estimated from signal MC sample. The fractional five-dimensional volume of each bin is also given.

The reconstruction efficiencies of  $D \rightarrow K_S^0 \pi^+ \pi^- \pi^0$  decays in the different bins are obtained from signal MC events. The fractional five-dimensional volume of each bin is also determined. The efficiency and fractional volume in each bin are given in Table 3.15. Due to the finite resolution of the detector, reconstructed decays may migrate to other bins in phase space. This effect is studied by looking at simulated signal events and a  $9 \times 9$  migration matrix  $M$ , is calculated. Each of its elements gives the ratio of the number of events reconstructed to those generated in a bin. The migration matrix obtained from signal MC events is shown in Table 3.16.

Bin	1	2	3	4	5	6	7	8	9
1	<b>0.823</b>	0.013	0.020	0.039	0.029	0.021	0.003	0.003	0.052
2	0.001	<b>0.938</b>	0.009	0.007	0.003	0.005	0.003	0.001	0.032
3	0.002	0.016	<b>0.874</b>	0.010	0.010	0.010	0.006	0.005	0.069
4	0.003	0.009	0.008	<b>0.927</b>	0.007	0.006	0.001	0.003	0.035
5	0.004	0.009	0.013	0.011	<b>0.914</b>	0.006	0.003	0.000	0.039
6	0.003	0.007	0.005	0.005	0.004	<b>0.931</b>	0.005	0.004	0.035
7	0.000	0.011	0.006	0.002	0.004	0.009	<b>0.934</b>	0.007	0.028
8	0.000	0.004	0.012	0.004	0.002	0.008	0.007	<b>0.926</b>	0.036
9	0.007	0.002	0.003	0.005	0.005	0.012	0.007	0.007	<b>0.953</b>

Table 3.16: Migration matrix obtained from  $D \rightarrow K_S^0 \pi^+ \pi^- \pi^0$  signal MC events. The rows and columns represent the reconstructed and true bins, respectively.

Bin	$K_i$	$\overline{K}_i$
1	$0.222 \pm 0.019$	$0.177 \pm 0.017$
2	$0.393 \pm 0.022$	$0.191 \pm 0.017$
3	$0.089 \pm 0.013$	$0.318 \pm 0.021$
4	$0.077 \pm 0.012$	$0.047 \pm 0.009$
5	$0.058 \pm 0.011$	$0.066 \pm 0.011$
6	$0.061 \pm 0.011$	$0.093 \pm 0.013$
7	$0.045 \pm 0.009$	$0.045 \pm 0.009$
8	$0.023 \pm 0.007$	$0.020 \pm 0.006$
9	$0.032 \pm 0.008$	$0.045 \pm 0.009$

Table 3.17: Fraction of flavour-tagged  $D^0$  and  $\overline{D}^0$  events in each bin.

There is a significant loss of 20% from bin 1 due to the  $\omega$  resonance having a narrow decay width that is smaller than the invariant mass resolution. The double-tagged yields ( $Y$ ) for each mode are corrected for the migration effects as  $Y_i = \sum_j M_{ij} Y_j$ , where  $i$  and  $j$  run from 1 to 9. The fraction of  $D^0$  and  $\overline{D}^0$  events,  $K_i$  and  $\overline{K}_i$ , are calculated from the corresponding yields after the correction applied as  $K_i = \sum_j M_{ij}^{-1} Y_j$ . They are shown in Table 5.3.

The background subtracted and migration corrected double-tagged yields for  $CP$  tags, quasi- $CP$  tag and other self-conjugate modes are obtained in each of the bins. These inputs are used in a Poissonian log-likelihood fit with  $\chi^2$  of the form

$$\chi^2 = N_{\text{pred}} - N_{\text{meas}} - \left[ N_{\text{meas}} \log \left( \left| \frac{N_{\text{pred}}}{N_{\text{meas}}} \right| \right) \right], \quad (3.30)$$

with  $c_i$  and  $s_i$  values as fit parameters. Here,  $N_{\text{pred}}$  and  $N_{\text{meas}}$  are the expected and measured yields, respectively. The fit assumes that the data follow Eqs. (1.48) – (1.51). The expected yields in each bin is compared to the raw number of events and the background yield is added to the expected yield.

The  $CP$  and quasi- $CP$  tags provide sensitivity only to  $c_i$  values. The tags  $K_S^0 \pi^+ \pi^-$  and  $K_L^0 \pi^+ \pi^-$  give sensitivity to both  $c_i$  and  $s_i$  values. The already measured strong-phase parameters for  $D \rightarrow K_{S,L}^0 \pi^+ \pi^-$  are used as inputs in the fit. The sample of doubly-tagged  $K_S^0 \pi^+ \pi^- \pi^0$  events is also useful in providing information on  $s_i$  values.

The uncertainties on the input strong-phase parameters of  $K_S^0 \pi^+ \pi^-$  and  $K_L^0 \pi^+ \pi^-$  are accounted as Gaussian constraints in the fit including the correlations among the parameters. The normalization constant for the  $CP$ -tagged yield in Eq. (1.48),  $h_{CP}$

is chosen as a free parameter for one  $CP$  tag,  $K^+K^-$  in the fit. Then all the other normalizations for modes not involving a  $K_L^0$  meson are defined as  $\frac{S(\text{tag})}{S(K^+K^-)}h_{CP}$  in the fit, where  $S$  represents the single-tagged yield. The single-tagged yield measurements are taken from Ref. [76].

The nature of the symmetry within the bins leads to certain constraints that can be imposed in the fit. Bins 1, 6 and 9 are  $CP$  self-conjugate, and hence the strong-phase difference between the decays  $D^0 \rightarrow f$  and  $\overline{D^0} \rightarrow f$  will be zero in those regions, which implies that

$$s_1 = 0, s_6 = 0, s_9 = 0. \quad (3.31)$$

Bin 9 is  $CP$  self-conjugate because the region corresponding to the sum of bins 1 to 8 is  $CP$  self-conjugate. The bins 2 and 3 are  $CP$ -conjugate pairs of each other. Thus we have

$$s_2\sqrt{K_2\overline{K_2}} = \int_{\mathcal{D}} |A||\overline{A}| \sin \Delta\delta_D d\mathcal{D} \quad (3.32)$$

and

$$s_3\sqrt{K_3\overline{K_3}} = \int_{\mathcal{D}} |A||\overline{A}| \sin(-\Delta\delta_D) d\mathcal{D} \quad (3.33)$$

for the  $CP$ -conjugate region which results in the relation

$$s_2\sqrt{K_2\overline{K_2}} + s_3\sqrt{K_3\overline{K_3}} = 0. \quad (3.34)$$

We have similar relations for bins 4 and 5 and bins 7 and 8 as,

$$s_4\sqrt{K_4\overline{K_4}} + s_5\sqrt{K_5\overline{K_5}} = 0, \quad (3.35)$$

$$s_7\sqrt{K_7\overline{K_7}} + s_8\sqrt{K_8\overline{K_8}} = 0. \quad (3.36)$$

In the fit, we constrain  $s_3$ ,  $s_5$  and  $s_8$  using Eqs. (3.34)–(3.36) along with fixing  $s_1$ ,  $s_6$  and  $s_9$  to zero.

### 3.6.1 Systematic uncertainties

Several sources of systematic uncertainty are considered in the  $c_i$  and  $s_i$  determination. The fitter assumptions are tested using pseudo experiments. The yields are calculated

for a given set of  $c_i$  and  $s_i$  values and they are fitted back to see the deviations in the result from the input values. The input values are given within the physically allowed region of  $c_i^2 + s_i^2 \leq 1$ . The yields in each bin are multiplied by a factor of 100, and 400 such experiments are performed. This scaling is to avoid bias due to statistical fluctuations in certain bins where the  $c_i$  values are unphysical. The mean of the pull distribution multiplied by the statistical uncertainty on the nominal value is taken as the systematic uncertainty due to a possible bias in the fit assumptions. The negative and positive deviations from the nominal value are summed in quadrature. The background events are fluctuated to  $+1\sigma$  and  $-1\sigma$ , where  $\sigma$  is the statistical uncertainty, and the fits are run to obtain  $c_i$  and  $s_i$  values. The difference from the nominal values are taken as the systematic uncertainty. The signal-side backgrounds are fluctuated bin-by-bin, whereas the tag-side backgrounds are changed simultaneously for each mode owing to the correlations across the bins in the signal-side.

The limited statistics of the MC sample used to determine the migration matrix can cause variations in phase-space acceptance that might bias the results. The elements of migration matrix are smeared by  $+1\%$  and  $-1\%$  independently to account for this possible bias. The resulting change in  $c_i$  and  $s_i$  are assigned as the systematic uncertainty. The single-tagged yields used in the normalization of the fit are fluctuated independently to  $+1\sigma$  and  $-1\sigma$ , where  $\sigma$  is the statistical uncertainty on the yield and the change in  $c_i$  and  $s_i$  values are taken as the systematic uncertainty.

The uncertainty on  $K_i$  and  $\overline{K}_i$  values is taken as a Gaussian constraint in the fit, so there is no need to assign a corresponding systematic uncertainty. The Gaussian constraints are added in the fit for the external output values of  $c_i$ ,  $s_i$ ,  $K_i$  and  $\overline{K}_i$  from  $K_{S,L}^0 \pi^+ \pi^-$  decays. We investigate the change in migration matrix due to momentum resolution. Bin 1, which has the largest migration, hence the largest sensitivity to any data-MC discrepancy is chosen for the study. The  $\pi^+ \pi^- \pi^0$  invariant mass distribution is fitted with a double Gaussian and a first order polynomial PDFs in MC and data samples. The fit projections are given in Fig. 3.28 and 3.29. The invariant mass resolution in data and MC are found to be  $5.319 \pm 0.064$  MeV/c<sup>2</sup> and  $4.928 \pm 0.003$  MeV/c<sup>2</sup>, respectively. The invariant mass in data is smeared by the quadrature difference of these two resolutions  $2.019 \pm 0.064$  MeV/c<sup>2</sup> and the migration matrix is recalculated. The effect is minimal and hence we do not assign a systematic uncertainty for this in bin 1 or in any other bins.

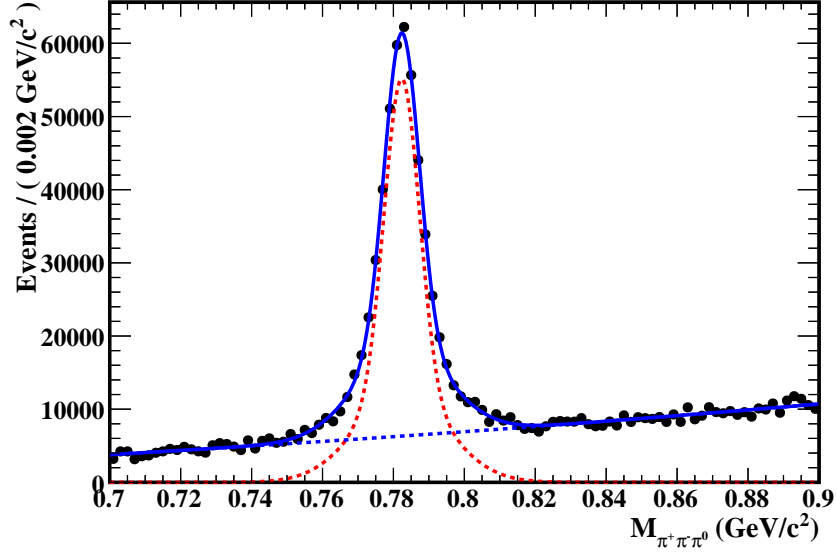


Figure 3.28:  $\pi^+\pi^-\pi^0$  invariant mass fitted with a double Gaussian and polynomial PDFs in MC sample. Blue solid curve represents the total fit and red and blue dashed curves are double Gaussian and polynomial functions, respectively.

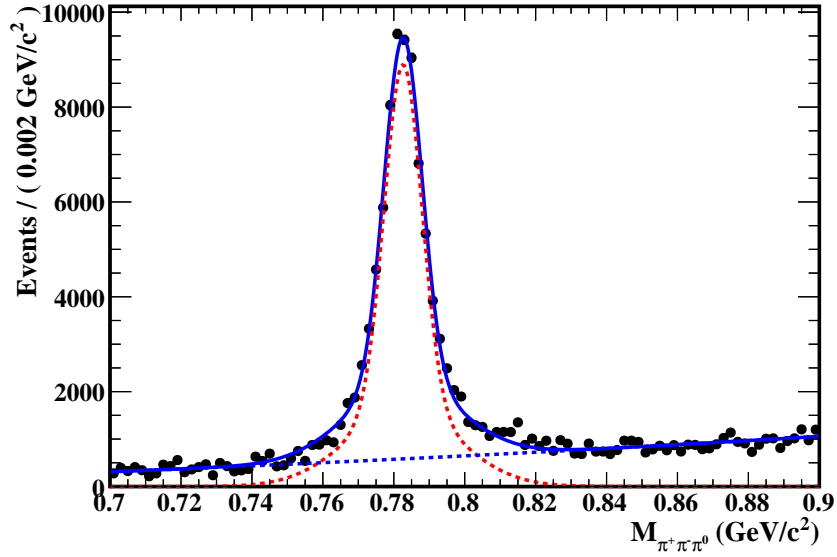


Figure 3.29:  $\pi^+\pi^-\pi^0$  invariant mass fitted with a double Gaussian and polynomial PDFs in data sample. Blue solid curve represents the total fit and red and blue dashed curves are double Gaussian and polynomial functions, respectively.

The multiplicity distribution for each tag shows good agreement between data and MC. So the metric choosing the best-candidate in an event does not introduce a bias. Moreover, the 1% systematic deviation of migration matrix elements is large enough to take care of the effect of choosing a wrong candidate during multiple candidate selection. A summary of the systematic uncertainty evaluation is given in Table 3.18 and

Source	$c_1$	$c_2$	$c_3$	$c_4$	$c_5$	$c_6$	$c_7$	$c_8$	$c_9$
Fit bias	0.003	0.006	0.006	0.002	0.002	0.004	0.014	0.021	0.046
Peaking background	+0.010 -0.006	+0.004 -0.003	0.005	+0.027 -0.043	+0.016 -0.011	+0.011 -0.009	+0.021 -0.015	+0.013 -0.011	+0.052 -0.097
Flat background	+0.009 -0.011	+0.006 -0.008	+0.013 -0.010	+0.047 -0.013	+0.028 -0.021	0.018	+0.023 -0.017	+0.015 -0.017	+0.131 -0.051
Dalitz plot acceptance	0.006	0.002	0.002	+0.002 -0.003	0.003	0.002	0.002	0.002	0.003
Single-tagged yield	0.001	0.003	0.003	+0.001 -0.002	0.003	0.003	0.001	0.002	0.003
Total	+0.015 -0.014	+0.010 -0.011	+0.015 -0.013	+0.054 -0.045	+0.032 -0.024	+0.022 -0.021	+0.034 -0.026	0.029	+0.148 -0.119
Statistical uncertainty	0.09	0.05	0.07	0.09	0.12	0.11	0.11	0.18	0.15

Table 3.18: Systematic uncertainties on  $c_i$  values.

**3.19.** The systematic uncertainties are small compared to the statistical errors.

The final results of the  $c_i$  and  $s_i$  values are given in Table 3.20 and displayed graphically in Fig. 3.30. All the  $c_i$  values are less than zero and this trend corresponds to  $F_+ < 0.5$ . The statistical and systematic correlation coefficients between  $c_i$  and  $s_i$  values are given in Table 3.21 and Table 3.22, respectively.

Source	$s_2$	$s_4$	$s_7$
Fit bias	0.009	0.036	0.011
Peaking background	0.005	+0.041 -0.032	+0.025 -0.019
Flat background	+0.010 -0.012	+0.031 -0.040	+0.023 -0.017
Dalitz plot acceptance	0.000	+0.000 -0.002	0.000
Single-tagged yield	0.000	+0.000 -0.001	0.000
Total	+0.014 -0.015	0.063	+0.036 -0.027
Statistical uncertainty	0.09	0.18	0.19

Table 3.19: Systematic uncertainties on  $s_i$  values.

### 3.7 Estimation of sensitivity to $\phi_3$

In order to estimate the impact of these results on a future  $\phi_3$  measurement using  $B^\pm \rightarrow D(K_S^0 \pi^+ \pi^- \pi^0) K^\pm$  decays, we perform a simulation study based on the expected yield of this mode in the Belle data sample ( $\approx 1 \text{ ab}^{-1}$ ). The Belle sample of

Bin	$c_i$	$s_i$
1	$-1.11 \pm 0.09_{-0.01}^{+0.02}$	0.00
2	$-0.30 \pm 0.05 \pm 0.01$	$-0.03 \pm 0.09_{-0.02}^{+0.01}$
3	$-0.41 \pm 0.07_{-0.01}^{+0.02}$	$0.04 \pm 0.12_{-0.02}^{+0.01}$ *
4	$-0.79 \pm 0.09 \pm 0.05$	$-0.44 \pm 0.18 \pm 0.06$
5	$-0.62 \pm 0.12_{-0.02}^{+0.03}$	$0.42 \pm 0.20 \pm 0.06$ *
6	$-0.19 \pm 0.11 \pm 0.02$	0.00
7	$-0.82 \pm 0.11 \pm 0.03$	$-0.11 \pm 0.19_{-0.03}^{+0.04}$
8	$-0.63 \pm 0.18 \pm 0.03$	$0.23 \pm 0.41_{-0.03}^{+0.04}$ *
9	$-0.69 \pm 0.15_{-0.12}^{+0.15}$	0.00

Table 3.20: Final results for  $c_i$  and  $s_i$  values. The uncertainties are statistical and systematic, respectively. The  $s_i$  results marked by \* in bins 3, 5 and 8 are derived from those in other bins, according to the constraints of Eqs. (3.34)–(3.36).

	$c_2$	$c_3$	$c_4$	$c_5$	$c_6$	$c_7$	$c_8$	$c_9$	$s_2$	$s_4$	$s_7$
$c_1$	0.03	-0.01	-0.13	0.01	0.04	0.07	-0.05	0.06	0.00	0.01	0.00
$c_2$		0.08	0.02	0.06	0.08	-0.02	0.03	0.06	-0.01	-0.01	0.00
$c_3$			0.03	0.05	0.01	-0.08	-0.03	0.03	-0.03	-0.01	0.01
$c_4$				-0.01	-0.01	-0.01	0.03	-0.05	0.00	-0.13	-0.01
$c_5$					0.04	0.01	0.03	0.03	0.00	-0.01	0.01
$c_6$						0.01	-0.03	-0.01	0.00	0.00	0.00
$c_7$							0.00	0.00	0.01	0.00	-0.05
$c_8$								-0.03	-0.01	-0.01	0.02
$c_9$									0.00	0.00	0.00
$s_2$										-0.03	0.00
$s_4$											-0.02

Table 3.21: Statistical correlation coefficients between  $c_i$  and  $s_i$  values.

$B^\pm \rightarrow D(K_S^0 \pi^+ \pi^-) K^\pm$  [78] has  $\approx 1200$  events. Assuming that increase in branching fraction for  $K_S^0 \pi^+ \pi^- \pi^0$  compared to  $K_S^0 \pi^+ \pi^-$  is compensated by the loss of efficiency due to a  $\pi^0$  in the final state [79, 80], we expect a similar yield for  $B^\pm \rightarrow D(K_S^0 \pi^+ \pi^- \pi^0) K^\pm$ . The  $\phi_3$  sensitivity is estimated in a GGSZ [34, 35] framework. We run 1000 pseudo experiments with  $c_i$ ,  $s_i$ ,  $K_i$ , and  $\bar{K}_i$  values as inputs with each experiment consisting of  $\approx 1200$  events. The input values of  $\phi_3$  and the hadronic parameters  $r_B$  and  $\delta_B$  are taken from Ref. [22]. This results in  $\sigma_{\phi_3} \approx 25^\circ$  from this single mode. The next two Chapters of this thesis will describe the implementation of this method on the Belle data set.

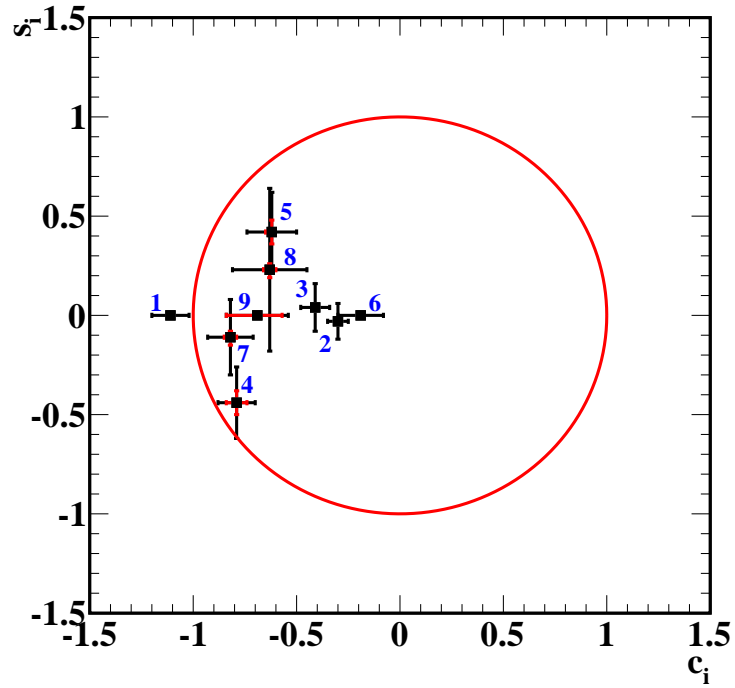


Figure 3.30:  $c_i$  and  $s_i$  values in each bin. The black and red error bars represent statistical and systematic uncertainties, respectively.

	$c_2$	$c_3$	$c_4$	$c_5$	$c_6$	$c_7$	$c_8$	$c_9$	$s_2$	$s_4$	$s_7$
$c_1$	0.02	0.02	0.00	0.02	0.02	0.00	0.01	0.01	0.00	0.00	0.00
$c_2$		0.07	0.01	0.04	0.06	0.01	0.02	0.01	0.01	0.00	0.00
$c_3$			0.01	0.04	0.06	0.01	0.02	0.01	0.01	0.00	0.00
$c_4$				0.01	0.01	0.00	0.00	0.00	0.00	0.00	0.00
$c_5$					0.05	0.01	0.01	0.01	0.01	0.00	0.00
$c_6$						0.01	0.02	0.02	0.02	0.00	0.00
$c_7$							0.00	0.00	0.00	0.00	0.00
$c_8$								0.00	0.00	0.00	0.00
$c_9$									0.00	0.00	0.00
$s_2$										0.00	0.00
$s_4$											0.00

Table 3.22: Systematic correlation coefficients between  $c_i$  and  $s_i$  values.

# CHAPTER 4

## Selection of $B^+ \rightarrow D(K_S^0\pi^+\pi^-\pi^0)h^+$ , $h = K, \pi$ and $D^{*+} \rightarrow D(K_S^0\pi^+\pi^-\pi^0)\pi^+$ events at Belle

### 4.1 Introduction

The reconstruction of  $D \rightarrow K_S^0\pi^+\pi^-\pi^0$  candidates in  $B^+ \rightarrow Dh^+$ ,  $h = K, \pi$  and  $D^{*+} \rightarrow D\pi^+$  decays at Belle is described in this chapter. The  $B^+ \rightarrow DK^+$  sample is the signal mode of interest, which is sensitive to the CKM angle  $\phi_3$ . The mode  $B^+ \rightarrow D\pi^+$  serves as a good calibration mode for the entire signal extraction procedure, due to it having an identical topology to that of  $B^+ \rightarrow DK^+$ , but with negligible  $CP$  violation expected [81]. The branching fraction of  $B^+ \rightarrow D\pi^+$  is larger than  $B^+ \rightarrow DK^+$  because of the Cabibbo-favoured nature of the decay. The simultaneous analysis of these two modes also allows for the determination of  $K - \pi$  misidentification background directly from data. The  $D^{*+} \rightarrow D\pi^+$  sample is used to determine the fraction of  $D^0$  and  $\bar{D}^0$  events in bins of  $D$  phase space.

The rest of this Chapter is arranged as follows: the data sample is described in Sec. 4.2. A detailed description of the event selection is given in Sec. 4.3 and the background suppression is discussed in Sec. 4.4. The best-candidate selection is explained in Sec. 4.5. Finally, the efficiency and migration matrix calculation is summarized in Sec. 4.6.

### 4.2 Data sample

Belle detects the  $B\bar{B}$  pairs produced in  $e^+e^-$  collisions at a centre-of-mass energy  $\sqrt{s}$  corresponding to the  $\Upsilon(4S)$  resonance, as described in Chapter 2. Many  $D^{*+}$  mesons are also produced because  $\sqrt{s} = 10.58$  GeV is very much higher than the production of charm mesons via  $e^+e^- \rightarrow c\bar{c}$ . The full Belle dataset of  $772 \times 10^6$   $B\bar{B}$  pairs, corresponding to an integrated luminosity of  $711 \text{ fb}^{-1}$ , is used in the analysis described here.

The clean environment at the KEKB  $e^+e^-$  collider allows efficient detection of final state particles at Belle. The stable or long-lived particles are detected by the various subsystems as explained in Chapter 2. The  $D$ ,  $D^*$  and  $B$  meson candidates are then further reconstructed from these detected particles using a custom made C++ algorithm within the Belle Analysis Software Framework [82].

Simulated signal MC events are used to estimate selection efficiencies. Independent generic MC samples, each with a size corresponding to an integrated luminosity equivalent to that of the dataset, are used to determine various background contributions, optimize the selection criteria and devise a fit model for signal extraction. The EvtGen [68] and Geant 3 [69] packages are used to generate the decays and model the detector response, respectively. The final-state radiation effects associated with charged particles are simulated with PHOTOS [70].

### 4.3 Event selection

The  $D$  candidates are reconstructed from the four daughter particles  $K_S^0$ ,  $\pi^+$ ,  $\pi^-$  and  $\pi^0$ , where the  $K_S^0$  candidates are made from two charged pions and the  $\pi^0$  candidates are formed from a pair of photons. The  $D^{*+}$  and  $B^+$  candidates are then reconstructed by adding a  $\pi^+$  or  $K^+$  to the  $D$  candidates appropriately. The  $B$  meson reconstruction chain is

$$e^+e^- \rightarrow \Upsilon(4S) \rightarrow B^+B^-; \quad B^\mp \rightarrow D^0(\overline{D}^0)h^\mp; \quad D^0(\overline{D}^0) \rightarrow K_S^0\pi^+\pi^-\pi^0, \quad (4.1)$$

and the  $D^*$  meson reconstruction chain is

$$e^+e^- \rightarrow \gamma^* \rightarrow D^{*\pm}X; \quad D^{*\pm} \rightarrow D^0(\overline{D}^0)\pi^\pm; \quad D^0(\overline{D}^0) \rightarrow K_S^0\pi^+\pi^-\pi^0, \quad (4.2)$$

where  $X$  is any collection of hadrons produced along with  $D^*$ . A detailed description of the selection criteria for different final state particles is given in the following subsections.

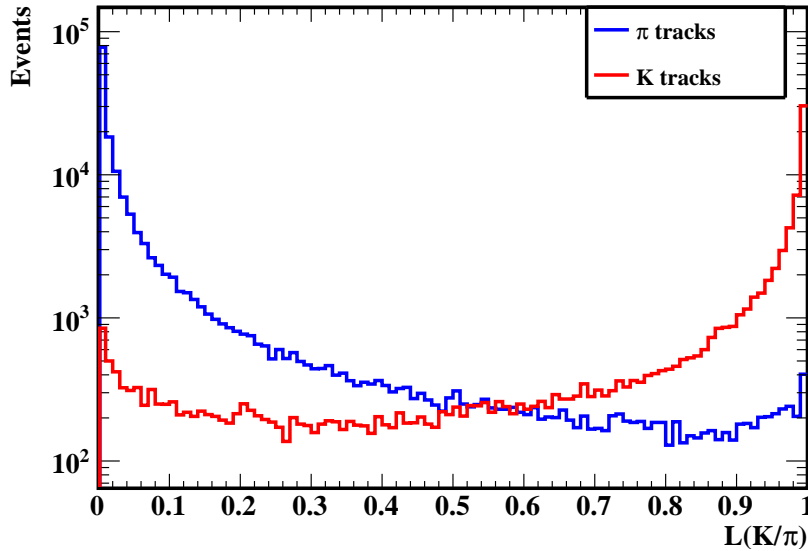


Figure 4.1:  $L(K/\pi)$  distributions for charged pion and kaon tracks in the signal MC sample.

### 4.3.1 Selection of $K^+$ and $\pi^+$ candidates

The charged tracks are required to come from within 0.5 cm from the IP in the radial direction and 3.0 cm along the  $z$  direction. This removes tracks that do not originate from the IP, such as those related to beam-induced background and material interactions. The kaon and pion tracks are distinguished using the combined measurements from CDC, TOF and ACC subdetectors as described in Chapter 2. A likelihood function of the form

$$L(K/\pi) = \frac{L_K}{L_K + L_\pi}, \quad (4.3)$$

is defined where  $L_K$ ,  $L_\pi$  and  $L(K/\pi)$  are the likelihood values of kaon, pion and kaon over pion, respectively [83]. The  $L(K/\pi)$  distributions for charged pion and kaon tracks in signal MC sample is shown in Fig. 4.1. A selection of  $L(K/\pi) < 0.4$  is applied to select good pion candidates and this identifies a true pion 92% of the time and the chance of a kaon getting misidentified as a pion is 8%. The criterion  $L(K/\pi) > 0.6$  selects good kaon candidates and the efficiency is 84% with a pion fake rate of 15% [84]. It is essential to distinguish between kaons and pions efficiently to separate the  $B^+ \rightarrow DK^+$  and  $B^+ \rightarrow D\pi^+$  decay candidates.

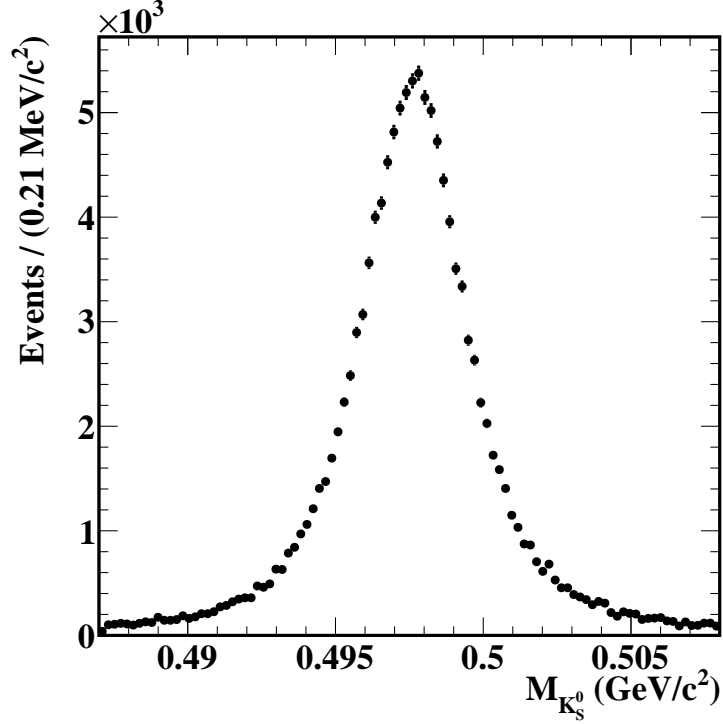


Figure 4.2:  $M_{K_S^0}$  distribution after applying the selection criteria in  $B^+ \rightarrow D(K_S^0 \pi^+ \pi^- \pi^0) K^+$  signal MC sample.

### 4.3.2 Selection of $K_S^0$ candidates

A  $K_S^0$  meson candidate is reconstructed from a pair of charged pion tracks. These charged tracks are not required to originate from close to the IP, because the  $K_S^0$  candidates travel a significant distance [ $\mathcal{O}(\text{cm})$ ] before decaying to two charged pions. No likelihood selection is applied to the pions to distinguish them from kaons. The invariant mass of the two pion candidates is required to be in the range  $(0.487, 0.508) \text{ GeV}/c^2$ , which is approximately  $\pm 3\sigma$  about the nominal mass of  $K_S^0$  [14]. Here,  $\sigma$  is the invariant mass resolution. A neural network (NN) [85] based selection is applied to the pion tracks to remove background from random combinations of pions [86]. The input variables used by the neural network are the  $K_S^0$  momentum in the lab frame, the distance between the two track helices along the  $z$ -axis at their point of closest approach, the  $K_S^0$  flight length in the radial direction, the angle between the  $K_S^0$  momentum and the vector joining the IP to the  $K_S^0$  decay vertex, the angle between the  $K_S^0$  momentum in the lab frame and pion momentum in the  $K_S^0$  rest frame, the distances of closest approach in the radial direction between the IP and the two pion helices, the number of hits in the CDC for each pion track and the presence of hits in the SVD for each pion track. The  $K_S^0$  selection efficiency is 87%. The  $\pi^+ \pi^-$  invariant mass distribution after applying

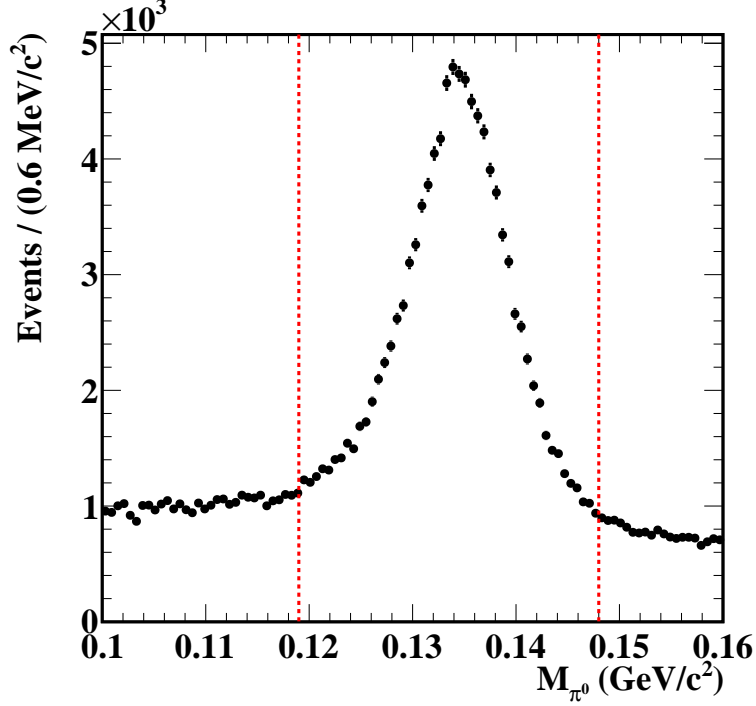


Figure 4.3:  $M_{\pi^0}$  distribution in  $B^+ \rightarrow D(K_S^0 \pi^+ \pi^- \pi^0) K^+$  signal MC sample. The vertical dotted lines indicate the selected region.

all these selection criteria is given in Fig. 4.2. A kinematic constraint on the  $\pi^+ \pi^-$ -invariant mass to the nominal  $K_S^0$  mass is applied and both the charged pion tracks are required to come from a common vertex point.

### 4.3.3 Selection of $\pi^0$ candidates

The  $\pi^0$  candidates are reconstructed from a pair of photons detected in the ECL. A basic energy threshold criterion of 50 MeV is applied on all photon candidates at preselection level to reduce beam-induced background and ECL noise. We select  $\pi^0$  candidates with a photon pair invariant mass  $M_{\pi^0}$  in the range (0.119, 0.148)  $\text{GeV}/c^2$ , which corresponds to  $3\sigma$  about the nominal  $\pi^0$  mass [14]. The distribution is shown in Fig. 4.3. The diphoton invariant mass is kinematically constrained to the nominal mass of  $\pi^0$  to improve the momentum resolution.

### 4.3.4 Selection of $D$ candidates

The  $K_S^0$ ,  $\pi^+$ ,  $\pi^-$  and  $\pi^0$  candidates are combined to form  $D$  meson candidates. The daughter particles invariant mass,  $M_D$  is required to be in the range (1.835, 1.890)  $\text{GeV}/c^2$ ,

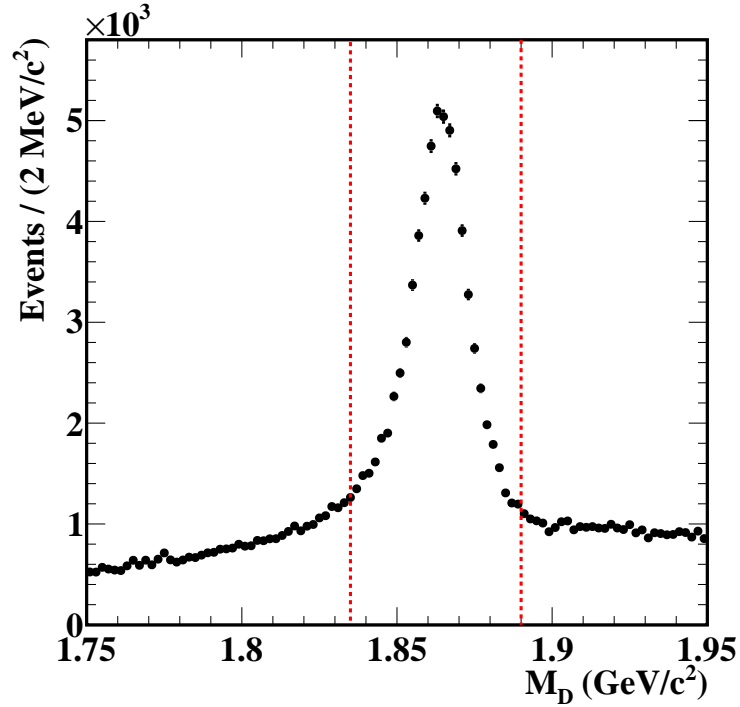


Figure 4.4:  $M_D$  distribution in  $B^+ \rightarrow D(K_S^0\pi^+\pi^-\pi^0)K^+$  signal MC sample. The vertical dotted lines indicate the selected region.

which approximately corresponds to  $\pm 3\sigma$  region around the nominal  $D$  mass [14]. All the four final state particles are required to come from a common vertex point to ensure that they are essentially the products of a  $D$  meson decay. The  $M_D$  distribution is asymmetric due to the presence of a  $\pi^0$  candidate in the final state as illustrated in Fig. 4.4. Even in a sample of signal MC, the amount of combinatorial background is large because of random combinations of the four final state particles. A kinematic constraint is applied on  $M_D$  to the nominal mass of  $D$  meson [14] and this improves the momentum resolution of the daughter particles.

#### 4.3.5 Selection of $B$ candidates

A  $D$  candidate is combined with a charged kaon (pion) track to form a  $B^+ \rightarrow DK^+$  ( $B^+ \rightarrow D\pi^+$ ) candidate. The signal candidates are identified using two kinematic variables, the energy difference  $\Delta E$  and the beam-constrained mass  $M_{bc}$ , which are defined as  $\Delta E = E_B - E_{\text{beam}}$  and  $M_{bc} = c^{-2}\sqrt{E_{\text{beam}}^2 - |\vec{\mathbf{p}}_B|^2c^2}$ , where  $E_B$  ( $\vec{\mathbf{p}}_B$ ) is the energy (momentum) of the  $B$  candidate and  $E_{\text{beam}}$  is the beam energy in the centre-of-mass frame. The distributions of correctly reconstructed events will peak at the nominal  $B$  meson mass in  $M_{bc}$  and zero in  $\Delta E$ . We select candidates that satisfy

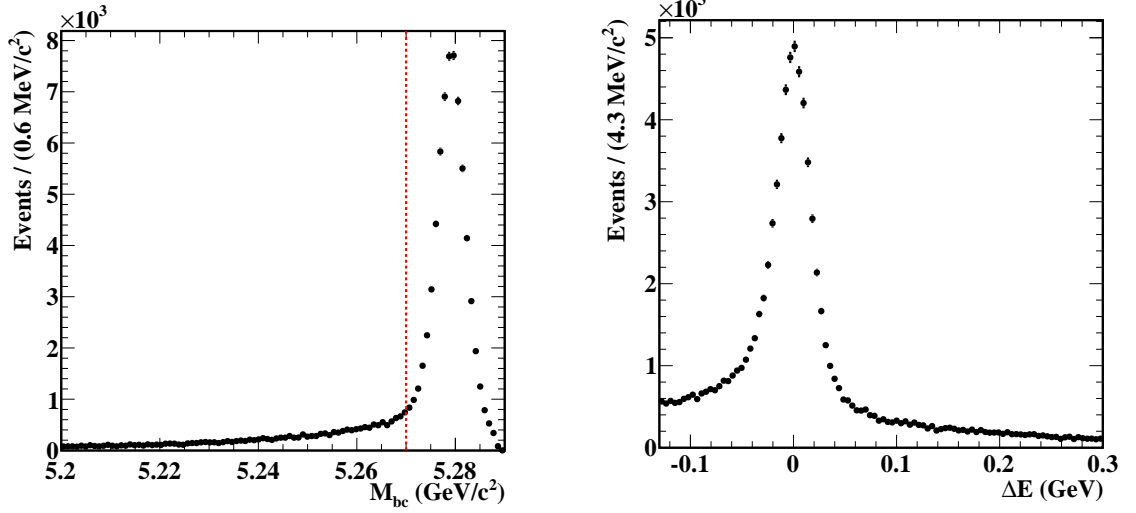


Figure 4.5:  $M_{bc}$  (left) and  $\Delta E$  (right) distributions in  $B^+ \rightarrow D(K_S^0 \pi^+ \pi^- \pi^0) K^+$  signal MC sample. The vertical dotted line indicates the selected region in  $M_{bc}$ .

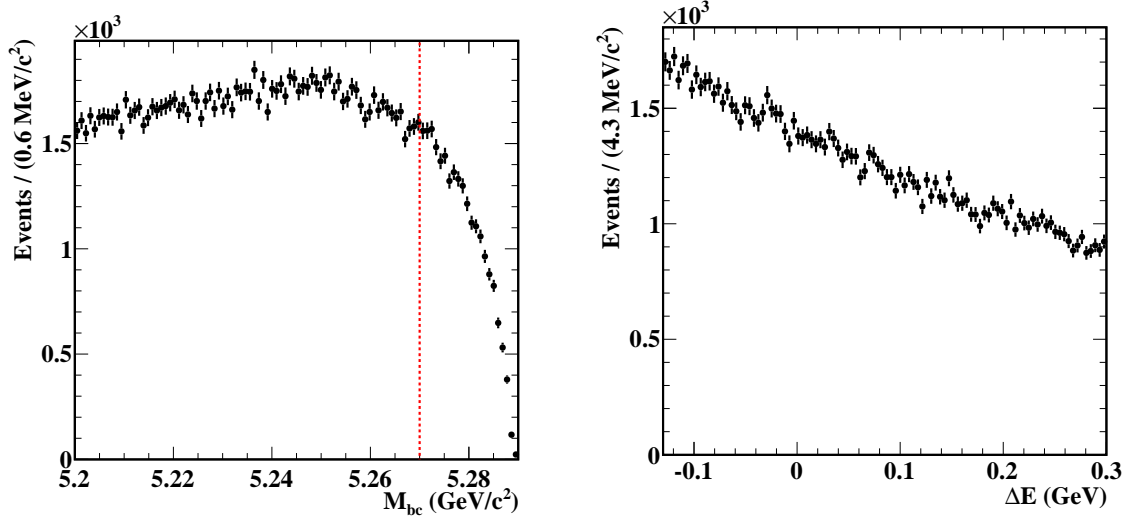


Figure 4.6:  $M_{bc}$  (left) and  $\Delta E$  (right) distributions in  $B^+ \rightarrow D(K_S^0 \pi^+ \pi^- \pi^0) K^+$  generic background MC sample. The vertical dotted line indicates the selected region in  $M_{bc}$ .

the criteria  $M_{bc} > 5.27 \text{ GeV}/c^2$  and  $-0.13 < \Delta E < 0.30 \text{ GeV}$ .  $\Delta E$  is a fit variable in our signal extraction procedure, hence sideband regions dominated by background are also included in the selection. The  $M_{bc}$  and  $\Delta E$  distributions of signal and generic background MC events are shown in Fig. 4.5 and 4.6, respectively. The asymmetric  $\Delta E$  window is chosen to avoid modelling the peaking structure appearing at lower values from partially reconstructed  $B^+ \rightarrow D^{(*)} K^{(*)+}$  decays when performing the likelihood fit to extract the signal. The  $B$  daughter particles are constrained to a common vertex point. The kinematic constraints on  $K_S^0$ ,  $\pi^0$ ,  $D$  and  $B^+$  improve the  $\Delta E$  resolution as illustrated in Fig. 4.7. To obtain the resolution, the  $\Delta E$  distribution is fitted with the

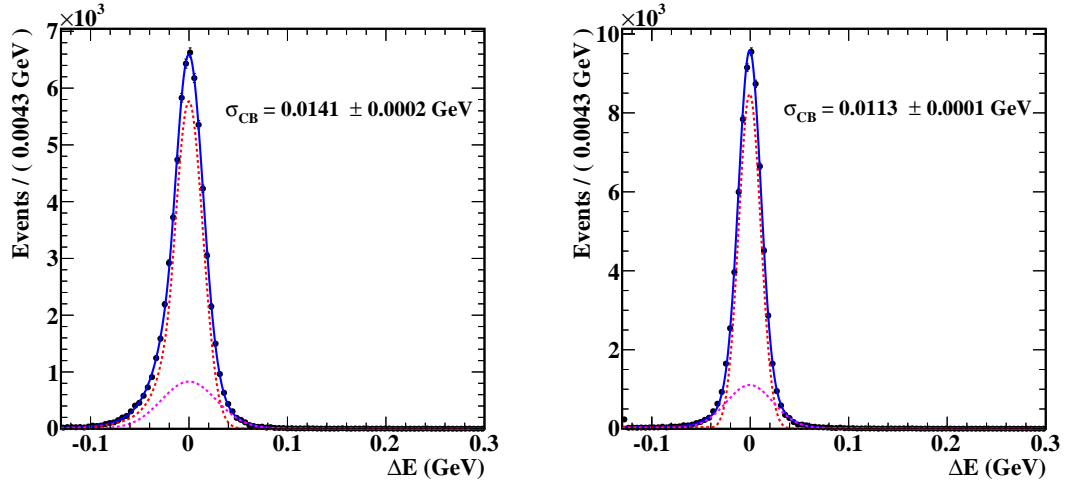


Figure 4.7:  $\Delta E$  distribution in the  $B^+ \rightarrow D(K_S^0 \pi^+ \pi^- \pi^0) K^+$  signal MC sample before applying any kinematic or vertex constraints (left) and after applying mass-vertex constraints on  $K_S^0$ ,  $\pi^0$  and  $D$  and vertex constraint on  $B^+$  (right). Black points with error bar are signal MC sample and blue solid curve represent the total fit.  $\sigma_{CB}$  is the resolution of the core Crystal Ball function shown by the red dotted curve. The double Gaussian is shown by the blue dotted curve.

sum of a Crystal Ball [75] and two Gaussian functions. There is  $\sim 20\%$  reduction in the width of the Crystal Ball function  $\sigma_{CB}$  after the fit.

### 4.3.6 Selection of $D^*$ candidates

A  $D$  candidate is combined with a charged pion track, which is not used in the  $D$  reconstruction, to obtain  $D^*$  meson candidates. These charged pion tracks have very low momentum ( $200 \text{ MeV}/c$ ), because of the limited phase space of the decay that results in it having lower momentum on average than other final-state particles, hence, they are referred to as “slow pions”. The momentum distribution of the slow pions is given in Fig. 4.8. Thus the SVD information is essential in identifying them. At least one hit in the SVD is required to reduce the slow-pion candidate multiplicity. Signal  $D^{*+}$  candidates are identified by the kinematic variables  $M_D$  and  $\Delta M$ , the difference in the invariant masses of  $D^{*+}$  and  $D$  meson candidates. For a correctly reconstructed event,  $\Delta M$  will peak at  $0.145 \text{ GeV}/c^2$ , the nominal mass difference [14]. The events that satisfy the criteria,  $1.80 < M_D < 1.95 \text{ GeV}/c^2$  and  $\Delta M < 0.15 \text{ GeV}/c^2$  are retained as shown in Fig. 4.9. A wide  $M_D$  range is selected for extracting the yields from a fit. The  $D$  and  $\pi^+$  candidates are constrained to come from a common vertex

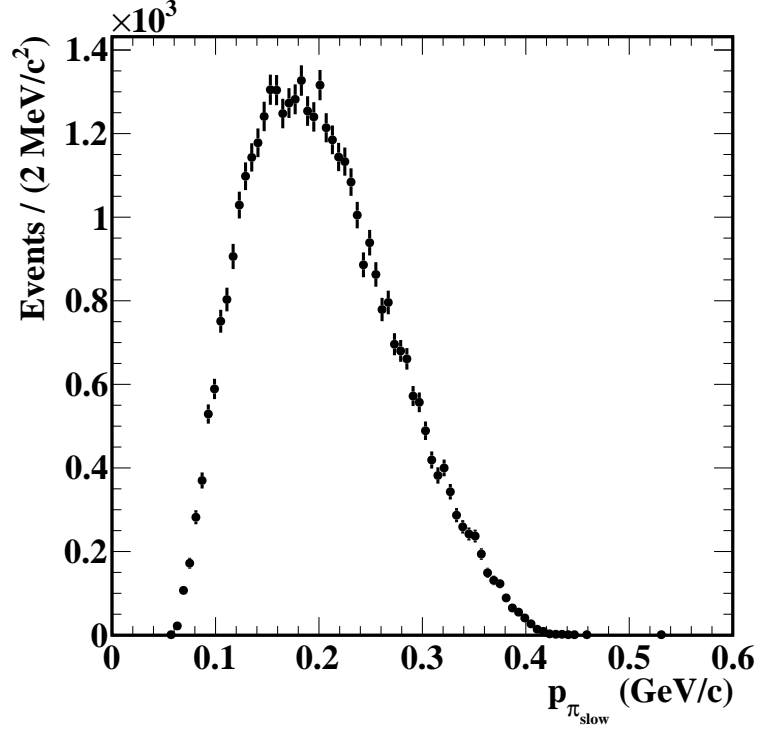


Figure 4.8: Slow pion momentum distribution in the  $D^{*+} \rightarrow D(K_S^0 \pi^+ \pi^- \pi^0) \pi^+$  signal MC sample.

point to ensure that they are products of  $D^{*+}$  decay. The  $D$  meson momentum in the laboratory frame is chosen to be between 1–4 GeV/c to approximately match the range of  $D$  momentum in the  $B^+ \rightarrow Dh^+$  ( $h = K/\pi$ ) sample, as illustrated in Fig. 4.10.

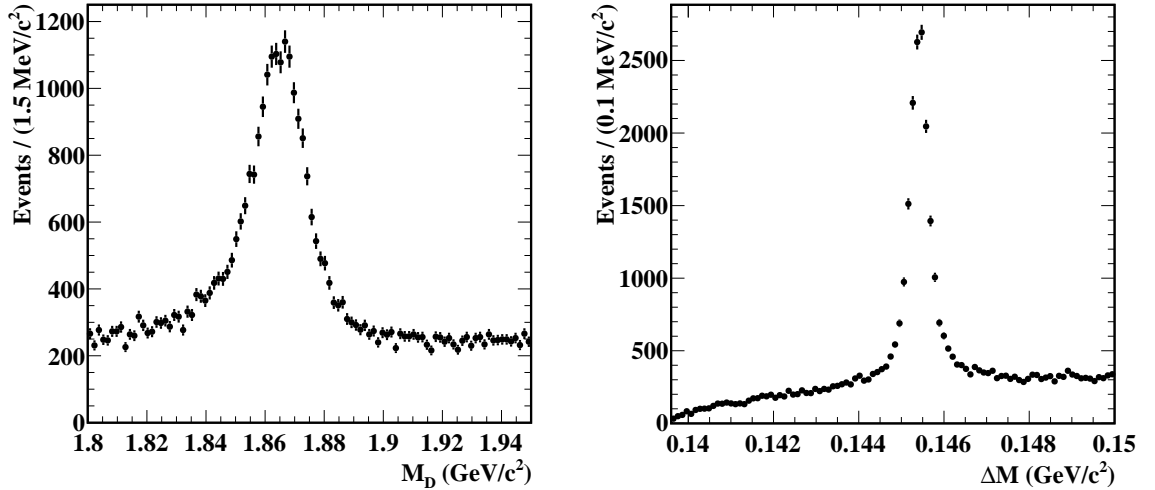


Figure 4.9:  $M_D$  (left) and  $\Delta M$  (right) distributions in  $D^{*+} \rightarrow D(K_S^0 \pi^+ \pi^- \pi^0) \pi_{\text{slow}}^+$  signal MC sample.

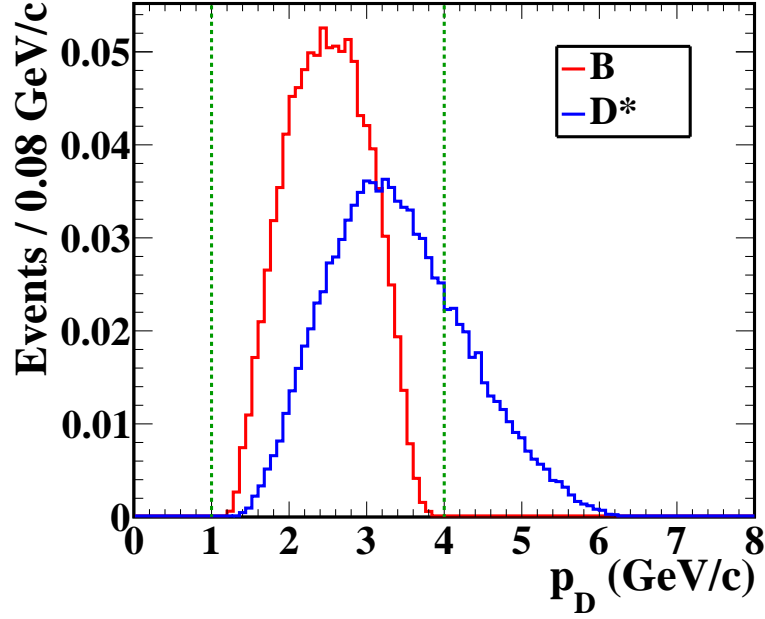


Figure 4.10:  $p_D$  distribution in the lab frame for (blue)  $D^{*+}$  and (red)  $B^+ \rightarrow Dh^+$  signal MC samples. The vertical dotted line indicates the selected region.

## 4.4 Background suppression

The data sample contains different types of backgrounds, even after applying the selection criteria as in Sec. 4.3. The main components are background due to misreconstruction of  $\pi^0$  candidates in the final state and for the  $B^+ \rightarrow Dh^+$  sample continuum events from  $e^+e^- \rightarrow q\bar{q}$  ( $q = u, d, s, c$ ). The following subsections discuss the suppression of these background components in detail.

### 4.4.1 Misreconstructed $\pi^0$ background

The presence of a  $\pi^0$  in the final state makes the reconstruction of the signal mode more challenging. Signal MC studies indicated that misreconstructed  $\pi^0$  events cause many misreconstructed signal events. These events are problematic because they are often reconstructed in the wrong bin in  $D$  phase space, hence they have to be removed. The helicity and shower-shape variables are studied for any possible background discrimination, but the distributions do not show any significant difference between the signal and background events. So the effect of changing the photon energy ( $E_\gamma$ ) threshold is analysed.

The studies on MC samples suggest that 98.5% of the events fall into the following

$\gamma_1$	$\gamma_2$	$E_{\gamma_1}$ (MeV)	$E_{\gamma_2}$ (MeV)	Fraction of candidates
Barrel	Barrel	70	65	0.70
FWD ec	Barrel	220	65	0.18
Barrel	BWD ec	65	95	0.09
FWD ec	FWD ec	150	210	0.02
Others	Others	50	50	0.01

Table 4.1: Optimized  $E_\gamma$  thresholds for the photon candidates.

four categories in terms of the detected position of the photon in the ECL:

1. both photons detected in the barrel,
2.  $\gamma_1$  detected in the forward endcap (FWD ec),  $\gamma_2$  in the barrel,
3.  $\gamma_1$  detected in the barrel and  $\gamma_2$  in the backward endcap (BWD ec), and
4. both photons detected in the FWD ec.

Here  $\gamma_1$  is defined as having higher energy than  $\gamma_2$ . The photon energy thresholds are optimized separately for photon candidates in the above mentioned four categories. In each category a two-dimensional optimization is performed for both the photons. This is done by maximizing the significance  $S/\sqrt{S+B}$ , where  $S$  and  $B$  are the number of signal and background events selected from MC samples in the signal region, respectively. The signal region used while performing the optimization of the selection is  $|\Delta E| < 0.05$  GeV. The significance and efficiency distributions in the four categories are given in Figs 4.11, 4.12, 4.13 and 4.14. The optimized selection criteria are given in Table 4.1. The preselection energy threshold of 50 MeV is applied on the 1.5% of five other combinations of photon positions.

The optimization is repeated after applying the selection on the NN output to reject the continuum background events (in Sec. 4.4.2) and consistent results are obtained. This selection rejects 70% of the background, while 27% signal is lost.

There is no selection criteria applied on the momentum of  $\pi^0$  ( $p_{\pi^0}$ ), as this could possibly bias the phase space acceptance, especially in bin 1 with low momentum  $\pi^0$  coming from  $\omega$  resonance. A comparison study between  $E_\gamma$  selection and  $p_{\pi^0}$  selection is done in  $B^+ \rightarrow D(K_S^0 \omega(\pi^+ \pi^- \pi^0)) K^+$  signal MC sample. As illustrated in Fig 4.15, the efficiency loss is less with an  $E_\gamma$  criterion than with a  $p_{\pi^0}$  selection. The signal

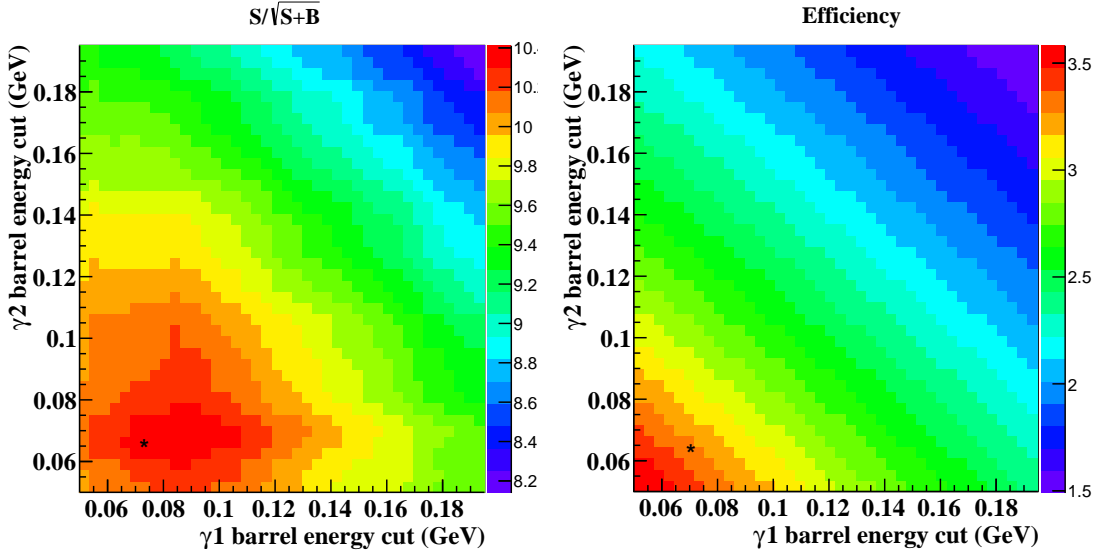


Figure 4.11:  $S/\sqrt{S+B}$  and efficiency distributions after the two dimensional optimization of the photon energy requirements in the MC sample for events with both the photons coming from barrel region of the ECL. The black point shows the optimized requirement.

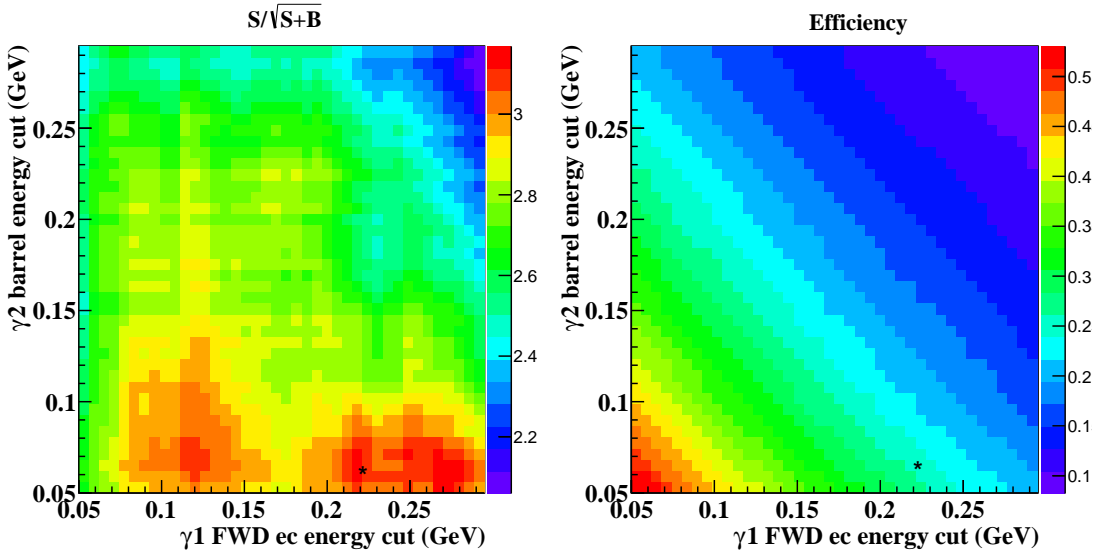


Figure 4.12:  $S/\sqrt{S+B}$  and efficiency distributions after the two dimensional optimization of the photon energy requirements in the MC sample for events with one photon coming from FWD endcap and the other from barrel regions of the ECL. The black point shows the optimized requirement.

significance for  $E_\gamma$  selection is better than that for  $p_{\pi^0}$  selection, which is shown in Fig 4.15.

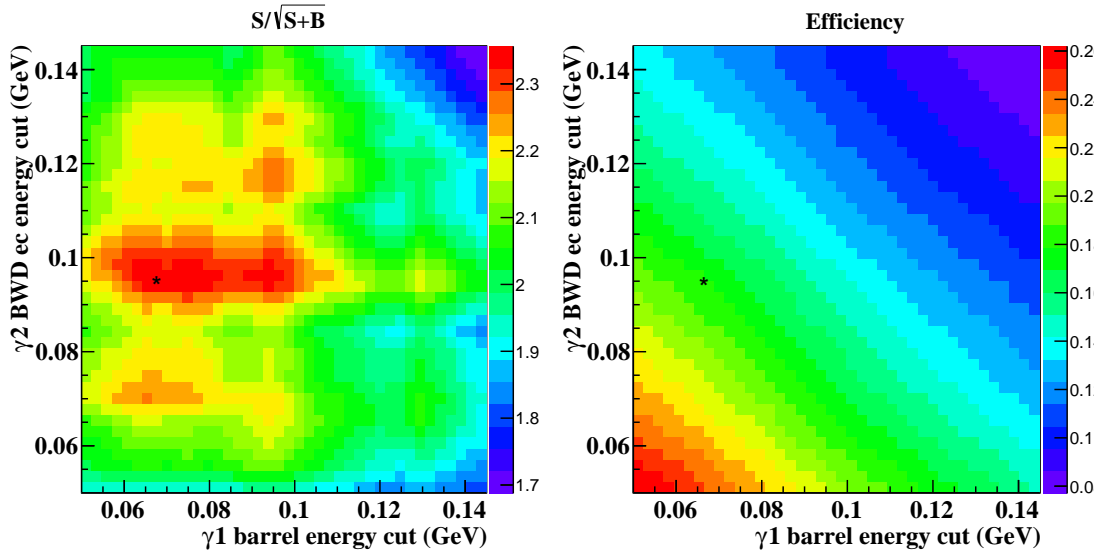


Figure 4.13:  $S/\sqrt{S+B}$  and efficiency distributions after the two dimensional optimization of the photon energy requirements in the MC sample for events with both one photon coming from barrel and the other from BWD end-cap regions of the ECL. The black point shows the optimized requirement.

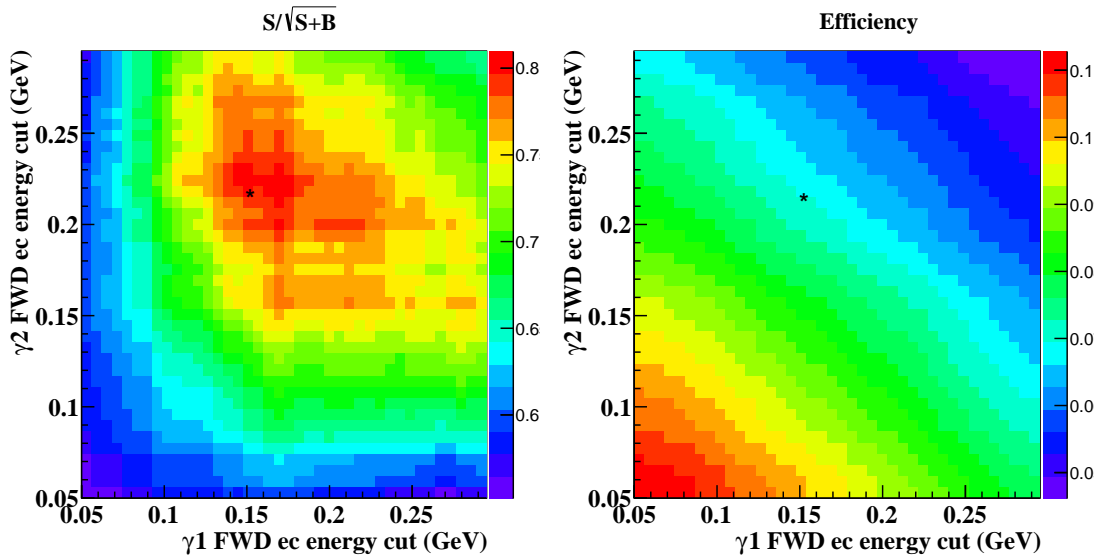


Figure 4.14:  $S/\sqrt{S+B}$  and efficiency distributions after the two dimensional optimization of the photon energy requirements in the MC sample for events with both the photons coming from FWD endcap region of the ECL. The black point shows the optimized requirement.

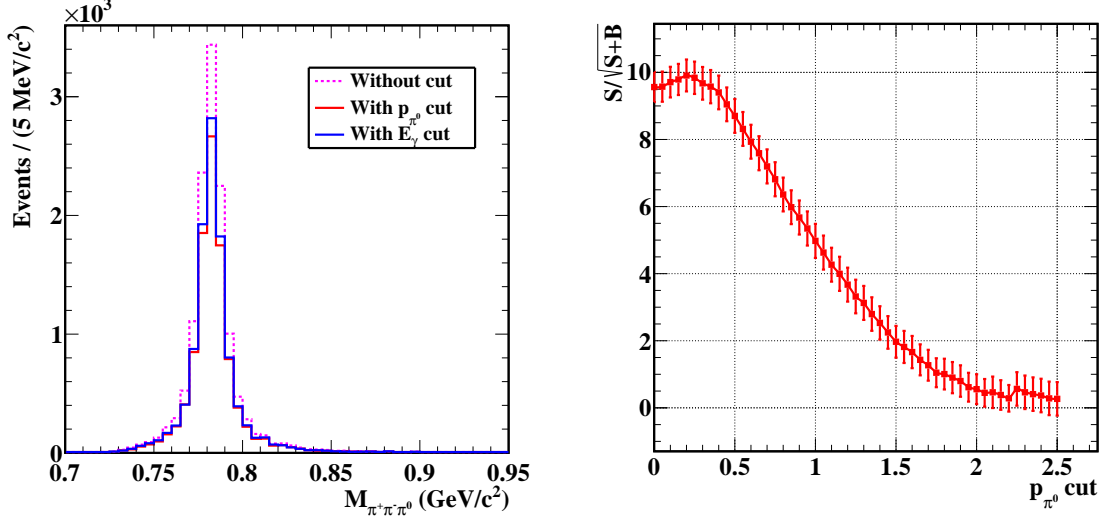


Figure 4.15:  $\pi^+\pi^-\pi^0$  invariant mass distribution with  $p_{\pi^0} > 0.3$  GeV/c and with optimized  $E_\gamma$  threshold criteria in  $B^+ \rightarrow D(K_S^0\omega(\pi^+\pi^-\pi^0))K^+$  signal MC sample (left) and the  $S/\sqrt{S+B}$  distribution with different  $p_{\pi^0}$  selection criteria

#### 4.4.2 Continuum background

The dominant background for any  $B$  meson decay is due to the  $e^+e^- \rightarrow q\bar{q}$  continuum processes. Differences in the event topology between  $B$  meson pairs and continuum events are used to suppress this background. The  $B$  meson pairs produced from the decay of the  $\Upsilon(4S)$  are almost at rest in the centre-of-mass frame, because the available energy is just above the threshold to form a  $B\bar{B}$  pair. As  $B$  mesons have spin zero, there is no preferred direction in space for the decay products. Thus the  $B\bar{B}$  events follow a uniform spherical topology. But lighter-quark pairs are produced with large initial momentum and hence two back-to-back jets are formed in an event. This is illustrated in Fig. 4.16. Other variables related to the displaced vertices and associated leptons/kaons in the other  $B$  are also used to improve the background rejection. An algorithm based on a NN [85] with eight input variables is used to separate the two event types. The most discriminating input variable is the likelihood ratio obtained via Fisher discriminants [87] formed from modified Super-Fox-Wolfram moments [88, 89]. The Fox-Wolfram moment is defined as

$$H_l = \sum_{i,j} |p_i||p_j|P_l(\cos\theta_{ij}), \quad (4.4)$$

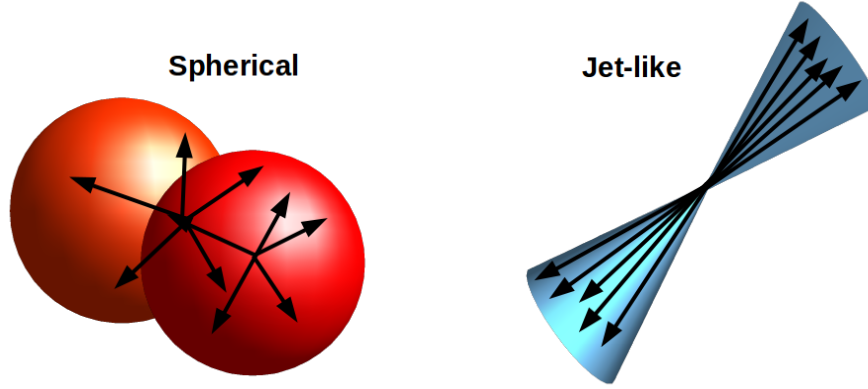


Figure 4.16: The event topology of  $e^+e^- \rightarrow \Upsilon(4S) \rightarrow B\bar{B}$  (left) and  $e^+e^- \rightarrow q\bar{q}$  (right) events.

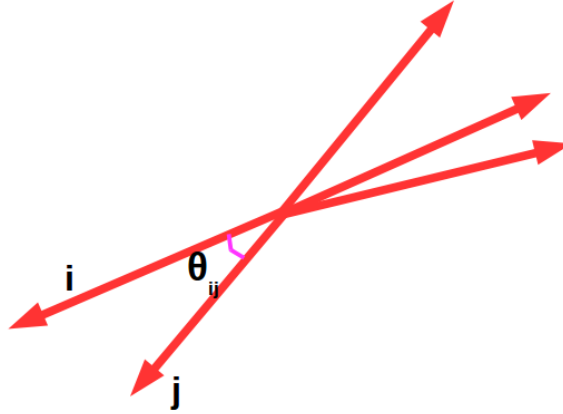


Figure 4.17: Directions of momenta of particles  $i$  and  $j$  in an event and the angle between them,  $\theta_{ij}$ .

where  $p_i$  and  $p_j$  are the momenta of the  $i^{\text{th}}$  and  $j^{\text{th}}$  particle in the event,  $P_l$  is  $l^{\text{th}}$  order Legendre polynomial and  $\theta_{ij}$  is the angle between the momenta of particles  $i$  and  $j$  as illustrated in Fig. 4.17. The ratios of these moments can describe the event topology in  $e^+e^-$  collisions. Modified Super-Fox-Wolfram moments are defined based on these ratios and energy (or mass) of any missing particle in the event. These moments are correlated, hence Fisher discriminants [87] are constructed taking into account the correlations between them. The likelihood ratio (LR) output formed from these Fisher discriminants varies from 0 to 1 depending on whether the event is continuum-like or  $B\bar{B}$ -like. The parameters used to define the LR are determined from signal and continuum MC samples. The LR distribution in the MC sample is shown in Fig. 4.18.

The absolute value of the cosine of the angle between the  $B$  candidate and the beam axis in the  $e^+e^-$  centre-of-mass frame, denoted as  $|\cos\theta_B|$ , is used as one of

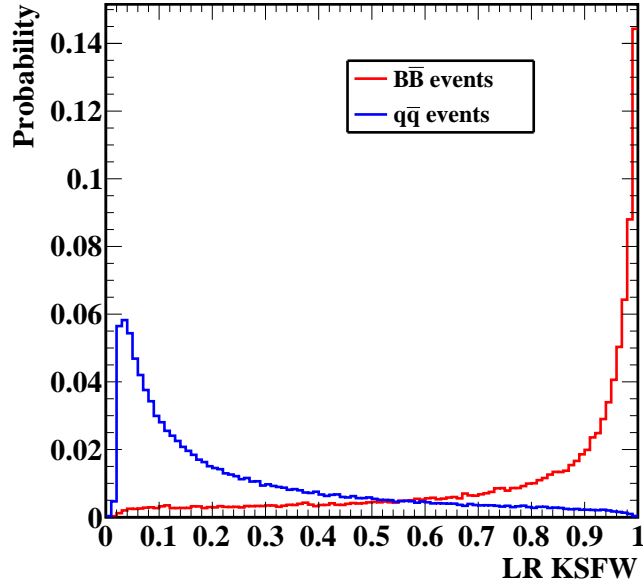


Figure 4.18: Distribution of the likelihood ratio formed from the Fisher discriminants in MC sample. The red and blue histograms show  $B\bar{B}$  and  $q\bar{q}$  events, respectively.

the input variables. The  $\cos\theta_B$  distribution for  $B\bar{B}$  events follows  $1 - \cos^2\theta$  function because of conservation of angular momentum in the decay of the  $\Upsilon(4S)$ , which is a vector meson produced with its spin along the beam direction.  $B$  candidates formed from random combinations of tracks in continuum events have a uniform distribution in  $\cos\theta_B$ . Another important angular variable is the absolute value of the cosine of the angle between the thrust axis of the  $B$  candidate and that of the rest of the event in centre-of-mass frame, where the thrust axis is oriented in such a way that the sum of momentum projections is maximized. The variable is denoted as  $|\cos\theta_T|$  and it peaks at one for continuum events and is uniform for  $B\bar{B}$  events. This is because  $B$  mesons decay isotropically and will have a random thrust direction, resulting in a flat  $|\cos\theta_T|$  distribution. The continuum events have collinear thrust axes and hence  $|\cos\theta_T|$  peaks at one. The distributions are given in Fig. 4.19.

The separation between the decay vertices of the two  $B$  candidates along the  $z$ -axis [90] also aids the event type separation. If the event contains a  $B\bar{B}$  pair, then the vertex separation ( $\Delta z$ ) is large due to the longer lifetime of  $B$  mesons. So the  $\Delta z$  distribution will be broader for  $B\bar{B}$  events than continuum events. The information on the other  $B$  in the event is obtained from the flavour tagging [91] algorithm. This algorithm uses the charges of the following particles as input: high-momentum leptons

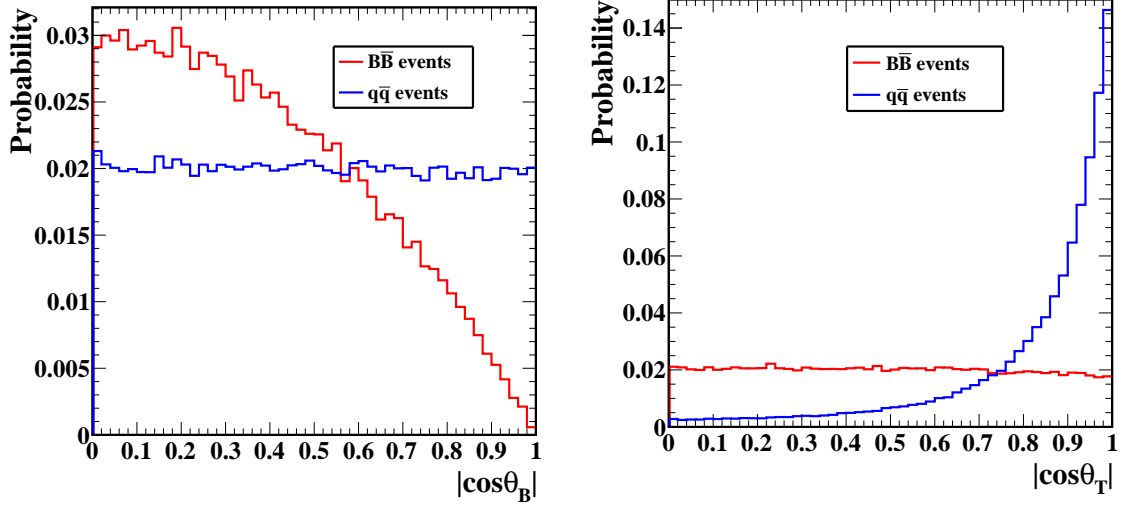


Figure 4.19:  $|\cos \theta_B|$  (left) and  $|\cos \theta_T|$  (right) distributions in MC sample. The red and blue histograms show  $B\bar{B}$  and  $q\bar{q}$  events, respectively.

from  $B^0 \rightarrow Xl^+\nu$  decays, kaons, intermediate momentum leptons from  $\bar{b} \rightarrow \bar{c} \rightarrow \bar{s}l^-\bar{\nu}$  decays, high momentum pions coming from  $B^0 \rightarrow D^{(*)}\pi^+X$  decays, slow pions from  $B^0 \rightarrow D^{*-}X$ ,  $D^{*-} \rightarrow \bar{D}^0\pi^-$  decays, and  $\bar{\Lambda}$  baryons from the cascade decay  $\bar{b} \rightarrow \bar{c} \rightarrow \bar{s}$ . This is also an important input variable to the NN. Its absolute value is denoted as  $|qr|$ , where  $q$  is the  $B$  flavour and  $r$  the quality of tagging. Additional information about the rest of the event gives more discriminating power to the NN. The difference between the sum of the charges of particles in the hemisphere about the  $D$  meson flight direction and the one in the opposite hemisphere in the centre-of-mass frame, excluding the particles used for the reconstruction of  $B$  is one such useful variable, denoted as  $\Delta Q$ . This gives zero for a  $B\bar{B}$  event and non-zero for continuum events because of the spherical and jet topologies of the events, respectively. The product of the charge of the signal  $B$  and the sum of the charges of all kaons not used for reconstruction of  $B$ , denoted as  $Q_B Q_K$ , is another input variable. The distribution is likely to peak below zero for  $B\bar{B}$  events, as the  $B$  meson tends to produce the  $K$  meson of the same charge. It peaks at zero for continuum events. The cosine of the angle between the  $D$  direction and the opposite direction to  $\Upsilon(4S)$  in the  $B$  rest frame, denoted as  $\cos \theta_B^D$ , is also used. It can distinguish  $B\bar{B}$  and continuum events to some extent. The distributions of these input variables in MC sample are given in Fig. 4.20 and 4.21.

Signal and continuum MC samples of 100,000 events each are used to train the NN. Independent MC samples are used to check its performance and that it is not over-trained *i.e.* the NN is not picking up possible unique properties of the training sample.

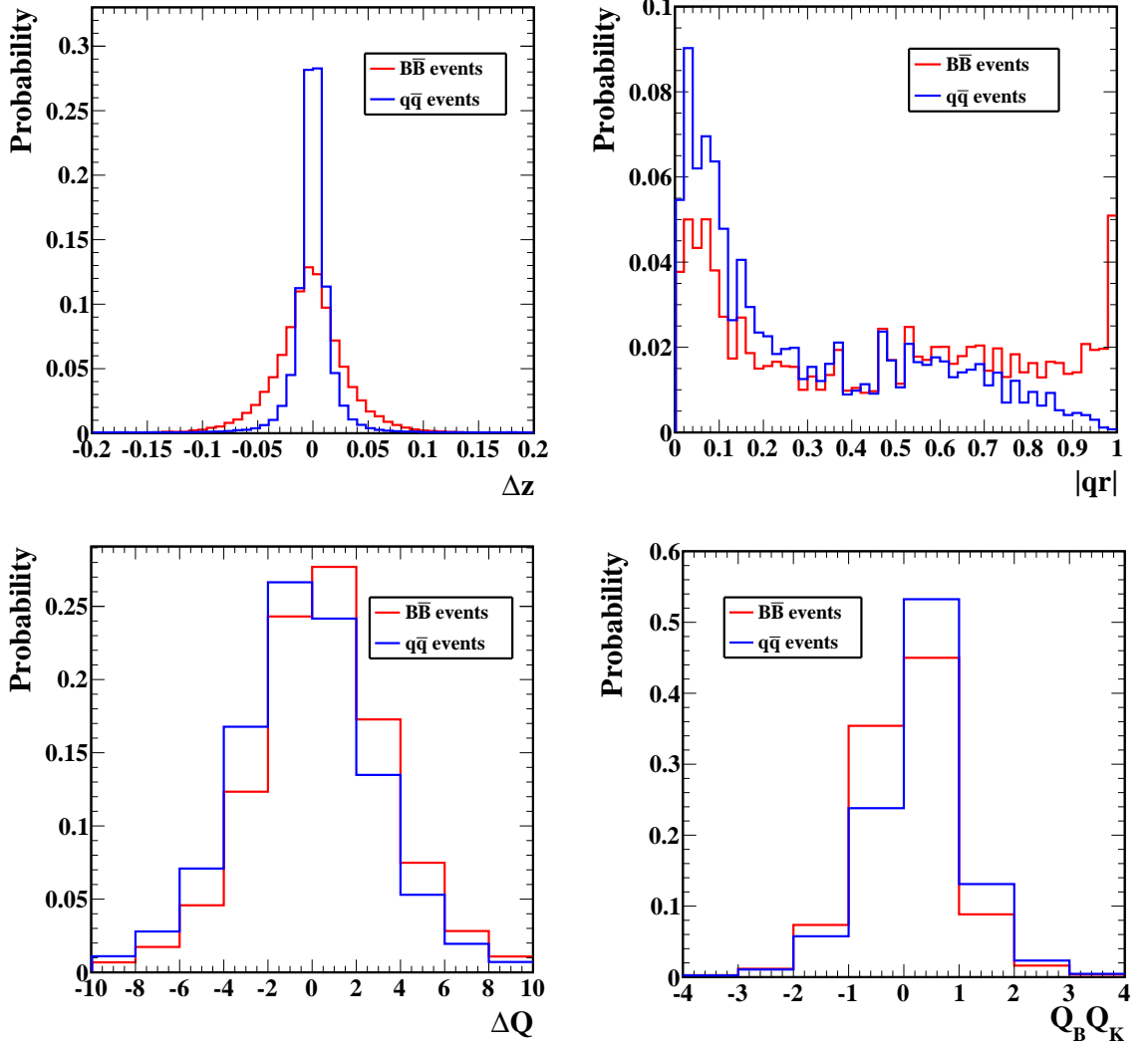


Figure 4.20:  $\Delta z$  ( top left),  $|qr|$  (top right),  $\Delta Q$  (bottom left) and  $Q_B Q_K$  (bottom right) distributions in MC sample. The red and blue histograms show  $B\bar{B}$  and  $q\bar{q}$  events, respectively.

The output peaks at  $-1$  for continuum and  $1$  for  $B\bar{B}$  events as shown in Fig 4.22. The relative importance of the eight input variables are given in Table 4.2. The signal efficiency vs. background rejection performance of the NN is illustrated in the receiver operating characteristic (ROC) curve in Fig. 4.23. It is evident that the use of NN with eight input variables improves the background rejection capacity significantly (at most 10%) when compared to using the LR variable alone. The NN provides 95% background reduction with 20% loss in signal.

The NN output  $C_{NN}$  is required to be greater than  $-0.6$ , this reduces the continuum background by 67% with the loss of only 5% of the signal. The value of  $C_{NN}$  is then

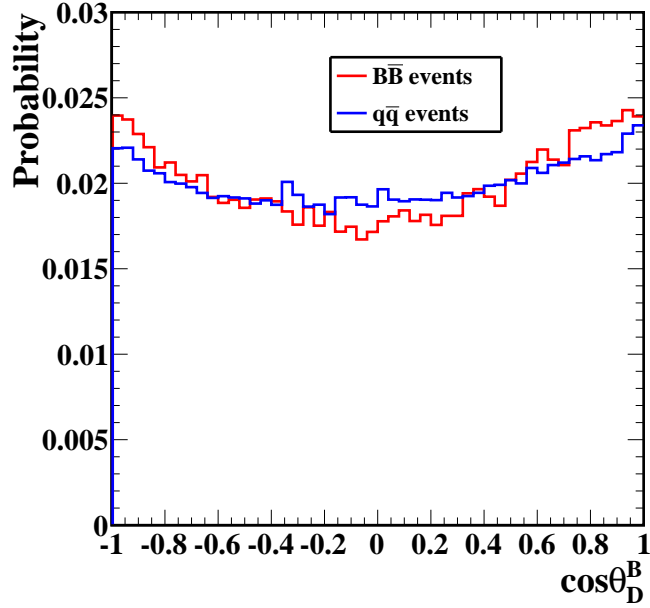


Figure 4.21:  $\cos \theta_D^B$  distribution in MC sample. The red and blue histograms show  $B\bar{B}$  and  $q\bar{q}$  events, respectively.

Rank	variable	only this ( $\sigma$ )	without this ( $\sigma$ )	correlation to others
1	LR KSFW	357	160	0.77
2	$\Delta z$	189	94	0.27
3	$ \cos \theta_B $	129	59	0.23
4	$ \cos \theta_T $	299	50	0.74
5	$ qr $	143	37	0.36
6	$Q_B Q_K$	74	24	0.23
7	$\Delta Q$	43	7	0.13
8	$\cos \theta_B^D$	10	2	0.13

Table 4.2: Input variables of NN ranked according to their significance ( $\sigma$ ) . Here  $\sigma$  is defined as the linear-correlation factor multiplied by  $\sqrt{n}$ , where  $n$  is the sample size.

transformed as

$$C'_{\text{NN}} = \log \left( \frac{C_{\text{NN}} - C_{\text{NN low}}}{C_{\text{NN high}} - C_{\text{NN}}} \right), \quad (4.5)$$

where  $C_{\text{NN low}} = -0.6$  and  $C_{\text{NN high}} = 0.9985$  are the minimum and maximum values of  $C_{\text{NN}}$  in the samples used, respectively. The transformation allows an analytic model for the PDFs to describe the  $C'_{\text{NN}}$  distributions while performing signal extraction, which is not possible for  $C_{\text{NN}}$ . The distribution of  $C'_{\text{NN}}$  is given in Fig. 4.22.

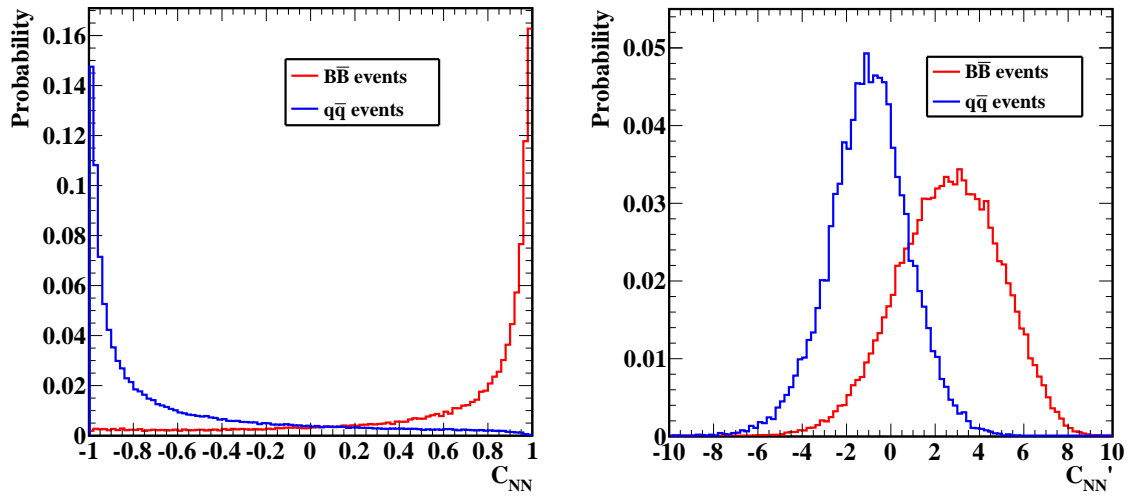


Figure 4.22:  $C_{NN}$  (left) and  $C'_{NN}$  (right) distributions in the MC samples. The red and blue histograms show  $B\bar{B}$  and  $q\bar{q}$  events, respectively.

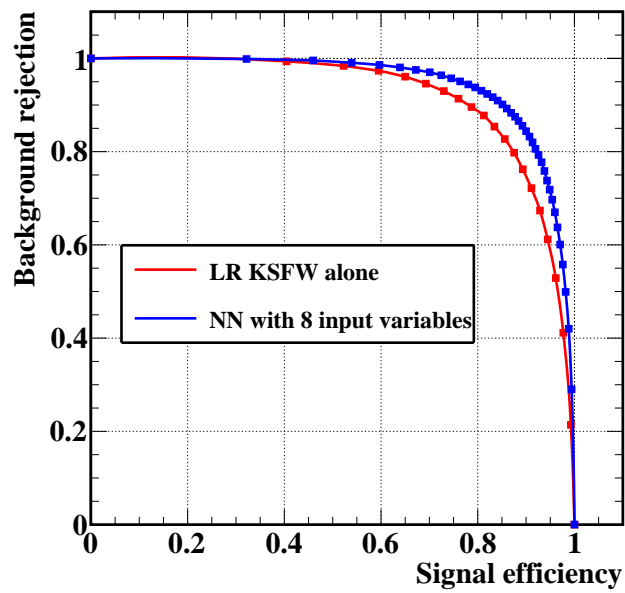


Figure 4.23: ROC curve demonstrating the signal efficiency *vs.* background rejection of the NN. The performance of the LR is also shown in red solid line.

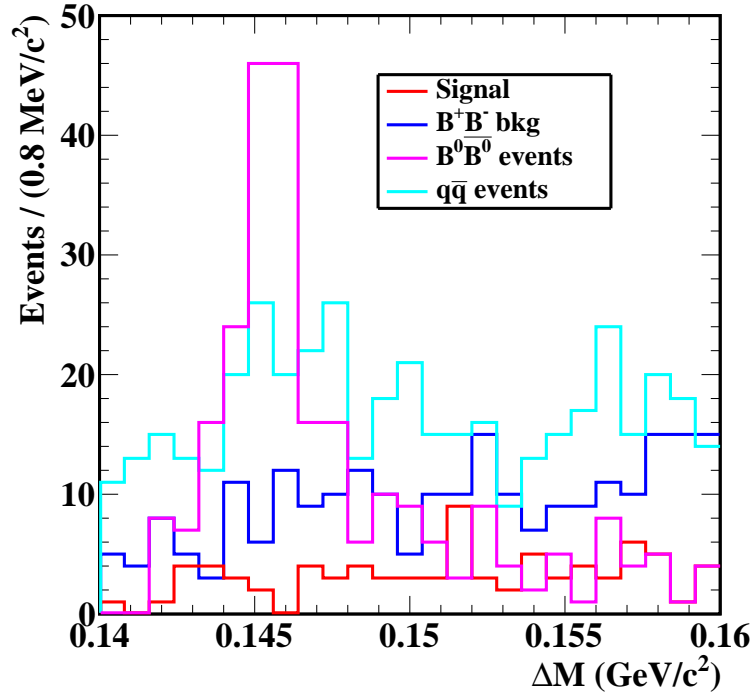


Figure 4.24: The  $\Delta M$  distribution in  $B^+ \rightarrow D(K_S^0\pi^+\pi^-\pi^0)K^+$  generic MC sample. The range is zoomed in near to 0.145 GeV/c.

#### 4.4.3 Background from $D^*$ events

There is possible background in the  $B$  sample due to  $D$  events originating from  $D^* \rightarrow D\pi$  decays. This can be vetoed by applying an appropriate selection on the  $\Delta M$  variable. The  $D^*$  candidates are reconstructed from a  $D$  and a  $\pi$  candidate that is not used in the reconstruction of the  $B$  candidate. If there are more than one such  $\pi$  candidate, then the one that gives a  $\Delta M$  value closest to 0.142 GeV is chosen. The  $\Delta M$  distribution is shown in Fig. 4.24. The amount of background seen in generic MC is very small (3%) and hence no selection criteria is applied.

### 4.5 Multiplicity and best-candidate selection

There are multiple  $B^+$  or  $D^{*+}$  candidates in an event due to different combinations of the final state particles that satisfy the selection criteria. The multiplicity distribution, after applying all the selection criteria, for  $B^+$  and  $D^{*+}$  candidates in the respective samples are shown in Fig. 4.25. The average multiplicity is 1.3 and 1.6 for  $B^+$  and  $D^{*+}$  candidates, respectively. A best-candidate selection (BCS) is performed in each event

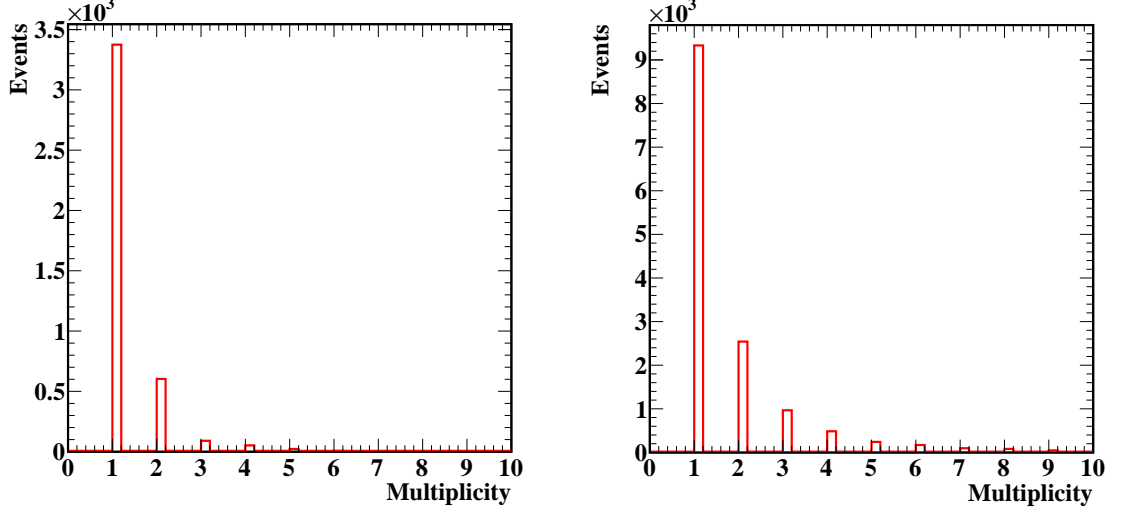


Figure 4.25:  $B^+$  (left) and  $D^{*+}$  (right) candidate multiplicities after applying all the selection criteria in  $B^+ \rightarrow D(K_S^0 \pi^+ \pi^- \pi^0) K^+$  and  $D^{*+} \rightarrow D(K_S^0 \pi^+ \pi^- \pi^0) \pi^+$  signal MC samples, respectively.

to avoid double counting.

Different metrics involving  $M_{bc}$ ,  $M_D$  and  $M_{\pi^0}$  are studied for the BCS in the  $B$  sample. The resolutions of these distributions are obtained from signal MC samples as shown in Fig. 4.26 and 4.27. The effective resolution is 2.6 MeV, 9.2 MeV and 4.2 MeV for  $M_{bc}$ ,  $M_D$  and  $M_{\pi^0}$ , respectively. The different metrics and the corresponding efficiencies are shown in Table 4.3.

BCS metric	$\epsilon$ (%)
$\left(\frac{M_{bc} - M_B^{\text{PDG}}}{\sigma_{M_{bc}}}\right)^2$	$74.5 \pm 0.5$
$\left(\frac{M_D - M_D^{\text{PDG}}}{\sigma_{M_D}}\right)^2$	$75.4 \pm 0.5$
$\left(\frac{M_{bc} - M_B^{\text{PDG}}}{\sigma_{M_{bc}}}\right)^2 + \left(\frac{M_D - M_D^{\text{PDG}}}{\sigma_{M_D}}\right)^2$	$79.3 \pm 0.5$
$\left(\frac{M_{bc} - M_B^{\text{PDG}}}{\sigma_{M_{bc}}}\right)^2 + \left(\frac{M_{\pi^0} - M_{\pi^0}^{\text{PDG}}}{\sigma_{M_{\pi^0}}}\right)^2$	$77.2 \pm 0.5$
$\left(\frac{M_D - M_D^{\text{PDG}}}{\sigma_{M_D}}\right)^2 + \left(\frac{M_{\pi^0} - M_{\pi^0}^{\text{PDG}}}{\sigma_{M_{\pi^0}}}\right)^2$	$77.3 \pm 0.5$
$\left(\frac{M_{bc} - M_B^{\text{PDG}}}{\sigma_{M_{bc}}}\right)^2 + \left(\frac{M_D - M_D^{\text{PDG}}}{\sigma_{M_D}}\right)^2 + \left(\frac{M_{\pi^0} - M_{\pi^0}^{\text{PDG}}}{\sigma_{M_{\pi^0}}}\right)^2$	$80.4 \pm 0.5$
$\left(\frac{M_{bc} - M_B^{\text{PDG}}}{\sigma_{M_{bc}}}\right)^2 + \chi^2(\pi^0)$	$77.0 \pm 0.5$
$\left(\frac{M_{bc} - M_B^{\text{PDG}}}{\sigma_{M_{bc}}}\right)^2 + \left(\frac{M_D - M_D^{\text{PDG}}}{\sigma_{M_D}}\right)^2 + \chi^2(\pi^0)$	$79.9 \pm 0.5$

Table 4.3: Different BCS metrics with the corresponding efficiencies. Here  $\chi^2(\pi^0)$  is the  $\chi^2$  of the mass-vertex fit on  $\pi^0$ .

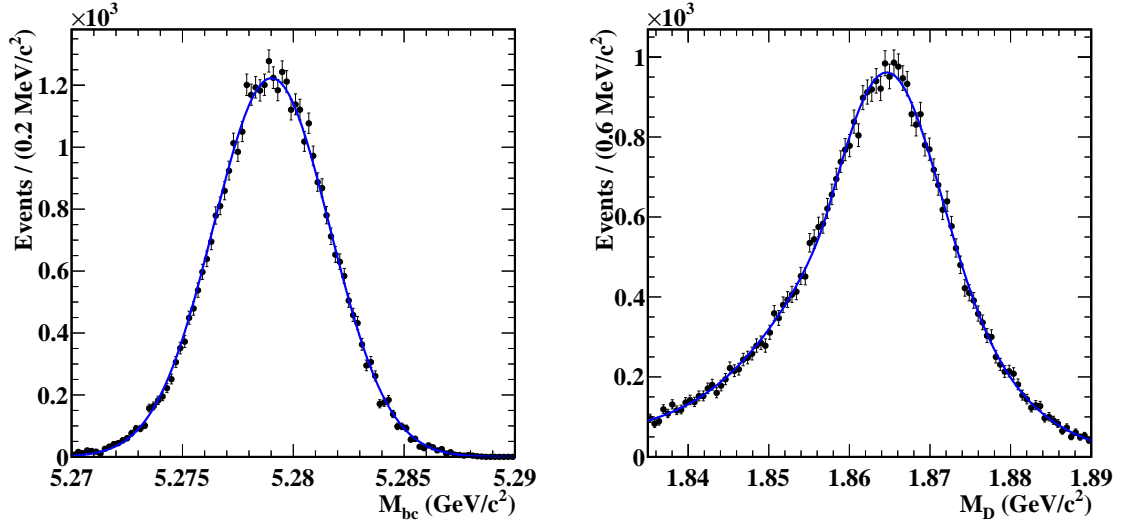


Figure 4.26:  $M_{bc}$  (left) and  $M_D$  (right) distributions in  $B^+ \rightarrow D(K_S^0 \pi^+ \pi^- \pi^0) K^+$  signal MC sample. Black points with error bar are data and blue solid line is the fit model.

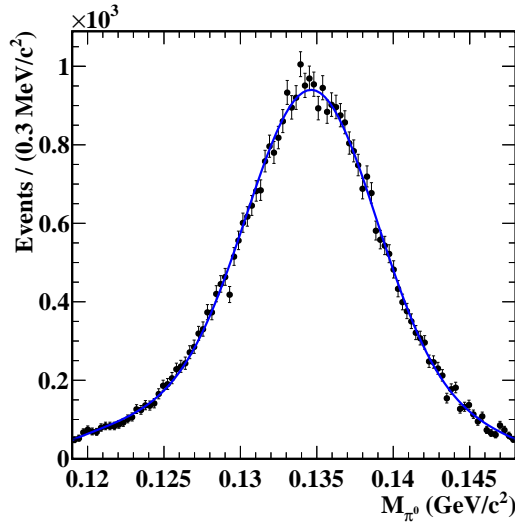


Figure 4.27:  $M_{\pi^0}$  distribution in  $B^+ \rightarrow D(K_S^0 \pi^+ \pi^- \pi^0) K^+$  signal MC sample. Black points with error bar are data and blue solid line is the fit model.

The metric  $\left(\frac{M_{bc} - M_B^{\text{PDG}}}{\sigma_{M_{bc}}}\right)^2 + \left(\frac{M_D - M_D^{\text{PDG}}}{\sigma_{M_D}}\right)^2 + \left(\frac{M_{\pi^0} - M_{\pi^0}^{\text{PDG}}}{\sigma_{M_{\pi^0}}}\right)^2$ , which has the highest efficiency, is chosen. The best-candidate selection in the  $D^*$  sample is performed with the  $\chi^2$  of the  $D^*$  vertex fit as the metric, which has a BCS efficiency of 69%.

Resonance	Branching fraction (%)
Non-resonant $D \rightarrow K^0 \pi^+ \pi^- \pi^0$	2.6
$K^0 \omega, \omega \rightarrow \pi^+ \pi^- \pi^0$	2.0
$K^0 \eta, \eta \rightarrow \pi^+ \pi^- \pi^0$	0.2
$K^{*-} \rho^+, K^{*-} \rightarrow K^0 \pi^-, \rho^+ \rightarrow \pi^+ \pi^0$	4.3
$K^{*0} \rho^0, K^{*0} \rightarrow K^0 \pi^0, \rho^0 \rightarrow \pi^+ \pi^-$	0.4
$K^{*0} \pi^+ \pi^-, K^{*0} \rightarrow K^0 \pi^0$	0.4
$K_1^- \pi^+, K_1^- \rightarrow K^0 \pi^- \pi^0$	0.4

Table 4.4: Different contributions to  $D \rightarrow K_S^0 \pi^+ \pi^- \pi^0$  final state used in signal MC generation [14].

Bin	$\epsilon$ (%)			
	$B^+ \rightarrow D\pi^+$	$B^- \rightarrow D\pi^-$	$B^+ \rightarrow DK^+$	$B^- \rightarrow DK^-$
1	$4.43 \pm 0.06$	$4.35 \pm 0.06$	$3.77 \pm 0.05$	$3.84 \pm 0.05$
2	$6.15 \pm 0.08$	$5.47 \pm 0.04$	$5.44 \pm 0.07$	$5.01 \pm 0.04$
3	$5.55 \pm 0.05$	$5.55 \pm 0.10$	$4.97 \pm 0.04$	$4.88 \pm 0.10$
4	$5.29 \pm 0.11$	$5.17 \pm 0.09$	$4.55 \pm 0.10$	$4.63 \pm 0.09$
5	$5.47 \pm 0.10$	$4.53 \pm 0.11$	$4.89 \pm 0.10$	$4.28 \pm 0.10$
6	$5.46 \pm 0.10$	$5.04 \pm 0.09$	$4.68 \pm 0.09$	$4.28 \pm 0.09$
7	$5.64 \pm 0.18$	$5.29 \pm 0.14$	$4.92 \pm 0.16$	$4.66 \pm 0.14$
8	$5.75 \pm 0.20$	$5.56 \pm 0.22$	$5.36 \pm 0.19$	$4.77 \pm 0.20$
9	$4.87 \pm 0.15$	$4.83 \pm 0.14$	$4.64 \pm 0.14$	$4.21 \pm 0.13$

Table 4.5: Efficiency of  $B^\pm \rightarrow D(K_S^0 \pi^+ \pi^- \pi^0) \pi^\pm$  and  $B^\pm \rightarrow D(K_S^0 \pi^+ \pi^- \pi^0) K^\pm$  samples in bins of  $D$  phase space.

## 4.6 Efficiency and migration

The reconstruction efficiency in the  $D$  phase space bins and the migration matrix have been calculated from four million signal MC events generated assuming various intermediate resonance contributions in  $D$  decay as listed in Table 4.4. Also  $\mathcal{B}(K^0 \rightarrow K_S^0) = 50\%$  is incorporated. The efficiency in the full phase space is 5.6% and 4.1% respectively, for  $B^+ \rightarrow D\pi^+$  and  $B^+ \rightarrow DK^+$  samples. The bin-efficiencies, after all the selection and best-candidate selection, are given in Table 4.5.

Four million signal MC events of  $D^{*+} \rightarrow D(K_S^0 \pi^+ \pi^- \pi^0) \pi^+$  are generated considering the different resonance contributions given in Table 4.4. The overall selection efficiency for sample is 3.7%. The determined efficiency values in the nine  $D$  phase space bins are given in Table 4.6.

Bin	$\epsilon$ (%)	
	$D^{*+} \rightarrow D^0 \pi^+$	$D^{*-} \rightarrow \bar{D}^0 \pi^-$
1	$3.07 \pm 0.06$	$3.02 \pm 0.06$
2	$3.77 \pm 0.05$	$4.83 \pm 0.09$
3	$5.66 \pm 0.14$	$3.66 \pm 0.05$
4	$3.60 \pm 0.11$	$3.72 \pm 0.12$
5	$3.77 \pm 0.14$	$3.38 \pm 0.11$
6	$3.71 \pm 0.11$	$3.45 \pm 0.11$
7	$3.87 \pm 0.17$	$4.03 \pm 0.19$
8	$3.36 \pm 0.24$	$3.53 \pm 0.21$
9	$3.32 \pm 0.16$	$3.21 \pm 0.16$

Table 4.6: Efficiency in each bin of the  $D$  phase space estimated from the  $D^{*\pm} \rightarrow D(K_S^0 \pi^+ \pi^- \pi^0) \pi^\pm$  signal MC sample.

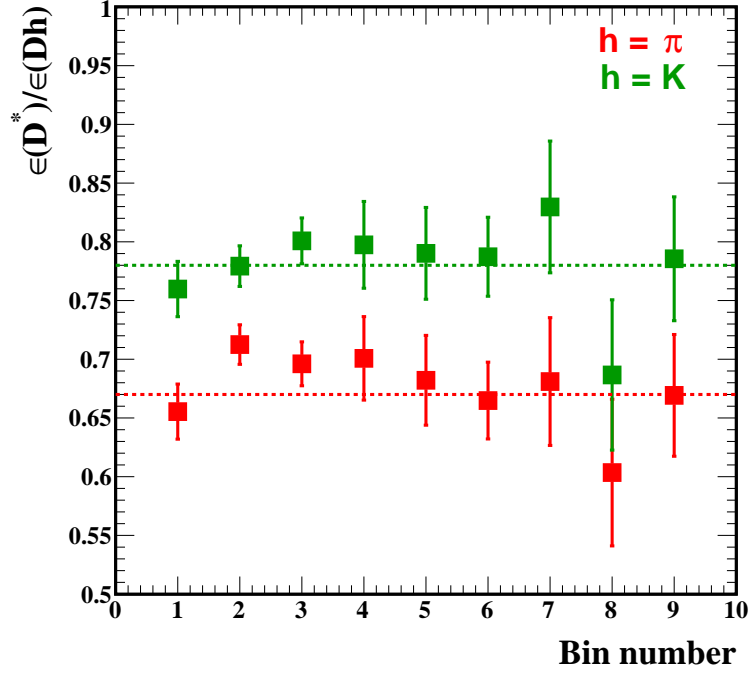


Figure 4.28: Ratio of  $D^*$  and  $B$  efficiencies across the nine  $D$  phase space bins.

The efficiency values of  $B^+$  and  $B^-$  samples are different in certain bins like bin 2. Bin 2 is not  $CP$  self-conjugate and the  $K^{*-} \rho^+$  final state is Cabibbo-favoured for a  $D^0$  decay and doubly-Cabibbo-suppressed for a  $\bar{D}^0$  decay. This results in asymmetric signal yields for  $B^+$  and  $B^-$  samples, so the efficiency values are different. The case is the same for bins 3, 4, 5, 7 and 8.

The efficiency of  $D^*$  and  $B$  samples are compared across the bins. The ratio of the efficiencies are shown in Fig. 4.28. The dotted line shows the average value and all the

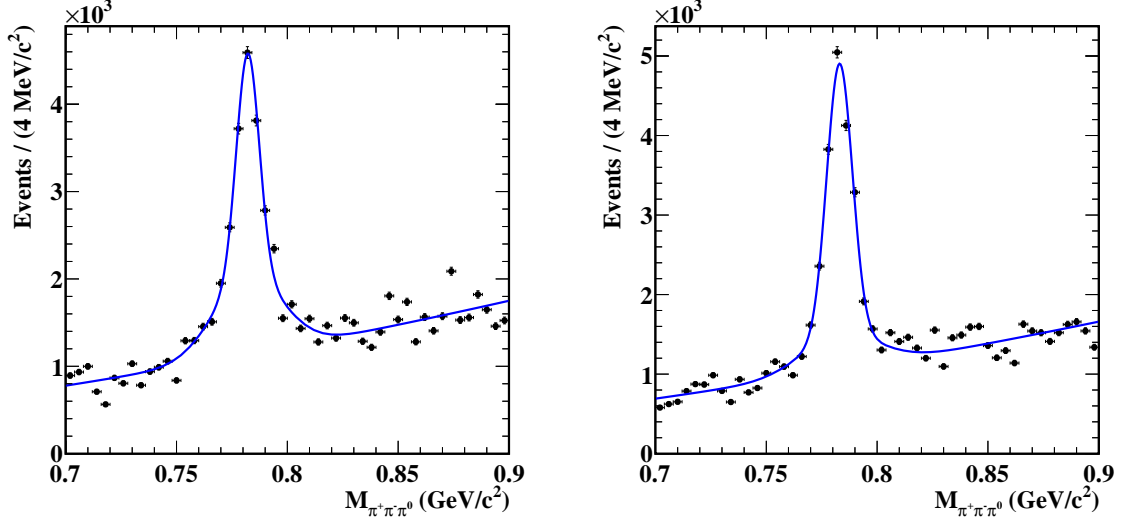


Figure 4.29:  $\pi^+\pi^-\pi^0$  invariant mass distribution in  $B^+ \rightarrow D(K_S^0\pi^+\pi^-\pi^0)\pi^+$  generic MC (left) and data (right) samples. Black points with error bars show the data and blue solid curve is the fit model.

bins are consistent with the average.

The bin-to-bin migration is quantified in terms of a  $9 \times 9$  matrix, which indicates how often an event is reconstructed in its true bin. Four million signal MC events, generated in accordance with the intermediate resonances, are used for the calculation. The resolution differences in data and MC are taken into account while determining the matrix. The momentum resolution in data and MC is analysed for  $B$  and  $D^*$  samples. Bin 1 ( $\omega$  resonance) has the narrowest width and hence the  $\pi^+\pi^-\pi^0$  invariant mass distribution is compared for data and MC. The distribution is fitted with the sum of two Gaussian PDFs and a first order polynomial function. The distributions in  $B$  and  $D^*$  samples are shown in Fig. 4.29 and 4.30, respectively.

The scale factors for the resolution in data, compared to that in MC, are obtained to be  $1.13 \pm 0.02$  and  $1.09 \pm 0.02$  for  $B$  and  $D^*$  samples, respectively. The  $\pi^+\pi^-\pi^0$  invariant mass distribution is smeared by the scale factor before calculating the elements in the first row of the matrix. The resonances in the other bins are narrow and the resolution difference is an order of magnitude smaller than the actual resolution. So this would not affect the values of migration matrix elements. The migration matrix obtained from respective signal MC samples are given in Table 4.7, 4.8 and 4.9.

The matrix is almost diagonal in all the three cases. However, corrections have been applied to the bin yields during the extraction of  $\phi_3$ -sensitive parameters. The next

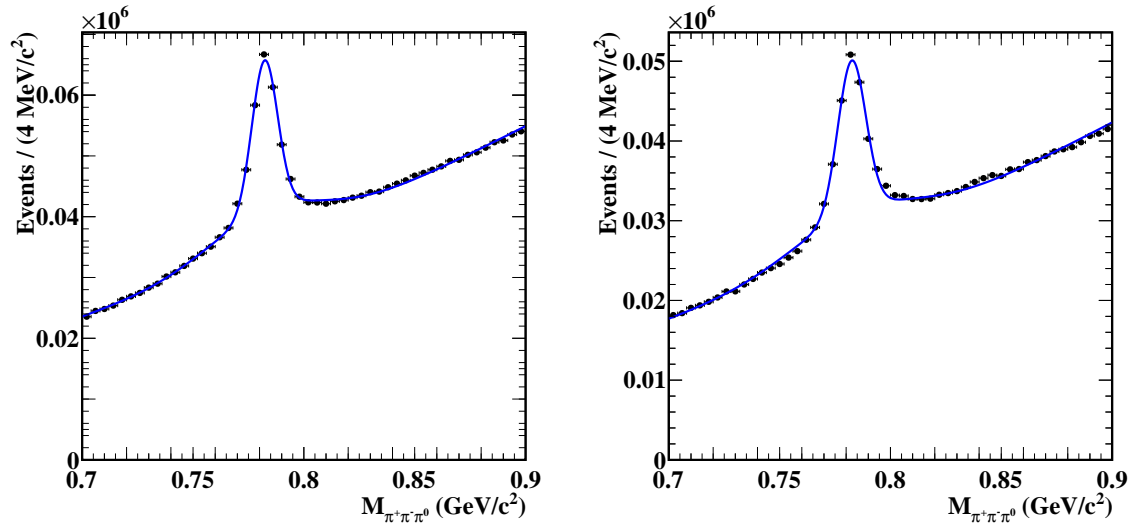


Figure 4.30:  $\pi^+\pi^-\pi^0$  invariant mass distribution in  $D^{*+} \rightarrow D(K_S^0\pi^+\pi^-\pi^0)\pi^+$  generic MC (left) and data (right) samples. Black points with error bars show the data and blue solid curve is the fit model.

Chapter contains a description of how the  $\phi_3$ -sensitive parameters are extracted from the selected samples.

Bin	1	2	3	4	5	6	7	8	9
1	<b>0.93</b>	0.01	0.01	0.01	0.01	0.01	0.00	0.00	0.01
2	0.01	<b>0.96</b>	0.02	0.00	0.00	0.00	0.00	0.00	0.00
3	0.01	0.02	<b>0.95</b>	0.01	0.00	0.00	0.00	0.00	0.00
4	0.03	0.02	0.02	<b>0.91</b>	0.00	0.01	0.00	0.00	0.00
5	0.03	0.02	0.02	0.01	<b>0.91</b>	0.01	0.00	0.00	0.01
6	0.02	0.02	0.01	0.01	0.00	<b>0.92</b>	0.00	0.00	0.01
7	0.01	0.03	0.02	0.00	0.00	0.01	<b>0.92</b>	0.00	0.01
8	0.01	0.01	0.02	0.00	0.01	0.01	0.01	<b>0.92</b>	0.01
9	0.05	0.02	0.01	0.01	0.01	0.01	0.01	0.01	<b>0.88</b>

Table 4.7: Migration matrix for  $B^\pm \rightarrow D(K_S^0\pi^+\pi^-\pi^0)\pi^\pm$  sample estimated from signal MC. The rows correspond to the true bins and columns show the reconstructed bins.

Bin	1	2	3	4	5	6	7	8	9
1	<b>0.93</b>	0.01	0.01	0.01	0.01	0.01	0.00	0.00	0.01
2	0.01	<b>0.96</b>	0.01	0.00	0.00	0.00	0.00	0.00	0.00
3	0.01	0.02	<b>0.95</b>	0.01	0.00	0.00	0.00	0.00	0.00
4	0.03	0.02	0.02	<b>0.91</b>	0.00	0.00	0.00	0.00	0.01
5	0.04	0.01	0.02	0.01	<b>0.91</b>	0.01	0.00	0.00	0.00
6	0.02	0.02	0.02	0.00	0.01	<b>0.92</b>	0.01	0.00	0.01
7	0.01	0.03	0.01	0.00	0.00	0.01	<b>0.92</b>	0.00	0.00
8	0.01	0.02	0.02	0.01	0.00	0.01	0.01	<b>0.91</b>	0.01
9	0.06	0.02	0.02	0.01	0.01	0.02	0.01	0.00	<b>0.85</b>

Table 4.8: Migration matrix for  $B^\pm \rightarrow D(K_S^0\pi^+\pi^-\pi^0)K^\pm$  sample estimated from signal MC. The rows correspond to the true bins and columns show the reconstructed bins.

Bin	1	2	3	4	5	6	7	8	9
1	<b>0.92</b>	0.01	0.01	0.02	0.02	0.01	0.00	0.00	0.02
2	0.00	<b>0.98</b>	0.01	0.00	0.00	0.00	0.00	0.00	0.00
3	0.00	0.01	<b>0.97</b>	0.00	0.00	0.00	0.00	0.00	0.00
4	0.04	0.02	0.01	<b>0.93</b>	0.00	0.01	0.00	0.00	0.00
5	0.04	0.01	0.02	0.01	<b>0.92</b>	0.01	0.00	0.00	0.01
6	0.02	0.01	0.01	0.01	0.01	<b>0.93</b>	0.00	0.00	0.01
7	0.00	0.02	0.01	0.00	0.00	0.02	<b>0.94</b>	0.01	0.00
8	0.00	0.01	0.02	0.00	0.00	0.01	0.01	<b>0.93</b>	0.01
9	0.08	0.00	0.00	0.01	0.01	0.02	0.01	0.01	<b>0.86</b>

Table 4.9: Migration matrix for  $D^{*\pm} \rightarrow D(K_S^0\pi^+\pi^-\pi^0)\pi^\pm$  sample estimated from signal MC. The rows correspond to the true bins and columns show the reconstructed bins.

# CHAPTER 5

## Measurement of $\phi_3$ at Belle

### 5.1 Introduction

The measurement of the CKM angle  $\phi_3$  from  $B^+ \rightarrow D(K_S^0 \pi^+ \pi^- \pi^0) K^+$  decays at Belle is described in detail in this Chapter. First, the  $K_i$  and  $\overline{K}_i$  parameters are determined from  $D^{*+} \rightarrow D(K_S^0 \pi^+ \pi^- \pi^0) \pi^+$  decays. Then the  $\phi_3$ -sensitive parameters  $x_{\pm}$  and  $y_{\pm}$  are extracted with  $c_i$ ,  $s_i$ ,  $K_i$  and  $\overline{K}_i$  values used as inputs. The physical parameters  $\phi_3$ ,  $r_B$  and  $\delta_B$  are obtained from the measured  $x_{\pm}$  and  $y_{\pm}$  values using a frequentist approach.

This Chapter is arranged as follows: the determination of  $K_i$  and  $\overline{K}_i$  values are discussed in Sec. 5.2. The measurement of  $x_{\pm}$  and  $y_{\pm}$  parameters is explained in Sec. 5.3 and the estimation of systematic uncertainties is described in Sec. 5.4. The measurement of  $\phi_3$ ,  $r_B$  and  $\delta_B$  parameters using a frequentist method is given in Sec. 5.5 followed by a combination of  $D \rightarrow K_S^0 \pi^+ \pi^-$  and  $D \rightarrow K_S^0 \pi^+ \pi^- \pi^0$  results from Belle in Sec. 5.6.

### 5.2 Determination of $K_i$ and $\overline{K}_i$

The fractions of  $D^0$  and  $\overline{D}^0$  events in each  $D$  phase space bin, represented as  $K_i$  and  $\overline{K}_i$ , are measured from the selected sample of  $D^{*+} \rightarrow D \pi^+$  candidates. The yield of signal events is obtained from a two-dimensional extended maximum-likelihood fit to the distribution of  $M_D$  and  $\Delta M$  for the selected candidates. In general, there are two types of background: *combinatorial background*, which is due to the random combination of final-state particles to form a  $D^{*+}$  candidate, and *random-slow-pion background*, in which a correctly reconstructed  $D$  meson combines with a  $\pi^+$ , which is not from a common  $D^{*+}$  decay, to form a fake candidate. The combinatorial background peaks neither in the  $M_D$  nor  $\Delta M$  distributions, whereas the random-slow-pion background peaks only in the  $M_D$  distribution.

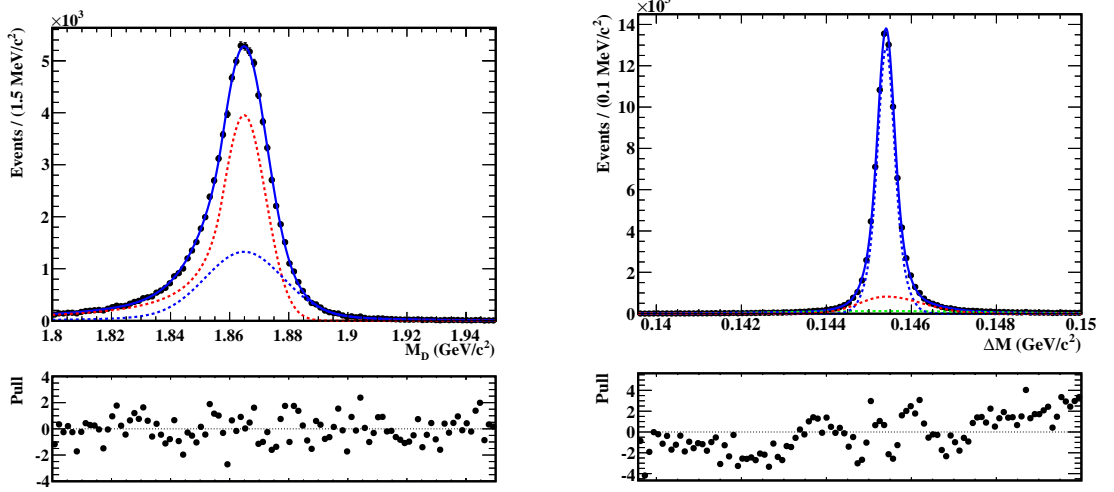


Figure 5.1: One-dimensional fit distributions of  $M_D$  (left) and  $\Delta M$  (right) signal component in  $D^{*\pm} \rightarrow D\pi^\pm$  generic MC sample. Black points with error bars indicate data and the solid blue curve is the total fit. The pull between the fit and the data is shown below the distributions. The red and blue dotted lines in  $M_D$  projection represent Crystal Ball and double Gaussian PDFs, respectively. In  $\Delta M$  projection, blue, red and green dotted lines indicate double Gaussian, asymmetric Gaussian and Gaussian PDFs, respectively.

The  $M_D$  and  $\Delta M$  distributions for signal and background components are individually modelled in the generic MC sample. The signal component of  $M_D$  is modelled by the sum of a Crystal Ball (see Eq. (3.17)) and two Gaussian PDFs with a common mean. The sum of three Gaussians and one asymmetric Gaussian PDFs, with a common mean, is used to model the  $\Delta M$  signal component. The fit projections are shown in Fig. 5.1.

The combinatorial component of  $M_D$  is modelled with a linear function,

$$f(M_D) = b_0 + b_1 M_D, \quad (5.1)$$

where  $b_0$  and  $b_1$  are parameters determined from the fit. The  $\Delta M$  combinatorial component is modelled with a threshold function of the form

$$f(\Delta M) = (\Delta M - m_\pi)^{\frac{1}{2}} + \alpha(\Delta M - m_\pi)^{\frac{3}{2}} + \beta(\Delta M - m_\pi)^{\frac{5}{2}}, \quad (5.2)$$

where  $m_\pi$  is the nominal mass of a charged pion [14] and  $\alpha$  and  $\beta$  are parameters determined by the fit. There is a peaking structure in the  $\Delta M$  combinatorial distribution due to candidates that include a misreconstructed  $\pi^0$ . These events are separated and analysed in generic MC sample; they are modelled with the sum of two Gaussian PDFs

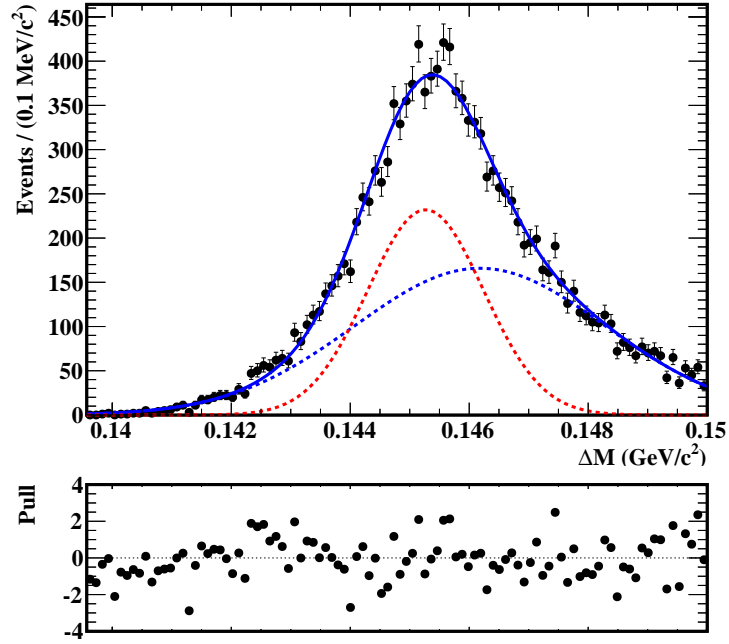


Figure 5.2:  $\Delta M$  distribution of misreconstructed  $\pi^0$  events in  $D^{*\pm} \rightarrow D\pi^\pm$  generic MC sample. Black points with error bars indicate data and the solid blue curve is the total fit. The blue and red dotted lines show the two Gaussian PDFs.

with different mean as shown in Fig. 5.2. The shape parameters of this model are fixed in the total combinatorial component fit. The one-dimensional fit projections of  $M_D$  and  $\Delta M$  combinatorial component are shown in Fig. 5.3.

The two-dimensional fit between  $M_D$  and  $\Delta M$  is trivial if there is no correlation between them. The one-dimensional PDFs can be simply multiplied for each component. But the signal component of these two variables are correlated. This is analysed by looking at the  $\Delta M$  distribution in different  $M_D$  regions. The resolution of  $\Delta M$  as a function of  $M_D$  is shown in Fig. 5.4. The distribution is approximately quadratic as reported in Ref. [79]. Therefore a similar fitting strategy is adopted here, by using conditional PDFs accounting for the correlation effects. Two-dimensional signal PDF is then given as the sum of a conditional and a non-conditional PDF

$$\mathcal{P}_{\text{signal}}(\Delta M, M_D) = f_1 \mathcal{P}_{\text{conditional}}(\Delta M, M_D) + (1 - f_1) \mathcal{P}_{\text{non-conditional}}(\Delta M, M_D), \quad (5.3)$$

where  $f_1$  is the fraction of the conditional PDF that includes the correlation. The con-

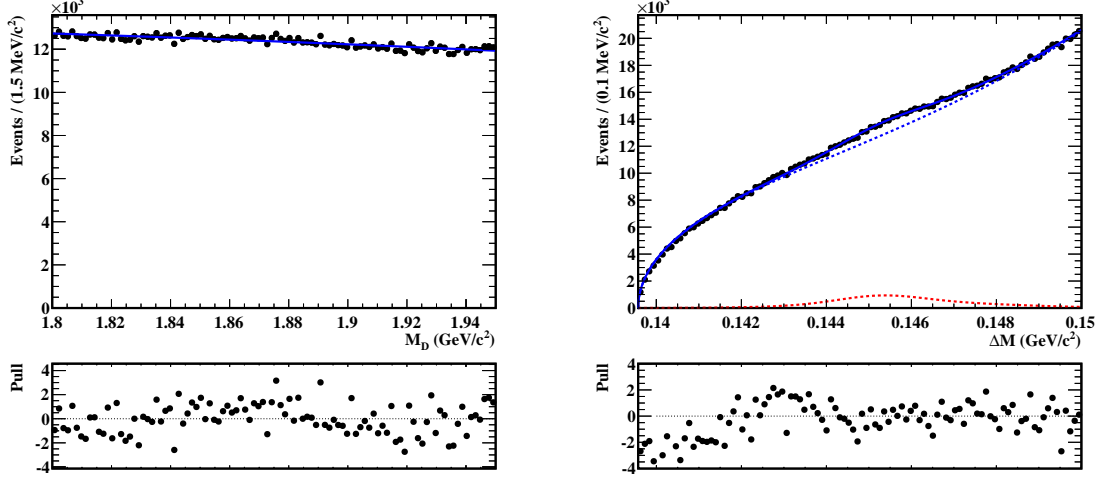


Figure 5.3: One-dimensional fit distributions of  $M_D$  (left) and  $\Delta M$  (right) combinatorial component in  $D^{*\pm} \rightarrow D\pi^\pm$  generic MC sample. Black points with error bars indicate data and the solid blue curve is the total fit. The pull between the fit and the data is shown below the distributions. The red and blue dotted lines in  $\Delta M$  projection represent the peaking component and threshold function PDF, respectively.

ditional PDF is formed as

$$\mathcal{P}_{\text{conditional}}(\Delta M, M_D) = [\text{DG}]_{\Delta M} \times [f_{\text{CB}}\text{CB} + (1 - f_{\text{CB}})G_1]_{M_{D^0}}, \quad (5.4)$$

where DG is the sum of two Gaussian PDFs, CB is Crystal Ball and G is Gaussian PDF. Here,  $f_{\text{CB}}$  is the fraction of Crystal Ball in  $M_D$  signal PDF. The non-conditional PDF without any correlation between  $\Delta M$  and  $M_D$  is formed as

$$\mathcal{P}_{\text{non-conditional}}(\Delta M, M_D) = [f_{\text{AG}}\text{AG} + (1 - f_{\text{AG}})G]_{\Delta M} \times [G_2]_{M_{D^0}}, \quad (5.5)$$

where AG is asymmetric Gaussian PDF and  $f_{\text{AG}}$  is the fraction of asymmetric Gaussian in the  $\Delta M$  signal PDF. The correlation is included in the core width of  $\Delta M$  by defining

$$\sigma(\Delta M) = a_0 + a_2(M_D - M_D^{\text{PDG}})^2, \quad (5.6)$$

where  $a_0$  is the width of the core Gaussian function in the  $\Delta M$  signal PDF and  $a_2$  parametrises the quadratic variation. The projections of  $M_D$  and  $\Delta M$  distributions from the two-dimensional fit to the signal component are shown in Fig. 5.5.

There is no correlation between the combinatorial components in  $M_D$  and  $\Delta M$ ,

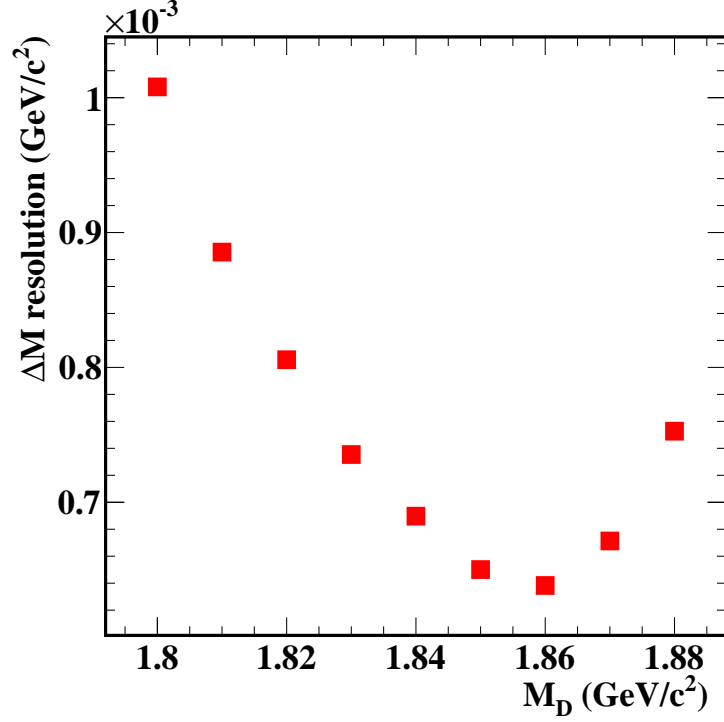


Figure 5.4: The resolution of  $\Delta M$  in different  $M_D$  regions determined from  $D^{*\pm} \rightarrow D\pi^\pm$  generic MC sample.

and hence the two-dimensional combinatorial PDF is obtained by multiplying the one-dimensional PDFs. The random-slow-pion background peaks in  $M_D$ , whereas in  $\Delta M$ , it follows the threshold function shape as given in Eq. (5.2). So only a two-dimensional modelling of  $M_D$  and  $\Delta M$  can distinguish this component from signal and combinatorial event types. The signal PDF of  $M_D$  and the threshold function in the  $\Delta M$  are used to model the random-slow-pion background. The two-dimensional PDF is the product of these two functions, as there is no correlation between the two fit variables for this component. The projections of  $M_D$  and  $\Delta M$  distributions from the two-dimensional fit to the random-slow-pion background component are shown in Fig. 5.6.

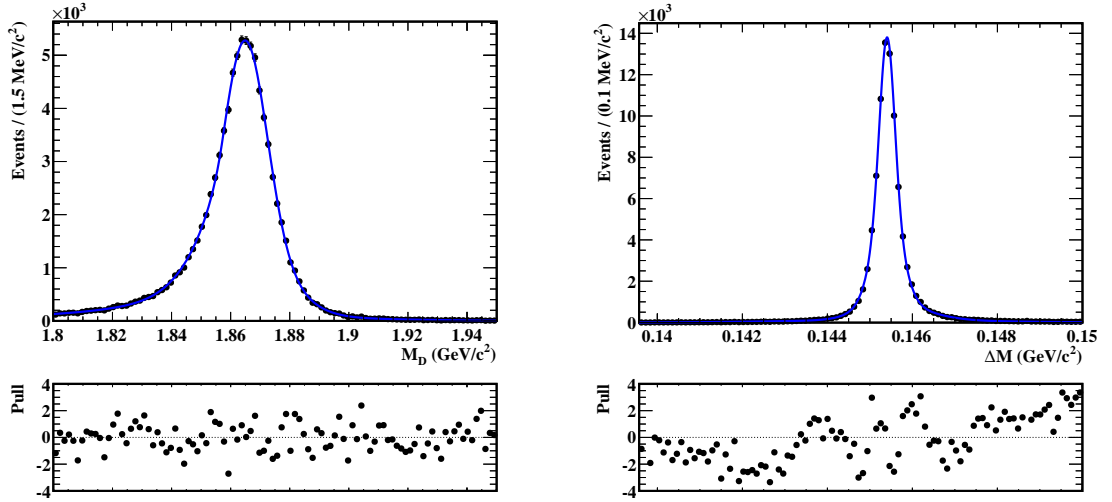


Figure 5.5: Projections of  $M_D$  (left) and  $\Delta M$  (right) from a two-dimensional fit to the signal component in  $D^{*\pm} \rightarrow D\pi^\pm$  generic MC sample. Black points with error bars indicate data and the solid blue curve is the total fit. The pull between the fit and the data is shown below the distributions.

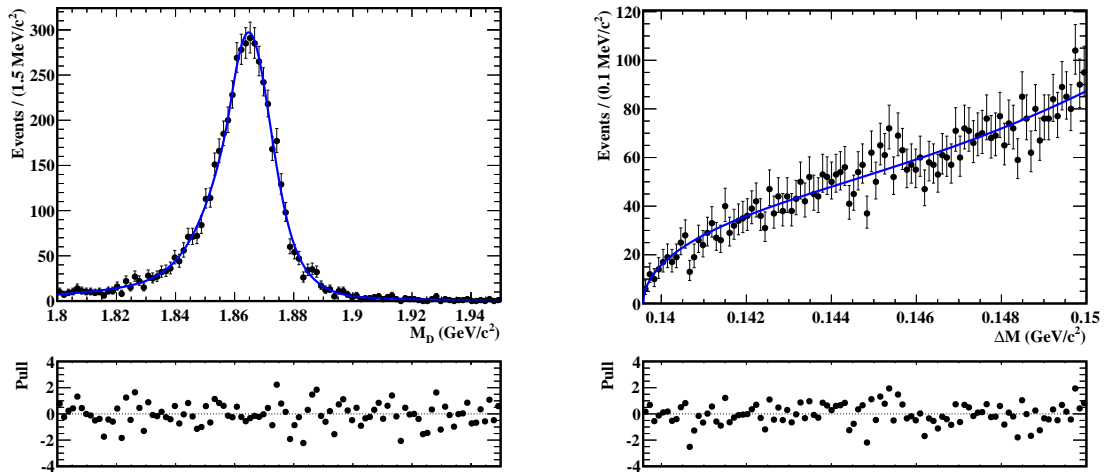


Figure 5.6: Projections of  $M_D$  (left) and  $\Delta M$  (right) from a two-dimensional fit to the random-slow-pion background component in  $D^{*\pm} \rightarrow D\pi^\pm$  generic MC sample. Black points with error bars indicate data and the solid blue curve is the total fit. The pull between the fit and the data is shown below the distributions.

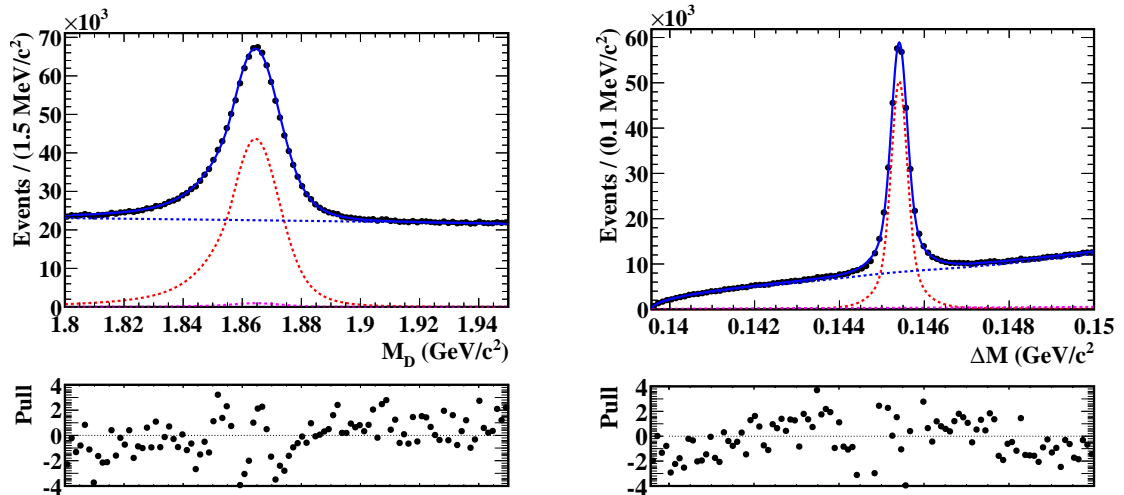


Figure 5.7: Signal-enhanced fit projections of  $M_D$  (left) and  $\Delta M$  (right) distributions from  $D^{*\pm} \rightarrow D\pi^\pm$  generic MC sample. The black points with error bars are the data and the solid blue curve shows the total fit. The dotted red, blue and magenta curves represent the signal, combinatorial and random-slow-pion backgrounds respectively. The pull between the fit and the data is shown below the distributions.

Component	True yield ( $\times 10^3$ )	Fit yield ( $\times 10^3$ )
Signal	821	$819 \pm 2$
Combinatorial	10947	$10912 \pm 4$
Random-slow-pion background	47	$85 \pm 3$

Table 5.1: Yields obtained from two-dimensional fit in  $D^{*\pm} \rightarrow D\pi^\pm$  generic MC sample.

The total two-dimensional fit is performed in  $D^{*\pm} \rightarrow D\pi^\pm$  generic MC sample with integrated luminosity equivalent to that of data ( $711 \text{ fb}^{-1}$ ). The component yields, the shape parameters  $a_0$  and  $a_2$ , as well as the means of the signal in both  $M_D$  and  $\Delta M$  are determined from the fit; all other parameters are fixed to the values obtained from fits to the corresponding component MC sample. The  $M_D$  and  $\Delta M$  fit projections from the total two-dimensional fit are given Fig. 5.7. These projections are signal-enhanced by projecting events in the signal region of the variable that is not plotted; the signal regions are defined as  $1.86 < M_D < 1.87 \text{ GeV}/c^2$  and  $0.144 < \Delta M < 0.146 \text{ GeV}/c^2$ .

The yields obtained from the fit, as well as their true values in  $D^{*\pm} \rightarrow D\pi^\pm$  generic MC sample, are given in Table 5.1. The signal yield obtained from the fit agrees with its true value within the uncertainty. Approximately 0.3% of the total number of events migrate from the combinatorial yield to random-slow-pion background yield. The most probable cause of this migration is some correlation that is not modeled in the PDFs.

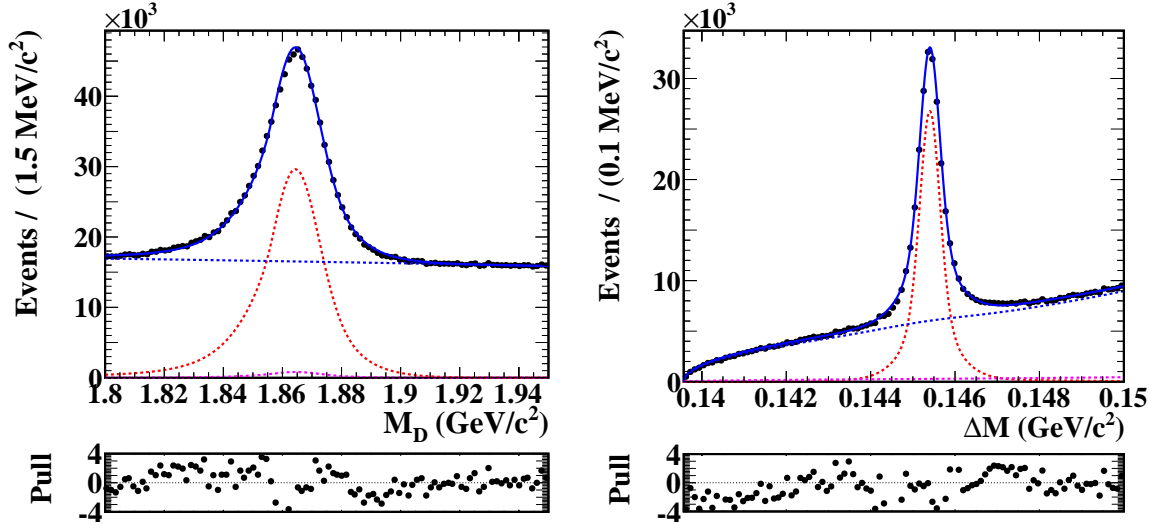


Figure 5.8: Signal-enhanced fit projections of  $M_D$  (left) and  $\Delta M$  (right) distributions from data. The black points with error bars are the data and the solid blue curve shows the total fit. The dotted red, blue and magenta curves represent the signal, combinatorial and random-slow-pion backgrounds respectively. The pull between the fit and the data is shown below the distributions.

Component	Total	$D^0$ yield ( $\times 10^3$ )	$\overline{D}^0$ yield ( $\times 10^3$ )
Signal	$615 \pm 2$	$311 \pm 1$	$304 \pm 1$
Combinatorial	$8011 \pm 4$	$3982 \pm 3$	$4031 \pm 3$
Random-slow-pion background	$77 \pm 3$	$36 \pm 2$	$39 \pm 2$

Table 5.2: Yields obtained from two-dimensional fit in data sample. The total as well as  $D^0$  and  $\overline{D}^0$  category yields are given.

However, as this is a small fraction and the signal yield is unbiased, this fit model is used to estimate the signal yield in data. The signal-enhanced projections of  $M_D$  and  $\Delta M$  from the total fit in the full Belle dataset of  $711 \text{ fb}^{-1}$  are shown in Fig. 5.8. The fit is then performed simultaneously for  $D^0$  and  $\overline{D}^0$  categories, which are identified from the charge of the slow pion. The yields obtained in data are summarized in Table 5.2. The uncertainties on the yields in data are comparable to that in generic MC sample.

The signal yields in the nine bins of  $D$  phase space are obtained from independent fits to data in each of them. This is possible because of the large statistics of the sample. The signal-enhanced projections of  $M_D$  and  $\Delta M$  distributions from the fit in bin 1 are shown in Fig. 5.9 and those in bins 2–9 are given in Appendix B. The  $D^0$  and  $\overline{D}^0$  signal yields are obtained in each bin and they are corrected for efficiency and migration effects. The yields are corrected for efficiency ( $\epsilon$ ) as  $Y'_i = Y_i/\epsilon_i$ . The  $K_i$  and  $\overline{K}_i$  parameters are determined from the fraction of these yields. They are corrected for

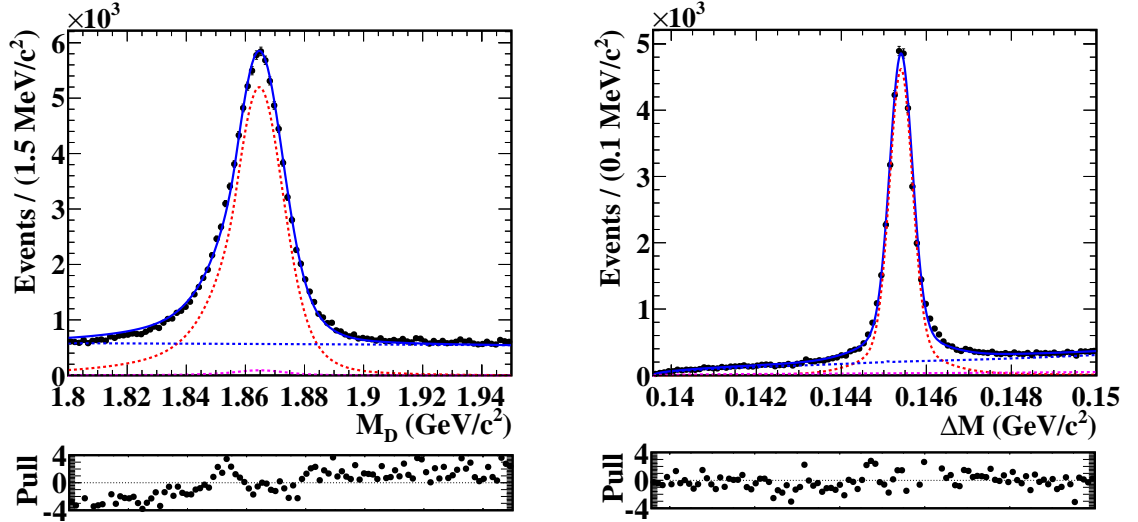


Figure 5.9: Signal-enhanced fit projections of  $M_D$  (left) and  $\Delta M$  (right) distributions from data in bin 1. The black points with error bars are the data and the solid blue curve shows the total fit. The dotted red, blue and magenta curves represent the signal, combinatorial and random-slow-pion backgrounds respectively. The pull between the fit and the data is shown below the distributions.

bin-to-bin migration using  $K_i = \sum_j M_{ij}^{-1} K_j$ , where  $M_{ij}$  is the migration matrix. The uncertainties on  $K_i$  and  $\overline{K}_i$  are multinomial. The results are given in Table 5.3.

Bin no.	$N_{D^0}$	$N_{\overline{D}^0}$	$K_i$	$\overline{K}_i$
1	$51048 \pm 282$	$50254 \pm 280$	$0.2229 \pm 0.0008$	$0.2249 \pm 0.0008$
2	$137245 \pm 535$	$58222 \pm 382$	$0.4410 \pm 0.0009$	$0.1871 \pm 0.0007$
3	$31027 \pm 297$	$105147 \pm 476$	$0.0954 \pm 0.0005$	$0.3481 \pm 0.0009$
4	$24203 \pm 280$	$16718 \pm 246$	$0.0726 \pm 0.0005$	$0.0478 \pm 0.0004$
5	$13517 \pm 220$	$20023 \pm 255$	$0.0371 \pm 0.0003$	$0.0611 \pm 0.0004$
6	$21278 \pm 269$	$20721 \pm 267$	$0.0672 \pm 0.0005$	$0.0679 \pm 0.0005$
7	$15784 \pm 221$	$13839 \pm 209$	$0.0403 \pm 0.0004$	$0.0394 \pm 0.0004$
8	$6270 \pm 148$	$7744 \pm 164$	$0.0165 \pm 0.0002$	$0.0183 \pm 0.0002$
9	$6849 \pm 193$	$6698 \pm 192$	$0.0070 \pm 0.0002$	$0.0054 \pm 0.0001$

Table 5.3:  $D^0$  and  $\overline{D}^0$  yield in each bin of  $D$  phase space along with  $K_i$  and  $\overline{K}_i$  values measured in  $D^{*\pm} \rightarrow D\pi^\pm$  data sample.

## 5.3 Measurement of $x_{\pm}$ and $y_{\pm}$

The  $\phi_3$ -sensitive parameters,  $x_{\pm}$  and  $y_{\pm}$  are estimated from  $B^+ \rightarrow D(K_S^0 \pi^+ \pi^- \pi^0)K^+$  decays. We select both  $B^+ \rightarrow DK^+$  and  $B^+ \rightarrow D\pi^+$  decays because they have an identical topology, but the latter is less sensitive to the effects of  $CP$ -violation because  $r_B^{D\pi}$  is approximately twenty times smaller than  $r_B^{DK}$ . However, the  $B^+ \rightarrow D\pi^+$  branching fraction is an order of magnitude larger than that of  $B^+ \rightarrow DK^+$  and hence it serves as an excellent calibration sample for the signal determination procedure. Furthermore, there is a significant background from  $B^+ \rightarrow D\pi^+$  decays in the  $B^+ \rightarrow DK^+$  sample from the misidentification of the charged pion coming from the  $B^+$  meson decay as a charged kaon; a simultaneous fit to both samples allows this cross-feed to be determined from data.

There are three types of backgrounds in this analysis:

- *continuum background* from  $e^+e^- \rightarrow q\bar{q}$  processes, where  $q = (u, d, s, c)$ ;
- *combinatorial  $B\bar{B}$  background*, in which the final state particles could be coming from both  $B$  mesons in an event; and
- *cross-feed peaking background* from  $B^+ \rightarrow Dh^+$ , where  $h = \pi, K$ , in which the charged kaon is misidentified as a charged pion or *vice versa*.

The signal extraction is performed using an extended maximum likelihood fit to  $\Delta E$  and  $C'_{\text{NN}}$  distributions simultaneously in both the samples. The fit variable distributions of signal and background components are modelled individually in MC samples. A two-dimensional simultaneous fit to the nine bins of  $B^+ \rightarrow DK^+$  and  $B^+ \rightarrow D\pi^+$  decays is performed to determine signal yields in each bin. The  $\phi_3$ -sensitive parameters  $x_{\pm}$  and  $y_{\pm}$  are extracted directly from the fit. The details of the signal extraction procedure are given in the following subsections.

### 5.3.1 Fit model for the $B^+ \rightarrow D\pi^+$ sample

First, a fit model is devised for the calibration mode  $B^+ \rightarrow D\pi^+$ . The  $\Delta E$  distribution of the signal component is fitted with the sum of Crystal Ball and two Gaussian PDFs with a common mean value. The fitted distribution obtained from signal MC sample is given in Fig. 5.10. The parameter values obtained from the fit are given in Table 5.4.

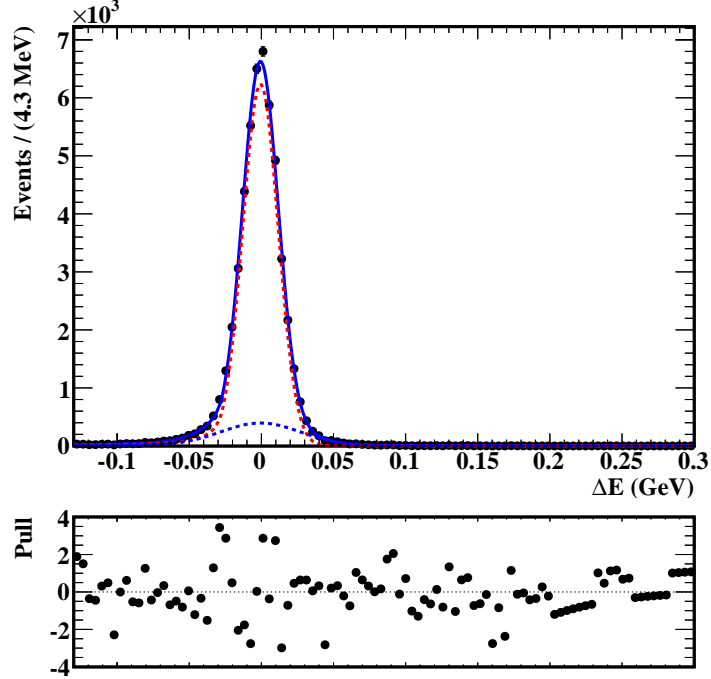


Figure 5.10: One-dimensional fit to the  $\Delta E$  distributions of signal component in  $B^+ \rightarrow D(K_S^0 \pi^+ \pi^- \pi^0) \pi^+$  signal MC sample. Black points with error bars indicate data and the solid blue curve is the total fit. The pull between the fit and the data is shown below the distributions. The red and blue dotted curves in represent Crystal Ball and double Gaussian PDFs, respectively.

Parameter	Description	Fit result
$\mu$	mean	$-(6.30 \pm 0.70) \times 10^{-4} \text{ GeV}$
$\sigma_{\text{CB}}$	$\sigma$ of Crystal Ball	$(1.23 \pm 0.01) \times 10^{-2} \text{ GeV}$
$\alpha_{\text{CB}}$	Crystal Ball parameter	$2.11 \pm 0.06$
$n_{\text{CB}}$	Crystal Ball parameter	$1.47 \pm 0.15$
$f_{\text{CB}}$	fraction of Crystal Ball PDF	$0.87 \pm 0.01$
$\sigma_1$	$\sigma$ of first Gaussian	$(2.70 \pm 0.10) \times 10^{-2} \text{ GeV}$
$\sigma_2$	$\sigma$ of second Gaussian	$(9.70 \pm 0.60) \times 10^{-2} \text{ GeV}$
$f_{G_1}$	fraction of first Gaussian	$0.91 \pm 0.01$

Table 5.4: Fit parameters for  $\Delta E$  distribution of signal events in  $B^+ \rightarrow D(K_S^0 \pi^+ \pi^- \pi^0) \pi^+$  signal MC sample.

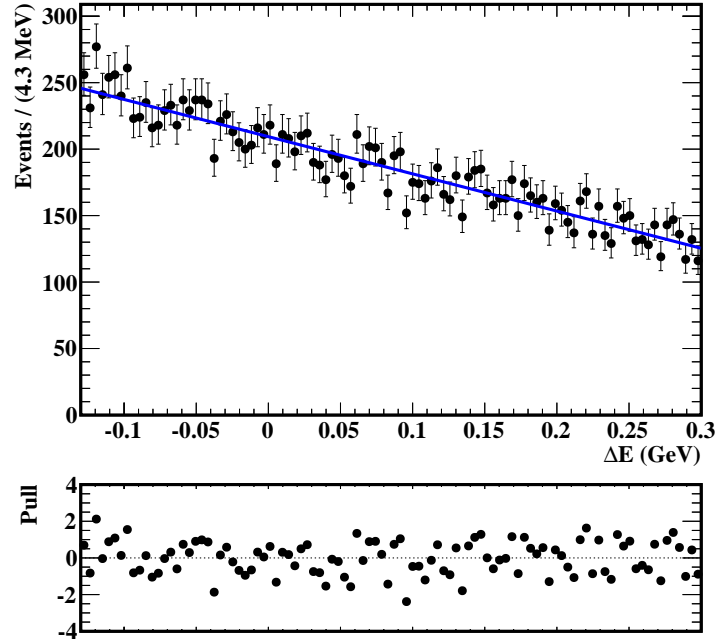


Figure 5.11: One-dimensional fit to the  $\Delta E$  distribution of continuum background events in  $B^+ \rightarrow D(K_S^0 \pi^+ \pi^- \pi^0) \pi^+$  generic MC sample. Black points with error bars indicate data and the solid blue curve is the total fit. The pull between the fit and the data is shown below the distributions.

The  $\Delta E$  distribution of continuum background events are modelled by a first-order Chebyshev polynomial function. The  $n^{\text{th}}$ -order Chebyshev polynomial is defined as

$$f(\Delta E) = 1 + \sum_{i=1,n} b_i T_i(\Delta E). \quad (5.7)$$

For the first order polynomial,  $T_1(\Delta E) = \Delta E$ . We choose Chebyshev polynomials over regular polynomials because of their stability in fits. The power terms in Chebyshev polynomials are reorganized in such a way that the correlations between the coefficients  $b_i$  are minimum and this results in more stability in fits. The fit projection is shown in Fig. 5.11. The value of parameter  $b_1$  is obtained to be  $-0.324 \pm 0.012$  from the fit.

The  $\Delta E$  distribution of combinatorial  $B\bar{B}$  background events is analysed in  $B^+ \rightarrow D(K_S^0 \pi^+ \pi^- \pi^0) \pi^+$  generic MC sample. There is a peaking like structure in the signal region ( $|\Delta E| < 0.05$  GeV). Different possible contributions are analysed by looking at the generated level information in generic MC sample. They are shown in Fig. 5.12. The major contribution is from misreconstructed  $\pi^0$  events. A small peak in the rest

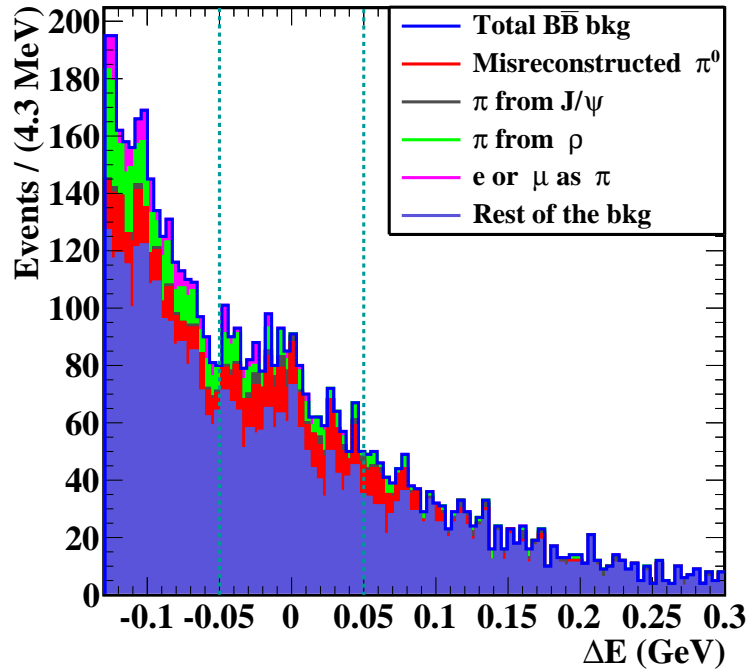


Figure 5.12:  $\Delta E$  distribution of combinatorial  $B\bar{B}$  background events in  $B^+ \rightarrow D(K_S^0\pi^+\pi^-\pi^0)\pi^+$  generic MC sample. Different possible contributions are separately shown as stacked histograms. The vertical lines show the signal region.

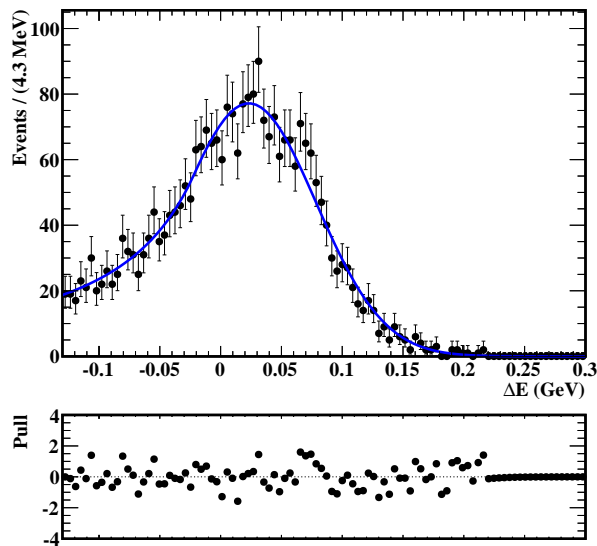


Figure 5.13:  $\Delta E$  distribution of misreconstructed  $\pi^0$  events in  $B^+ \rightarrow D(K_S^0\pi^+\pi^-\pi^0)\pi^+$  signal MC sample fitted with a Crystal Ball PDF. Black points with error bars indicate data and the solid blue curve is the total fit. The pull between the fit and the data is shown below the distributions.

of the background category can be due to  $D \rightarrow \pi^+\pi^-\pi^+\pi^-\pi^0$  events, but this forms

Parameter	description	Fit result
$\mu$	mean	$(2.3 \pm 0.2) \times 10^{-2}$ GeV
$\sigma_{\text{CB}}$	$\sigma$ of Crystal Ball	$(5.5 \pm 0.2) \times 10^{-2}$ GeV
$\alpha_{\text{CB}}$	Crystal Ball parameter	$0.8 \pm 0.2$
$n_{\text{CB}}$	Crystal Ball parameter	$1.5 \pm 1.4$

Table 5.5: Fit parameters for  $\Delta E$  distribution of misreconstructed  $\pi^0$  events in  $B^+ \rightarrow D(K_S^0 \pi^+ \pi^- \pi^0) \pi^+$  signal MC sample.

only a negligible fraction. The misreconstructed  $\pi^0$  events are separately modelled in  $B^+ \rightarrow D\pi^+$  signal MC sample with a Crystal Ball PDF. The fit projection is shown in Fig. 5.13 and parameter values obtained from the fit are given in Table 5.5. The combinatorial  $B\bar{B}$  background events are modelled with an exponential function in  $\Delta E$  and the PDF shape parameters for misreconstructed  $\pi^0$  events are fixed to the values in Table 5.5. The fit projection is shown in Fig. 5.14. The exponential parameter  $a$  is obtained from the fit to be  $-6.789 \pm 0.096$  and the fraction of Crystal Ball PDF is  $0.059 \pm 0.011$ .

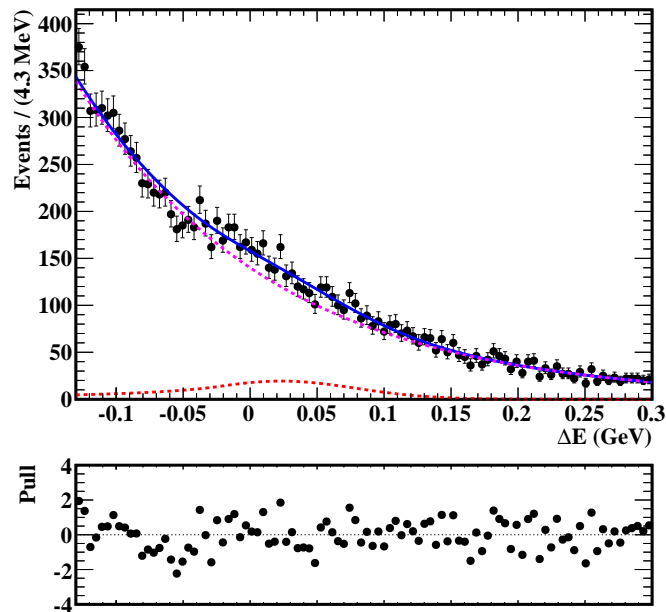


Figure 5.14: One-dimensional fit to the  $\Delta E$  distribution of combinatorial  $B\bar{B}$  background events in  $B^+ \rightarrow D(K_S^0 \pi^+ \pi^- \pi^0) \pi^+$  generic MC sample. Black points with error bars indicate data and the solid blue curve is the total fit. The pull between the fit and the data is shown below the distributions. The dotted magenta and red curves indicate the exponential and Crystal Ball PDFs, respectively.

The contribution of cross-feed peaking background events from  $B^+ \rightarrow DK^+$  in  $B^+ \rightarrow D\pi^+$  is significantly less than the cross-feed of  $B^+ \rightarrow D\pi^+$  to the  $B^+ \rightarrow DK^+$ , because the branching fraction of  $B^+ \rightarrow DK^+$  is an order of magnitude small. The  $\Delta E$  distribution is shifted by  $-50$  MeV due to the wrong-mass hypothesis associated to the  $\pi^+$ . The MC sample is prepared by generating  $B^+ \rightarrow DK^+$  events and then reconstructing them as  $B^+ \rightarrow D\pi^+$ . The  $\Delta E$  distribution is modelled with the sum of three Gaussian PDFs with a common mean as shown in Fig. 5.15 along with the fit results for the shape parameter values in Table 5.11.

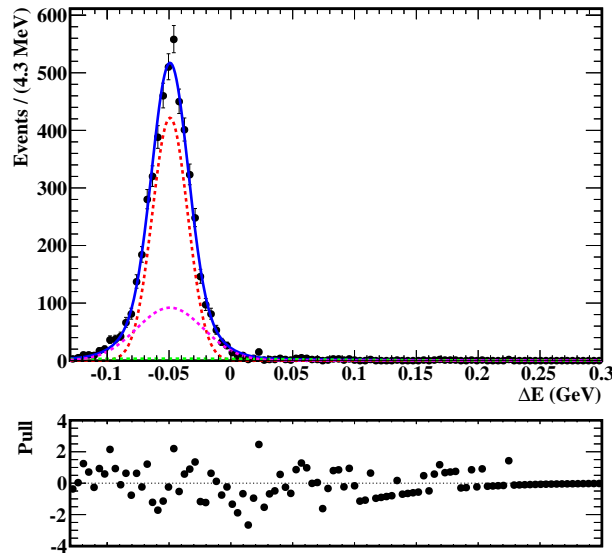


Figure 5.15: One-dimensional fit to the  $\Delta E$  distribution of cross-feed peaking background events from  $B^+ \rightarrow DK^+$  in  $B^+ \rightarrow D(K_S^0\pi^+\pi^-\pi^0)\pi^+$  sample. Black points with error bars indicate data and the solid blue curve is the total fit. The pull between the fit and the data is shown below the distributions. The dotted red, magenta and green curves indicate the three Gaussian PDFs.

Parameter	Description	Fit result
$\mu$	mean	$-(4.92 \pm 0.03) \times 10^{-2}$ GeV
$\sigma_1$	$\sigma$ of first Gaussian	$(1.43 \pm 0.06) \times 10^{-2}$ GeV
$\sigma_2$	$\sigma$ of second Gaussian	$0.11 \pm 0.01$ GeV
$\sigma_3$	$\sigma$ of third Gaussian	$(2.70 \pm 0.20) \times 10^{-2}$ GeV
$f_{G_1}$	fraction of first Gaussian	$0.68 \pm 0.01$
$f_{G_2}$	fraction of second Gaussian	$0.03 \pm 0.01$

Table 5.6: Fit parameters for  $\Delta E$  distribution of cross-feed peaking background events from  $B^+ \rightarrow DK^+$  in  $B^+ \rightarrow D(K_S^0\pi^+\pi^-\pi^0)\pi^+$  sample.

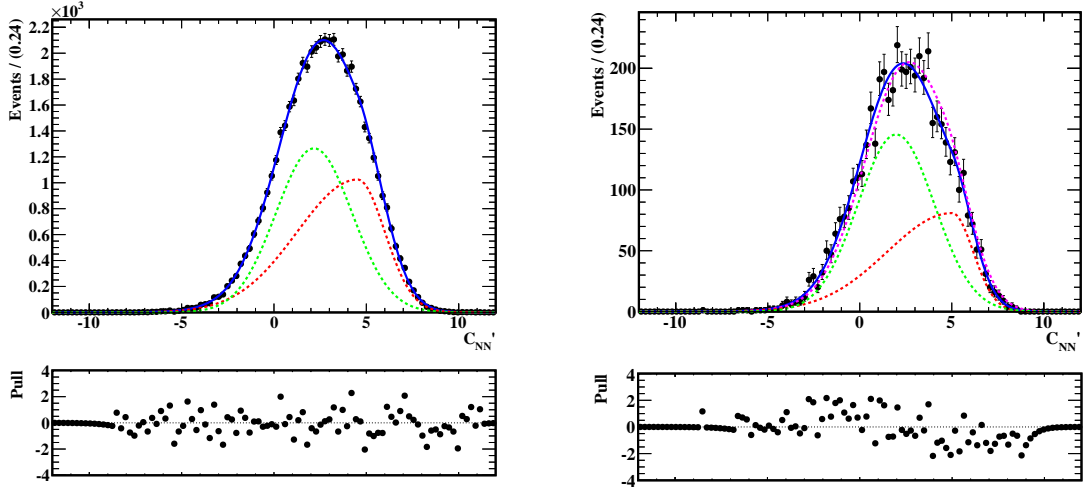


Figure 5.16: One-dimensional fit to the  $C'_{\text{NN}}$  distributions of signal (left) and cross-feed peaking background (right) events from  $B^+ \rightarrow D(K_S^0 \pi^+ \pi^- \pi^0) \pi^+$  signal MC sample. The black points with error bars are the data and the solid blue curve shows the total fit. The dotted red and green curves represent the Gaussian and asymmetric Gaussian PDFs, respectively. The dotted magenta curve shows the  $C'_{\text{NN}}$  signal PDF overlaid on the cross-feed peaking background model. The pull between the fit and the data is shown below the distributions.

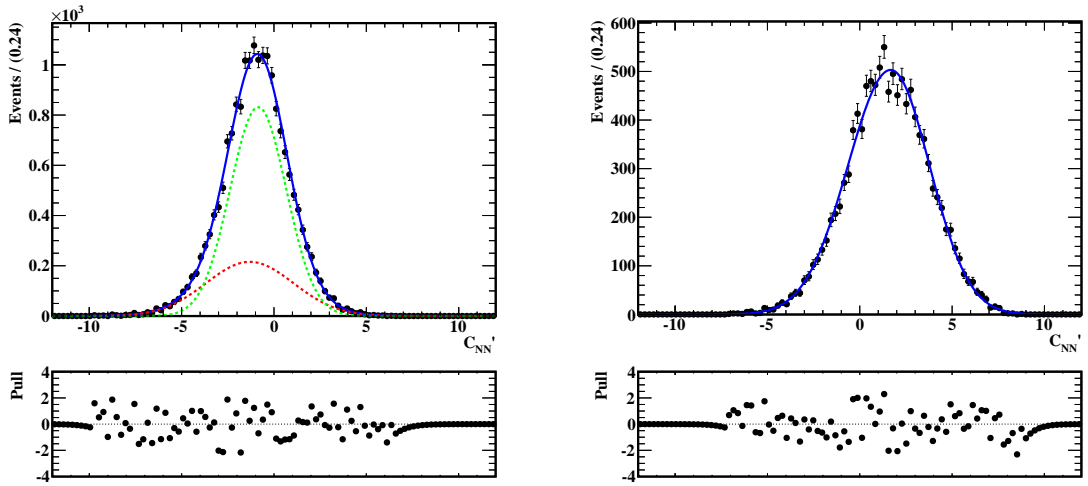


Figure 5.17: One-dimensional fit to the  $C'_{\text{NN}}$  distributions of continuum (left) and combinatorial  $B\bar{B}$  background (right) events from  $B^+ \rightarrow D(K_S^0 \pi^+ \pi^- \pi^0) \pi^+$  generic MC sample. The black points with error bars are the data and the solid blue curve shows the total fit. The dotted red and green curves represent the two Gaussian PDFs. The pull between the fit and the data is shown below the distributions.

The transformed NN output,  $C'_{\text{NN}}$  distribution is modelled separately for signal and the three background components. The sum of a Gaussian and an asymmetric Gaussian

Parameter	Description	Fit result
$\mu_1$	mean of asymmetric Gaussian	$4.53 \pm 0.14$
$\sigma_L$	left $\sigma$ of asymmetric Gaussian	$3.27 \pm 0.09$
$\sigma_R$	right $\sigma$ of asymmetric Gaussian	$1.48 \pm 0.07$
$\mu_2$	mean of Gaussian	$2.17 \pm 0.10$
$\sigma_G$	$\sigma$ of Gaussian	$2.06 \pm 0.06$
$f_G$	fraction of Gaussian	$0.52 \pm 0.07$

Table 5.7: Fit parameters for  $C'_{\text{NN}}$  distribution of signal component in  $B^+ \rightarrow D(K_S^0 \pi^+ \pi^- \pi^0) \pi^+$  signal MC sample.

Component	Parameter	Description	Fit result
Continuum background	$\mu_1$	mean of first Gaussian	$-1.31 \pm 0.08$
	$\sigma_1$	$\sigma$ of first Gaussian	$2.37 \pm 0.08$
	$\mu_2$	mean of second Gaussian	$-0.85 \pm 0.03$
	$\sigma_2$	$\sigma$ of second Gaussian	$1.52 \pm 0.04$
	$f_{G_1}$	fraction of first Gaussian	$0.29 \pm 0.06$
Combinatorial $B\bar{B}$ background	$\mu$	mean of asymmetric Gaussian	$1.68 \pm 0.05$
	$\sigma_L$	left $\sigma$ of asymmetric Gaussian	$2.33 \pm 0.03$
	$\sigma_R$	right $\sigma$ of asymmetric Gaussian	$2.11 \pm 0.03$

Table 5.8: Fit parameters for  $C'_{\text{NN}}$  distribution of background events in  $B^+ \rightarrow D(K_S^0 \pi^+ \pi^- \pi^0) \pi^+$  generic MC sample.

with different mean values is used to parametrize the PDF that describes the  $C'_{\text{NN}}$  signal component. The continuum background events are modelled with the sum of two Gaussian functions with different mean values, whereas the combinatorial  $B\bar{B}$  background events are fitted with an asymmetric Gaussian PDF. The cross-feed peaking background is fitted with the same PDF as used for the signal events. The fit projections are shown in Fig. 5.16 and 5.17. The results of shape parameter values are given in Table 5.7 and 5.8.

### 5.3.2 Data-MC comparison study

The selection optimization and PDF modelling are performed in MC sample. It is necessary to check if the relevant distributions in data agree with those in MC, before applying the selection and fit model to the data sample. The  $B^+$  candidate multiplicity distribution, after applying all the selection criteria mentioned in Chapter 4, is compared in generic MC and data samples of  $B^+ \rightarrow D(K_S^0 \pi^+ \pi^- \pi^0) \pi^+$  decays as shown

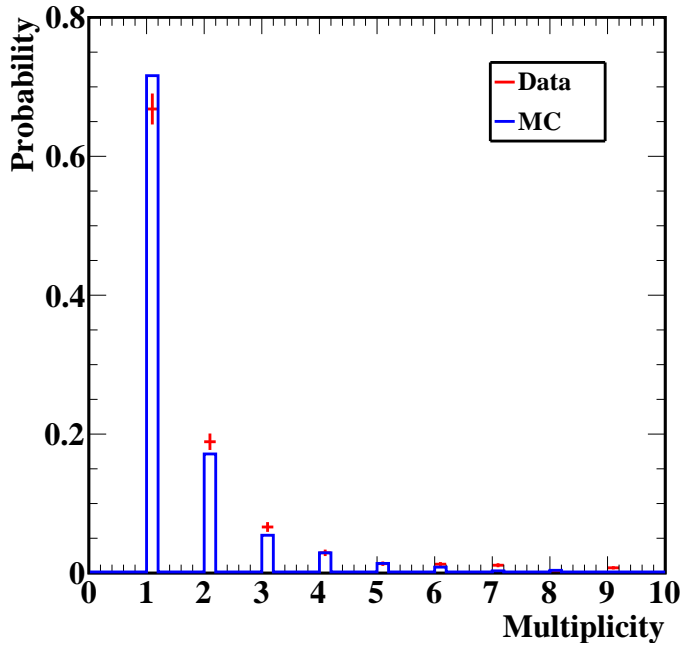


Figure 5.18:  $B^+$  candidate multiplicities in  $B^+ \rightarrow D(K_S^0 \pi^+ \pi^- \pi^0) \pi^+$  generic MC and data samples with equal integrated luminosities after applying all the selection criteria mentioned in Chapter 4.

in Fig. 5.18. There is reasonable agreement between data and MC and hence we conclude that the best-candidate selection procedure does not introduce any bias in the data sample. A comparison of the  $\Delta E$  and  $C'_{NN}$  distributions in  $B^+ \rightarrow D(K_S^0 \pi^+ \pi^- \pi^0) \pi^+$  generic MC sample before and after the best-candidate selection is given in Fig. 5.19. They show good agreement with each other and this shows that the fit variable distributions are not biased by the BCS.

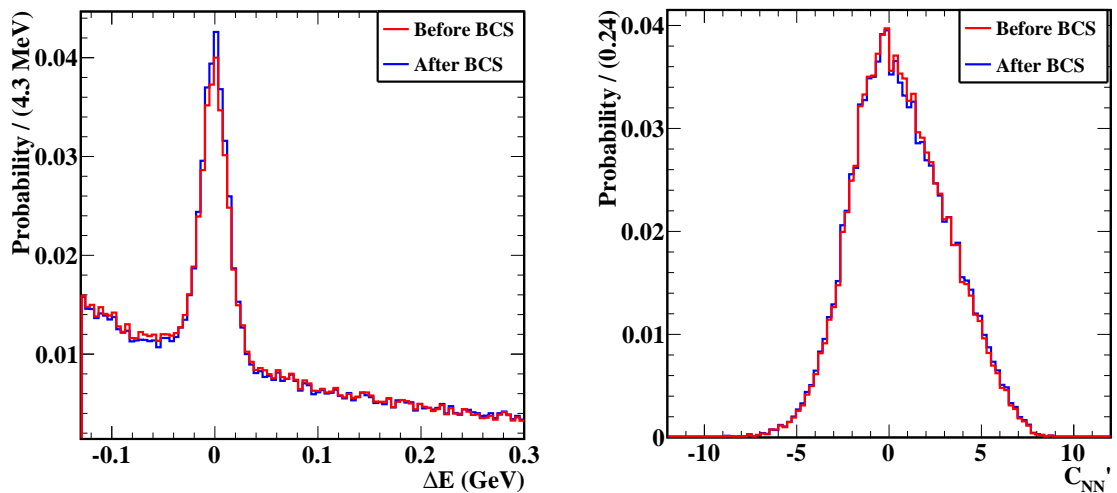


Figure 5.19:  $\Delta E$  (left) and  $C'_{NN}$  distributions in  $B^+ \rightarrow D(K_S^0 \pi^+ \pi^- \pi^0) \pi^+$  generic MC sample before and after the best-candidate selection.

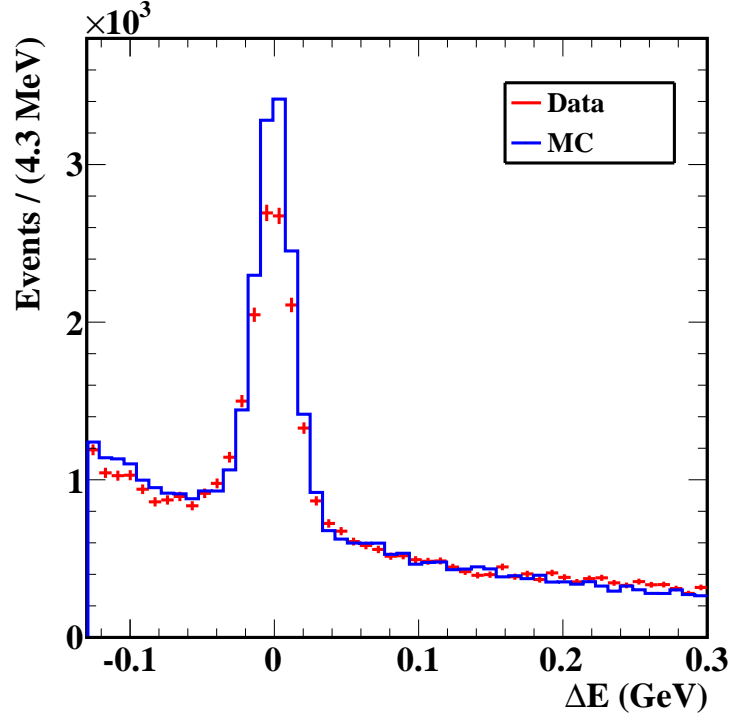


Figure 5.20:  $\Delta E$  distribution in  $B^+ \rightarrow D(K_S^0 \pi^+ \pi^- \pi^0) \pi^+$  generic MC and data samples with equal integrated luminosities.

The  $\Delta E$  distributions of  $B^+ \rightarrow D(K_S^0 \pi^+ \pi^- \pi^0) \pi^+$  decays in generic MC and data are compared as shown in Fig. 5.20. The distribution is broader in data owing to worse resolution than that in MC, but there is no shift in the mean position for either sample. The number of events in the signal peak in data is less than that in MC because events are generated assuming uniform acceptance across the  $D$  phase space in MC, which is not the case in data. The MC samples are generated assuming the branching fraction of the decay  $D \rightarrow K_S^0 \pi^+ \pi^- \pi^0$  to be 5.1%, whereas Ref. [14] reports it as 5.2%.

The  $C'_{\text{NN}}$  distributions in signal region and higher sideband of  $\Delta E$  ( $0.05 < \Delta E < 0.30$  GeV) are compared in  $B^+ \rightarrow D(K_S^0 \pi^+ \pi^- \pi^0) \pi^+$  generic MC and data samples. The contribution from the sidebands in the signal region is subtracted. This comparison gives information on data-MC agreement for signal and continuum background events (the latter dominates the higher sideband region of  $\Delta E$ ). The distributions are shown in Fig. 5.21. There is good agreement between data and MC in the signal region, but the distribution is slightly shifted in the higher sideband of  $\Delta E$ . The LR of KSFW moments and  $\Delta z$ , which are important variables used in the NN, are compared in the higher sideband region between data and MC. The distributions are shown in Fig. 5.22. There is slight mismatch in the lower values of LR and near the peak of  $\Delta z$  distributions.

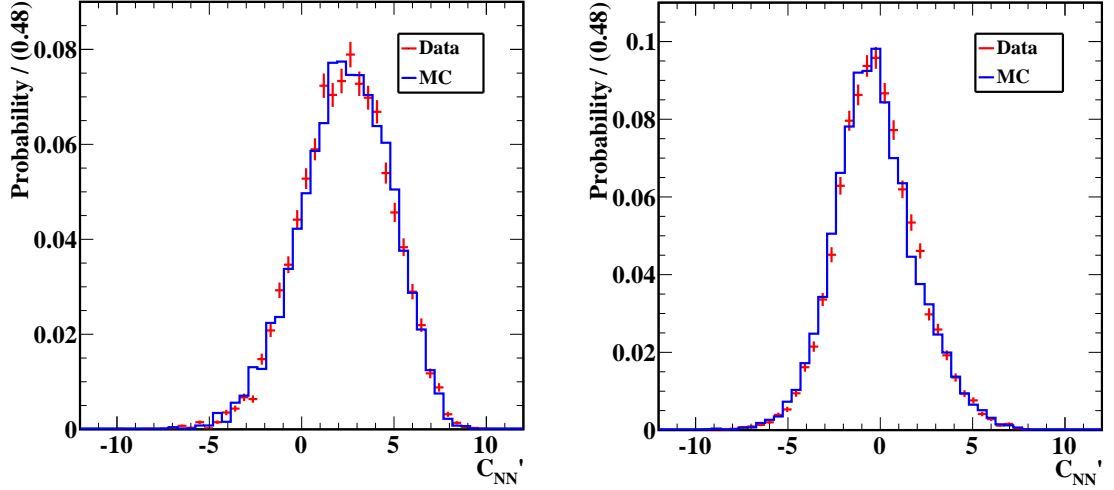


Figure 5.21:  $C'_{\text{NN}}$  distributions in signal (left) and higher sideband (right) regions of  $\Delta E$  in  $B^+ \rightarrow D(K_S^0 \pi^+ \pi^- \pi^0) \pi^+$  generic MC and data samples.

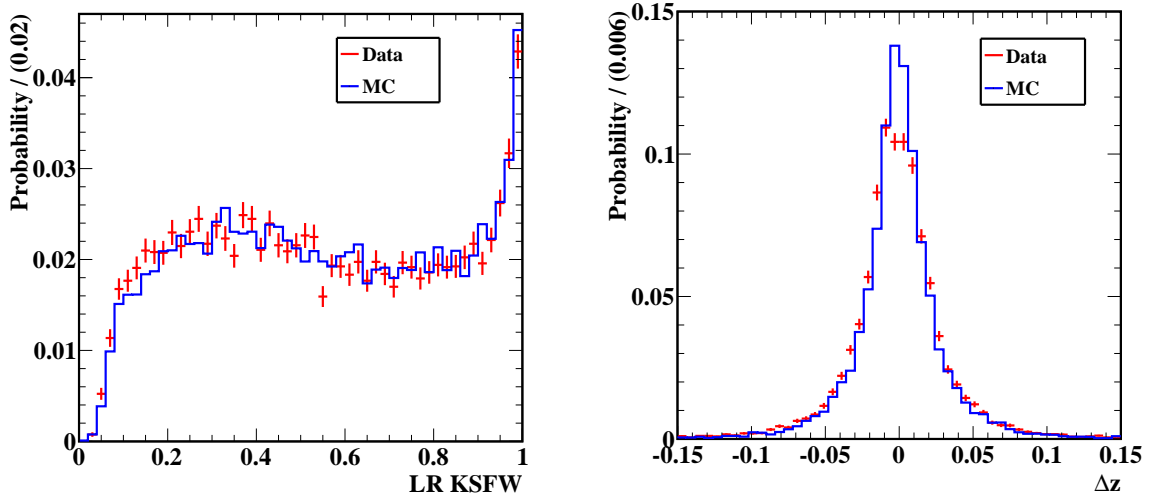


Figure 5.22: LR of KSFW moments (left) and  $\Delta z$  (right) distributions in higher  $\Delta E$  sideband region in  $B^+ \rightarrow D(K_S^0 \pi^+ \pi^- \pi^0) \pi^+$  generic MC and data samples.

Other input variables are found to have good agreement between data and MC. These differences in data and MC are considered while devising the fit model by leaving the relevant parameters free in the fit.

### 5.3.3 Fit model for $B^+ \rightarrow DK^+$ sample

The  $\Delta E$  and  $C'_{\text{NN}}$  distributions of signal and background events in  $B^+ \rightarrow DK^+$  sample are modelled individually in MC sample. The signal and continuum background shapes for  $\Delta E$  distribution are the same as that used in  $B^+ \rightarrow D\pi^+$  sample. The fit projections

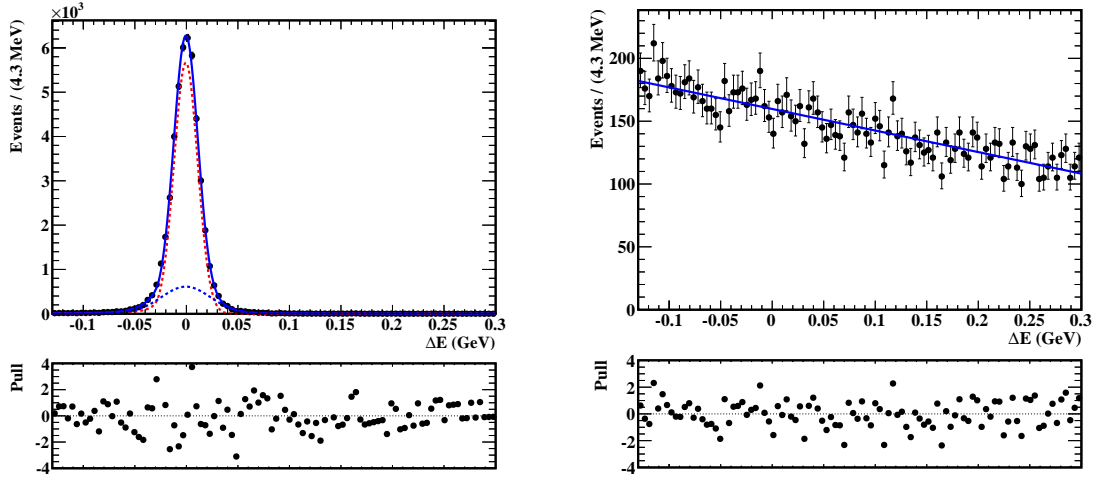


Figure 5.23: One-dimensional fit to the  $\Delta E$  distributions of signal (left) and continuum background (right) events in  $B^+ \rightarrow D(K_S^0 \pi^+ \pi^- \pi^0) K^+$  signal and generic MC samples, respectively. Black points with error bars indicate data and the solid blue curve is the total fit. The pull between the fit and the data is shown below the distributions. The red and blue dotted curves in represent Crystal Ball and double Gaussian PDFs, respectively.

are shown in Fig. 5.23 along with the parameter values in Table 5.9.

The combinatorial  $B\bar{B}$  background events have a steeper slope in  $\Delta E$  than that in  $B^+ \rightarrow D\pi^+$  sample. This is because of the presence of partially reconstructed  $B \rightarrow D^{(*)}K^{(*)}$  events. So a first-order Chebyshev polynomial is added to the exponential PDF. The fraction of misreconstructed  $\pi^0$  events is fixed from MC true value. The fit projection is shown in Fig. 5.24 and the parameter values obtained are given in Table 5.10.

The cross-feed peaking background of  $B^+ \rightarrow D\pi^+$  events in  $B^+ \rightarrow DK^+$  sample are studied in signal MC. The  $\Delta E$  distribution of these events is shifted by +50 MeV because of the wrong mass hypothesis assigned to the kaon. The fraction of this component is higher than that of in  $B^+ \rightarrow D\pi^+$  due to the larger branching fraction of  $B^+ \rightarrow D\pi^+$  decays. The  $\Delta E$  distribution of these events is fitted with the sum of three Gaussian PDFs as shown in Fig. 5.25. The fit results for the shape parameters are given in Table 5.11.

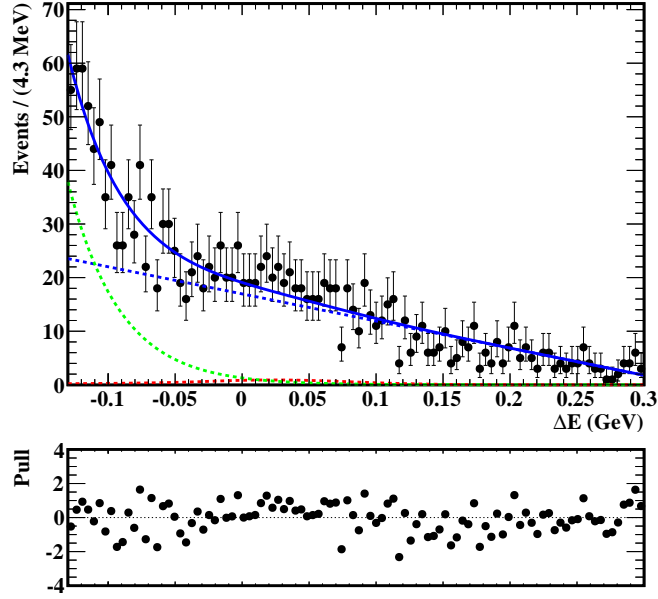


Figure 5.24: One-dimensional fit to the  $\Delta E$  distribution of combinatorial  $B\bar{B}$  background events in  $B^+ \rightarrow D(K_S^0\pi^+\pi^-\pi^0)K^+$  generic MC sample. Black points with error bars indicate data and the solid blue curve is the total fit. The pull between the fit and the data is shown below the distributions. The dotted blue, green and red curves indicate the Chebyshev polynomial, exponential function and Crystal Ball PDF, respectively.

Component	Parameter	Fit result
Signal	$\mu$	$-(5.02 \pm 0.02) \times 10^{-4} \text{ GeV}$
	$\sigma_{CB}$	$(1.15 \pm 0.01) \times 10^{-2} \text{ GeV}$
	$\alpha_{CB}$	$2.28 \pm 0.11$
	$n_{CB}$	$1.59 \pm 0.26$
	$f_{CB}$	$0.81 \pm 0.02$
	$\sigma_1$	$(2.37 \pm 0.09) \times 10^{-2} \text{ GeV}$
	$\sigma_2$	$(9.31 \pm 0.54) \times 10^{-2} \text{ GeV}$
	$f_{G_1}$	$0.92 \pm 0.01$
Continuum background	$b_0$	$-0.25 \pm 0.01$

Table 5.9: Fit parameters for  $\Delta E$  distribution of signal and continuum background events in  $B^+ \rightarrow D(K_S^0\pi^+\pi^-\pi^0)K^+$  signal and generic MC samples, respectively.

Parameter	Description	Fit result
$a$	exponential parameter	$-25.99 \pm 7.30$
$b_0$	Chebyshev parameter	$-0.86 \pm 0.04$
$f_{poly}$	fraction of Chebyshev	$0.79 \pm 0.05$

Table 5.10: Fit parameters for  $\Delta E$  distribution of combinatorial  $B\bar{B}$  events in  $B^+ \rightarrow D(K_S^0\pi^+\pi^-\pi^0)K^+$  generic MC sample.

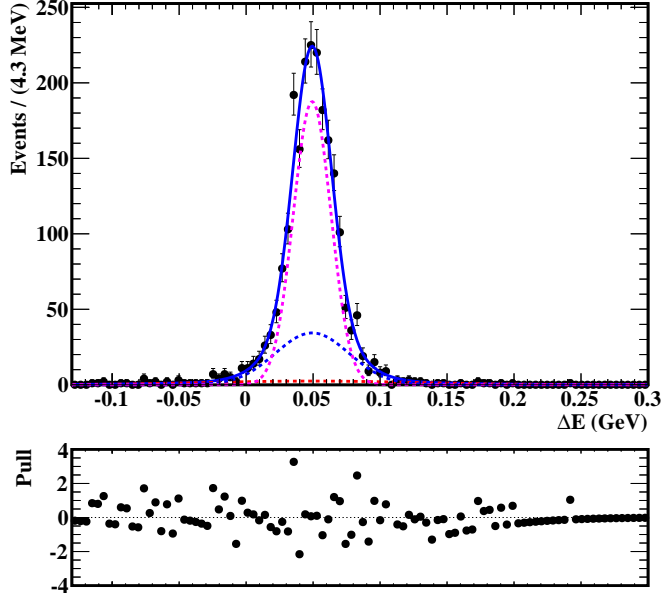


Figure 5.25: One-dimensional fit to the  $\Delta E$  distribution of cross-feed peaking background events from  $B^+ \rightarrow D\pi^+$  decays in  $B^+ \rightarrow D(K_S^0\pi^+\pi^-\pi^0)K^+$  sample. Black points with error bars indicate data and the solid blue curve is the total fit. The pull between the fit and the data is shown below the distributions. The dotted magenta, blue and red curves indicate the Gaussian PDFs.

Parameter	Fit result
$\mu$	$-(4.93 \pm 0.04) \times 10^{-2} \text{ GeV}$
$\sigma_1$	$0.08 \pm 0.01 \text{ GeV}$
$\sigma_2$	$0.03 \pm 0.01 \text{ GeV}$
$\sigma_3$	$0.01 \pm 0.00 \text{ GeV}$
$f_{G_1}$	$0.05 \pm 0.06$
$f_{G_2}$	$0.25 \pm 0.09$

Table 5.11: Fit parameters for  $\Delta E$  distribution of cross-feed peaking background events from  $B^+ \rightarrow D\pi^+$  in  $B^+ \rightarrow D(K_S^0\pi^+\pi^-\pi^0)K^+$  sample.

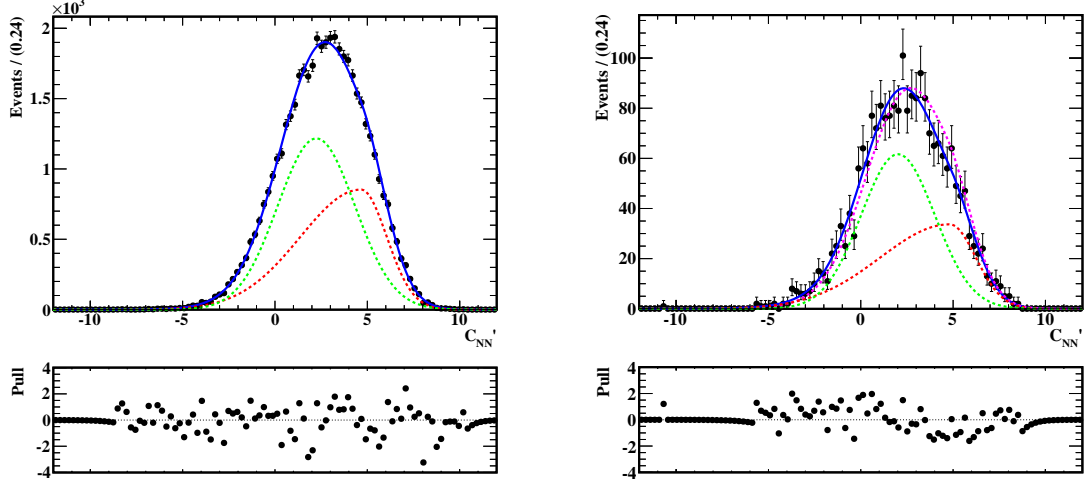


Figure 5.26: One-dimensional fit to the  $C'_{\text{NN}}$  distributions of signal (left) and cross-feed peaking background (right) events from  $B^+ \rightarrow D(K_S^0 \pi^+ \pi^- \pi^0) K^+$  signal MC sample. The black points with error bars are the data and the solid blue curve shows the total fit. The dotted red and green curves represent the Gaussian and asymmetric Gaussian PDFs, respectively. The dotted magenta curve shows the  $C'_{\text{NN}}$  signal PDF overlaid on the cross-feed peaking background model. The pull between the fit and the data is shown below the distributions.

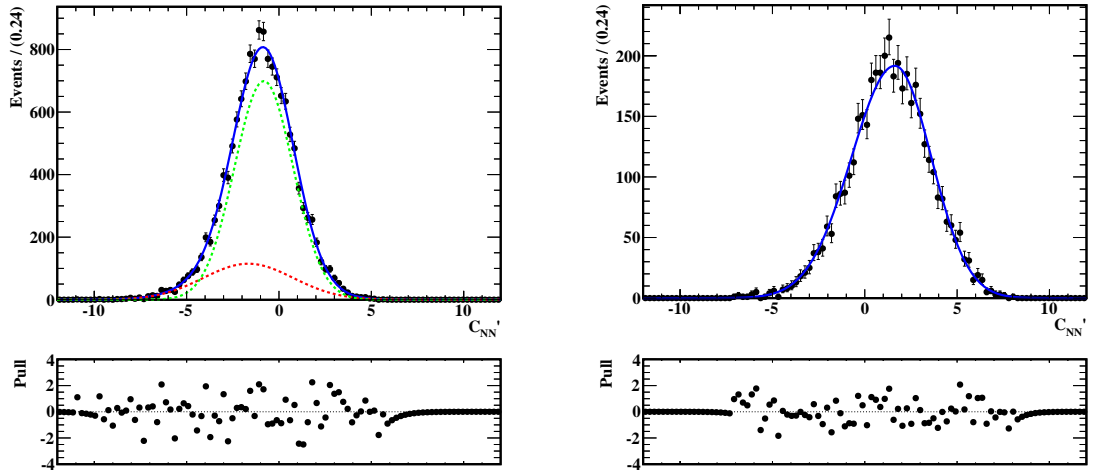


Figure 5.27: One-dimensional fit to the  $C'_{\text{NN}}$  distributions of continuum (left) and combinatorial  $B\bar{B}$  background (right) events from  $B^+ \rightarrow D(K_S^0 \pi^+ \pi^- \pi^0) K^+$  generic MC sample. The black points with error bars are the data and the solid blue curve shows the total fit. The dotted red and green curves represent the two Gaussian PDFs. The pull between the fit and the data is shown below the distributions.

The  $C'_{\text{NN}}$  distributions of all the four components are fitted with the same PDFs used in the  $B^+ \rightarrow D\pi^+$  sample. The fit projections are shown in Fig. 5.26 and 5.27. The signal PDF model can be used for the cross-feed peaking background as illustrated in

Component	Parameter	Fit result
Signal	$\mu_1$	$4.66 \pm 0.13$
	$\sigma_L$	$3.28 \pm 0.08$
	$\sigma_R$	$1.40 \pm 0.06$
	$\mu_2$	$2.24 \pm 0.07$
	$\sigma_G$	$2.09 \pm 0.03$
	$f_G$	$0.56 \pm 0.04$
Continuum background	$\mu_1$	$-1.66 \pm 0.19$
	$\sigma_1$	$2.43 \pm 0.09$
	$\mu_2$	$-0.82 \pm 0.03$
	$\sigma_2$	$1.59 \pm 0.04$
	$f_{G_1}$	$0.20 \pm 0.05$
Combinatorial	$\mu$	$1.63 \pm 0.08$
$B\bar{B}$ background	$\sigma_L$	$2.35 \pm 0.05$
	$\sigma_R$	$1.97 \pm 0.05$

Table 5.12: Fit parameters for  $C'_{\text{NN}}$  distribution of signal and background events in  $B^+ \rightarrow D(K_S^0 \pi^+ \pi^- \pi^0) \pi^+$  signal and generic MC samples, respectively.

Fig. 5.26. The parameter values obtained from the individual fits are given in Table 5.12.

### 5.3.4 Simultaneous fit to $B^+ \rightarrow D\pi^+$ and $B^+ \rightarrow DK^+$ samples

The signal extraction is performed in the  $B^+ \rightarrow D\pi^+$  and  $B^+ \rightarrow DK^+$  samples with a two-dimensional fit between  $\Delta E$  and  $C'_{\text{NN}}$ . The two-dimensional distributions of these variables are analysed for signal and background events separately to check if there is any correlation between them. They are shown in Fig. 5.28. There is no visible correlation observed between the variables. The correlation coefficients obtained are  $9.18 \times 10^{-5}$ , 0.01 and  $-0.04$  for signal, continuum background and combinatorial  $B\bar{B}$  background events, respectively. Since these values are small, the two-dimensional PDF is obtained by multiplying the corresponding one-dimensional PDFs.

A simultaneous extended maximum likelihood fit is performed to  $B^+ \rightarrow D\pi^+$  and  $B^+ \rightarrow DK^+$  samples. This allows for the cross-feed peaking background to be determined directly from data. The signal and cross-feed peaking background yields are expressed in terms of the kaon identification efficiency  $\epsilon = 0.8541 \pm 0.0006$  and pion fake rate  $\kappa = 0.0447 \pm 0.0003$  in MC [84]. From the total  $B^+ \rightarrow D\pi^+$  events ( $N_{D\pi}$ ) and total  $B^+ \rightarrow DK^+$  events ( $N_{DK}$ ), the following yields are calculated:

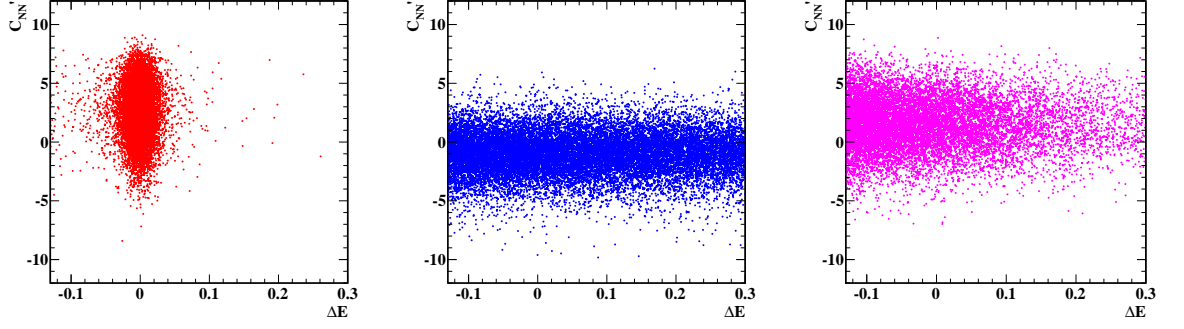


Figure 5.28: Two-dimensional distributions between  $\Delta E$  and  $C'_{NN}$  of signal (left), continuum (middle) and combinatorial  $B\bar{B}$  background (right) events from  $B^+ \rightarrow D(K_S^0 \pi^+ \pi^- \pi^0) \pi^+$  generic MC sample.

- $B^+ \rightarrow D\pi^+$  signal =  $N_{D\pi}(1 - \kappa)$ .
- $B^+ \rightarrow DK^+$  in  $B^+ \rightarrow D\pi^+$  peaking background =  $N_{DK}(1 - \epsilon)$ .
- $B^+ \rightarrow DK^+$  signal =  $N_{DK}\epsilon$ .
- $B^+ \rightarrow D\pi^+$  in  $B^+ \rightarrow DK^+$  peaking background =  $N_{D\pi}\kappa$ .

The signal and cross-feed peaking backgrounds are defined as mentioned above in the fit, where  $\epsilon$  and  $\kappa$  values are fixed parameters. The PDFs and the parameter information used in the simultaneous fit are summarized in Table 5.13. A scaling factor ( $f_{\Delta E}$ ) is applied on the  $\Delta E$  signal resolution. An additional shift ( $m_{\text{shift}}$ ) is applied on the continuum background mean value as well as a scaling factor ( $f_{C'_{NN}}$ ) to the resolution of  $C'_{NN}$ . They are introduced to account for the corresponding data-MC differences.

The final signal extraction to estimate  $x_{\pm}$  and  $y_{\pm}$  parameters requires the separation of  $B^+$  and  $B^-$  decays in each bin. So the simultaneous fit is performed in the following four categories:

- $B^+ \rightarrow D\pi^+$ ,
- $B^- \rightarrow D\pi^-$ ,
- $B^+ \rightarrow DK^+$  and
- $B^- \rightarrow DK^-$ ,

in the nine bins of  $D$  phase space.

Component	Category	$\Delta E$	$C'_{\text{NN}}$
Signal	$B^+ \rightarrow D\pi^+$	Crystal Ball + two Gaussians	Asymmetric Gaussian + Gaussian
	$B^+ \rightarrow DK^+$	same PDF mean separate other parameters common	same PDF mean separate other parameters common
Continuum background	$B^+ \rightarrow D\pi^+$	first-order Chebyshev	two Gaussians
	$B^+ \rightarrow DK^+$	same PDF $b_1$ separate	same PDF $f_{C'_{\text{NN}}}, m_{\text{shift}}$ common other parameters separate
Combinatorial $B\bar{B}$ background	$B^+ \rightarrow D\pi^+$	exponential + Crystal Ball	Asymmetric Gaussian
	$B^+ \rightarrow DK^+$	exponential + Crystal Ball + first-order Chebyshev $a$ separate Crystal Ball common	same PDF  all parameters common
Cross-feed peaking background	$B^+ \rightarrow D\pi^+$	three Gaussians	same as signal PDF no additional parameters
	$B^+ \rightarrow DK^+$	three Gaussians all parameters separate	same as signal PDF no additional parameters

Table 5.13: The PDFs used in the simultaneous fit of  $B^+ \rightarrow D\pi^+$  and  $B^+ \rightarrow DK^+$  decays along with the parameter information.

### Fit in $D$ phase space bins

The lower statistics of the  $B$  sample does not allow for independent fits to be performed in each bin. So a combined fit with a common likelihood in all the bins is performed to determine the signal yields in the respective bins.

The simultaneous fit is performed with 36 categories in total (9 phase space bins  $\times$  2 for charge of  $B \times$  2 for  $B \rightarrow D\pi$  and  $B \rightarrow DK$ ). The signal and background distributions in the bins are compared to check if a common model can be used to describe each of them. The  $\Delta E$  distributions are shown in Fig. 5.29, 5.30 and 5.31. The signal and continuum background distributions in each bin matches with the total shape. There is significant mismatch for combinatorial  $B\bar{B}$  background events in bin 1 compared to the rest of the bins. Hence a separate parameter is used in bin 1 to account for this difference possibly coming from partially reconstructed  $B \rightarrow \omega X$  modes.

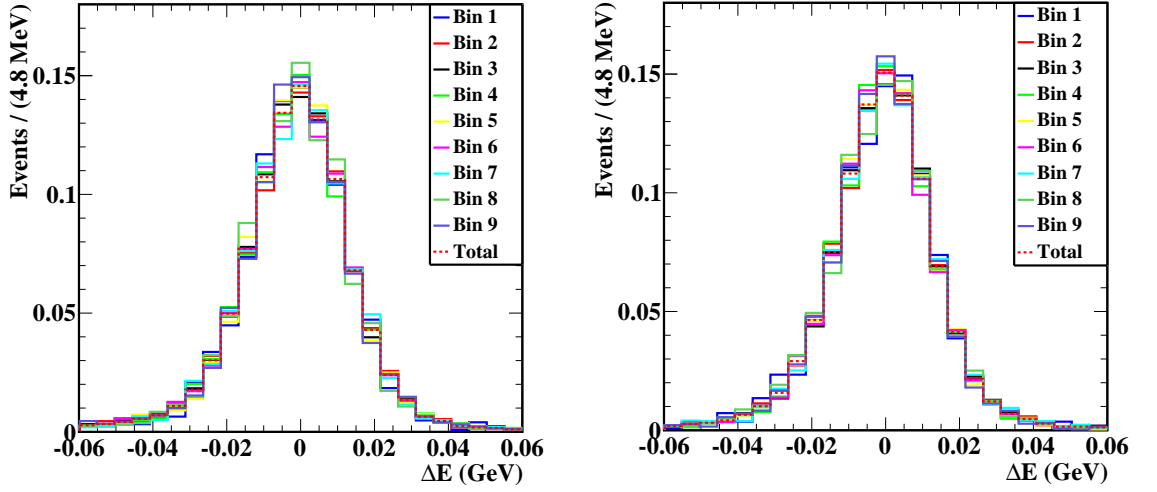


Figure 5.29:  $\Delta E$  distribution of signal events in  $B^+ \rightarrow D\pi^+$  (left) and  $B^+ \rightarrow DK^+$  decays in each bin as well as in the integrated  $D$  phase space in signal MC sample.

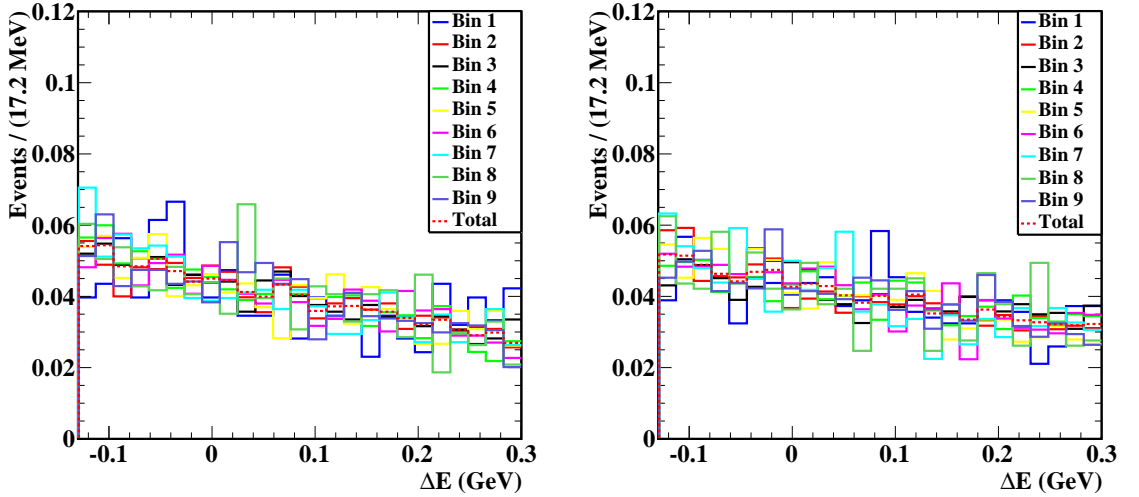


Figure 5.30:  $\Delta E$  distribution of continuum background events in  $B^+ \rightarrow D\pi^+$  (left) and  $B^+ \rightarrow DK^+$  decays in each bin as well as in the integrated  $D$  phase space in generic MC sample.

The  $C'_{NN}$  distributions in each bin for signal and background events are in good agreement with the respective total shapes as illustrated in Fig. 5.32, 5.33 and 5.34. So a common PDF model is used to describe the  $C'_{NN}$  distributions in each bin for the respective signal and background events. The parameters  $f_{\Delta E}$ ,  $f_{C'_{NN}}$  and  $m_{\text{shift}}$  along with the individual component yields,  $\Delta E$  signal mean,  $\Delta E$  continuum background parameter  $b_1$  and  $\Delta E$  combinatorial  $B\bar{B}$  background parameter  $a$  are set free in the fit, while all the other shape parameters are fixed to the values obtained in the one-dimensional component fits.

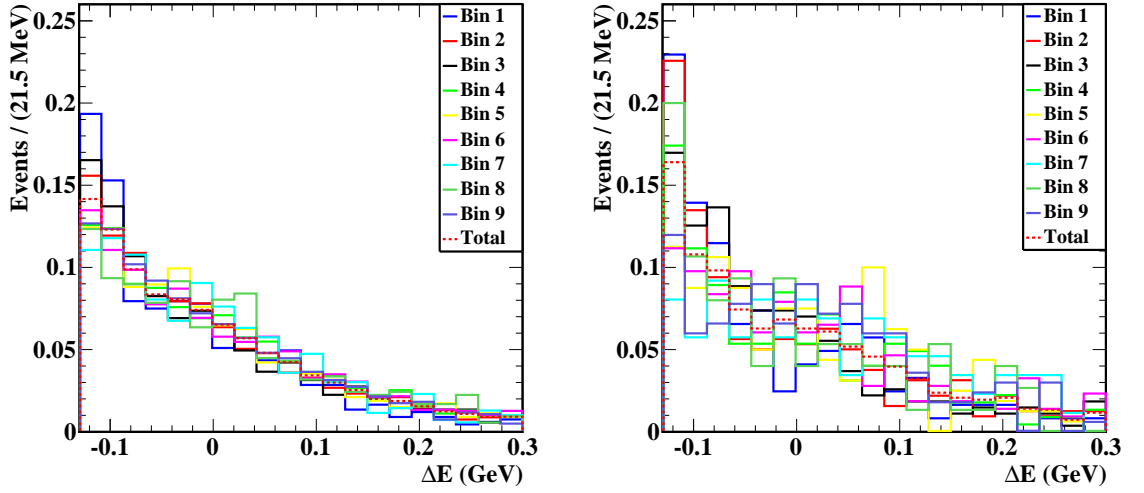


Figure 5.31:  $\Delta E$  distribution of combinatorial  $B\bar{B}$  background events in  $B^+ \rightarrow D\pi^+$  (left) and  $B^+ \rightarrow DK^+$  decays in each bin as well as in the integrated  $D$  phase space in generic MC sample.

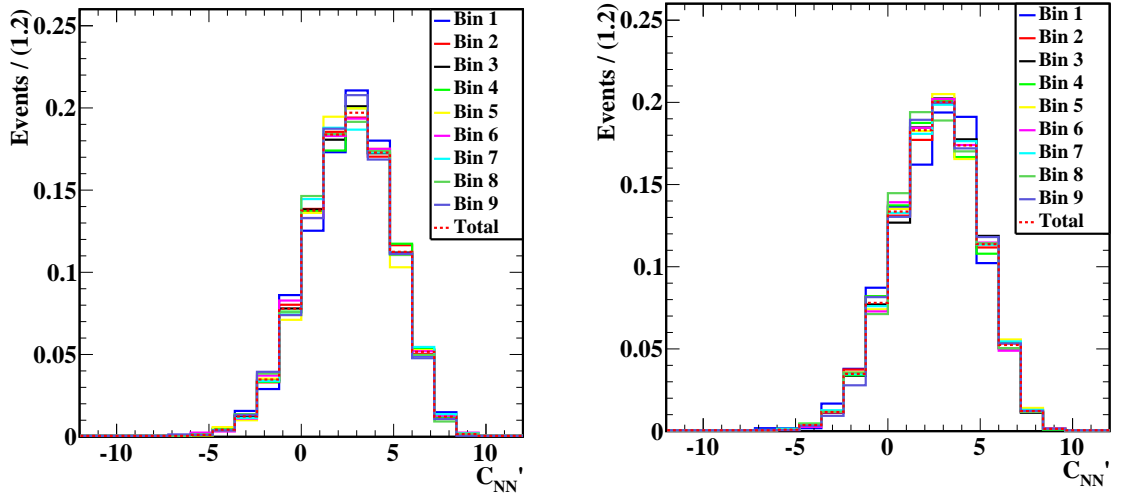


Figure 5.32:  $C'_{NN}$  distribution of signal events in  $B^+ \rightarrow D\pi^+$  (left) and  $B^+ \rightarrow DK^+$  decays in each bin as well as in the integrated  $D$  phase space in signal MC sample.

The fit is performed in generic MC sample having integrated luminosity equivalent to five times that of the data sample to reduce the statistical fluctuations and the deviations in the fit results of component yields from their true values are analysed. The residual values are given in Table 5.14. There are a total of 72 observables out of which 25 of them deviate above  $1\sigma$  from the true values. This is expected for a normally distributed sample and confirms that the fit model is not introducing any bias to the results. The signal-enhanced fit projections of  $\Delta E$  and  $C'_{NN}$  in bin 1 of  $B^\pm \rightarrow D\pi^\pm$  and  $B^\pm \rightarrow DK^\pm$  decays in generic MC sample having integrated luminosity equivalent

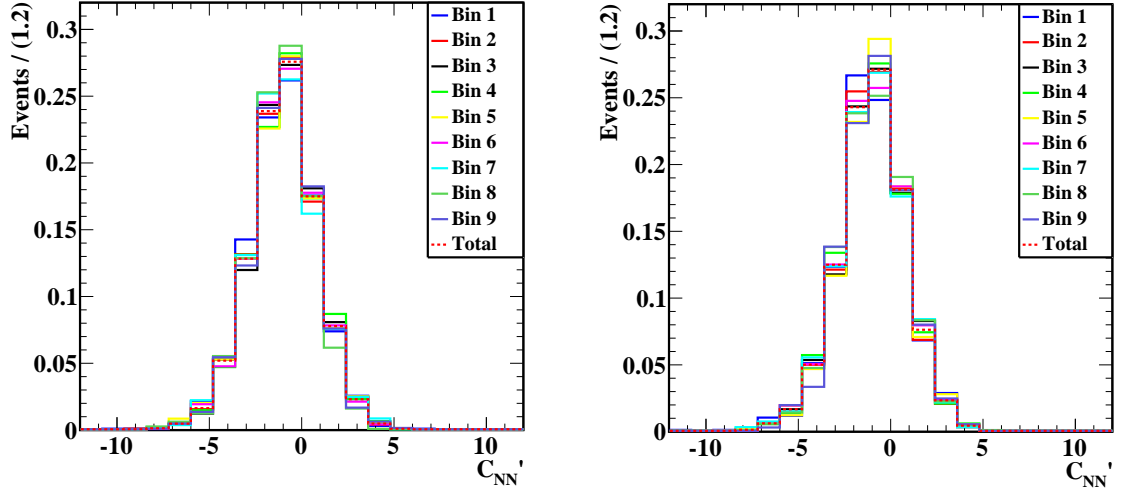


Figure 5.33:  $C'_{NN}$  distribution of continuum background events in  $B^+ \rightarrow D\pi^+$  (left) and  $B^+ \rightarrow DK^+$  decays in each bin as well as in the integrated  $D$  phase space in generic MC sample.

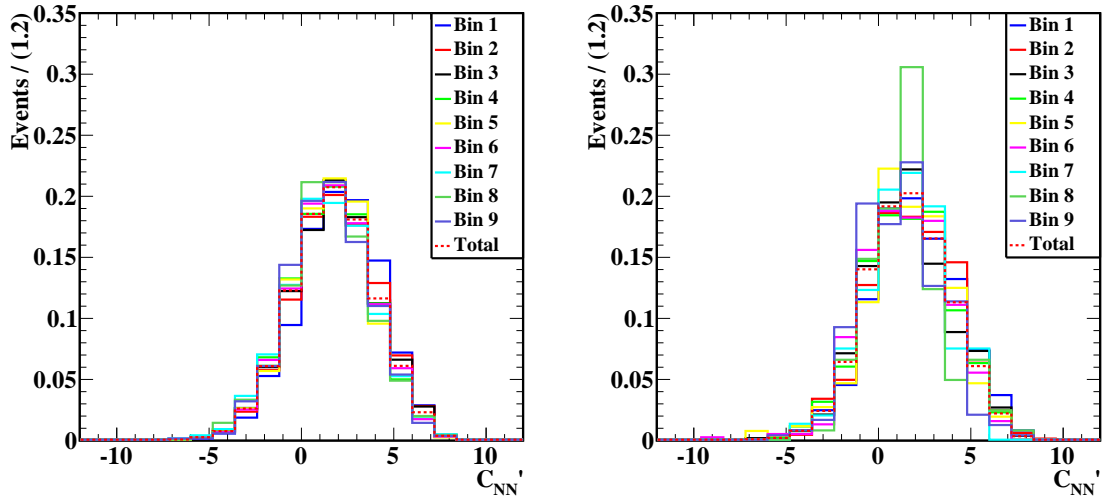


Figure 5.34:  $C'_{NN}$  distribution of combinatorial  $B\bar{B}$  background events in  $B^+ \rightarrow D\pi^+$  (left) and  $B^+ \rightarrow DK^+$  decays in each bin as well as in the integrated  $D$  phase space in generic MC sample.

lent to that of the data sample are shown in Fig. 5.35 and 5.36, the signal yields in each bin are given in Table 5.15 and the other shape parameters, which are set free in the fit, are given in Table 5.16. The corresponding fit projections for bins 2–9 are given in Appendix C. The signal regions are defined as  $|\Delta E| < 0.05$  GeV and  $C'_{NN} > 0$ . The scale factors and mean shift are consistent with their expected values of one and zero, respectively, in MC.

Bin	$N_{D\pi}$		$N_{DK}$		$N_{D\pi}^{q\bar{q}}$		$N_{DK}^{q\bar{q}}$		$N_{D\pi}^{BB}$		$N_{DK}^{BB}$	
	$B^+$	$B^-$	$B^+$	$B^-$	$B^+$	$B^-$	$B^+$	$B^-$	$B^+$	$B^-$	$B^+$	$B^-$
1	-0.7	-0.4	0.1	-0.5	-0.7	-1.2	-0.1	-0.9	0.9	1.4	0.7	1.7
2	-0.3	-1.8	-0.6	0.7	1.5	-2.4	-0.3	-1.7	-1.6	3.6	1.0	2.5
3	-1.0	-0.4	0.9	0.9	-0.7	3.1	-0.9	0.2	1.0	-3.4	1.9	0.7
4	-0.3	-1.2	0.5	-0.3	1.1	-0.3	0.4	0.1	-0.9	0.9	-0.9	0.2
5	0.2	-0.3	0.5	-0.5	0.7	1.0	-0.7	-0.1	-0.8	-0.9	0.7	0.2
6	-0.7	0.4	1.3	0.9	1.2	1.9	-0.1	0.1	-0.9	-2.2	-0.5	-0.3
7	0.4	0.6	-0.1	0.4	1.7	1.6	0.4	0.9	-2.1	-1.9	-0.6	-1.9
8	0.3	0.5	-0.3	1.8	2.6	0.7	-0.1	1.0	-2.9	1.2	0.2	2.5
9	-0.3	0.2	1.3	2.2	-0.2	-0.1	0.2	0.4	0.3	-0.1	-0.7	1.4

Table 5.14: Residuals of yields in nine bins from simultaneous fit to five independent samples of generic MC.

Bin	Resonance	$N_{D\pi}$		$N_{DK}$	
		$B^+$	$B^-$	$B^+$	$B^-$
1	$\omega$	$854 \pm 33$	$880 \pm 34$	$58 \pm 11$	$90 \pm 12$
2	$K^{*-}\rho^+$	$960 \pm 38$	$2578 \pm 60$	$53 \pm 13$	$173 \pm 19$
3	$K^{*+}\rho^-$	$1938 \pm 51$	$465 \pm 28$	$189 \pm 19$	$52 \pm 12$
4	$K^{*-}$	$340 \pm 25$	$413 \pm 28$	$46 \pm 11$	$28 \pm 10$
5	$K^{*+}$	$386 \pm 27$	$306 \pm 23$	$43 \pm 11$	$18 \pm 8$
6	$K^{*0}$	$409 \pm 27$	$378 \pm 27$	$48 \pm 11$	$11 \pm 8$
7	$\rho^+$	$180 \pm 18$	$189 \pm 19$	$10 \pm 7$	$9 \pm 5$
8	$\rho^-$	$118 \pm 15$	$85 \pm 13$	$5 \pm 5$	$19 \pm 7$
9	Remainder	$146 \pm 19$	$175 \pm 19$	$14 \pm 7$	$20 \pm 8$

Table 5.15: Signal yields in bins obtained from the total two-dimensional simultaneous fit to the nine bins of  $B^+ \rightarrow D\pi^+$  and  $B^+ \rightarrow DK^+$  decays in generic MC sample with integrated luminosity equivalent to that of data.

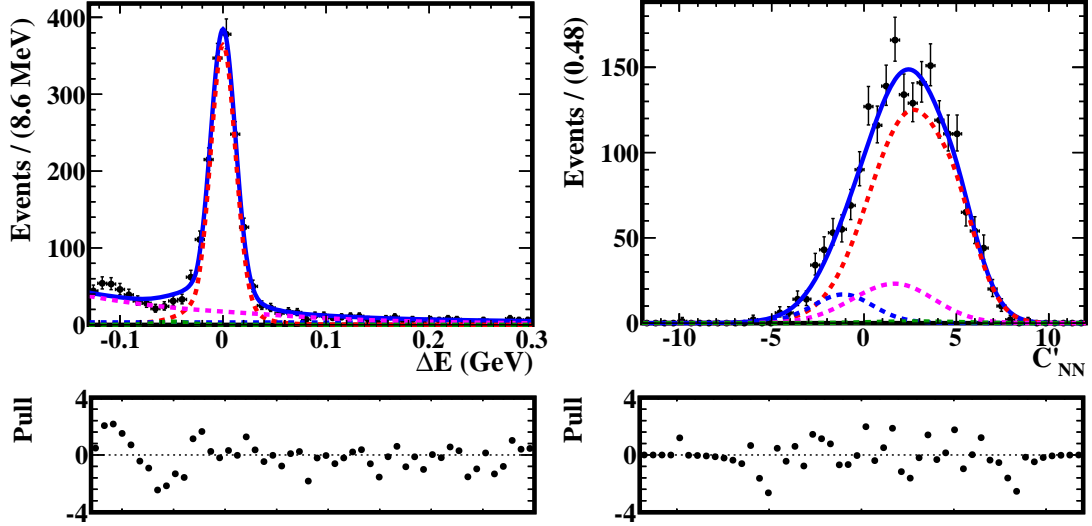


Figure 5.35: Signal-enhanced projections of  $\Delta E$  (left) and  $C'_{NN}$  (right) distributions of  $B^\pm \rightarrow D(K_S^0 \pi^+ \pi^- \pi^0) \pi^\pm$  decays in bin 1 from a two-dimensional simultaneous fit to  $B^\pm \rightarrow D\pi^\pm$  and  $B^\pm \rightarrow DK^\pm$  events in generic MC sample with integrated luminosity equivalent to that of data. The black points with error bars are the data and the solid blue curve is the total fit. The dotted red, blue, magenta, and green curves represent the signal, continuum, random  $B\bar{B}$  backgrounds and cross-feed peaking background components, respectively. The pull between the fit and the data is shown below the distributions.

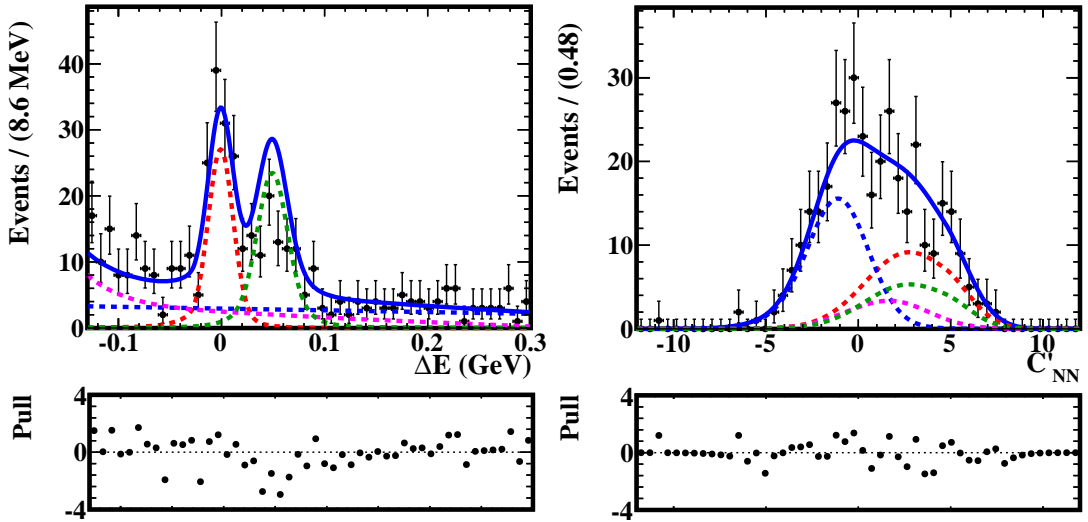


Figure 5.36: Signal-enhanced projections of  $\Delta E$  (left) and  $C'_{NN}$  (right) distributions of  $B^\pm \rightarrow D(K_S^0 \pi^+ \pi^- \pi^0) K^\pm$  decays in bin 1 from a two-dimensional simultaneous fit to  $B^\pm \rightarrow D\pi^\pm$  and  $B^\pm \rightarrow DK^\pm$  events in generic MC sample with integrated luminosity equivalent to that of data. The black points with error bars are the data and the solid blue curve is the total fit. The dotted red, blue, magenta, and green curves represent the signal, continuum, random  $B\bar{B}$  backgrounds and cross-feed peaking background components, respectively. The pull between the fit and the data is shown below the distributions.

Parameter	Fit result	
	$B^+ \rightarrow D\pi^+$	$B^+ \rightarrow DK^+$
$\Delta E$ mean	$-27.96 \pm 17.31$ MeV	$-1.170 \pm 0.765$ MeV
$f_{\Delta E}$	$0.991 \pm 0.013$	$0.991 \pm 0.013$
$f_{C'_{\text{NN}}}$	$0.995 \pm 0.006$	$0.995 \pm 0.006$
$m_{\text{shift}}$	$-0.003 \pm 0.014$	$-0.003 \pm 0.014$
$b_0$ of continuum background	$-0.318 \pm 0.015$	$-0.257 \pm 0.015$
$a_{\text{bin 1}}$ of combinatorial $B\bar{B}$ background	$-8.48 \pm 0.66$	$-54.89 \pm 2.15$
$a$ of combinatorial $B\bar{B}$ background	$-6.98 \pm 0.16$	$-40.50 \pm 6.76$

Table 5.16: PDF shape parameter values obtained from the total two-dimensional simultaneous fit to the nine bins of  $B^+ \rightarrow D\pi^+$  and  $B^+ \rightarrow DK^+$  generic MC sample with integrated luminosity equivalent to that of data.

The fit is then applied simultaneously to the nine bins in the total data sample. The kaon identification efficiency and pion fake rate in data,  $\epsilon = 0.8432 \pm 0.0039$  and  $\kappa = 0.0794 \pm 0.0031$  [84], are used in the fit. The signal-enhanced projections of  $\Delta E$  and  $C'_{\text{NN}}$  distributions in bin 1 for  $B^\pm \rightarrow D\pi^\pm$  and  $B^\pm \rightarrow DK^\pm$  decays are shown in Fig 5.37 and 5.38, respectively. The corresponding distributions for bins 2–9 are given in Appendix C. The signal yields in each bin obtained from the fit are given in Table 5.17. The PDF shape parameter values obtained from the fit are given in Table 5.18. The uncertainties on the yields in data are comparable to that obtained from MC. The resolution is found to be worse than that in MC and the additional shift on the continuum  $C'_{\text{NN}}$  mean is significantly away from zero. The  $B^+$  and  $B^-$  yields in bins 2, 3, 4, 5, 7 and 8 are significantly different from each other as the resonances in them are not  $CP$  self-conjugate. The  $B^+$  and  $B^-$  yields in  $CP$  self-conjugate bins (1, 6 and 9) are comparable to each other.

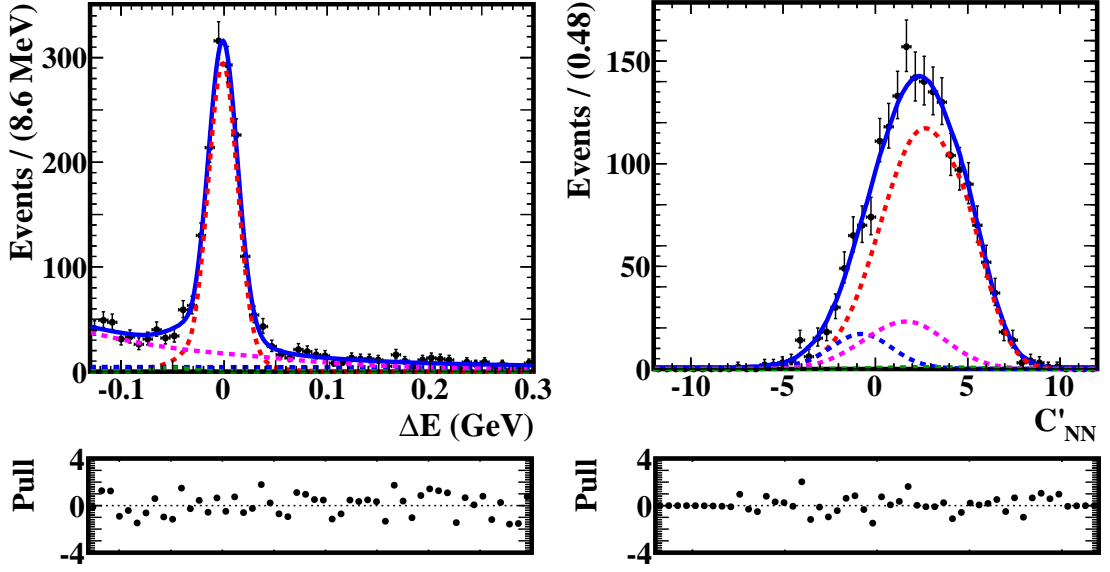


Figure 5.37: Signal-enhanced projections of  $\Delta E$  (left) and  $C'_{\text{NN}}$  (right) distributions of  $B^\pm \rightarrow D(K_S^0 \pi^+ \pi^- \pi^0) \pi^\pm$  decays in bin 1 from a two-dimensional simultaneous fit to  $B^\pm \rightarrow D\pi^\pm$  and  $B^\pm \rightarrow DK^\pm$  events in data. The black points with error bars are the data and the solid blue curve is the total fit. The dotted red, blue, magenta, and green curves represent the signal, continuum, random  $B\bar{B}$  backgrounds and cross-feed peaking background components, respectively. The pull between the fit and the data is shown below the distributions.

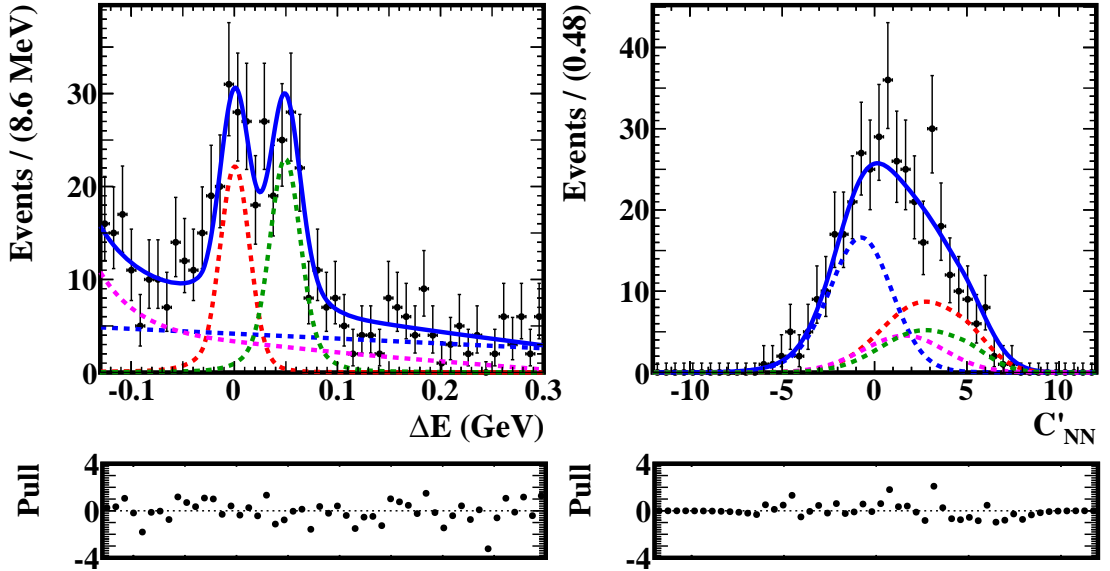


Figure 5.38: Signal-enhanced projections of  $\Delta E$  (left) and  $C'_{\text{NN}}$  (right) distributions of  $B^\pm \rightarrow D(K_S^0 \pi^+ \pi^- \pi^0) K^\pm$  decays in bin 1 from a two-dimensional simultaneous fit to  $B^\pm \rightarrow D\pi^\pm$  and  $B^\pm \rightarrow DK^\pm$  events in data. The black points with error bars are the data and the solid blue curve is the total fit. The dotted red, blue, magenta, and green curves represent the signal, continuum, random  $B\bar{B}$  backgrounds and cross-feed peaking background components, respectively. The pull between the fit and the data is shown below the distributions.

Bin	Resonance	$N_{D\pi}$		$N_{DK}$	
		$B^+$	$B^-$	$B^+$	$B^-$
1	$\omega$	$772 \pm 33$	$860 \pm 34$	$80 \pm 13$	$58 \pm 12$
2	$K^{*-}\rho^+$	$1077 \pm 41$	$2088 \pm 55$	$98 \pm 16$	$190 \pm 21$
3	$K^{*+}\rho^-$	$1639 \pm 49$	$450 \pm 28$	$121 \pm 18$	$57 \pm 13$
4	$K^{*-}$	$263 \pm 24$	$451 \pm 29$	$21 \pm 9$	$30 \pm 11$
5	$K^{*+}$	$377 \pm 27$	$256 \pm 23$	$23 \pm 9$	$18 \pm 9$
6	$K^{*0}$	$338 \pm 26$	$321 \pm 26$	$35 \pm 11$	$23 \pm 9$
7	$\rho^+$	$253 \pm 21$	$255 \pm 22$	$16 \pm 9$	$5 \pm 7$
8	$\rho^-$	$154 \pm 17$	$109 \pm 15$	$9 \pm 6$	$13 \pm 7$
9	Remainder	$162 \pm 19$	$138 \pm 19$	$21 \pm 9$	$30 \pm 10$

Table 5.17: Signal yield in nine  $D$  phase space bin for  $B^+ \rightarrow D\pi^+$  and  $B^+ \rightarrow DK^+$  decays in data.

Parameter	Fit result	
	$B^+ \rightarrow D\pi^+$	$B^+ \rightarrow DK^+$
$\Delta E$ mean	$-1.447 \pm 0.215$ MeV	$-1.835 \pm 1.050$ MeV
$f_{\Delta E}$	$1.123 \pm 0.017$	$1.123 \pm 0.017$
$f_{C'_{NN}}$	$1.012 \pm 0.007$	$1.012 \pm 0.007$
$m_{\text{shift}}$	$0.204 \pm 0.017$	$0.204 \pm 0.017$
$b_0$ of continuum background	$-0.251 \pm 0.017$	$-0.252 \pm 0.017$
$a_{\text{bin } 1}$ of combinatorial $B\bar{B}$ background	$-6.38 \pm 0.50$	$-52.55 \pm 2.42$
$a$ of combinatorial $B\bar{B}$ background	$-6.65 \pm 0.17$	$-31.38 \pm 4.52$

Table 5.18: PDF shape parameter values obtained from the total two-dimensional simultaneous fit to the nine bins of  $B^+ \rightarrow D\pi^+$  and  $B^+ \rightarrow DK^+$  decays in data sample.

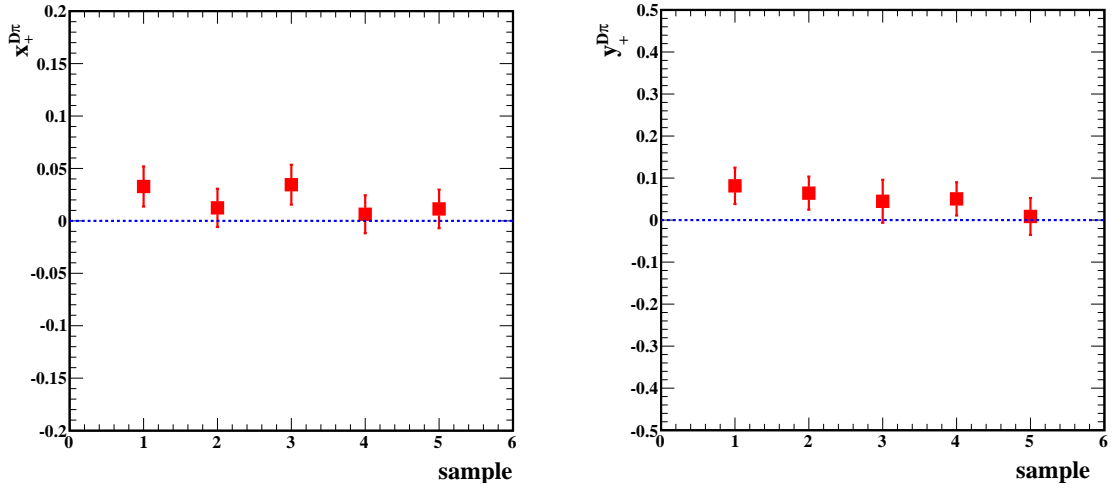


Figure 5.39:  $x_+$  (left) and  $y_+$  (right) results for  $B^+ \rightarrow D\pi^+$  decays in five independent generic MC samples.

### 5.3.5 Extraction of $x_{\pm}$ and $y_{\pm}$ parameters

The  $x_{\pm}$  and  $y_{\pm}$  parameters are directly extracted from the simultaneous fit by expressing  $N_{D\pi}$  and  $N_{DK}$ , the total number of  $B^+ \rightarrow D\pi^+$  and  $B^+ \rightarrow DK^+$  yields, as in Eq. (1.32) and (1.33). The  $c_i$ ,  $s_i$ ,  $K_i$  and  $\bar{K}_i$  parameters are external inputs, which are fixed to the values of  $c_i$  and  $s_i$  reported in Ref. [92] and  $K_i$  and  $\bar{K}_i$  reported in Sec. 5.2. The yields are corrected for efficiency ( $\epsilon$ ) as  $Y_i' = Y_i/\epsilon_i$  and the bin-to-bin migration is corrected as  $Y_i = \sum_j M_{ij} Y_j$ , where  $M_{ij}$  is the migration matrix. The fit is performed in five independent generic MC samples and the results are given in Fig. 5.39, 5.40, 5.41 and 5.42.

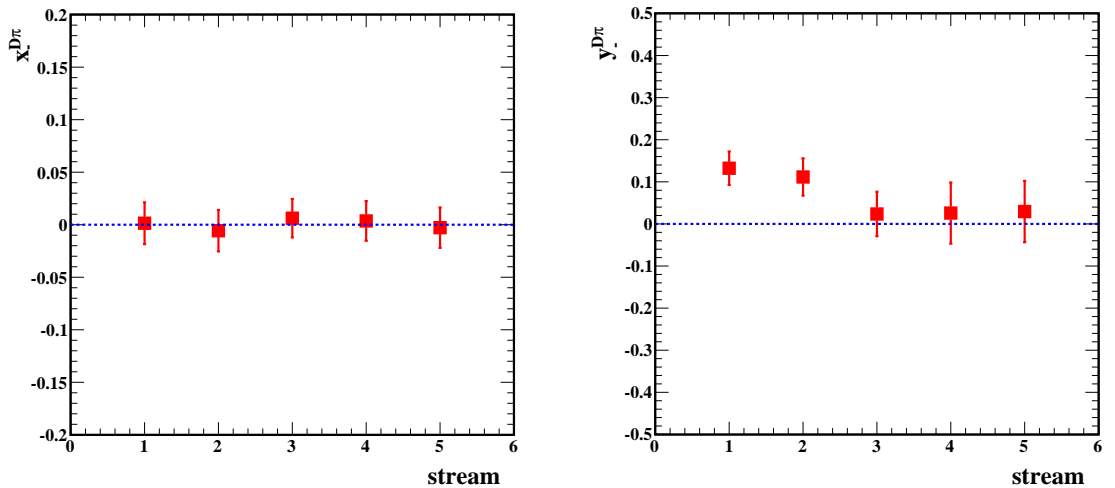


Figure 5.40:  $x_-$  (left) and  $y_-$  (right) results for  $B^- \rightarrow D\pi^-$  decays in five independent generic MC samples.

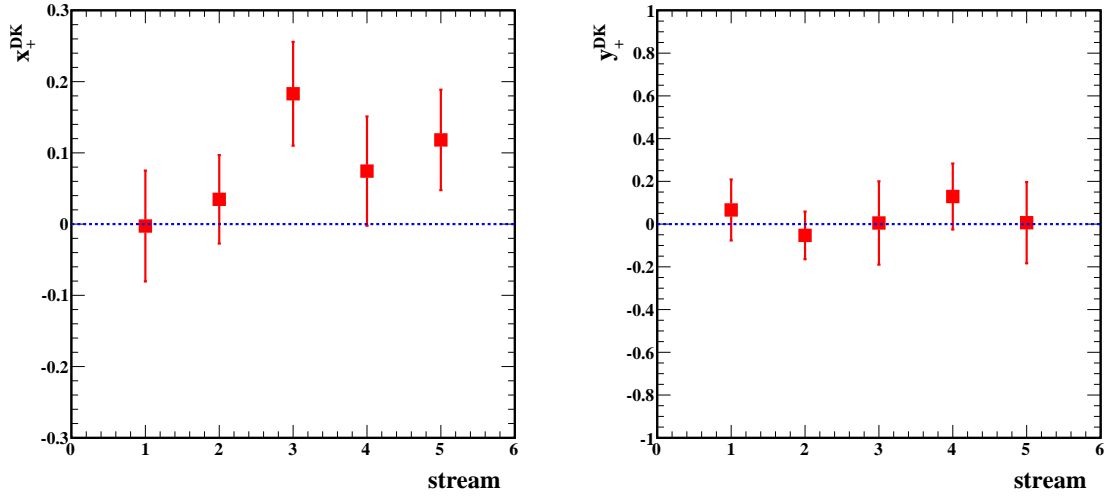


Figure 5.41:  $x_+$  (left) and  $y_+$  (right) results for  $B^+ \rightarrow DK^+$  decays in five independent generic MC samples.

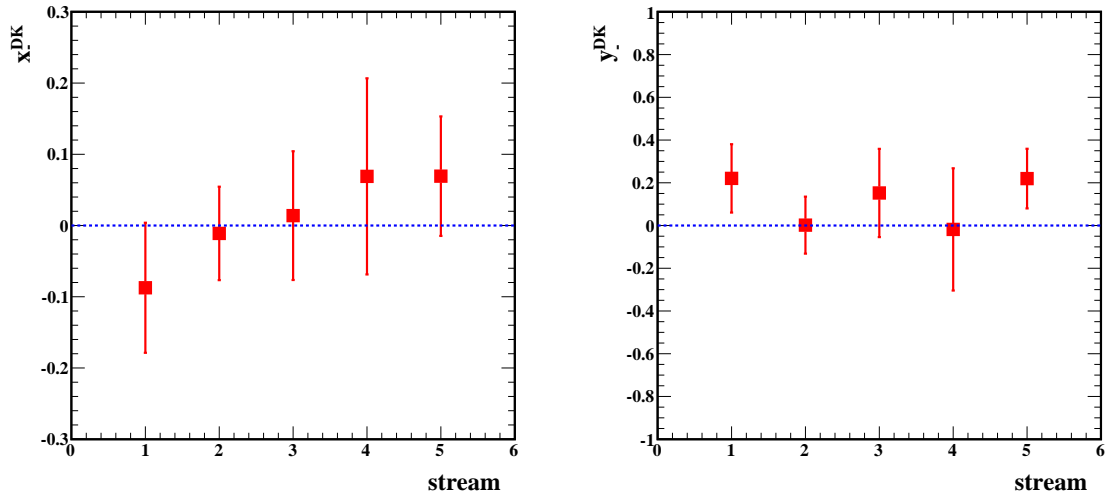


Figure 5.42:  $x_-$  (left) and  $y_-$  (right) results for  $B^- \rightarrow DK^-$  decays in five independent generic MC samples.

The results in MC are consistent with zero for the  $x_{\pm}$  and  $y_{\pm}$  parameters. The statistical likelihood contours for one set of generic MC sample are shown in Fig. 5.43. They intersect at (0,0) as expected in MC, where there is no  $CP$  violation effects. The results obtained in the remaining four sets of generic MC samples are also consistent with no  $CP$  violation. The measured and expected yields for one set of the binned  $B^+$  and  $B^-$  generic MC samples are compared in Fig. 5.44 and 5.45. There are no persistent deviations observed in any particular bin in the MC samples.

We have performed 250 pseudo-experiments to check if there is any bias in the measurement of  $x_{\pm}$  and  $y_{\pm}$  parameters introduced by the fit model. Samples are generated

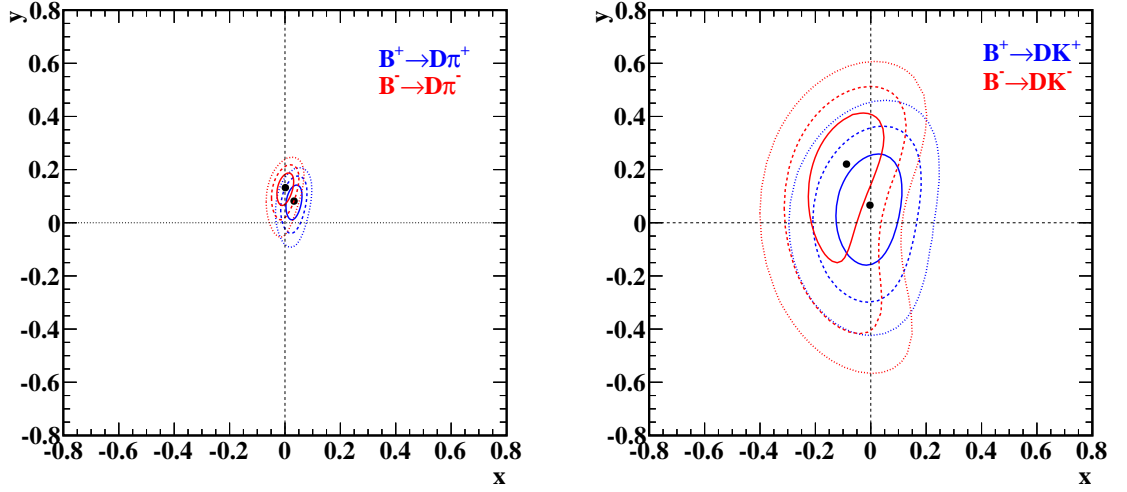


Figure 5.43: One (solid line), two (dashed line), and three (dotted line) standard deviation likelihood contours for the  $(x_{\pm}, y_{\pm})$  parameters for  $B^{\pm} \rightarrow D\pi^{\pm}$  (left) and  $B^{\pm} \rightarrow DK^{\pm}$  (right) decays in generic MC sample. The point marks the best fit value.

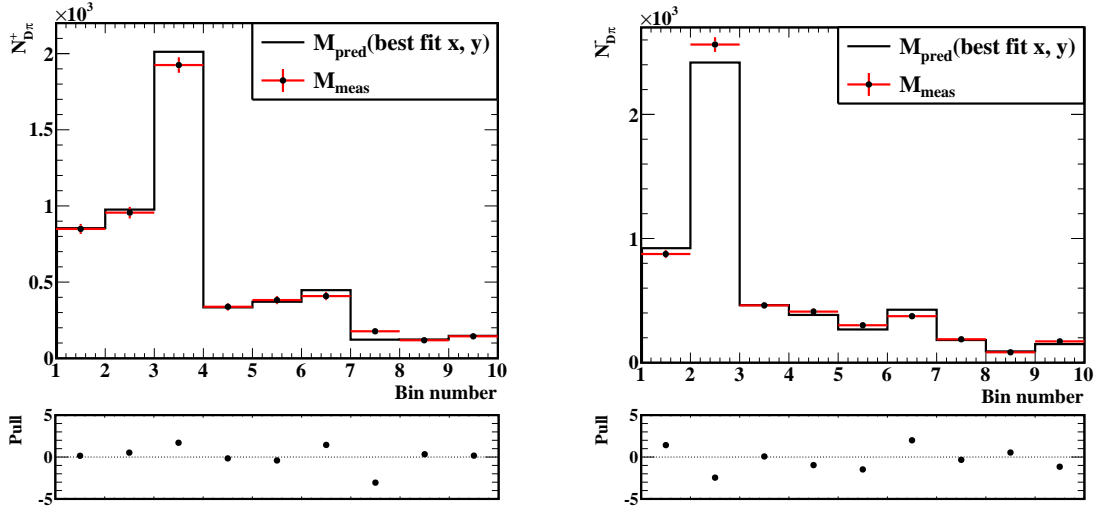


Figure 5.44: Measured and expected yields in bins for  $B^+ \rightarrow D\pi^+$  (left) and  $B^- \rightarrow D\pi^-$  (right) decays in generic MC sample. The data points with error bars are the measured yields and the solid histogram is the expected yield from the best fit  $(x_{\pm}, y_{\pm})$  parameter values.

according to the fit model and then they are fitted back to check the results. The pull distributions are fitted with a Gaussian PDF and we found that all the mean and width are consistent with 0 and 1, respectively, within their uncertainties as given in Table 5.19. This confirms that the fit model is unbiased and ready to be used on the data sample. The pull, error and parameter values of  $x_{\pm}$  and  $y_{\pm}$  returned from these fits are shown in Appendix D.

The  $x_{\pm}$  and  $y_{\pm}$  parameters are determined in data sample for  $B^+ \rightarrow D\pi^+$  and

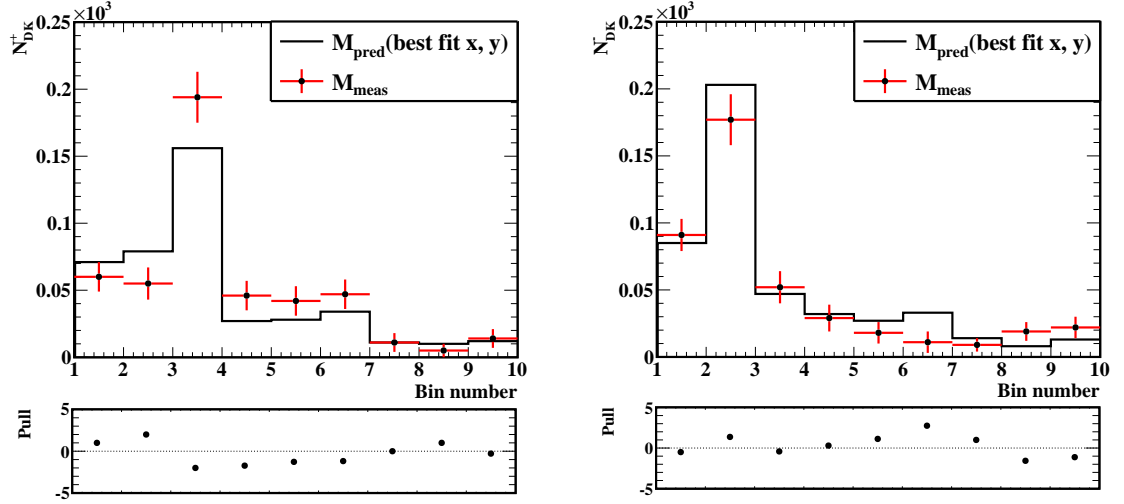


Figure 5.45: Measured and expected yields in bins for  $B^+ \rightarrow DK^+$  (left) and  $B^- \rightarrow DK^-$  (right) decays in generic MC sample. The data points with error bars are the measured yields and the solid histogram is the expected yield from the best fit  $(x_{\pm}, y_{\pm})$  parameter values.

Parameter	Pull mean	Pull width
$x_+^{D\pi}$	$0.009 \pm 0.087$	$0.927 \pm 0.063$
$y_+^{D\pi}$	$-0.092 \pm 0.106$	$1.046 \pm 0.096$
$x_-^{D\pi}$	$-0.041 \pm 0.090$	$0.965 \pm 0.060$
$y_-^{D\pi}$	$0.022 \pm 0.101$	$0.889 \pm 0.078$
$x_+^{DK}$	$0.188 \pm 0.101$	$1.035 \pm 0.068$
$y_+^{DK}$	$-0.008 \pm 0.108$	$1.261 \pm 0.099$
$x_-^{DK}$	$0.168 \pm 0.096$	$0.907 \pm 0.066$
$y_-^{DK}$	$-0.030 \pm 0.123$	$1.413 \pm 0.122$

Table 5.19: Mean and width of the pull distributions of  $x_{\pm}$  and  $y_{\pm}$  parameters from 250 pseudo-experiments.

$B^+ \rightarrow DK^+$  decays, simultaneously from the fit. The results obtained after the efficiency and migration corrections are given in Table 5.20. The asymmetric uncertainties are obtained from MINOS minimizer in RooFit. The statistical likelihood contours are shown in Fig. 5.46. The contours are consistent with (0,0) for  $B^{\pm} \rightarrow D\pi^{\pm}$  decays as they are not sensitive to  $\phi_3$  owing to the small value of  $r_B$ . The  $x_{\pm}$  and  $y_{\pm}$  results from  $B^{\pm} \rightarrow DK^{\pm}$  decays are consistent with the current world average values [29] within  $1\sigma$ . The statistical correlation matrices are given in Table 5.21 and 5.22. The measured and expected yields for the binned  $B^+$  and  $B^-$  data are compared in Fig. 5.47 and 5.48. There are no large deviations between the values in any of the bins.

Mode	$x_+$	$y_+$	$x_-$	$y_-$
$B^\pm \rightarrow D\pi^\pm$	$0.039 \pm 0.024$	$-0.196^{+0.080}_{-0.059}$	$-0.014 \pm 0.021$	$-0.033 \pm 0.059$
$B^\pm \rightarrow DK^\pm$	$-0.030 \pm 0.121$	$0.220^{+0.182}_{-0.541}$	$0.095 \pm 0.121$	$0.354^{+0.144}_{-0.197}$

Table 5.20:  $x_\pm$  and  $y_\pm$  results from  $B^\pm \rightarrow D\pi^\pm$  and  $B^\pm \rightarrow DK^\pm$  decays in data.

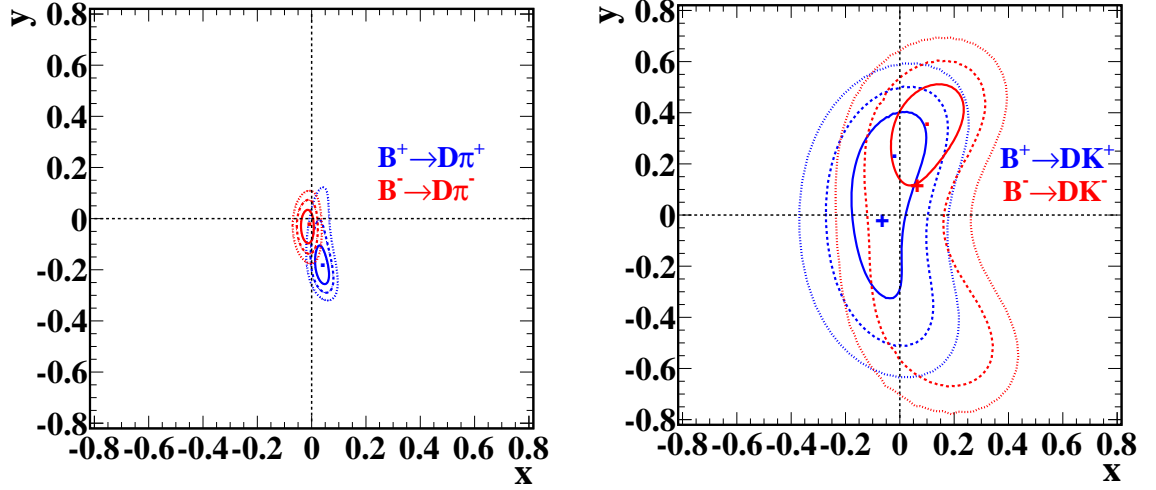


Figure 5.46: One (solid line), two (dashed line), and three (dotted line) standard deviation likelihood contours for the  $(x_\pm, y_\pm)$  parameters for  $B^\pm \rightarrow D\pi^\pm$  (left) and  $B^\pm \rightarrow DK^\pm$  (right) decays in data. The point marks the best fit value and the cross marks the expected value from the world average values of  $\phi_3$ ,  $r_B^{DK}$ , and  $\delta_B^{DK}$  [29].

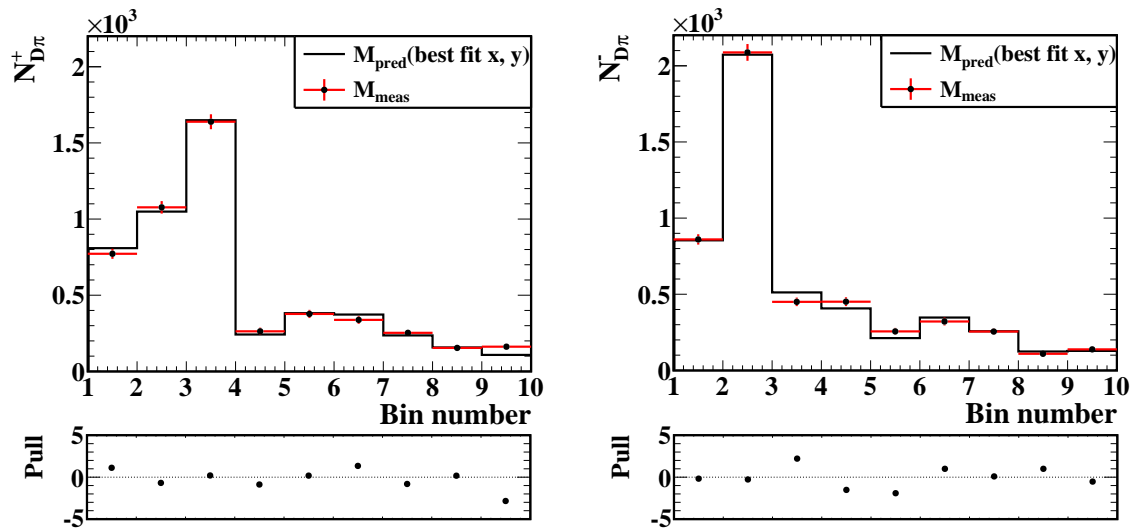


Figure 5.47: Measured and expected yields in bins for  $B^+ \rightarrow D\pi^+$  (left) and  $B^- \rightarrow D\pi^-$  (right) data samples. The data points with error bars are the measured yields and the solid histogram is the expected yield from the best fit  $(x_\pm, y_\pm)$  parameter values.

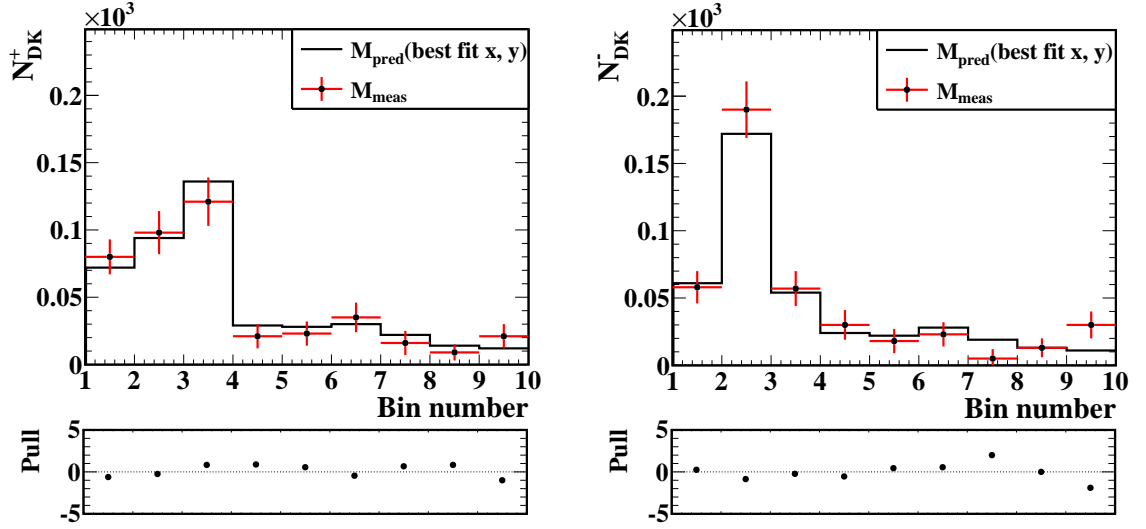


Figure 5.48: Measured and expected yields in bins for  $B^+ \rightarrow DK^+$  (left) and  $B^- \rightarrow DK^-$  (right) data samples. The data points with error bars are the measured yields and the solid histogram is the expected yield from the best fit  $(x_{\pm}, y_{\pm})$  parameter values.

	$x_+$	$y_+$	$x_-$	$y_-$
$x_+$	1	-0.364	0.314	0.050
$y_+$		1	0.347	0.055
$x_-$			1	-0.032
$y_-$				1

Table 5.21: Statistical correlation matrix for  $(x_+, y_+, x_-, y_-)$  measured from the  $B^{\pm} \rightarrow D\pi^{\pm}$  data sample

	$x_+$	$y_+$	$x_-$	$y_-$
$x_+$	1	0.486	0.172	-0.231
$y_+$		1	-0.127	0.179
$x_-$			1	0.365
$y_-$				1

Table 5.22: Statistical correlation matrix for  $(x_+, y_+, x_-, y_-)$  measured from the  $B^\pm \rightarrow DK^\pm$  data sample

## 5.4 Systematic uncertainties

We consider several possible sources of systematic uncertainty. The simultaneous fit performed in  $B^+ \rightarrow D\pi^+$  and  $B^+ \rightarrow DK^+$  decays ensures that systematic uncertainties arising from the reconstruction efficiencies of  $D$  meson final states are cancelled. The systematic uncertainties associated with the different sources are summarized in Table 5.23. The remainder of the section describes how the uncertainties are estimated.

The size of the signal MC sample used for estimating the efficiency and the migration matrix is a source of systematic uncertainty. Efficiencies in  $B$  and  $D^*$  samples are varied by their statistical uncertainty ( $\pm 1\sigma$ ) in each bin independently. The resultant negative and positive deviations in  $(x_\pm, y_\pm)$  are separately summed in quadrature. Similarly the migration matrix elements are varied by their statistical uncertainty in  $B$  and  $D^*$  samples, each element at a time. The resultant positive and negative deviations are considered separately. The effect of the difference in the efficiency variation across the bins for  $B$  and  $D^*$  samples is studied and we find no deviation in  $K_i$  and  $\overline{K}_i$  values within their statistical uncertainty, when the  $D^*$  efficiencies are varied by the maximum deviation found between the samples or  $D$  momentum range is changed to 1–3 GeV/ $c$ .

The systematic uncertainty from the difference in invariant mass resolution between data and the MC samples is considered by smearing the  $\pi^+\pi^-\pi^0$  invariant mass distribution by the uncertainty on the resolution scale factor obtained in data, when compared to that in MC. The resultant deviations in  $(x_\pm, y_\pm)$  are taken as the systematic uncertainty from this source. All the other resonances are wide and the resolution difference is an order of magnitude smaller than the resolution, thus the modelling of the resolution does not affect our measurements. The systematic effect of the uncertainty on the  $K_i$  and  $\overline{K}_i$  values is estimated by varying them by their statistical uncertainties independently. The resultant sum of deviations in quadrature is taken as the associated

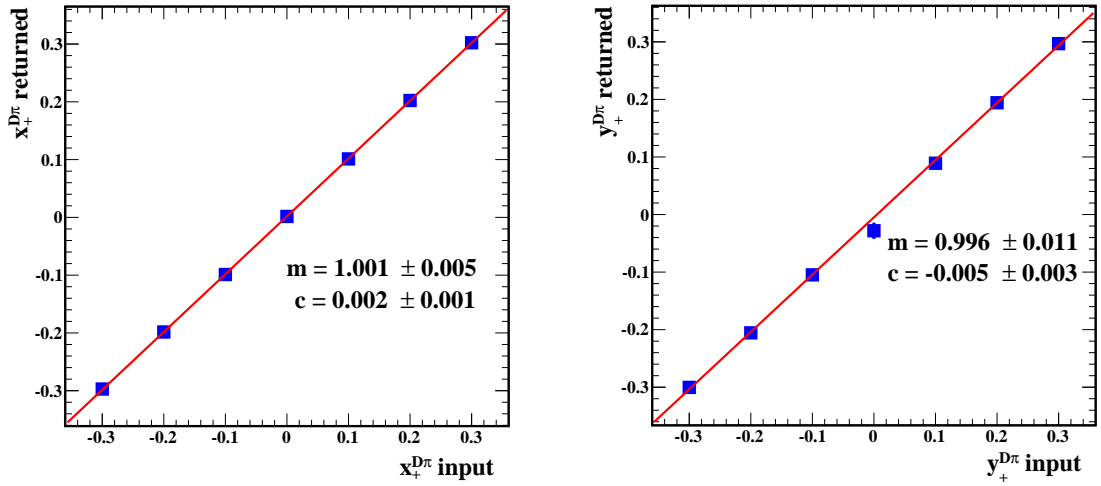


Figure 5.49:  $x_+^{D\pi}$  (left) and  $y_+^{D\pi}$  (right) results for different input values in 250 pseudo experiment sets each.

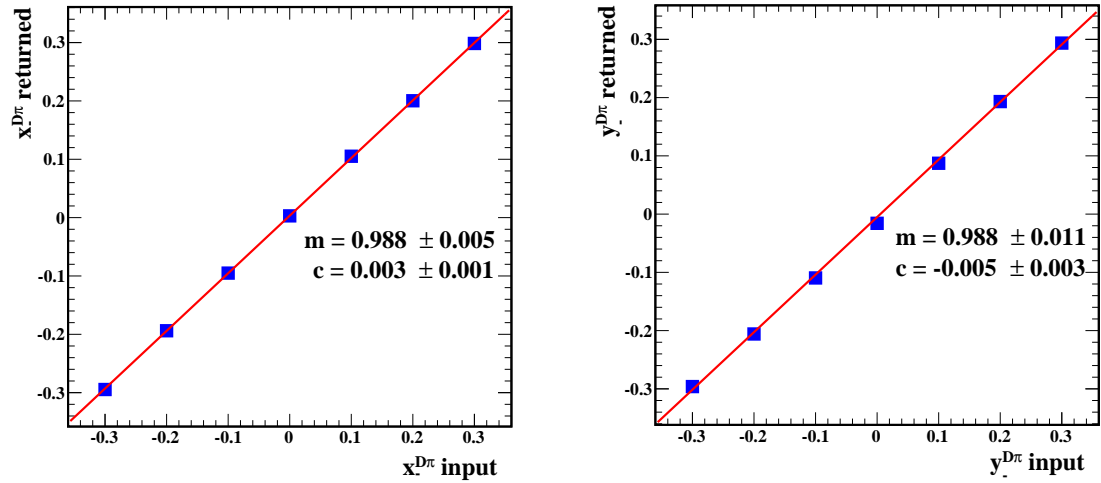


Figure 5.50:  $x_-^{D\pi}$  (left) and  $y_-^{D\pi}$  (right) results for different input values in 250 pseudo experiment sets each.

systematic uncertainty.

Modelling the data with PDFs that have parameters fixed to values obtained from MC samples is another source of systematic uncertainty. There are 14 signal shape parameters and 23 background shape parameters fixed in the  $B^\pm \rightarrow Dh^\pm$  simultaneous fit. These are fixed to the values obtained from MC. The uncertainty due to PDF modelling is taken into account by repeating the fit by individually varying the fixed parameters by  $\pm 1\sigma$ , where  $\sigma$  is the uncertainty on these parameters in MC component fits, and taking the difference in quadrature as the uncertainty.

Any possible bias in the fit is studied with a set of 250 pseudo-experiments with

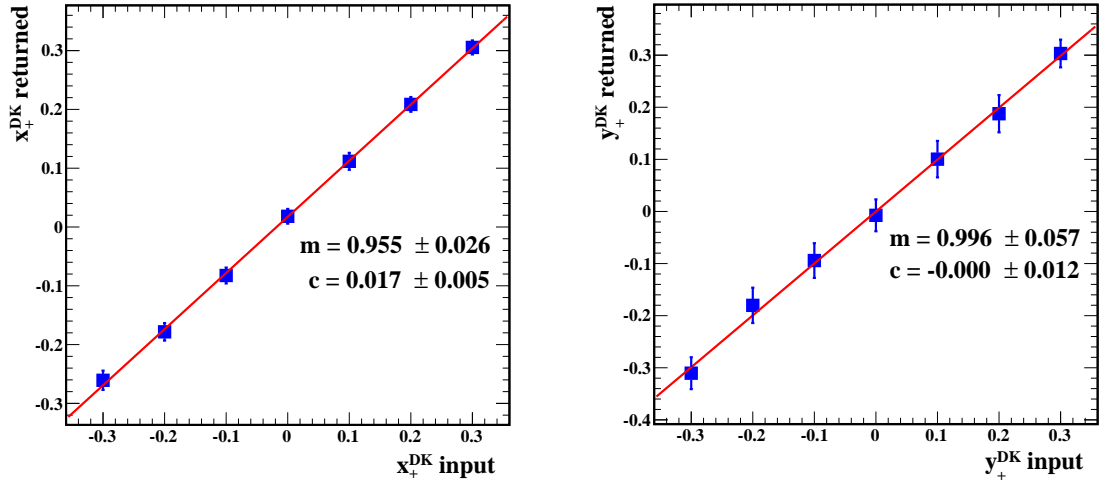


Figure 5.51:  $x_+^{DK}$  (left) and  $y_+^{DK}$  (right) results for different input values in 250 pseudo experiment sets each.

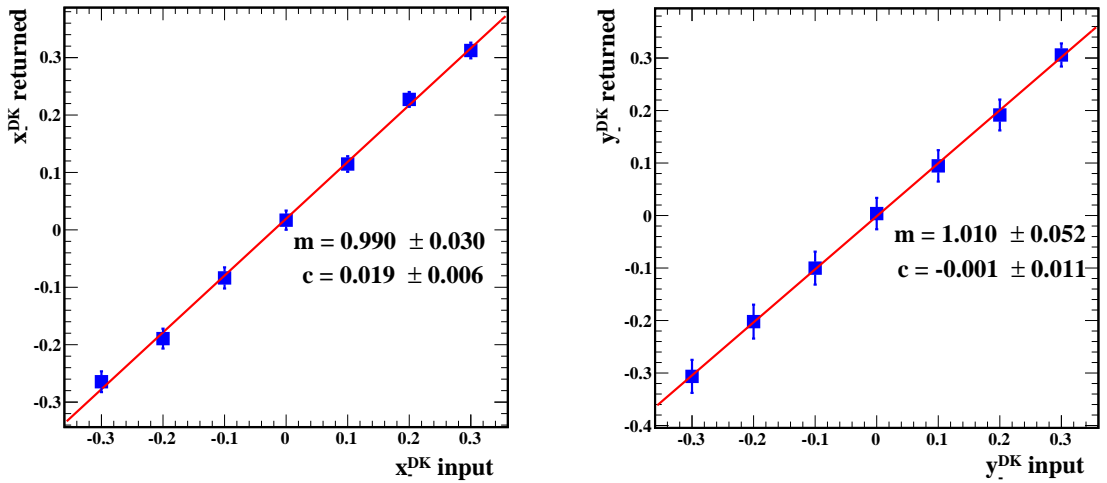


Figure 5.52:  $x_-^{DK}$  (left) and  $y_-^{DK}$  (right) results for different input values in 250 pseudo experiment sets each.

different input values for  $x_{\pm}$  and  $y_{\pm}$  as  $0, \pm 0.1, \pm 0.2$  and  $\pm 0.3$ . A plot between the input value and the fit result is expected to be a linear function with slope,  $m = 1$  and intercept,  $c = 0$ . The results obtained are shown in Fig. 5.51–5.52. The fit is found to give an unbiased response within the statistical uncertainties from the finite number of pseudo experiments, which is taken as the systematic uncertainty from this source. There is about  $3\sigma$  deviation in the  $c$  parameters of  $x_{\pm}^{DK}$  from their expected values, but this is negligible as it amounts to only 10% of the statistical uncertainty. There is no bias in the values of  $c$  for the larger statistics sample of  $B^+ \rightarrow D\pi^+$  decays.

The kaon identification efficiency and pion fake rate used in the fit are also fixed

Source	$B^\pm \rightarrow D\pi^\pm$				$B^\pm \rightarrow DK^\pm$			
	$x_+$	$y_+$	$x_-$	$y_-$	$x_+$	$y_+$	$x_-$	$y_-$
Efficiency	+0.013	+0.030	+0.012	+0.012	+0.012	+0.022	+0.012	+0.013
uncertainty	-0.009	-0.027	-0.008	-0.013	-0.013	-0.023	-0.012	-0.016
Migration matrix	+0.011	+0.021	+0.011	+0.013	+0.007	+0.015	+0.007	+0.006
uncertainty	-0.004	-0.019	-0.003	-0.014	-0.008	-0.016	-0.007	-0.012
$m_{\pi\pi\pi^0}$ resolution	0.003	0.001	0.004	0.001	0.001	0.001	0.001	0.003
$K_i, \bar{K}_i$	+0.004	+0.007	+0.004	+0.002	+0.001	+0.001	+0.002	+0.001
uncertainty	-0.001	-0.006	-0.001	-0.002	-0.002	-0.001	-0.002	-0.001
PDF shape	+0.004	+0.004	+0.004	+0.001	+0.009	+0.017	+0.009	+0.001
	-0.008	-0.003	-0.004	-0.001	-0.008	-0.016	-0.007	-0.005
Fit bias	0.000	0.001	0.000	0.000	0.001	0.001	0.001	0.003
PID	0.001	0.001	0.001	0.000	0.002	0.001	0.002	0.001
Total systematic	+0.018	+0.038	+0.018	+0.018	+0.017	+0.032	+0.017	+0.015
uncertainty	-0.013	-0.034	-0.010	-0.019	-0.018	-0.032	-0.016	-0.021
$c_i, s_i$	+0.014	+0.032	+0.010	+0.019	+0.019	+0.072	+0.023	+0.032
uncertainty	-0.012	-0.030	-0.006	-0.010	-0.018	-0.071	-0.025	-0.049
Total statistical	+0.024	+0.080	+0.021	+0.059	+0.121	+0.182	+0.121	+0.144
uncertainty	-0.024	-0.059	-0.021	-0.059	-0.121	-0.541	-0.121	-0.197

Table 5.23: Systematic uncertainties from various sources in  $B^\pm \rightarrow D\pi^\pm$  and  $B^\pm \rightarrow DK^\pm$  data samples.

parameters that are determined from control samples of  $D^{*+} \rightarrow D^0\pi^+$ ,  $D^0 \rightarrow K^-\pi^+$ . They are varied by  $\pm 1\sigma$  and the resultant deviations in the nominal  $(x_\pm, y_\pm)$  values are assigned as the systematic uncertainty. The uncertainty on the  $c_i, s_i$  inputs are also considered by varying  $c_i, s_i$  by them, then considering the corresponding deviations in  $(x_\pm, y_\pm)$  from the nominal values as the systematic uncertainty. Here, the correlation between  $c_i, s_i$  is taken into account. The  $x_\pm$  and  $y_\pm$  results with statistical and systematic uncertainties are summarized in Table 5.24.

The dominant source of systematic uncertainty is due to the uncertainty on  $c_i$  and  $s_i$  input values. The next largest source of systematic uncertainty is the statistics of the signal MC sample used to calculate the efficiency and migration matrix. If the signal MC statistics is further increased, the data-MC resolution difference will be worse. As this measurement is statistically dominated, any small improvements in systematic uncertainty will have negligible impact.

	$B^\pm \rightarrow D\pi^\pm$	$B^\pm \rightarrow DK^\pm$
$x_+$	$0.039 \pm 0.024$ $^{+0.018}_{-0.013}$ $^{+0.014}_{-0.012}$	$-0.030 \pm 0.121$ $^{+0.017}_{-0.018}$ $^{+0.019}_{-0.018}$
$y_+$	$-0.196$ $^{+0.080}_{-0.059}$ $^{+0.038}_{-0.034}$ $^{+0.032}_{-0.030}$	$0.220$ $^{+0.182}_{-0.541} \pm 0.032$ $^{+0.072}_{-0.071}$
$x_-$	$-0.014 \pm 0.021$ $^{+0.018}_{-0.010}$ $^{+0.019}_{-0.010}$	$0.095 \pm 0.121$ $^{+0.017}_{-0.016}$ $^{+0.023}_{-0.025}$
$y_-$	$-0.033 \pm 0.059$ $^{+0.018}_{-0.019}$ $^{+0.019}_{-0.010}$	$0.354$ $^{+0.144}_{-0.197}$ $^{+0.015}_{-0.021}$ $^{+0.032}_{-0.049}$

Table 5.24:  $x_\pm$  and  $y_\pm$  parameters from a combined fit to  $B^\pm \rightarrow D\pi^\pm$  and  $B^\pm \rightarrow DK^\pm$  data samples. The first uncertainty is statistical, the second is systematic, and the third is due to the uncertainty on the  $c_i, s_i$  measurements.

## 5.5 Determination of $\phi_3, r_B$ and $\delta_B$

We use the frequentist treatment, which includes the Feldman-Cousins ordering [93], to obtain the physical parameters

$$\mu = (\phi_3, r_B, \delta_B),$$

from the measured parameters

$$z = (x_+, y_+, x_-, y_-),$$

in  $B^\pm \rightarrow DK^\pm$  sample; this is the same procedure as used in Ref. [78]. The confidence level is calculated as

$$\alpha(\mu) = \frac{\int_{\mathcal{D}(\mu)} p(z|\mu) dz}{\int_{\infty} p(z|\mu) dz}, \quad (5.8)$$

where  $p(z|\mu)$  is the probability density to observe the measurements  $z$  given the set of physical parameters  $\mu$ . The integration domain  $\mathcal{D}(\mu)$  is given by the likelihood ratio ordering in the Feldman-Cousins method as

$$\lambda = \frac{p(z|\mu)}{p(z|\mu_{\text{best}}(z))}, \quad (5.9)$$

where the denominator is the likelihood of the best possible parameter  $\mu_{\text{best}}$  given the data  $z$ . The domain is chosen beginning with the highest value of  $\lambda$  and then including the lower values until the desired value of  $\alpha$  is achieved. The PDF  $p(z|\mu)$  is a multivariate Gaussian PDF with the uncertainties and correlations between  $(x_\pm, y_\pm)$  taken from the experimental measurements.

Parameter	Results	$2\sigma$ interval
$\phi_3$ ( $^\circ$ )	$5.7^{+10.2}_{-8.8} \pm 3.5 \pm 5.7$	$(-29.7, 109.5)$
$\delta_B$ ( $^\circ$ )	$83.4^{+18.3}_{-16.6} \pm 3.1 \pm 4.0$	$(35.7, 175.0)$
$r_B$	$0.323 \pm 0.147 \pm 0.023 \pm 0.051$	$(0.031, 0.616)$

Table 5.25:  $(\phi_3, \delta_B, r_B)$  obtained from the  $B^\pm \rightarrow DK^\pm$  data sample. The first uncertainty is statistical, second is systematic and, the third one is due to the uncertainty on  $c_i, s_i$  measurements.

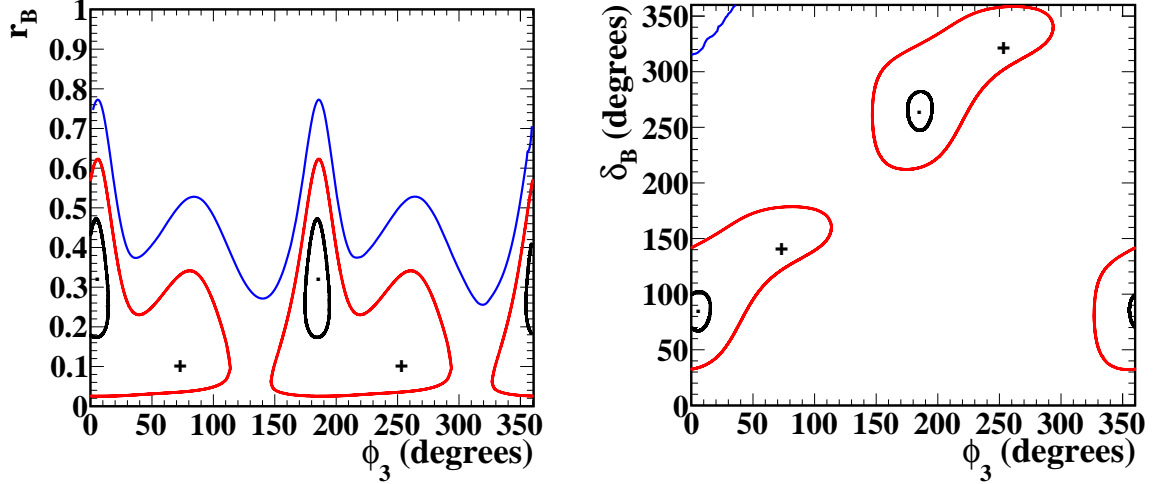


Figure 5.53: Projection of the statistical confidence intervals in the  $\phi_3 - r_B$  (left) and  $\phi_3 - \delta_B$  (right) planes. The black, red, and blue contours represent the one, two, and three standard deviation regions, respectively. The crosses show the positions of the world-average values [29].

We obtain the parameters  $\mu = (\phi_3, r_B, \delta_B)$  from the fit as given in Table 5.25. The systematic uncertainty is estimated by varying the  $z$  parameters by their corresponding systematic uncertainties. Figure 5.53 shows the statistical confidence level contours representing the one, two, and three standard deviation in  $(\phi_3, r_B)$  and  $(\phi_3, \delta_B)$  planes.

We performed a check of the assumption that the  $(x_\pm, y_\pm)$  likelihood can be approximated to be Gaussian when using the Feldman-Cousins method to extract  $(\phi_3, r_B, \delta_B)$ . The check used the measured confidence intervals in  $(\phi_3, r_B, \delta_B)$  to generate an ensemble of simulated data sets. Each simulated data set was then fit to form a distribution of  $(x_\pm, y_\pm)$ , which was found to be consistent with the  $(x_\pm, y_\pm)$  confidence intervals measured. The results are shown in Fig. 5.54 and Table 5.26. Hence we conclude that the reported confidence intervals for  $(\phi_3, r_B, \delta_B)$  are giving appropriate statistical coverage.

There is a two-fold ambiguity in  $\phi_3$  and  $\delta_B$  results with  $\phi_3 + 180^\circ$  and  $\delta_B + 180^\circ$ . We choose the solution that satisfies  $0^\circ < \phi_3 < 180^\circ$ . This result includes the current

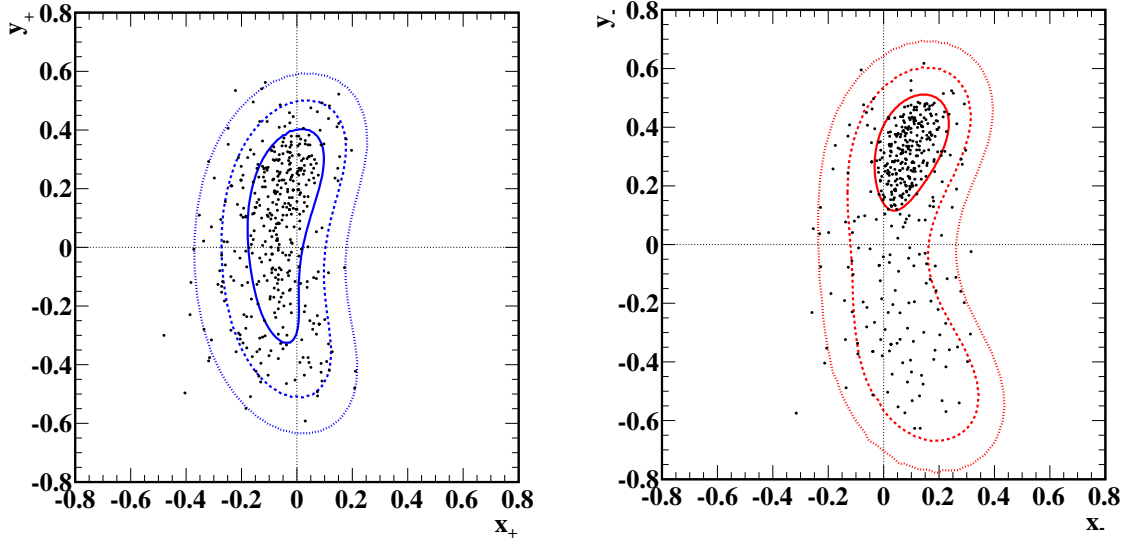


Figure 5.54:  $x_+ - y_+$  (left) and  $x_- - y_-$  (right) results obtained from a set of 400 pseudo-experiments. The likelihood contours from data are included for comparison.

Region ( $\sigma$ )	% of events	
	$x_+, y_+$ contour	$x_-, y_-$ contour
0–1	$0.66 \pm 0.02$	$0.65 \pm 0.02$
1–2	$0.28 \pm 0.02$	$0.28 \pm 0.02$
2–3	$0.04 \pm 0.01$	$0.06 \pm 0.01$
>3	$0.02 \pm 0.01$	$0.01 \pm 0.01$

Table 5.26: Fraction of events in one, two, and three standard deviation regions of  $x_{\pm} - y_{\pm}$  plane from the simulated dataset.

world-average value [29] within two standard deviations. We observe that there is a local minimum around  $\phi_3 = 75^\circ$  and  $\delta_B = 155^\circ$ .

## 5.6 Combination of $D \rightarrow K_S^0 \pi^+ \pi^- (\pi^0)$ results from Belle

We combine the results presented here with the model-independent measurements from  $B^+ \rightarrow D(K_S^0 \pi^+ \pi^-) K^+$  [78] and  $B^0 \rightarrow D^0(K_S^0 \pi^+ \pi^-) K^{*0}$  [94] decays, which use the full dataset collected by the Belle detector. Without our measurement, the combination leads to  $\phi_3 = (78_{-15}^{+14})^\circ$ . Including our measurement, the combination gives  $\phi_3 = (74_{-14}^{+13})^\circ$ . The distributions of p-values for the  $\phi_3$  measurements from the in-

dividual  $D$  final states and the combination are given in Fig. 5.55. The separate measurements and the combined likelihood contours in the  $(\phi_3, r_B)$  plane are shown in Fig. 5.56.

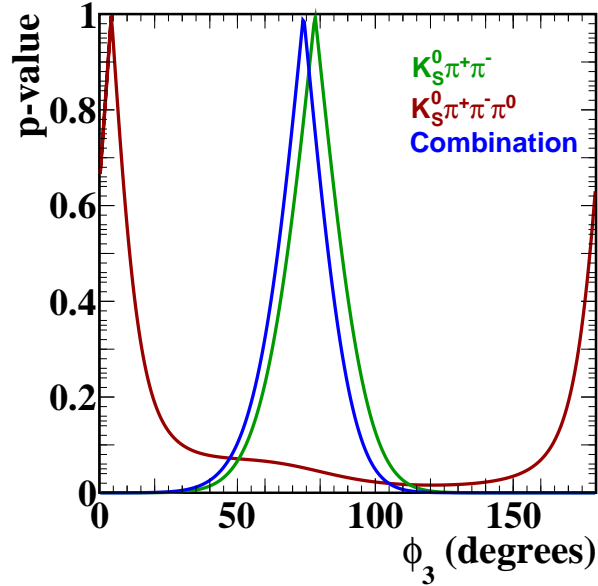


Figure 5.55: Distribution of p-value for  $\phi_3$  from multibody  $D$  final states at Belle, which is shown by the solid blue curve. The results from  $B \rightarrow DK^{(*)}$  decays with  $D \rightarrow K_S^0 \pi^+ \pi^-$  are shown by the solid green curve and the  $D \rightarrow K_S^0 \pi^+ \pi^- \pi^0$  final states are shown by the solid brown curve [78, 94].

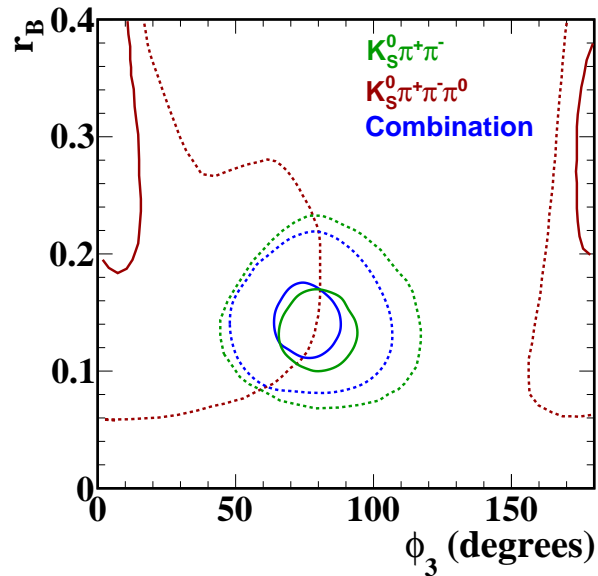


Figure 5.56: Projections of the confidence intervals in the  $\phi_3 - r_B$  plane from multibody  $D$  final states at Belle, which is shown by the blue intervals. The results from  $B \rightarrow DK^{(*)}$  decays with  $D \rightarrow K_S^0 \pi^+ \pi^-$  are shown by the green intervals and the  $D \rightarrow K_S^0 \pi^+ \pi^- \pi^0$  final states are shown by the brown intervals. The solid and dashed curves correspond to one and two standard deviation contours, respectively [78, 94].



# CHAPTER 6

## Prospects at Belle II

This Chapter describes the physics prospects at Belle II, an upgrade of the Belle experiment. A brief description of the detector is given in Sec. 6.1. Section 6.2 gives a detailed description of the construction and characterisation of the silicon vertex detector at Belle II. The results from the early physics run of Belle II in 2018 are presented in Sec. 6.3.

### 6.1 Belle II detector

The Belle II detector [95] is a substantial upgrade of its predecessor Belle, aiming to collect 50 times more data. The KEKB accelerator is upgraded to deliver 40 times larger instantaneous luminosity and become a Super- $B$  factory. The same accelerator ring is used for the upgrade, SuperKEKB [96], and the beam parameters are optimized to increase the instantaneous luminosity. A schematic view of the accelerator system is given in Fig. 6.1.

The instantaneous luminosity can be defined in terms of the beam parameters as

$$L = \frac{\gamma_{e^\pm}}{2er_e} \left(1 + \frac{\sigma_y^*}{\sigma_x^*}\right) \left(\frac{I_{e^\pm} \xi_y^{e^\pm}}{\beta_y^*}\right) \left(\frac{R_L}{R_{\xi_y}}\right), \quad (6.1)$$

where  $\gamma_{e^\pm}$  is the Lorentz factor,  $e$  the elementary electric charge,  $r_e$  the classical electron radius and  $\sigma_{x(y)}^*$  is the beam size. The parameters  $I_e$ ,  $\xi_y^{e^\pm}$  and  $\beta_y^*$  are the total beam current, vertical beam-beam parameter and the vertical beta function at the IP. The parameter  $R_L$  is a reduction factor to the luminosity to account for the crossing angle. The design beam current is twice the value of that at KEKB and the  $\beta_y^*$  is reduced by a factor of 20, which results in a 40-fold increase in the instantaneous luminosity at SuperKEKB. The design value of the instantaneous luminosity  $8 \times 10^{35} \text{ cm}^{-2}\text{s}^{-1}$ . To accomplish these improvements the Nano-Beam scheme is introduced, where the overlap region of the  $e^+$  and  $e^-$  beams is minimized. Another consequence of this

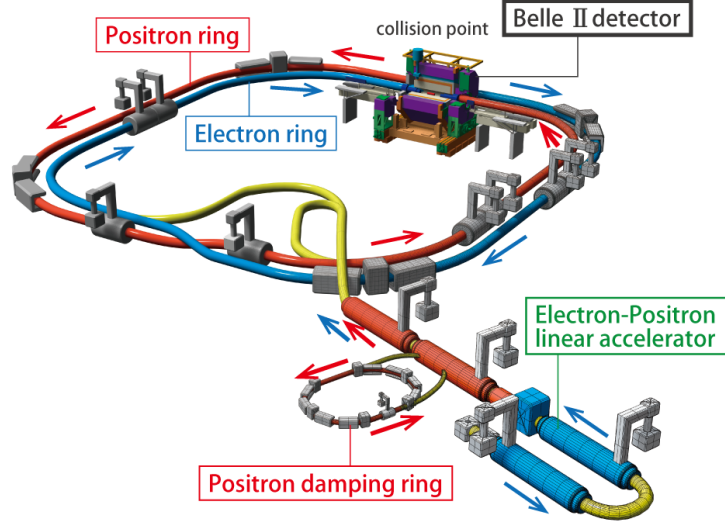


Figure 6.1: Schematic view of SuperKEKB accelerator units along with the Belle II detector position [96].

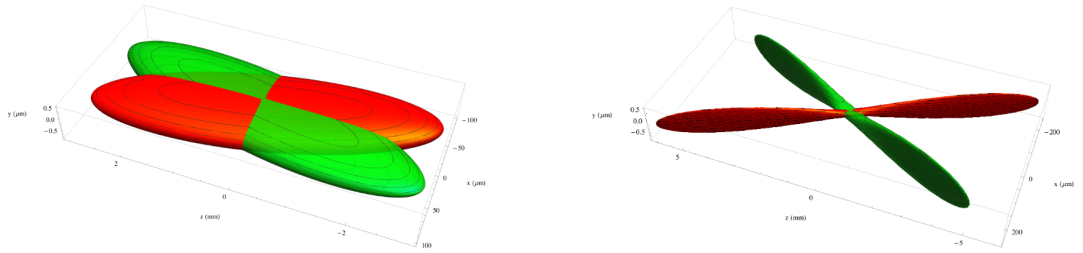


Figure 6.2: Schematic view of the beam crossing at the interaction region of Belle (left) and Belle II (right). The spread of the  $z$  vertex distribution is expected to be 1 cm and 0.05 cm at Belle and Belle II, respectively [97].

scheme is a relatively large crossing angle. A comparison of beam crossing at Belle and Belle II is illustrated in Fig. 6.2. The parameter  $\xi$  is proportional to  $\sqrt{\frac{\beta_y^*}{\text{emittance}}}$ , so one has to work at reducing the emittance with the reduced  $\beta_y^*$  to prevent the reduction in luminosity with  $\xi$ . Therefore, a damping ring is introduced at SuperKEKB.

The  $e^+$  and  $e^-$  beam energies have been changed from that of KEKB. The  $e^+$  beam energy is increased from 3.5 to 4.0 GeV. This increase helps to combat the beam emittance growth due to intra-beam scattering and short lifetime of beams because of the Touschek effect, which is the loss of charged particles due to scattering in a storage ring. The  $e^-$  beam energy is reduced from 8.0 to 7.0 GeV, which also enables lower emittance to be achieved. The change in energies cause a reduction in the Lorentz boost of the centre-of-mass system as the beam energies are less asymmetric than of KEKB.

Higher backgrounds and reduced boost factor demand for an upgraded detector de-

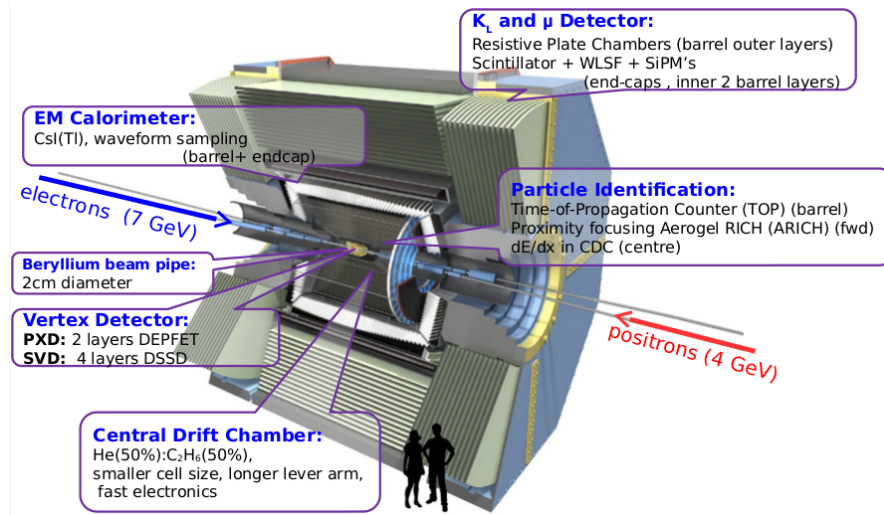


Figure 6.3: Schematic view of the Belle II detector [98].

sign. Hence Belle II was designed to cope with these challenges. A schematic view of the Belle II detector is given in Fig. 6.3. The vertex detector system is completely new with two layers of depleted p-channel field-effect transistor pixel detectors and four layers of DSSD strips. The DSSD layers are referred to as the Silicon Vertex Detector (SVD). The new system provides extended coverage and better resolution. The impact parameter resolution is  $20 \mu\text{m}$  at  $2 \text{ GeV}/c$  [95], which is almost half that of Belle. The reconstruction efficiency of low momentum particles and relatively long-lived particles like  $K_S^0$  will be improved due to the larger radius of the outermost SVD layer. The reduced Lorentz boost will result in less separation between the decay vertices of the two  $B$  mesons. So a vertex detector with good resolution is essential for measuring this vertex separation in time-dependent  $CP$ -violation measurements.

The CDC has been made with smaller cell size and longer lever arm. The inner radius has been changed from 77 mm to 160 mm to avoid the high background near the IP and to provide more space for the new vertex subsystem. The CDC outer radius is 1130 mm as the barrel PID system is more compact than Belle. The PID system is completely new, which consists of the time-of-propagation (TOP) counter in the barrel region and aerogel RICH (ARICH) detector in the forward endcap region. In the TOP, the time-of-propagation of the internally reflected Cherenkov photons produced in the quartz crystal is measured. The position and precise timing information is used to reconstruct the Cherenkov image and subsequently distinguish the identity of the charged tracks. The ARICH detects the Cherenkov rings produced in the aerogel radiator by the charged tracks. The material budget of the upgraded PID system is smaller than that in

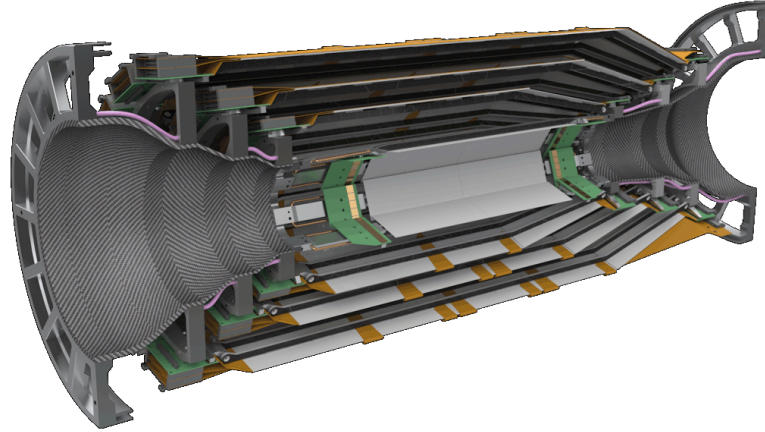


Figure 6.4: A cross-section view of the Belle II SVD [99].

Belle and this helps to improve the calorimeter response. The ECL uses the same CsI crystals doped with Thallium. In the KLM detector, the RPCs in the inner and forward region are replaced with scintillators. The associated electronics of all the subsystems have been upgraded to match with the higher occupancy at Belle II.

The SuperKEKB accelerator was commissioned in 2016 with  $e^+$  and  $e^-$  beams circulating in the rings, but there were no collisions. This is known as the phase I of Belle II. In early 2018, the Belle II detector, apart from the full vertex subsystem, was integrated at the collision point of SuperKEKB. A prototype vertex detector with one module in each layer was installed to test its performance and radiation hardness. The first collision between the beams were recorded on 25 April 2018 and the physics run continued till 17 July 2018. This is known as the phase II of Belle II and a total of  $472 \text{ pb}^{-1}$  of data were collected during this period.

## 6.2 Silicon Vertex Detector at Belle II

The Belle II SVD has four layers and its construction is a global effort involving groups from Asia, Australia and Europe. Layers 3, 4, 5 and 6 (L3, L4, L5 and L6) are built by University of Melbourne, TIFR India, HEPHY Vienna and Kavli IPMU Japan, respectively. The forward and backward modules for L4, L5 and L6 are produced by INFN Pisa.

A cross-sectional view of the SVD is shown in Fig. 6.4. L3, L4, L5 and L6 are made up of seven, 10, 12 and 16 modules (also referred to as “ladders”), respectively. The

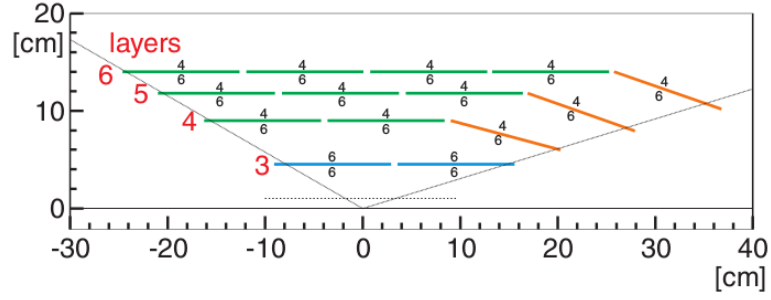


Figure 6.5: Schematic configuration of the Belle II SVD showing the different sensor geometries and the number of readout chips [95].

angular acceptance is  $17^\circ < \theta < 150^\circ$ . The innermost layer (L3) has a radius of 39 mm and the outermost one (L6) is 135 mm in radius. The radii for L4 and L5 are 80 mm and 104 mm, respectively. In comparison, the radius of the outermost SVD layer at Belle was 88 mm [100]. The whole structure has a lantern shape to complement the forward boost of the centre-of-mass system because of the asymmetric beam energies (4 GeV  $e^+$  and 7 GeV  $e^-$ ). To facilitate this, L4, L5 and L6 have slant angles of  $11.9^\circ$ ,  $17.2^\circ$  and  $21.1^\circ$ , respectively. A schematic configuration of this geometry is shown in Fig. 6.5. This structure reduces the material budget without affecting the performance. I have taken part in the construction and quality assurance tests of L4.

### 6.2.1 Components

Three types of DSSDs, which are  $p$ -in- $n$  type, are used to build the ladders of the SVD. They are six inches long with differing width and have thickness 300 or 320  $\mu\text{m}$ . The small rectangular DSSDs are used in L3 whereas large rectangular ones are used in L4, L5 and L6. The forward slanted part is built using trapezoidal DSSDs with varying width. The DSSDs are shown in Fig. 6.6 and their specifications are given in Table 6.1.



Figure 6.6: Rectangular (left) and trapezoidal (right) sensors.

Sensor	Rectangular (large)	Rectangular (small)	Trapezoidal
# of p-strips	768	768	768
p-strip pitch ( $\mu\text{m}$ )	75	50	50–75
# of n-strips	512	768	512
n-strip pitch ( $\mu\text{m}$ )	240	160	240

Table 6.1: DSSD specifications used in the SVD.

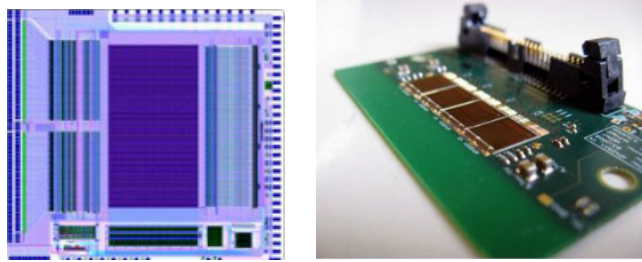


Figure 6.7: Image of the APV25 readout chip showing the features and bond pads (left); four APV25 readout chips mounted on a hybrid (right).

The  $p$ -side strips are aligned parallel to the beam direction and  $n$ -side strips are perpendicular to the beam direction. The L3 DSSDs have their  $n$ -side facing the beam pipe whereas L4, L5 and L6 DSSDs are oppositely arranged. This design avoids any interference of L3 support structure with the PXD system. The rectangular DSSDs are manufactured at Hamamatsu Photonics in Japan and the trapezoidal DSSDs are built at Micron Semiconductor in the UK.

The readout chip must have a short signal shaping time in order to cope with the high hit rate expected at Belle II. The APV25 chips [101], originally developed for the CMS Collaboration, is used for this purpose, which has an integration time of 50 ns. It is radiation hard and can tolerate up to 1 MGy, which is far beyond the radiation dose expected at Belle II (about 50 Gy). It also has a 192 cell deep analog pipeline, which reduces the detector dead-time. The chip is shown in Fig. 6.7.

The APV25 needs to be placed as close to the DSSD as possible to reduce the capacitive noise, which is proportional to the length of the connectors. This is done with the “origami” chip-on-sensor concept [102]. This novel design allows for the readout chips to be on a single side of the DSSD. The readout channels from the other side are wrapped around via flexible electronic circuits so that the APV25 chips can be

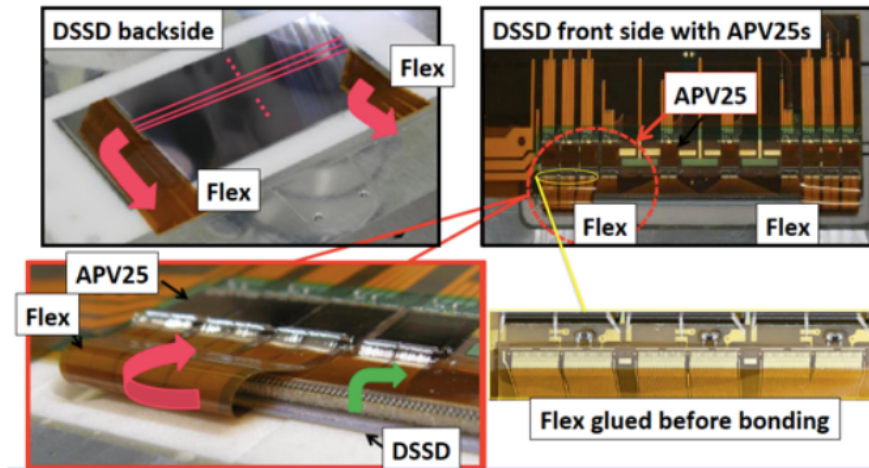


Figure 6.8: Origami chip-on-sensor concept where the readout from the other side of the DSSD is wrapped around using flexible circuits and connected to APV25 chips in a single line on the DSSD.

placed on a single line (see Fig. 6.8). This, in turn, helps in allowing for a single cooling channel, thus reducing the material budget. This origami concept is adopted in the inner DSSDs of L4, L5 and L6. The full L3 ladder and the forward and backward DSSDs are read out from the edges. A dual-phase CO<sub>2</sub> cooling system at  $-20^{\circ}\text{C}$  is employed to deal with the heat dissipated, approximately 700 W, from all the APV25 chips.

## 6.2.2 Construction

The ladder assembly procedure [103] is complex because the DSSDs are aligned precisely using assembly jigs. Vacuum chucking is used to fix the sensors to the jigs. There are different jigs used for various purposes during the entire assembly of one ladder. The flexible circuits are glued to the sensor and the electrical connections are made via wire-bonding. Araldite® 2011 glue is used and the dispensing is controlled by robotic arm. A uniform glue thickness is achieved with the robotic system as demonstrated in Fig. 6.9.

The wire-bonding machine uses aluminium wire for the connections. The machine parameters are fine tuned to realize a yield greater than 99% and pull strength  $f$  such that the mean  $\mu_f > 5 \text{ g}$  and  $\frac{\sigma_f}{f} < 20\%$ , where  $\sigma_f$  is the standard deviation in  $f$ , as shown in Fig. 6.10. The pull strength is measured using a wire pull tester that effectively pulls the wirebond away by applying an upward force and this is expressed in gram-force units.

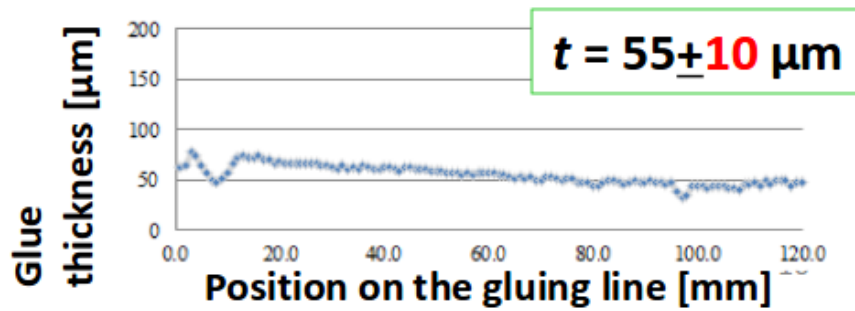


Figure 6.9: Thickness of the glue dispensed by the robotic arm.

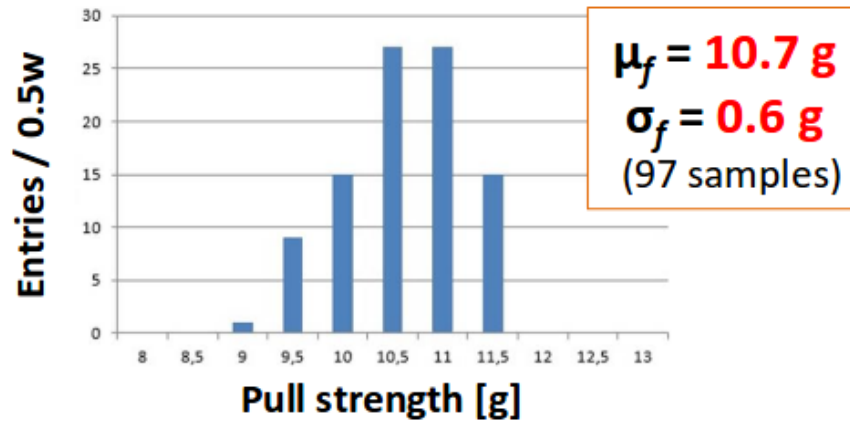


Figure 6.10: Pull strength measured for 97 samples of wire-bonds.

Thermally insulating Airex sheets (light-weight styrofoam) are placed between the DSSD and the readout circuits to minimize the heat transfer between them. This also provides electrical isolation and hence avoids the signal cross-talk. The APV25 chips on the origami flexible circuits are thinned down to  $100 \mu\text{m}$  to further reduce the material budget. Each ladder is supported by ribs built from carbon-fiber reinforced Airex foam, which is very light but strong and stiff. A completed L4 ladder is shown in Fig. 6.11.

A major challenge during the mass production was that the glue joint between the flexible circuit and the forward DSSD was found to be lifting off on some L4 and L6 ladders. The likely cause was the small overlap between the sensor and the circuit and the stress due to the bending angle. A glue reinforcement strategy is implemented to tackle this issue.

### 6.2.3 Quality assurance

The geometrical and electrical quality of the produced ladders are rigorously tested at the assembly sites, as well as at KEK, where the ladders are mounted to the support

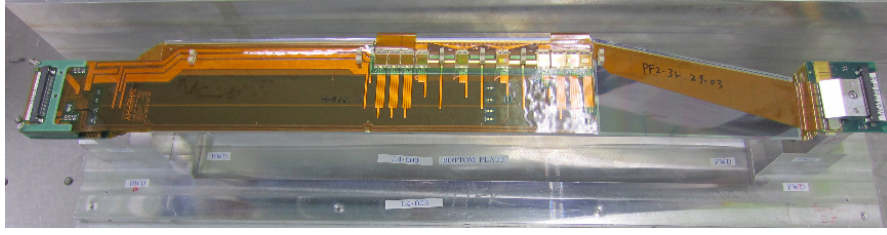


Figure 6.11: A completed layer 4 ladder.

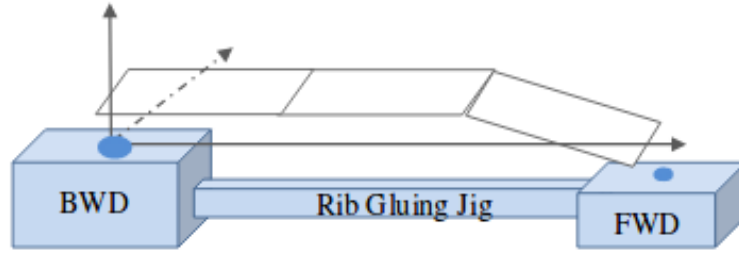


Figure 6.12: Ladder coordinate frame for L4.

structure. The geometrical precision is measured with an optical Coordinate Measuring Machine (CMM). The position of each sensor is measured and the deviations from the designed values are calculated. The coordinate system used is shown in Fig. 6.12 with the  $x$  axis is pointing in the direction of forward DSSD, the  $z$  axis is in the vertically upward direction and the  $y$  axis is defined to be perpendicular to the  $x$  and  $z$  axes.

Deviation up to  $150 \mu\text{m}$  in the  $x$ - $y$  plane and  $200 \mu\text{m}$  along the  $z$  axis are allowed. The deviations are found to be within the tolerance limits for all the ladders in all the layers. An example of CMM results for an L4 ladder is given in Table 6.2. Plot of a forward DSSD from the measured points by CMM is shown in Fig. 6.13.

Electrical quality of the connections between the sensor and the readout chips is tested. Electrical signals are randomly triggered to evaluate noise, raw noise and the pedestal for each channel. A typical response curve is shown in Fig. 6.14. From this

	FW	CE	BW	Tolerance
$\Delta x (\mu\text{m})$	-44.01	6.00	-47.36	150
$\Delta y (\mu\text{m})$	25.21	-20.95	-9.41	150
$\Delta z (\mu\text{m})$	173.91	-139.13	-81.28	200
Slant angle ( $^\circ$ )	-11.91	-0.07	-0.03	-
Tilt angle ( $^\circ$ )	0.09	0.09	0.02	-

Table 6.2: Typical CMM results for an L4 ladder. FW, CE and BW stands for forward, central and backward DSSDs.

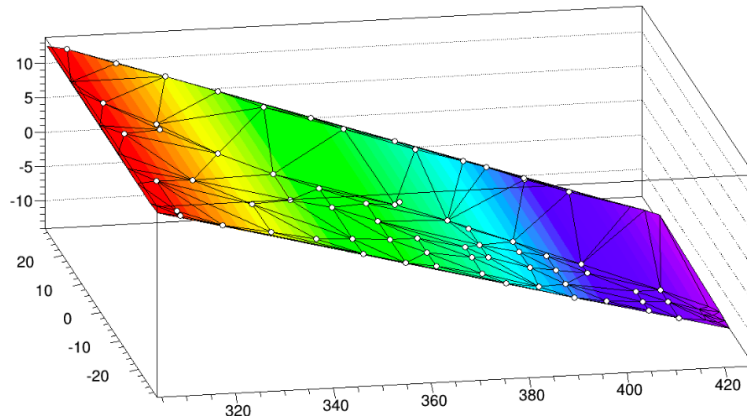


Figure 6.13: Plot of a forward DSSD in L4 from CMM data.

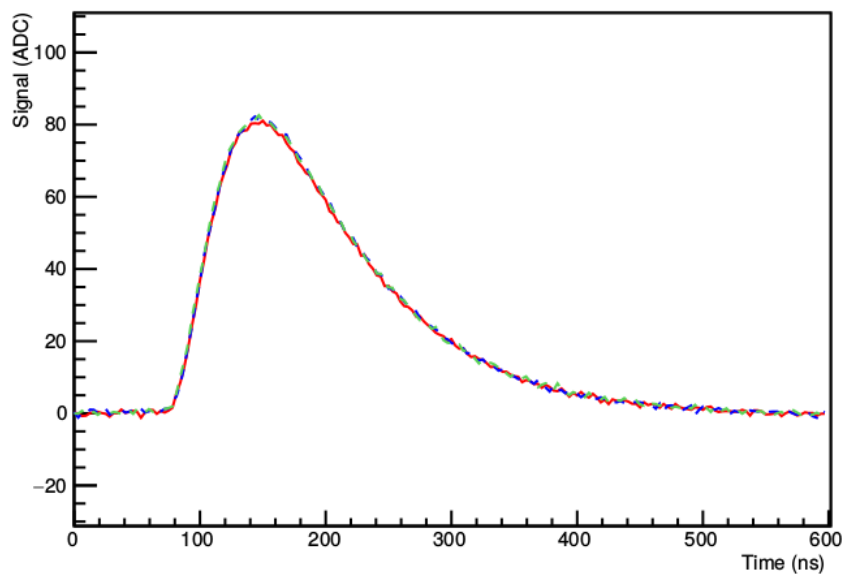


Figure 6.14: Signal *vs.* time plot for three different channels of a readout chip.

signal *vs.* time plot, the maximum amplitude and the peaking time are determined via a fit to the curve. The defective connections can be open, noisy or short. These defects are identified by looking at the response curve. The noise will be very high with fluctuating response curve for “open” channels and their adjacent ones. An example of the response curve for an “open” channel is shown in Fig. 6.15. Short defects will involve at least two adjacent channels. These channels will have lower values of the maximum amplitude and higher peaking time as shown in the example in Fig. 6.16. These tests are done to check the quality of the 768 strips on *p*-side and 512 chips on *n*-side of each DSSD. The numbers of various defective strips on one of the L4 ladders are given in Table 6.3 as an illustration.

In addition, the I-V characteristics of each sensor are analysed and a typical plot is given in Fig. 6.17. All ladders have been tested to have good electrical response.

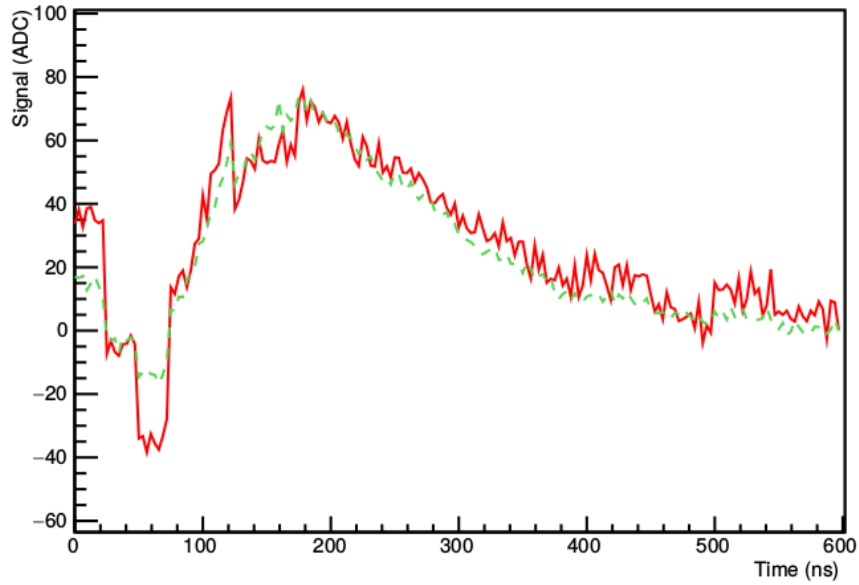


Figure 6.15: Signal *vs.* time plot for an “open” channel of a readout chip. The red curve shows the “open” channel and green curve shows its adjacent one.

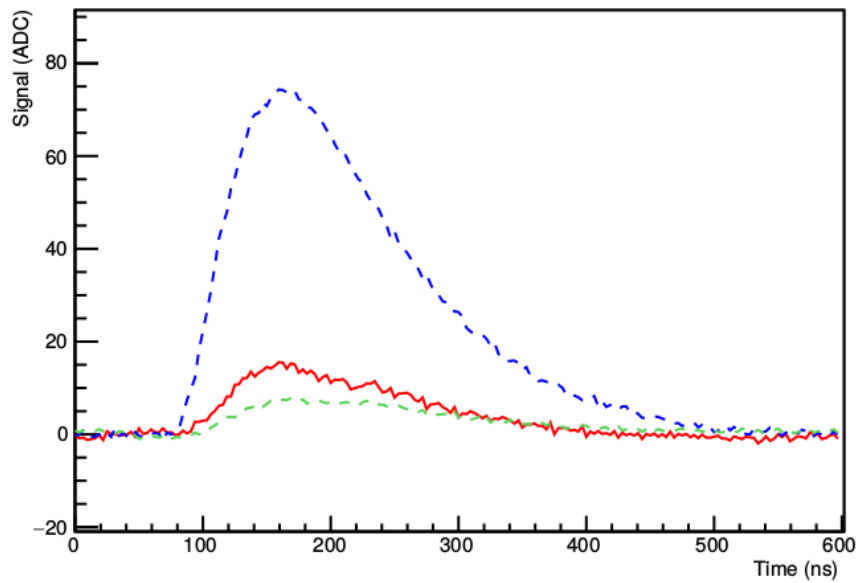


Figure 6.16: Signal *vs.* time plot for two adjacent “short” channels of a readout chip. The red and green curves show the “short” channels and blue curve represents a good channel.

	FW		CE		BW	
	<i>p</i>	<i>n</i>	<i>p</i>	<i>n</i>	<i>p</i>	<i>n</i>
Open	0	1	1	1	0	0
Short	0	2	0	0	0	0
Noisy	0	1	3	1	0	2

Table 6.3: Number of defective strips on *p*- and *n*-sides of a DSSD of an L4 ladder.

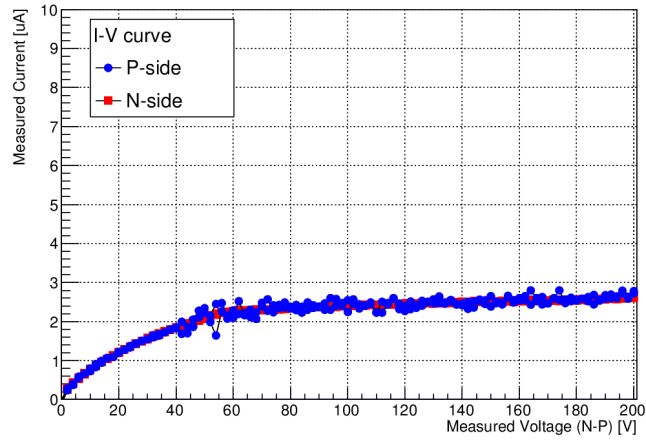


Figure 6.17: I-V characteristics for an L4 DSSD.

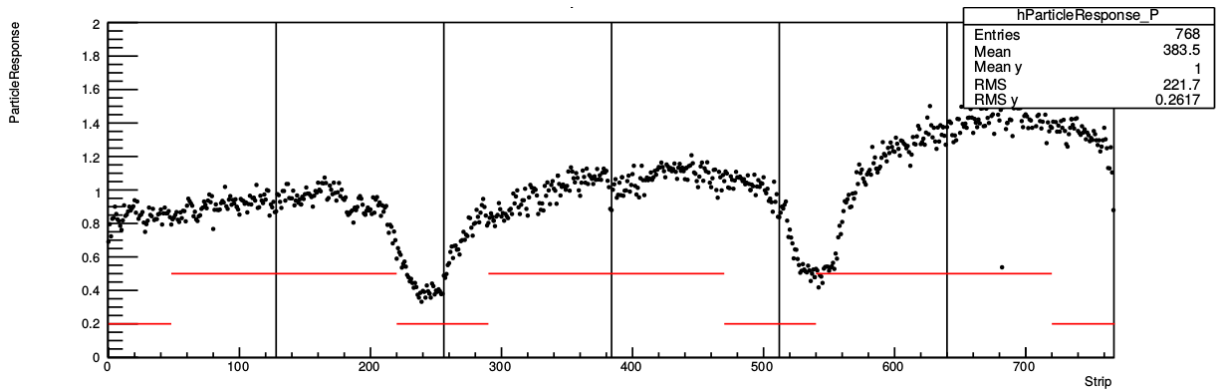


Figure 6.18: Particle response to a source scan of  $p$ -side of a DSSD in an L4 ladder.

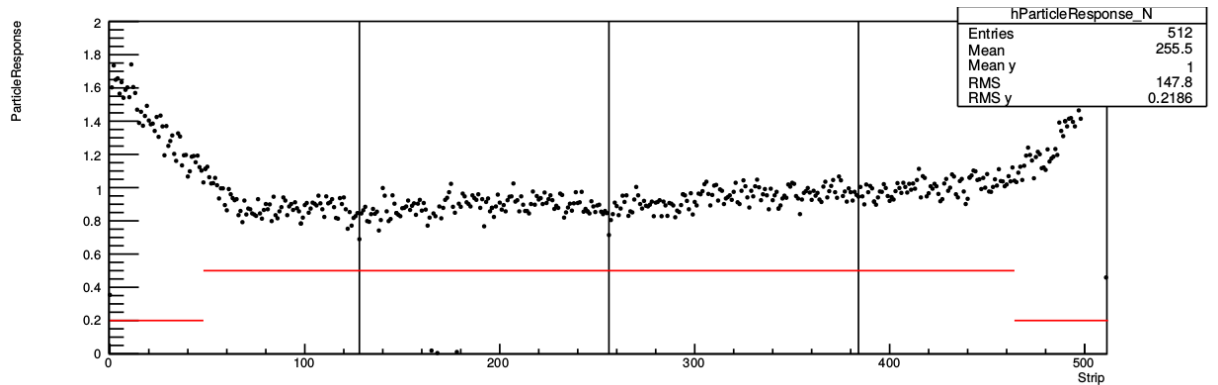


Figure 6.19: Particle response to a source scan of  $n$ -side of a DSSD in an L4 ladder.

A source scan is performed using a  $\beta$  source ( $^{90}\text{Sr}$ ). This test is done to make sure that the DSSDs respond when particles are passed through them. The response is quantified as

$$\text{Response} = \frac{\text{number of hits on a strip}}{\text{average number of hits on a strip of } p\text{- or } n\text{- side}}. \quad (6.2)$$

This is expected to be near to one for a good strip. An example of the response plots for

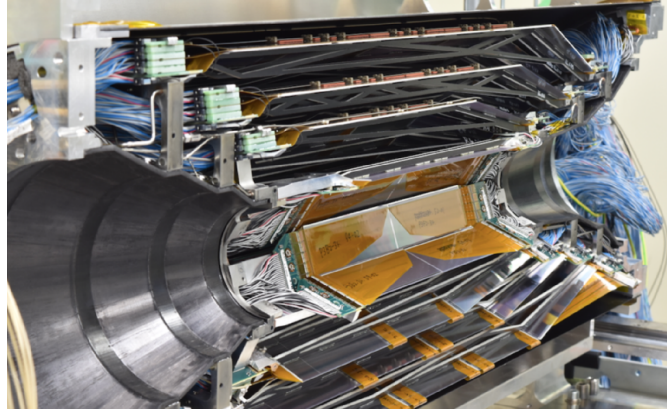


Figure 6.20: One half-shell of SVD mounted to the final structure.

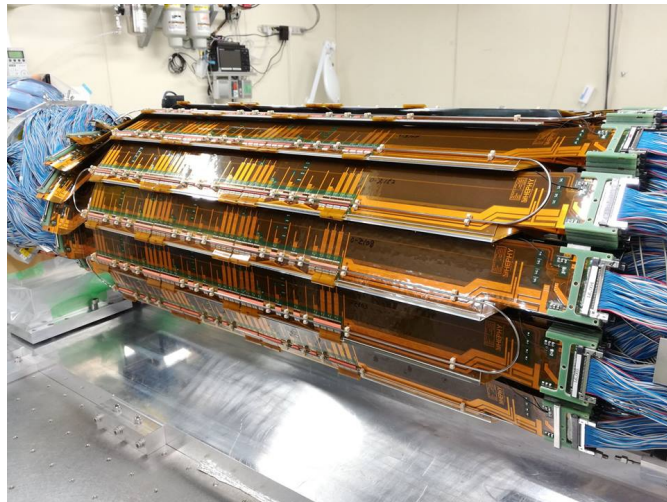


Figure 6.21: Full SVD mounted to the final structure.

$p$ - and  $n$ -side of a DSSD are shown in Fig. 6.18 and 6.19, respectively. The deviations from one at certain strip positions is due to the presence of support structures in the ladder.

A module with one ladder from each layer was tested at DESY beam line in April 2016 [104]. Excellent strip hit efficiency of  $> 99\%$  was obtained. This module is also tested during the phase II run of Belle II during April–July 2018. The obtained signal to noise ratio and hit time resolutions are in agreement with the MC expectations. Then, all the SVD ladders have been mounted to the final structure successfully. First, one half-shell is mounted followed by the other to form the full vertex detector. The half-shell and full SVD after mounting the ladders are shown in Fig. 6.20 and 6.21, respectively. An event display of the first track, induced by a cosmic ray muon, is shown in Fig 6.22.

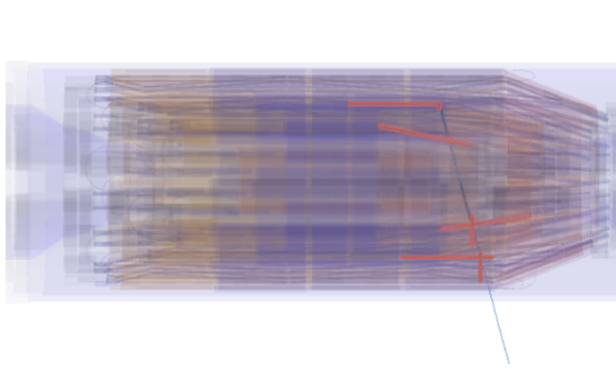


Figure 6.22: First cosmic track seen in the full SVD on July 17, 2018.

### 6.3 Results from phase II

The data from the phase II run is essential to gauge the accelerator and detector performances. I have been part of the first selection and reconstruction of  $B$  decays in this  $472 \text{ pb}^{-1}$  data. At first, it is checked whether the  $e^+e^-$  collisions happen at the  $\Upsilon(4S)$  resonance or not. This is done by looking at the event shape variable  $R_2$ , which is the ratio of second and zeroth Fox-Wolfram moment as given in Eq. (4.4). If the event is  $B\bar{B}$ , then the  $R_2$  value tends to be closer to zero due to its spherical topology. For  $e^+e^- \rightarrow q\bar{q}$  events,  $R_2$  takes higher values because they form back-to-back jets. The  $R_2$  distribution in data is shown in Fig. 6.23 along with the MC predictions. It is evident from the peak close to zero that there are  $B\bar{B}$  events produced, which in turn confirms that the  $e^+e^-$  collisions happen at the  $\Upsilon(4S)$  resonance.

A number of  $D^*$  and  $B$  decay modes have been rediscovered. The Cabibbo-favoured  $D$  decays  $K^-\pi^+$ ,  $K^-\pi^+\pi^0$  and  $K^-\pi^+\pi^-\pi^+$  are reconstructed from a  $D^*$ -tagged sample (see Sec. 4.1). A set of basic selection criteria mentioned in Table 6.4 are applied on the final state particles.

The  $M_D$  and  $\Delta M$  distributions for  $K^-\pi^+$  final state are given in Fig. 6.24 and 6.25, respectively. Similarly Fig. 6.26 and 6.27 show the  $M_D$  and  $\Delta M$  distributions of  $D^{*+} \rightarrow D^0(K^-\pi^+\pi^0)\pi^+$  decays. The  $M_D$  and  $\Delta M$  distributions for  $K^-\pi^+\pi^-\pi^+$  final state are shown in Fig. 6.28 and 6.29.

The mass resolutions of  $K^-\pi^+$  and  $K^-\pi^+\pi^-\pi^+$  final states are comparable but it is worse for  $K^-\pi^+\pi^0$ , because of the presence of  $\pi^0$  in the final state. There is good agree-

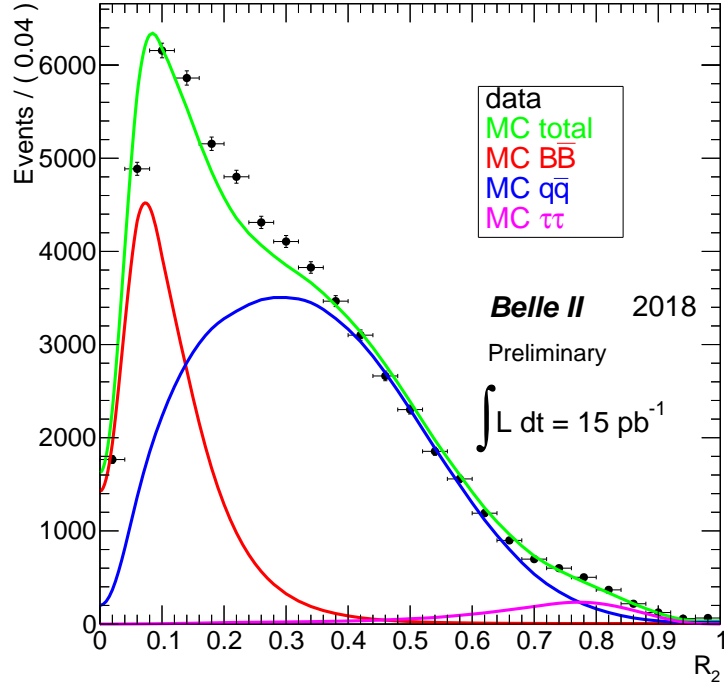


Figure 6.23:  $R_2$  distribution in phase II data along with MC predictions.

Variable	Selection criteria
$d_0$	$<0.5$ cm
$z_0$	$<3.0$ cm
$p_{D^*}^*$	$>2.5$ GeV/ $c$
$M_D$	$(1.7, 2.1)$ GeV/ $c^2$
$\Delta M$	$<0.16$ GeV/ $c^2$
$L(K/\pi)$ for $K$	$>0.5$

Table 6.4: Selection criteria to reconstruct  $D^*$  candidates in phase II data.

ment between data and MC expectations as illustrated in Table 6.5. The combinatorial background is also large in  $D \rightarrow K^- \pi^+ \pi^0$  decays. These Cabibbo-favoured modes are used as calibration samples for various measurements of  $CP$ -violating parameters in  $D$  decays.

The singly Cabibbo-suppressed decay  $D \rightarrow K^+ K^-$  is reconstructed in phase II data. This is also a  $CP$ -even eigenstate used in  $\phi_3$  determination from  $B^+ \rightarrow DK^+$  decays as mentioned in Sec. 5.5. The same selection criteria as that of the Cabibbo-favoured decays are used. The corresponding  $M_D$  and  $\Delta M$  distributions are shown in Fig. 6.30 and 6.31, respectively. The resolution is found to be similar to that of  $D \rightarrow K^- \pi^+$  decays.

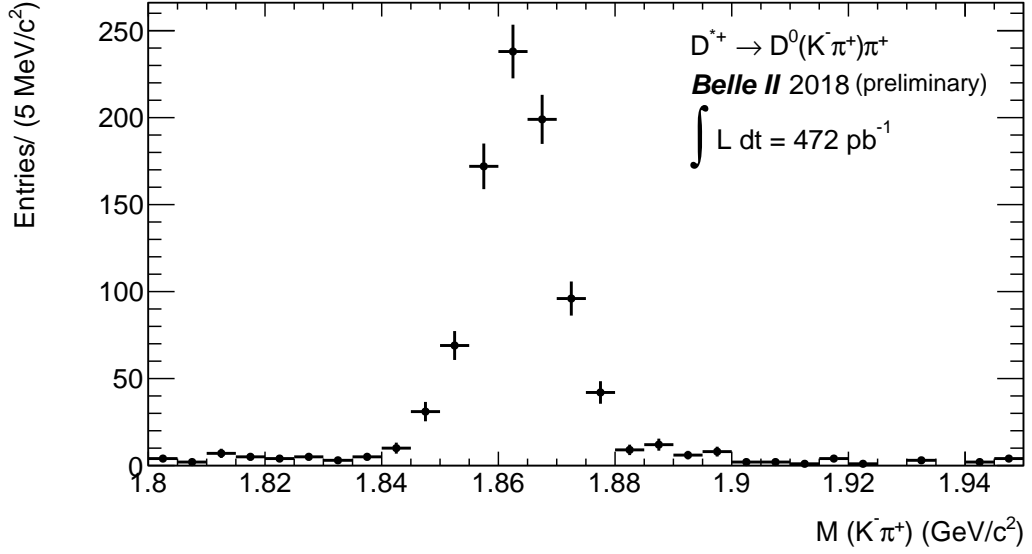


Figure 6.24:  $M(K^-\pi^+)$  distribution of  $D^{*+} \rightarrow D^0(K^-\pi^+)\pi^+$  decays in phase II data.

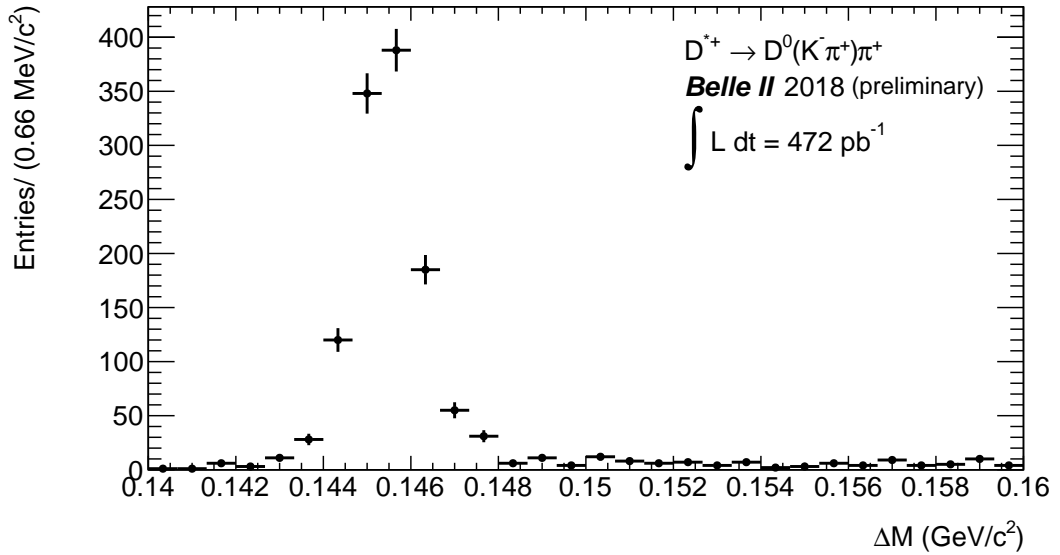


Figure 6.25:  $\Delta M$  distribution of  $D^{*+} \rightarrow D^0(K^-\pi^+)\pi^+$  decays in phase II data.

The multibody self-conjugate states of  $D \rightarrow K_S^0\pi^+\pi^-$  and  $D \rightarrow K_S^0\pi^+\pi^-\pi^0$  are rediscovered in the  $D^*$ -tagged decays. These modes are crucial of model-independent determination of  $\phi_3$  from  $B^+ \rightarrow DK^+$  decays as described in Chapters 4 and 5. The same selection criteria are applied on the final state particles as given in Table 6.4. The  $M_D$  and  $\Delta M$  distributions of  $K_S^0\pi^+\pi^-$  final state are shown in Fig. 6.32 and 6.33, respectively. Similarly Fig. 6.34 and 6.35 show the  $M_D$  and  $\Delta M$  distributions of  $D^{*+} \rightarrow D^0(K_S^0\pi^+\pi^-\pi^0)\pi^+$  decays. The signal yields in both the cases are comparable, as the larger branching fraction of the latter is compensated by the loss in efficiency due to the presence of a  $\pi^0$  in the final state. This shows that both these decay modes

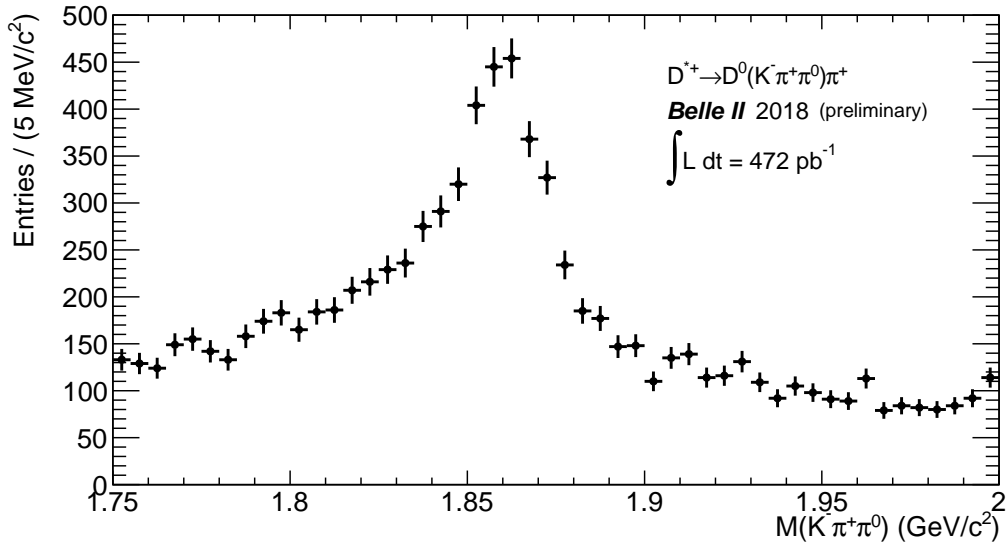


Figure 6.26:  $M(K^- \pi^+ \pi^0)$  distribution of  $D^{*+} \rightarrow D^0(K^- \pi^+ \pi^0)\pi^+$  decays in phase II data.

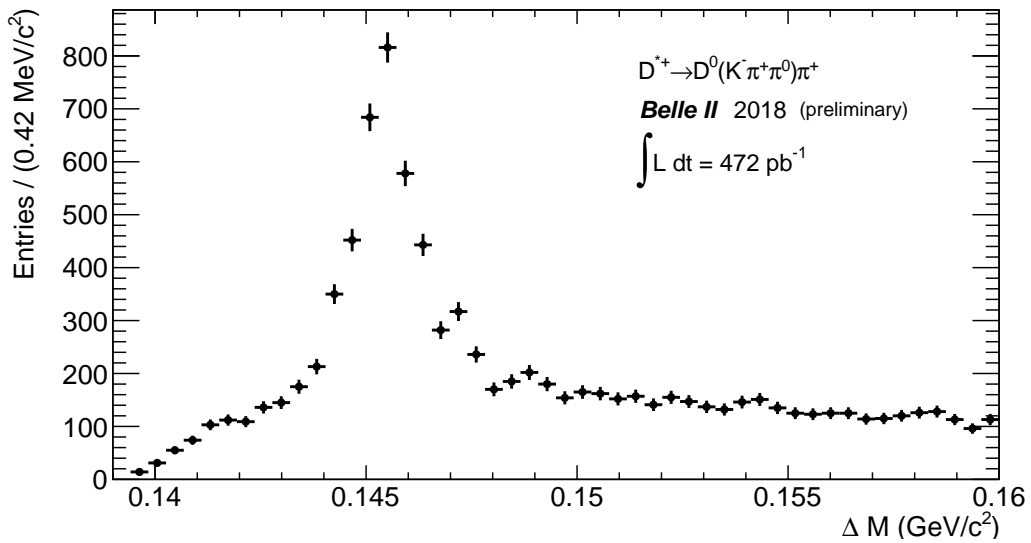


Figure 6.27:  $\Delta M$  distribution of  $D^{*+} \rightarrow D^0(K^- \pi^+ \pi^0)\pi^+$  decays in phase II data.

will play a prominent role in  $\phi_3$  determination at Belle II.

The  $B$  meson has been rediscovered decaying to a variety of hadronic final states. The value of  $M_D$  is required to be in the range  $(1.84, 1.89) \text{ GeV}/c^2$ . The value of  $R_2$  is selected to be less than 0.3 to remove the background from  $e^+e^- \rightarrow q\bar{q}$  continuum processes. The kinematic variables  $M_{bc}$  and  $\Delta E$  are chosen to be in the ranges  $(5.20, 5.29) \text{ GeV}/c^2$  and  $(-0.2, 0.2) \text{ GeV}$ , respectively. The PID criterion and impact parameter selection are the same as in the case of  $D^*$  decays. The  $\Delta E$  and  $M_{bc}$  distribution are shown in Fig. 6.36 and 6.37.

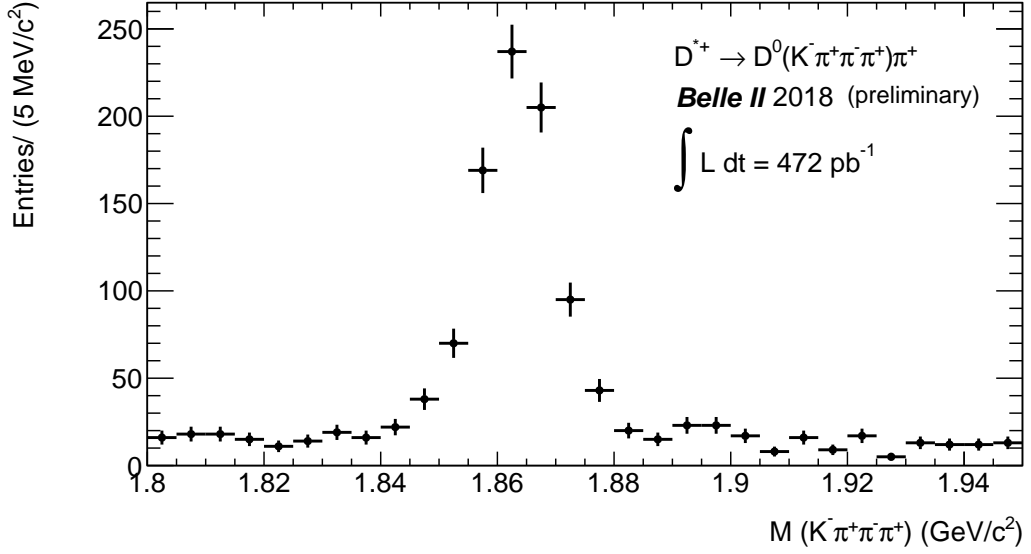


Figure 6.28:  $M(K^-\pi^+\pi^-\pi^+)$  distribution of  $D^{*+} \rightarrow D^0(K^-\pi^+\pi^-\pi^+)\pi^+$  decays in phase II data.

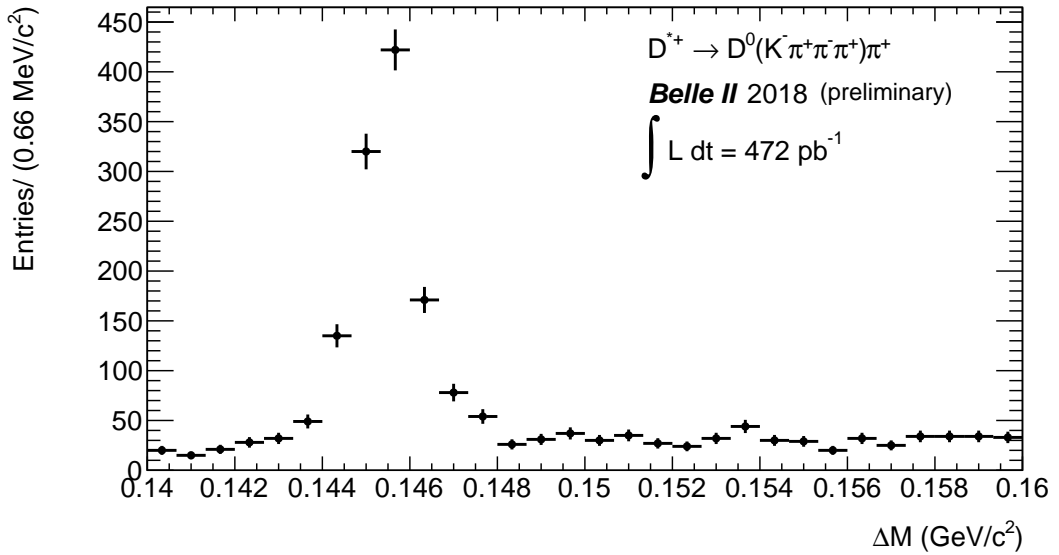


Figure 6.29:  $\Delta M$  distribution of  $D^{*+} \rightarrow D^0(K^-\pi^+\pi^-\pi^+)\pi^+$  decays in phase II data.

The signal yield is extracted by a two-dimensional maximum likelihood fit to  $\Delta E$  and  $M_{bc}$ . The sample is divided into two categories: sample without and with a  $\pi^0$  in the final state. The  $\Delta E$  distribution is asymmetric for the latter category and hence an asymmetric Gaussian PDF is used to model the component. The  $\Delta E$  signal for the first category and  $M_{bc}$  signal components are modelled by a Gaussian PDF. The  $M_{bc}$  distribution of background events are modelled by an ARGUS PDF [74] and their  $\Delta E$  distribution is modelled by a Landau PDF. The signal-enhanced fit projections are shown in Fig. 6.38 and 6.39, where the signal regions are defined as  $|\Delta E| < 0.05$  GeV and  $M_{bc} > 5.27$  GeV/ $c^2$ .

Mode	$M_D$		$\Delta M$	
	MC	Data	MC	Data
	resolution (GeV/c <sup>2</sup> )	scale factor	resolution (GeV/c <sup>2</sup> )	scale factor
$K^-\pi^+$	$0.00882 \pm 0.00019$	$0.924 \pm 0.076$	$0.00065 \pm 0.00001$	$1.204 \pm 0.094$
$K^-\pi^+\pi^-\pi^+$	$0.00893 \pm 0.00083$	$1.010 \pm 0.086$	$0.00064 \pm 0.00007$	$0.929 \pm 0.087$

Table 6.5: Resolution in MC and scale factor on that in data for Cabibbo-favoured  $D$  final states in phase II data.

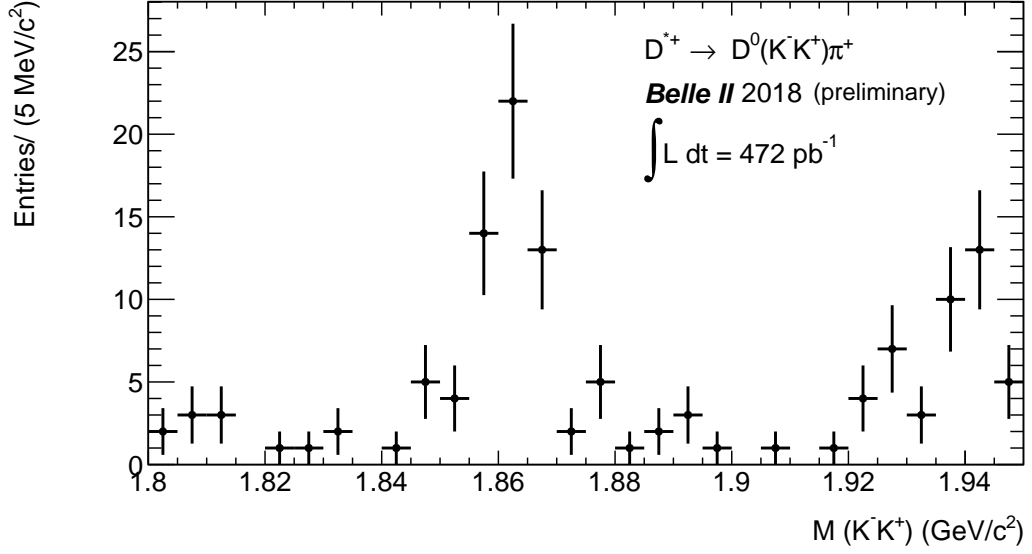


Figure 6.30:  $M(K^-K^+)$  distribution of  $D^{*+} \rightarrow D^0(K^-K^+)\pi^+$  decays in phase II data.

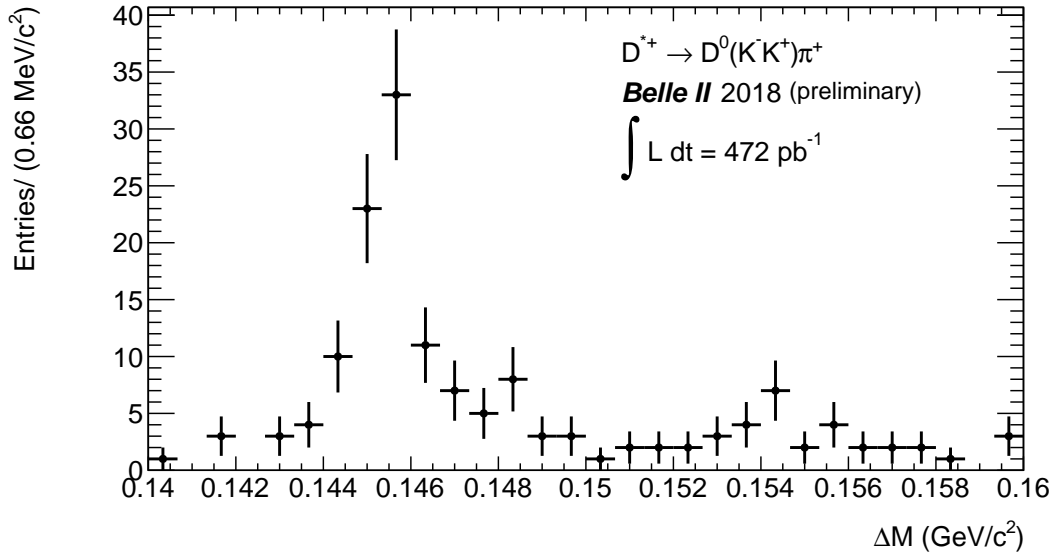


Figure 6.31:  $\Delta M$  distribution of  $D^{*+} \rightarrow D^0(K^-K^+)\pi^+$  decays in phase II data.

The total signal yield obtained from the fit is  $268 \pm 20$ . The scale factor on the data resolution when compared to that of MC is  $0.856 \pm 0.059$  for  $M_{bc}$ ,  $0.992 \pm 0.095$

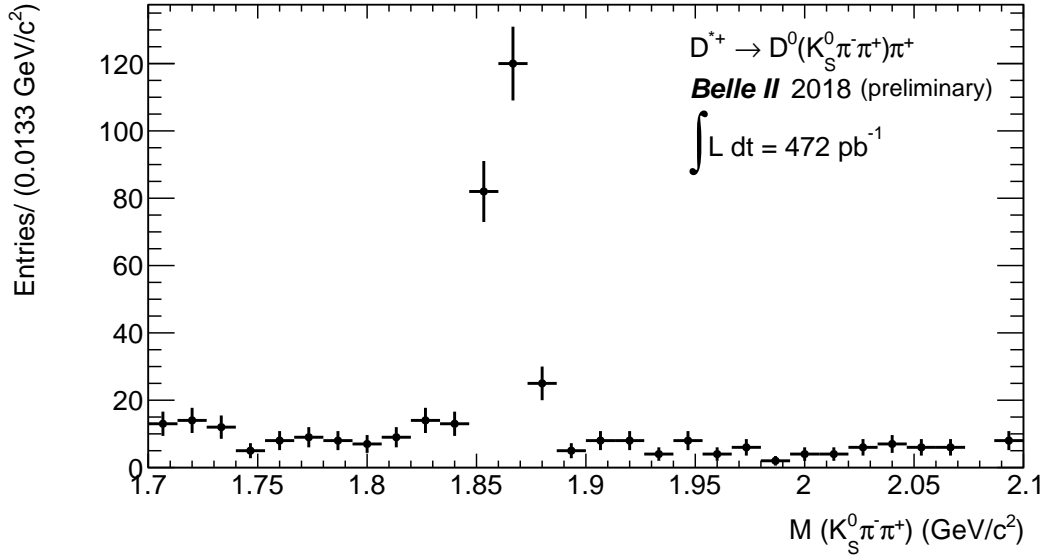


Figure 6.32:  $M(K_S^0\pi^+\pi^-)$  distribution of  $D^{*+} \rightarrow D^0(K_S^0\pi^+\pi^-)\pi^+$  decays in phase II data.

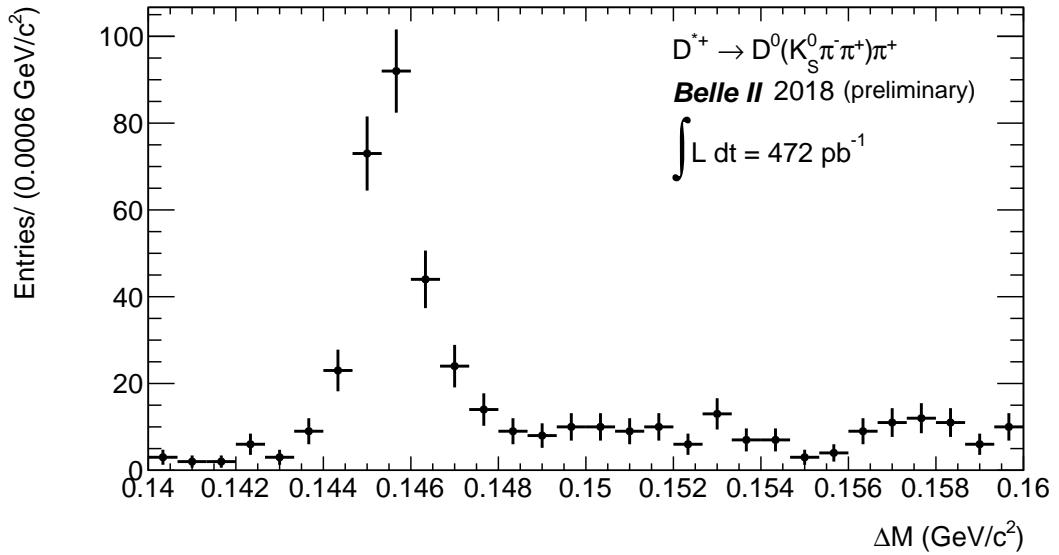


Figure 6.33:  $\Delta M$  distribution of  $D^{*+} \rightarrow D^0(K_S^0\pi^+\pi^-)\pi^+$  decays in phase II data.

for  $\Delta E$  of first category and  $1.210 \pm 0.160$  for  $\Delta E$  of events in second category. The signal yield is comparable to that by earlier experiment ARGUS [105] that accumulated a data sample of similar size in which 280  $B$  candidates were observed.

The  $B^+ \rightarrow D^{(*)}\pi^+$  decays are used as an important calibration samples for  $\phi_3$  determination. The decays  $B^0 \rightarrow D^{(*)+}\pi^-$  [106] and  $B^0 \rightarrow D^{(*)+}\rho^-$  [107] are used to extract  $\phi_3$  via time-dependent  $CP$ -violation measurements. The CKM angle  $\phi_1$  is determined from  $B^0 \rightarrow J/\psi K_S^0$  decays. So these  $B$  rediscoveries illustrate the good prospects for measurements of various CKM parameters at Belle II.

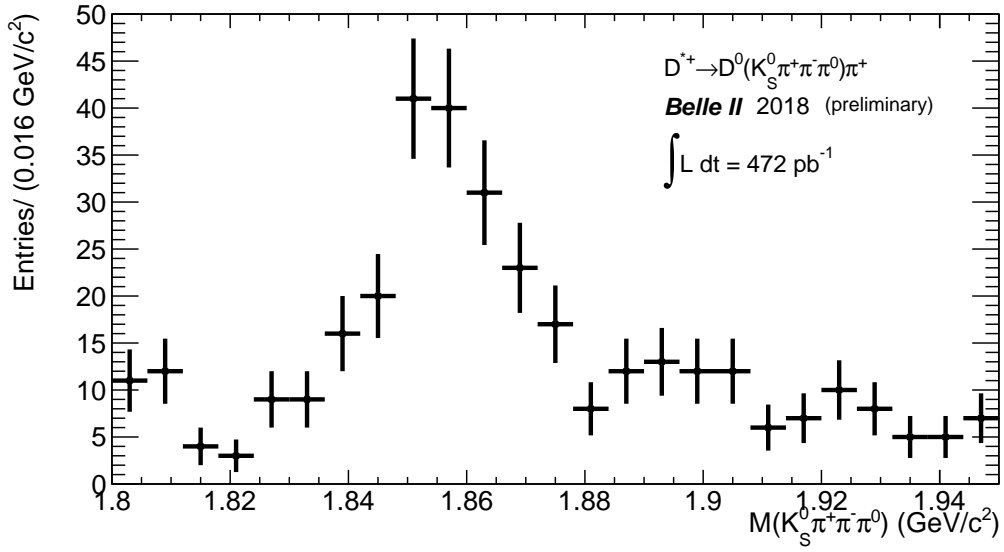


Figure 6.34:  $M(K_S^0\pi^+\pi^-\pi^0)$  distribution of  $D^{*+} \rightarrow D^0(K_S^0\pi^+\pi^-\pi^0)\pi^+$  decays in phase II data.

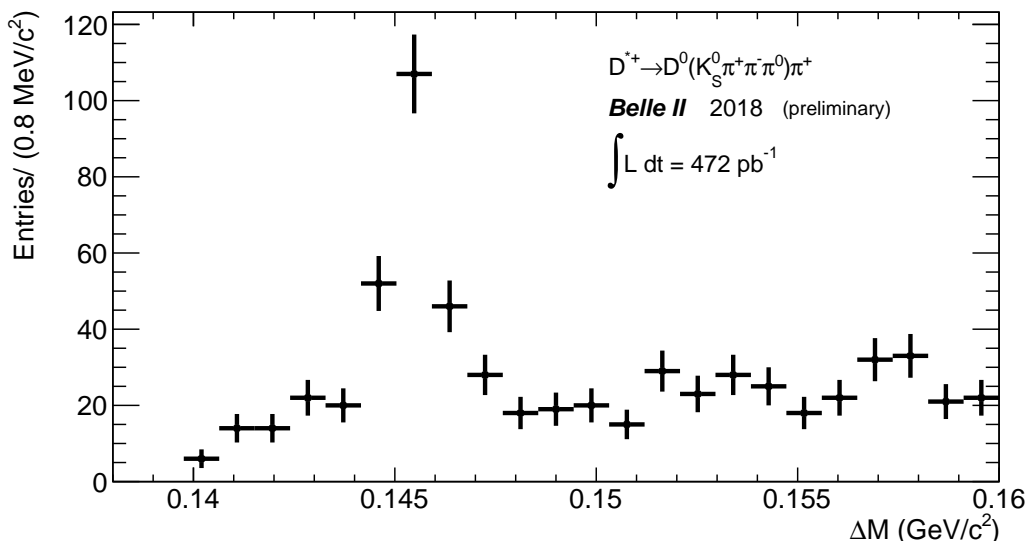


Figure 6.35:  $\Delta M$  distribution of  $D^{*+} \rightarrow D^0(K_S^0\pi^+\pi^-\pi^0)\pi^+$  decays in phase II data.

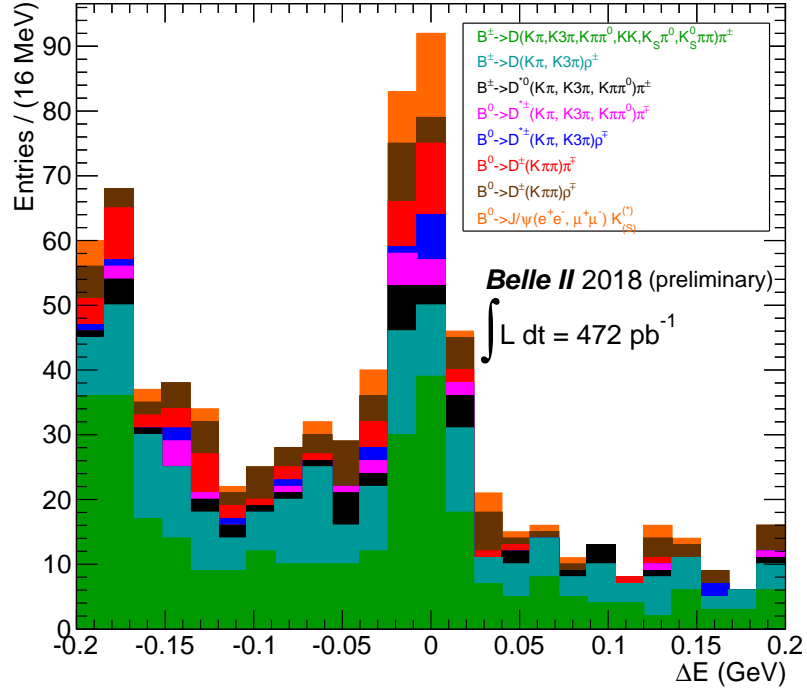


Figure 6.36:  $\Delta E$  distribution of various  $B$  decay modes in phase II data.

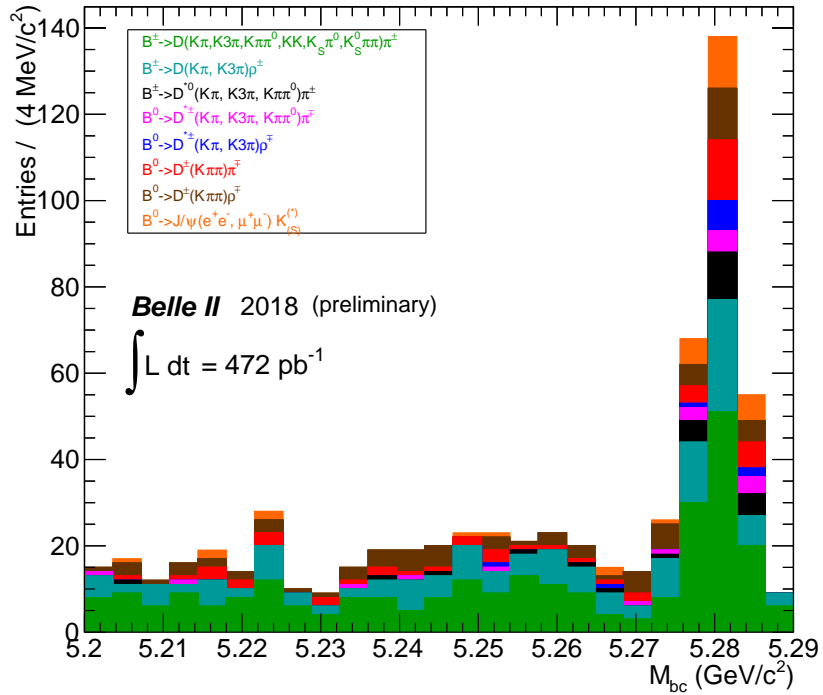


Figure 6.37:  $M_{bc}$  distribution of various  $B$  decay modes in phase II data.

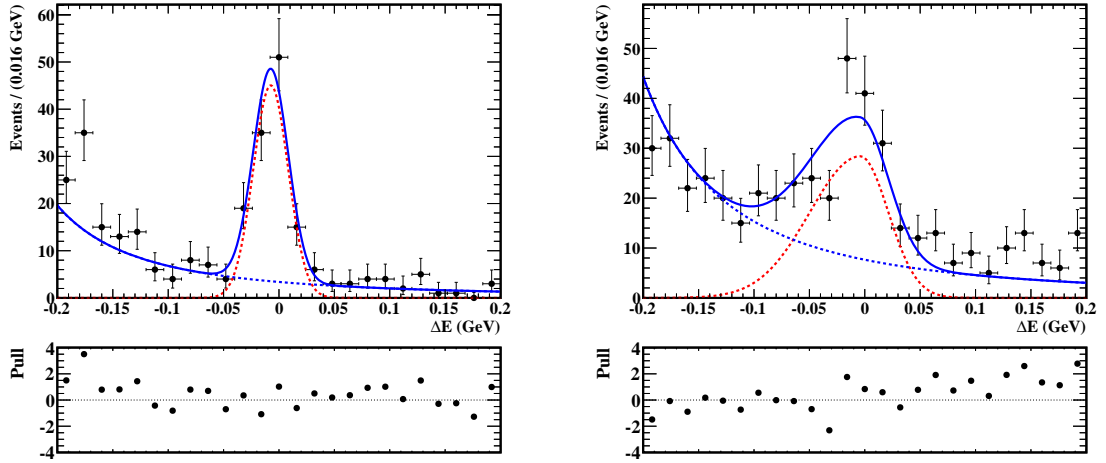


Figure 6.38: Signal-enhanced projections of  $\Delta E$  distribution of  $B$  events without (left) and with (right) a  $\pi^0$  in the final state in phase II data. The black points with error bars show data and solid blue curve indicate the total fit. The dotted red and blue curves show signal and background components, respectively.

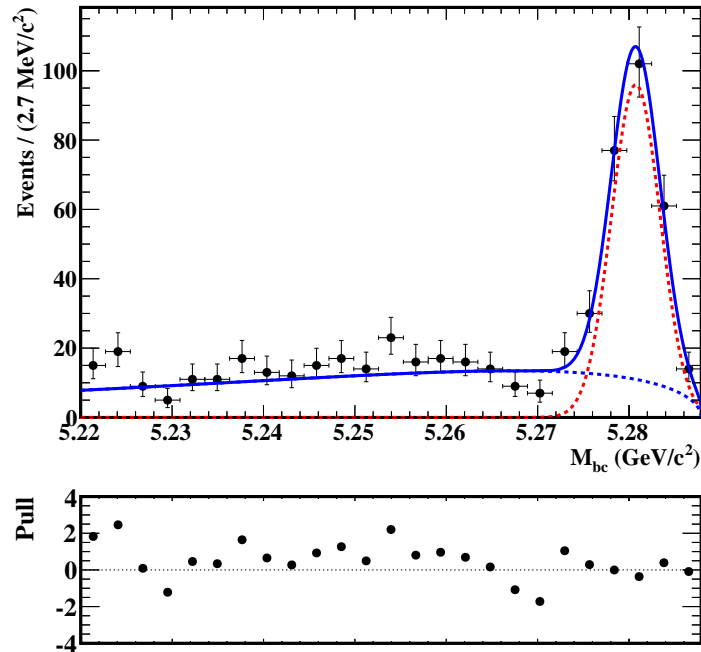


Figure 6.39: Signal-enhanced projection of  $M_{bc}$  distribution of  $B$  events in phase II data. The black points with error bars show data and solid blue curve indicate the total fit. The dotted red and blue curves show signal and background components, respectively.



# CHAPTER 7

## Conclusions

The CKM angle  $\phi_3$  is an important probe to test  $CP$  violation in the SM. The current experimental uncertainty on  $\phi_3$  measurements from  $B \rightarrow D^{(*)}K^{(*)}$  limits such tests. The precision can be improved by harnessing new  $D$  decay modes and this means exploiting new multibody states. We find that  $D \rightarrow K_S^0\pi^+\pi^-\pi^0$  is a good addition due to its larger branching fraction [14] and rich resonance substructure. We present the first measurement of the  $CP$ -even fraction  $F_+$  for the decay  $D \rightarrow K_S^0\pi^+\pi^-\pi^0$  which gives  $F_+ = 0.238 \pm 0.012 \pm 0.012$ , where the uncertainties are statistical and systematic, respectively. This measurement is performed with quantum-correlated  $D$  decays at CLEO-c that corresponds to an integrated luminosity of  $0.8 \text{ fb}^{-1}$ . The  $F_+$  measurement can be used in a quasi-GLW analysis in which there is no binning of the  $D \rightarrow K_S\pi^+\pi^-\pi^0$  phase space, although this does not provide single-mode sensitivity to  $\phi_3$ .

A model-independent formalism to measure  $\phi_3$  from a single  $D$  final state in  $B^+ \rightarrow DK^+$  decays requires the knowledge of strong-phase difference between  $D^0$  and  $\bar{D}^0$  across the  $D$  phase space. These strong-phase parameters  $c_i$  and  $s_i$  are measured from quantum-correlated  $D$  decays at CLEO-c that corresponds to an integrated luminosity of  $0.8 \text{ fb}^{-1}$ . This is done in nine regions of the decay phase space binned according to the intermediate resonances present.

The measurement of  $\phi_3$  is performed with  $B^+ \rightarrow D(K_S^0\pi^+\pi^-\pi^0)K^+$  decays for the first time in a data sample containing  $772 \times 10^6 B\bar{B}$  pairs collected by the Belle detector. The  $K_i$  and  $\bar{K}_i$  parameters, which are the fraction of  $D^0$  and  $\bar{D}^0$  yields in each bin, are determined from  $D^{*+} \rightarrow D(K_S^0\pi^+\pi^-\pi^0)\pi^+$  decays. The  $c_i$ ,  $s_i$ ,  $K_i$  and  $\bar{K}_i$  measurements are used as external inputs to the measurement of  $\phi_3$ -sensitive parameters  $x_{\pm}$  and  $y_{\pm}$ . We use  $B^+ \rightarrow D(K_S^0\pi^+\pi^-\pi^0)\pi^+$  decays as a calibration sample to test the entire signal extraction procedure because of their similar topology and larger sample size. The physical parameters  $\phi_3$ ,  $r_B$  and  $\delta_B$  are extracted from the measured values of  $x_{\pm}$  and  $y_{\pm}$  via a frequentist method with Feldman-Cousins [93] ordering. The result

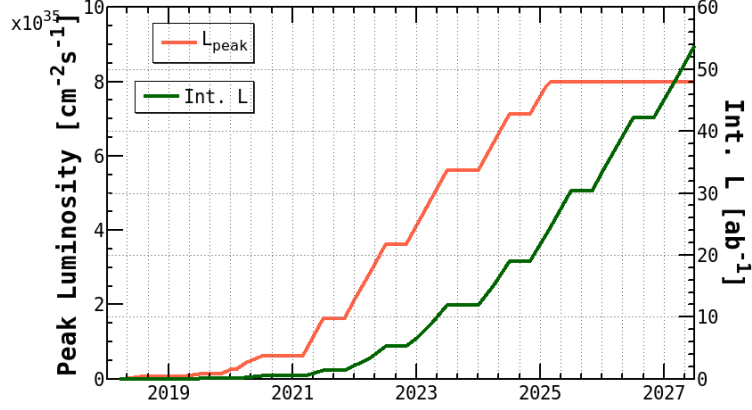


Figure 7.1: Projection of instantaneous and integrated luminosities at Super KEKB as function of time [96].

obtained is  $\phi_3 = (5.7_{-8.8}^{+10.2} \pm 3.5 \pm 5.7)^\circ$  and the  $2\sigma$  interval is  $(-29.7, 109.5)^\circ$ . The first uncertainty is statistical, the second is systematic, and the third is due to the uncertainty on the  $c_i$  and  $s_i$  measurements. The ratio of the suppressed and favoured amplitudes is  $r_B = 0.323 \pm 0.147 \pm 0.023 \pm 0.051$ . The results are statistically limited and can be improved with a larger sample at Belle II.

The Belle II experiment has started collecting data from  $e^+e^-$  collisions at  $\Upsilon(4S)$  resonance. The phase II run collected data corresponding to an integrated luminosity of  $472 \text{ pb}^{-1}$  and this was used to study the accelerator and detector performances. About 250  $B$  candidates were rediscovered from a variety of hadronic final states and this showed the capability of Belle II to reconstruct different final-state particles. The full vertex subsystem, barring one layer of the PXD, has been integrated to the other sub-detectors of Belle II. The physics run with this full system started on 25<sup>th</sup> of March 2019 and this is known as phase III of Belle II. This is expected to continue till  $50 \text{ ab}^{-1}$  of data is accumulated. The Super KEKB schedule is shown in Fig 7.1.

The sensitivity of this measurement at Belle II is analysed with a set of pseudo-experiments. The  $B^+ \rightarrow D(K_S^0 \pi^+ \pi^- \pi^0) K^+$  signal yield is expected to be 60,000 when extrapolated to the  $50 \text{ ab}^{-1}$  data set anticipated at Belle II. The  $\phi_3$  sensitivity is estimated from 1000 pseudo-experiment in a model-independent framework with  $c_i$ ,  $s_i$ ,  $K_i$ , and  $\bar{K}_i$  values as inputs with each experiment consisting of  $\approx 60,000$  events. The estimated uncertainty on  $\phi_3$  is  $\sigma_{\phi_3} = 4.4^\circ$  as illustrated in Fig. 7.2. This sensitivity is very promising and only a factor two worse than that anticipated from studying  $B^\pm \rightarrow D(K_S^0 \pi^+ \pi^-) K^\pm$  [108] decays.

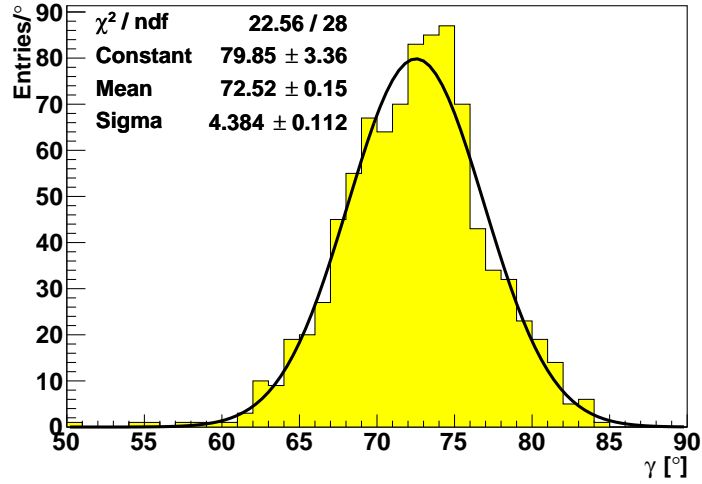


Figure 7.2:  $\phi_3$  sensitivity with  $50 \text{ ab}^{-1}$  Belle II sample.

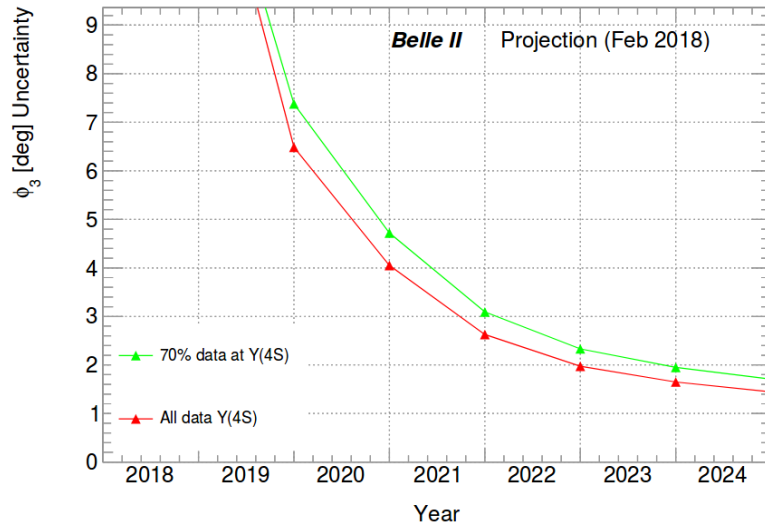


Figure 7.3: Projection of  $\phi_3$  sensitivity from all possible  $B \rightarrow D^{(*)}K^{(*)}$  final states at Belle II [108].

The current measurement can be improved upon once a suitable amplitude model for  $D^0 \rightarrow K_S^0 \pi^+ \pi^- \pi^0$  is available to provide guidance in choosing a more sensitive binning. Furthermore, the larger sample of  $e^+e^- \rightarrow \psi(3770)$  data that has been collected by BESIII will determine  $c_i$  and  $s_i$  more precisely, thus reducing the systematic uncertainty. The results presented here, combined with the improvements in binning and the increased sample of  $B$  decays that will be available at Belle II, mean that model-independent analysis of  $B^+ \rightarrow D(K_S^0 \pi^+ \pi^- \pi^0)K^+$  is a very promising addition to the suite of modes to be used to determine  $\phi_3$  to a precision of  $1\text{--}2^\circ$  [108]. The expected  $\phi_3$  sensitivity from all possible  $B \rightarrow D^{(*)}K^{(*)}$  final states at Belle II is shown in Fig. 7.3.



# APPENDIX A

## Measurement of $F_+$

We perform the  $F_+$  measurements with four different types of tag mode -  $CP$  eigenstates, quasi- $CP$  eigenstates, self-conjugate final states  $K_{S,L}^0\pi^+\pi^-$  and  $K_S^0\pi^+\pi^-\pi^0$  self-tags - using the relations presented in Sec. 1.4.1. With  $CP$ -eigenstate tags, the ratios between the double-tagged and single-tagged yields,  $N^+$  and  $N^-$ , when mode  $g$  is a  $CP$ -odd ( $\lambda_{CP}^g = -1$ ) or  $CP$ -even ( $\lambda_{CP}^g = 1$ ), are written as

$$N^\pm = \frac{M(f|g)}{S(g)} \propto \mathcal{B}(f) \left[ 1 \mp (2F_+^f - 1) \right], \quad (\text{A.1})$$

where  $f$  is the final state of the other  $D$  meson. This leads to the definition of  $F_+^f$  in terms of  $N^+$  and  $N^-$  as

$$F_+^f \equiv \frac{N^+}{N^+ + N^-}. \quad (\text{A.2})$$

We also use the tag mode  $\pi^+\pi^-\pi^0$  with already known  $F_+$ , to determine  $F_+^f$ . We can define a quantity  $N^g$  as the ratio of double-tagged and single-tagged yields as

$$N^g \propto \mathcal{B}(f) \left[ 1 - (2F_+^f - 1)(2F_+^g - 1) \right]. \quad (\text{A.3})$$

Then using Eq. (A.3) along with Eq. (A.1), we get

$$F_+^f = \frac{N^+ F_+^g}{N^g - N^+ + 2N^+ F_+^g}. \quad (\text{A.4})$$

The  $g$  mode can also be multibody modes like  $K_S^0\pi^+\pi^-$ ,  $K_L^0\pi^+\pi^-$  or  $K_S^0\pi^+\pi^-\pi^0$  for which the average strong-phase difference has been determined in bins of phase space. Hence the double-tagged yields measured in each bin have sensitivity to  $F_+^f$  as given in Eq. (1.46). The results for the different tags are discussed in the following subsections.

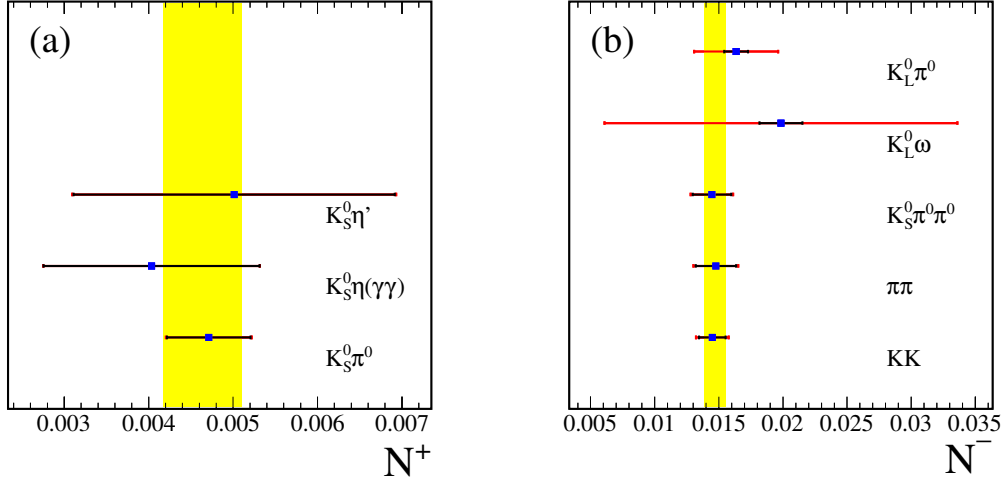


Figure A.1:  $N^+$  values for the  $CP$ -odd modes (left) and  $N^-$  values for the  $CP$ -even modes (right). The yellow region shows the average value. The horizontal black and red error bars show the statistical and the total uncertainty, respectively.

### A.0.1 $CP$ and quasi- $CP$ tags method

The double-tagged yields involving a  $CP$  eigenstate tag are used to obtain  $N^+$  and  $N^-$ . The dependence on branching fraction and reconstruction efficiency is removed by the normalization to the single-tagged yields. The effect of  $D^0 \bar{D}^0$  mixing is accounted for by applying a correction factor to the measured single-tagged yields  $S_{\text{meas}}$  [31] to estimate the uncorrelated yield  $S$  required to normalize the expressions given in Eqs. (A.2) and (A.4) as

$$S = S_{\text{meas}} / (1 - \lambda_{CP} y_D), \quad (\text{A.5})$$

where  $y_D = (0.69 \pm 0.06)\%$  is the  $D$ -mixing parameter [29] related to the width difference between the mass eigenstates. The  $N^+$  and  $N^-$  values are shown in Fig. A.1. It can be seen that there is consistency among the values obtained from different  $CP$  eigenstates. From these results, a value of  $F_+ = 0.240 \pm 0.018 \pm 0.011$  is calculated using Eq. (A.2). The uncertainties are statistical and systematic, respectively. This value indicates that the mode  $K_S^0 \pi^+ \pi^- \pi^0$  is significantly  $CP$ -odd. This is the first measurement of a  $D$  decay having  $F_+$  value close to zero, as the previous measurements of modes  $\pi^+ \pi^- \pi^0$ ,  $K^+ K^- \pi^0$  and  $\pi^+ \pi^- \pi^+ \pi^-$  are predominantly  $CP$ -even [31, 76].

The dominant systematic uncertainty comes from the determination of the single-tagged yields: in particular the fit shapes, assumed branching fraction and the reconstruction efficiency values used for  $K_L^0$  modes. The single-tagged yields are varied by

their statistical uncertainty and the resultant deviations in  $F_+$  value are noted. The PDF shape parameters that are fixed in the nominal fit are varied by  $\pm 1\sigma$ , where  $\sigma$  is the uncertainty of each parameter, and the fit is performed again. The deviations in  $F_+$  from the nominal result are considered as the systematic uncertainty. The single-tagged yields for modes involving a  $K_L^0$  meson are calculated from the efficiency, branching fraction and total number of  $D\bar{D}$  pairs in data, as it is not possible to identify such a state without reconstructing the full event.

Using the quasi- $CP$  tag  $\pi^+\pi^-\pi^0$ , whose  $F_+$  value is  $0.973 \pm 0.017$  [76], the  $CP$ -even fraction for  $K_S^0\pi^+\pi^-\pi^0$  is calculated from Eq. (A.4). The result obtained with this quasi- $CP$  mode is  $0.244 \pm 0.020 \pm 0.007$ . The systematic uncertainty is estimated in the same manner as in the case of  $CP$  tags. The additional contribution from the uncertainty on  $F_+^{\pi^+\pi^-\pi^0}$  is also considered as a systematic uncertainty.

## A.0.2 $K_S^0\pi^+\pi^-$ and $K_L^0\pi^+\pi^-$ tags method

The  $K_S^0\pi^+\pi^-$  and  $K_L^0\pi^+\pi^-$  Dalitz plots are studied and binned according to the Equal  $\delta_D$  scheme reported in Ref. [77] based on the amplitude model described in Ref. [109]. The double-tagged decays with  $K_S^0\pi^+\pi^-$  and  $K_L^0\pi^+\pi^-$  are analysed by dividing the Dalitz plot of the tag mode into eight pairs of symmetric bins. The symmetric bins are folded across the line  $m_+^2 = m_-^2$  to make a total of eight bins. The double-tagged yield in each of the folded bins is related to  $F_+$  as given in Eq. (1.46). Therefore  $F_+$  can be extracted from a combined log-likelihood fit to the yields.

The background subtracted yields are determined in each of the bins for both the modes. The events in sidebands, where the tag mode is correctly reconstructed, are distributed across the Dalitz plane according to the  $K_i$  and  $\bar{K}_i$  values. The signal-side peaking background estimated from MC simulations are also distributed in the same manner in each of the bins. All other backgrounds are uniformly distributed across the Dalitz plane.

The reconstruction efficiency in each bin is obtained from simulated signal samples and a correction is applied to the yields to account for the variation of efficiency across the bins, which varies by typically 3%, bin-to-bin. Table A.1 shows the background subtracted efficiency corrected yields in each of the eight bins.

Bin	$K_S^0\pi^+\pi^-$	$K_L^0\pi^+\pi^-$
1	$166 \pm 14$	$164 \pm 21$
2	$57 \pm 8$	$75 \pm 13$
3	$47 \pm 7$	$69 \pm 14$
4	$8 \pm 3$	$69 \pm 11$
5	$34 \pm 6$	$141 \pm 19$
6	$30 \pm 6$	$86 \pm 14$
7	$61 \pm 8$	$132 \pm 16$
8	$95 \pm 10$	$106 \pm 16$

Table A.1: Background subtracted efficiency corrected yields of  $D \rightarrow K_S^0\pi^+\pi^-\pi^0$  decays tagged with  $K_S^0\pi^+\pi^-$  and  $K_L^0\pi^+\pi^-$  modes in bins of the tagging decay.

Tag	$F_+$	$\chi^2/DoF$
$K_S^0\pi^+\pi^-$	$0.194 \pm 0.040$	0.96
$K_L^0\pi^+\pi^-$	$0.322 \pm 0.044$	1.33
$K_{S,L}^0\pi^+\pi^-$	$0.255 \pm 0.029$	1.42

Table A.2:  $F_+$  results for the mode  $K_S^0\pi^+\pi^-\pi^0$  from the tags  $K_S^0\pi^+\pi^-$  and  $K_L^0\pi^+\pi^-$ . The row  $K_{S,L}^0\pi^+\pi^-$  indicates that the combined fit includes both the samples. The fit quality metric  $\chi^2/DoF$  is also shown, where  $DoF$  stands for the number of degrees of freedom.

A log-likelihood fit is performed with the input yields following the form of Eq. (1.46) with the  $CP$ -even fraction and overall normalization as fit parameters. The uncertainty on the  $K_i$ ,  $\overline{K}_i$ , and  $c_i$  input parameters are added as Gaussian constraints in the fit. These input parameters are taken from [77]. The fit is performed separately for  $K_S^0\pi^+\pi^-$  and  $K_L^0\pi^+\pi^-$  and then for both the tags combined. All the fits have good quality and the results are presented in Table A.2. The measured and predicted yields in each bin are given in Fig. A.2 for both tags.

There is a two standard deviation difference between the results from each of the tags alone, however the combined result agrees with  $F_+$  from the other tag methods. The non-uniform acceptance of the  $K_{S,L}^0\pi^+\pi^-$  Dalitz plane is studied by varying the efficiency by 3% independently in each bin. The resulting change of  $^{+0.007}_{-0.008}$  in  $F_+$  is assigned as the systematic uncertainty related to this source.

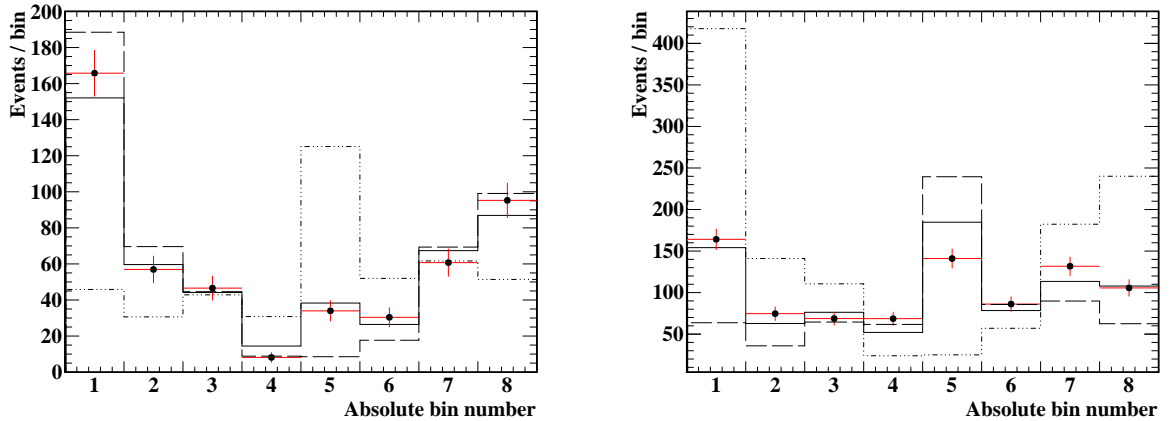


Figure A.2: Predicted and measured yields for  $K_S^0\pi^+\pi^-$  (left) and  $K_L^0\pi^+\pi^-$  (right) in each bin obtained from the combined fit of both the modes. The histogram shows the predicted values from the fit, points show the measured values, the dashed line corresponds to  $F_+ = 0$  and the dotted line shows  $F_+ = 1$ .

Tag method	$F_+$
$CP$ tags	$0.240 \pm 0.018 \pm 0.011$
quasi- $CP$ tag	$0.244 \pm 0.020 \pm 0.007$
$K_{S,L}^0\pi^+\pi^-$	$0.255 \pm 0.029^{+0.007}_{-0.008}$
$K_S^0\pi^+\pi^-\pi^0$ self-tag	$0.226 \pm 0.019 \pm 0.004$
Average	$0.238 \pm 0.012 \pm 0.003$

Table A.3:  $F_+$  results from different tag methods.

### A.0.3 $K_S^0\pi^+\pi^-\pi^0$ self-tags method and combined result

The double-tagged modes in which both the  $D$  mesons decay to the same final state of  $K_S^0\pi^+\pi^-\pi^0$  can also give information about  $F_+$  following the relation given in Eq. (1.47). The value is obtained to be  $0.226 \pm 0.019 \pm 0.004$ . Here, the systematic uncertainty arises from the uncertainty on external input values used in the calculation such as the number of  $D\bar{D}$  pairs and the branching fraction of the decay.

The value of  $F_+$  from all the different tag modes are given in Table A.3. They are consistent with each other and the combined result obtained via a weighted averaging is  $0.238 \pm 0.012 \pm 0.003$ , where the correlation due to the use of  $N^+$  for  $CP$  tags as well as the  $\pi^+\pi^-\pi^0$  tag is taken into account.

We need to consider another source of systematic uncertainty common to all methods: the non-uniform acceptance across the phase space of  $D \rightarrow K_S^0\pi^+\pi^-\pi^0$ , which

will bias the result with respect to the flat acceptance case. We estimate the acceptance systematic uncertainty by calculating  $F_+$  from the  $c_i$  strong-phase difference results given in Sec. 3.6, which have bin-wise efficiency corrections. The value of  $F_+$  is related to  $c_i$  by

$$F_+ = \frac{1}{2} \left( 1 + \sum_i c_i \sqrt{K_i \overline{K}_i} \right). \quad (\text{A.6})$$

The same data are used, so any difference can be attributed to the absence of acceptance corrections in the inclusive method. The obtained result is  $0.226 \pm 0.020$ . There is a one standard deviation difference between the value obtained from Eq. (A.6) and the averaged unbinned  $F_+$  result. The difference, 0.012, is taken as the systematic uncertainty from this source. Including this uncertainty the combined result becomes  $0.238 \pm 0.012 \pm 0.012$ .

## APPENDIX B

### Fit projections in bins of $D^{*\pm} \rightarrow D\pi^\pm$ sample

The signal-enhanced projections of  $M_D$  and  $\Delta M$  distributions from the two-dimensional fit in bins 2–9 of  $D^{*\pm} \rightarrow D\pi^\pm$  sample in data are shown in Fig. B.1–B.8. In all the figures, the black points with error bars are the data and the solid blue curve shows the total fit. The dotted red, blue and magenta curves represent the signal, combinatorial and random-slow-pion backgrounds respectively. The pull between the fit and the data is shown below the distributions.

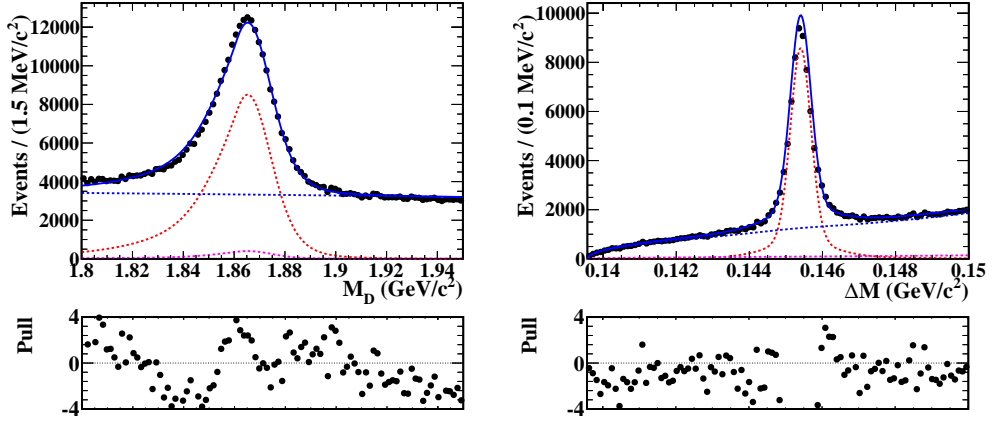


Figure B.1: Signal-enhanced fit projections of  $M_D$  (left) and  $\Delta M$  (right) distributions from data in bin 2.

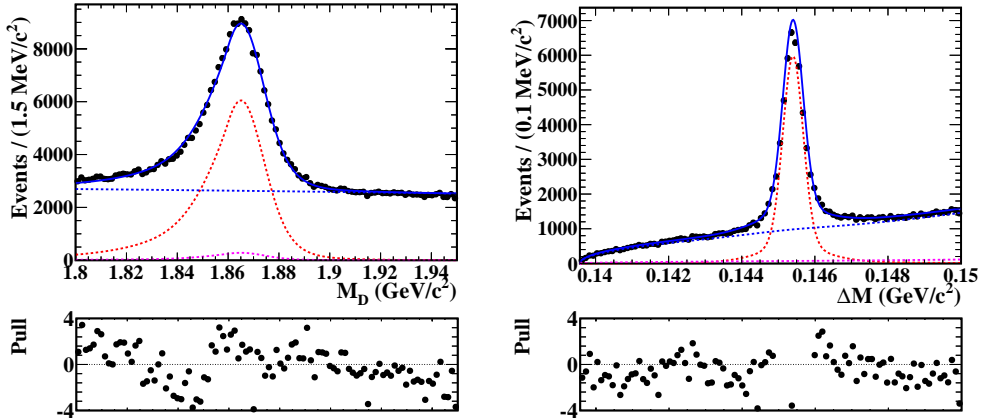


Figure B.2: Signal-enhanced fit projections of  $M_D$  (left) and  $\Delta M$  (right) distributions from data in bin 3.

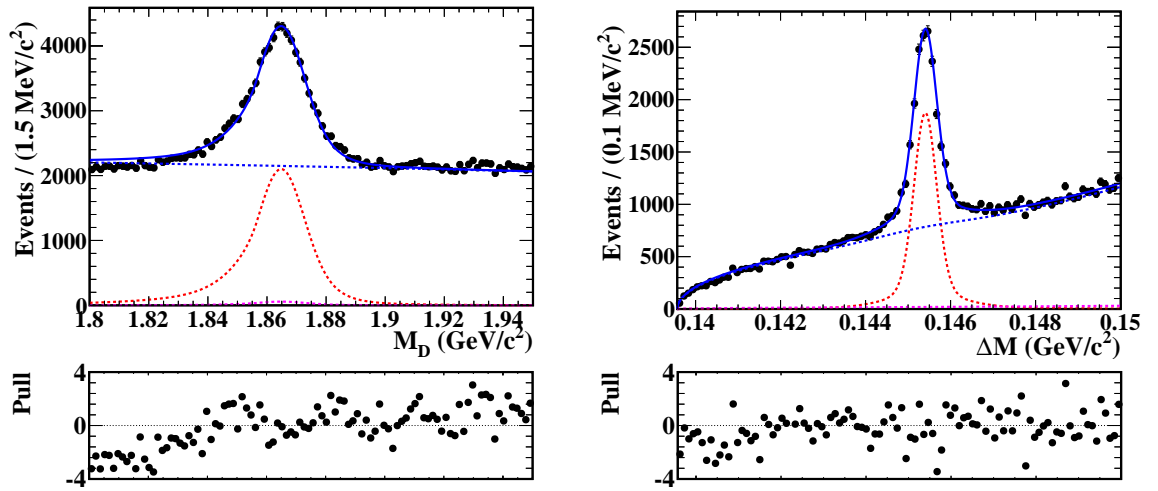


Figure B.3: Signal-enhanced fit projections of  $M_D$  (left) and  $\Delta M$  (right) distributions from data in bin 4.

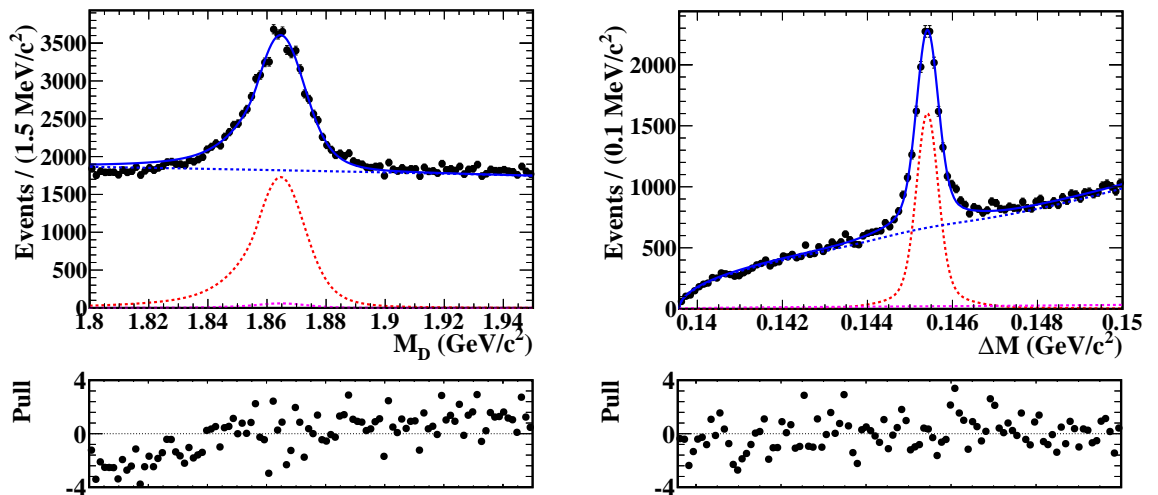


Figure B.4: Signal-enhanced fit projections of  $M_D$  (left) and  $\Delta M$  (right) distributions from data in bin 5.

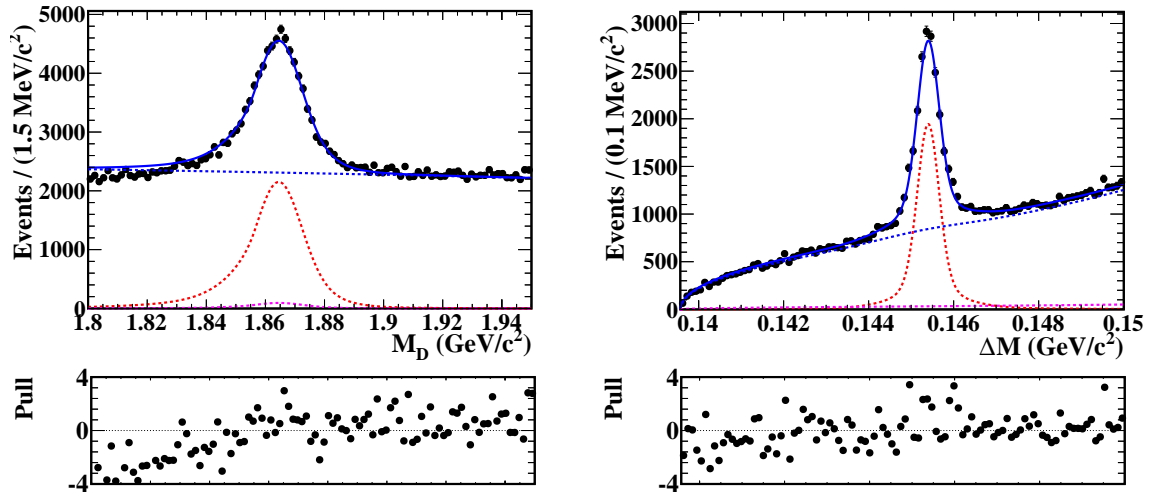


Figure B.5: Signal-enhanced fit projections of  $M_D$  (left) and  $\Delta M$  (right) distributions from data in bin 6.

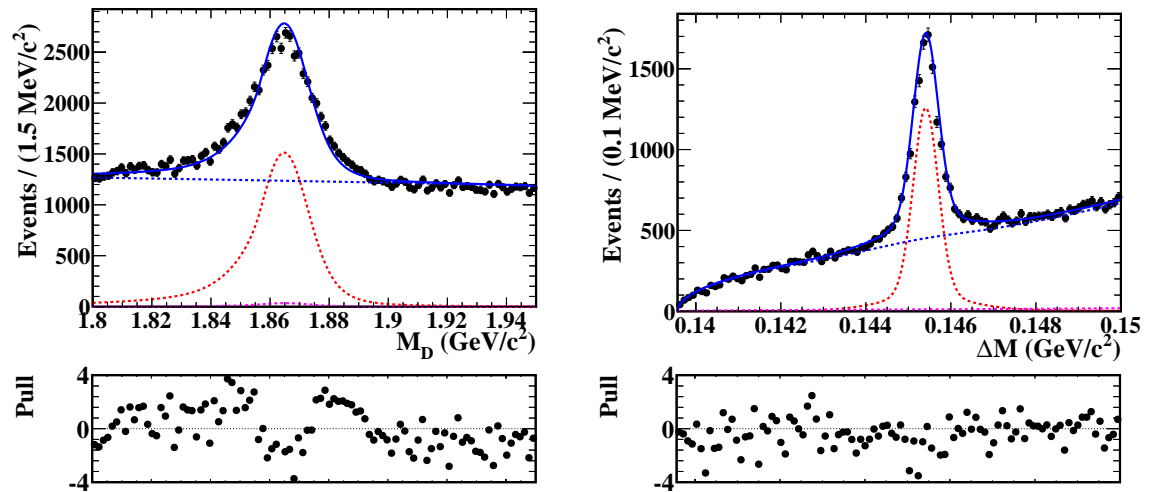


Figure B.6: Signal-enhanced fit projections of  $M_D$  (left) and  $\Delta M$  (right) distributions from data in bin 7.

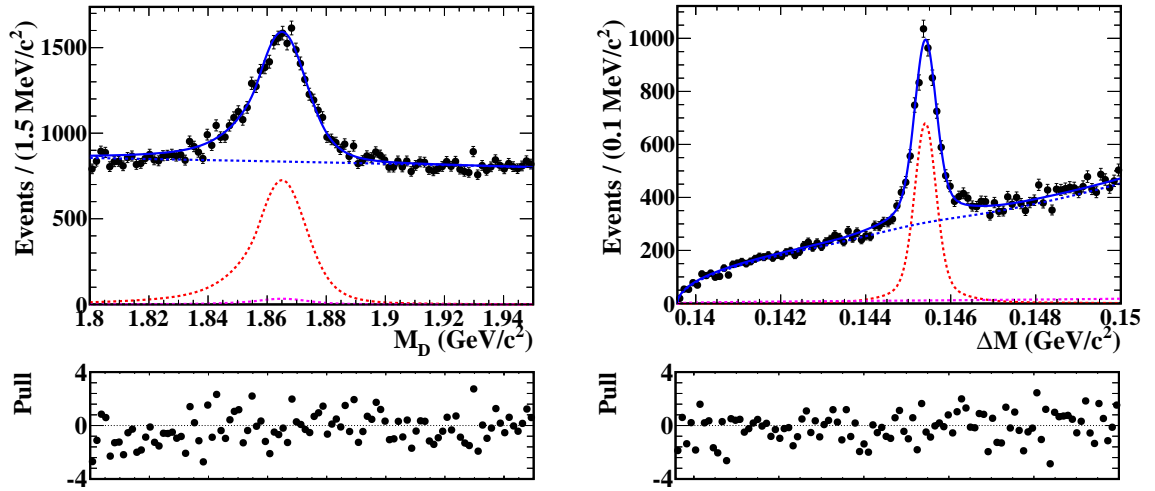


Figure B.7: Signal-enhanced fit projections of  $M_D$  (left) and  $\Delta M$  (right) distributions from data in bin 8.

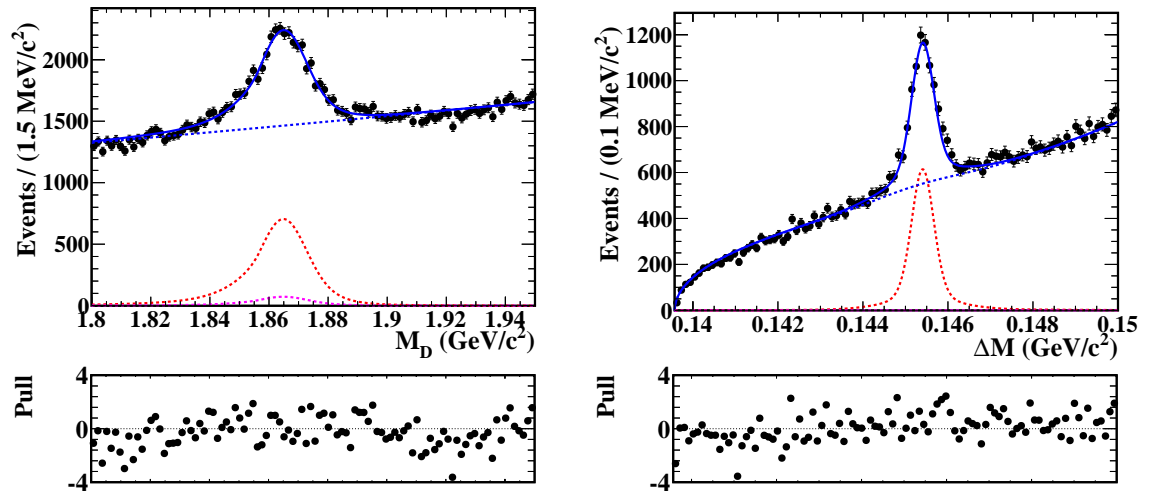


Figure B.8: Signal-enhanced fit projections of  $M_D$  (left) and  $\Delta M$  (right) distributions from data in bin 9.

## APPENDIX C

### Fit projections in bins of $B^\pm \rightarrow Dh^\pm$ sample

The signal-enhanced fit projections of  $\Delta E$  and  $C'_{\text{NN}}$  in bins 2–9 of  $B^\pm \rightarrow D\pi^\pm$  and  $B^\pm \rightarrow DK^\pm$  decays in generic MC sample having integrated luminosity equivalent to that of the data sample are shown in Fig. C.1–C.16. In each figure, the black points with error bars are the data and the solid blue curve is the total fit. The dotted red, blue, magenta, and green curves represent the signal, continuum, random  $B\bar{B}$  backgrounds and cross-feed peaking background components, respectively. The pull between the fit and the data is shown below the distributions.

The corresponding distributions of  $\Delta E$  and  $C'_{\text{NN}}$  in bins 2–9 of  $B^\pm \rightarrow D\pi^\pm$  and  $B^\pm \rightarrow DK^\pm$  decays in data sample are shown in Fig. C.17–C.32

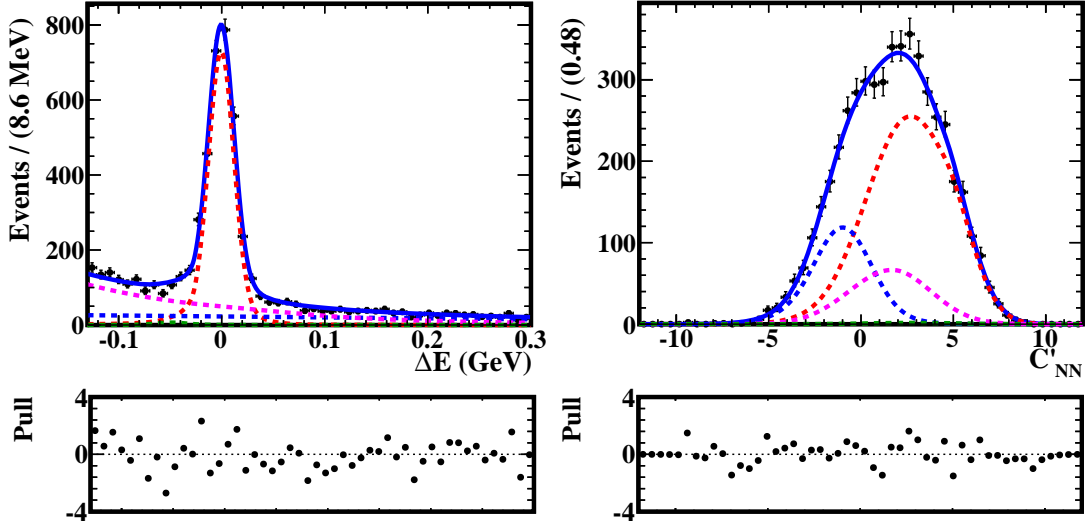


Figure C.1: Signal-enhanced projections of  $\Delta E$  (left) and  $C'_{\text{NN}}$  (right) distributions of  $B^\pm \rightarrow D(K_S^0 \pi^+ \pi^- \pi^0) \pi^\pm$  decays in bin 2 from a two-dimensional simultaneous fit to  $B^\pm \rightarrow D\pi^\pm$  and  $B^\pm \rightarrow DK^\pm$  events in generic MC sample with integrated luminosity equivalent to that of data.

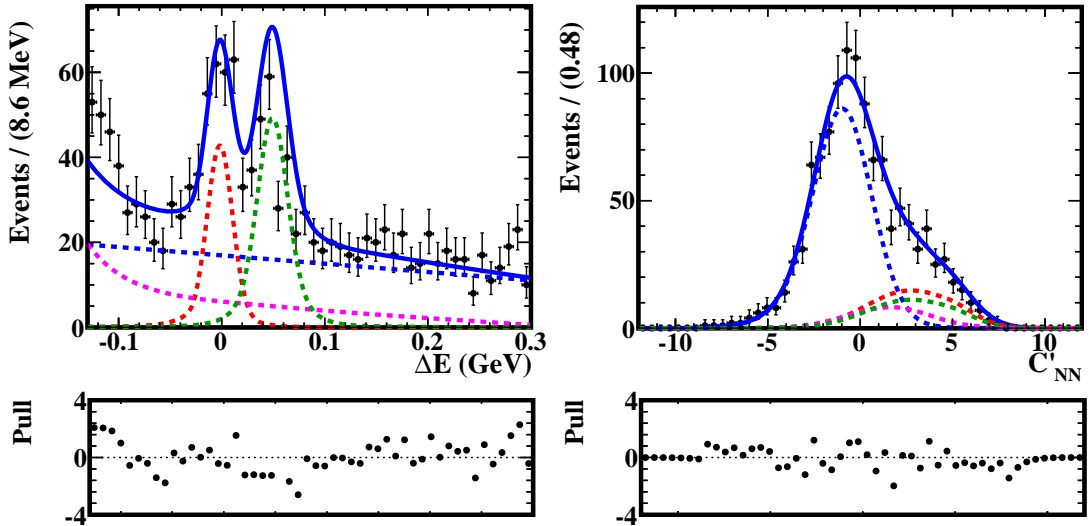


Figure C.2: Signal-enhanced projections of  $\Delta E$  (left) and  $C'_{\text{NN}}$  (right) distributions of  $B^\pm \rightarrow D(K_S^0 \pi^+ \pi^- \pi^0) K^\pm$  decays in bin 2 from a two-dimensional simultaneous fit to  $B^\pm \rightarrow D\pi^\pm$  and  $B^\pm \rightarrow DK^\pm$  events in generic MC sample with integrated luminosity equivalent to that of data.

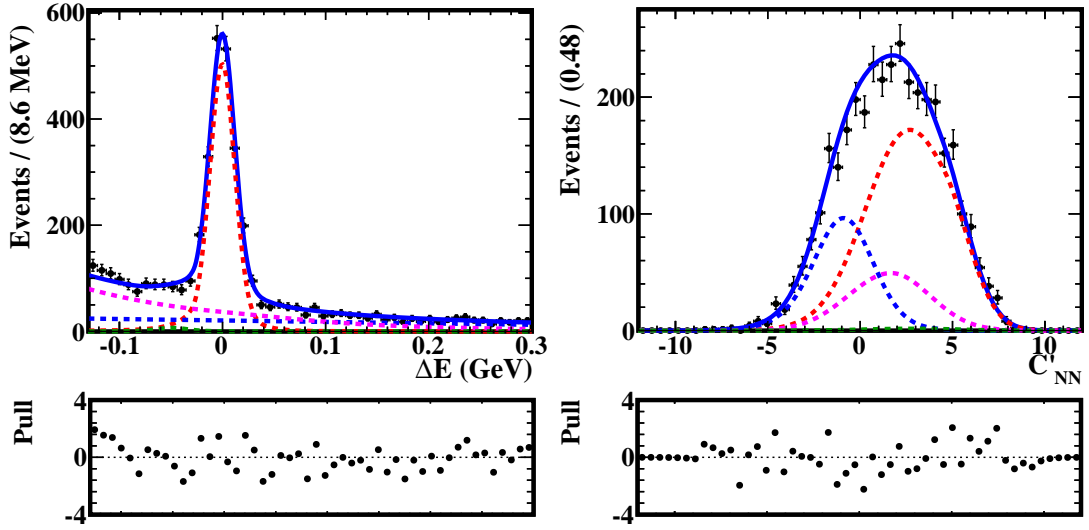


Figure C.3: Signal-enhanced projections of  $\Delta E$  (left) and  $C'_{\text{NN}}$  (right) distributions of  $B^\pm \rightarrow D(K_S^0 \pi^+ \pi^- \pi^0) \pi^\pm$  decays in bin 3 from a two-dimensional simultaneous fit to  $B^\pm \rightarrow D\pi^\pm$  and  $B^\pm \rightarrow DK^\pm$  events in generic MC sample with integrated luminosity equivalent to that of data.

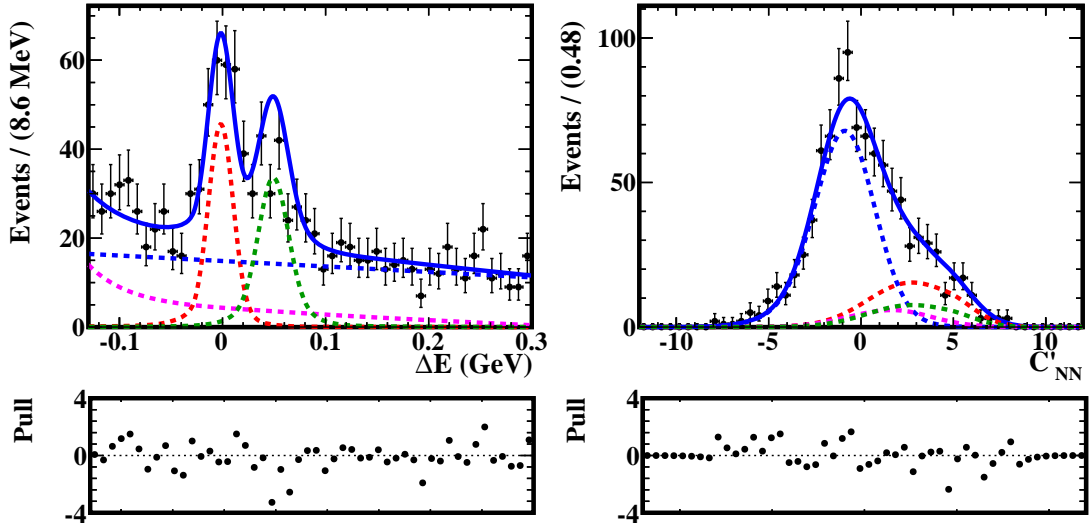


Figure C.4: Signal-enhanced projections of  $\Delta E$  (left) and  $C'_{\text{NN}}$  (right) distributions of  $B^\pm \rightarrow D(K_S^0 \pi^+ \pi^- \pi^0) K^\pm$  decays in bin 3 from a two-dimensional simultaneous fit to  $B^\pm \rightarrow D\pi^\pm$  and  $B^\pm \rightarrow DK^\pm$  events in generic MC sample with integrated luminosity equivalent to that of data.

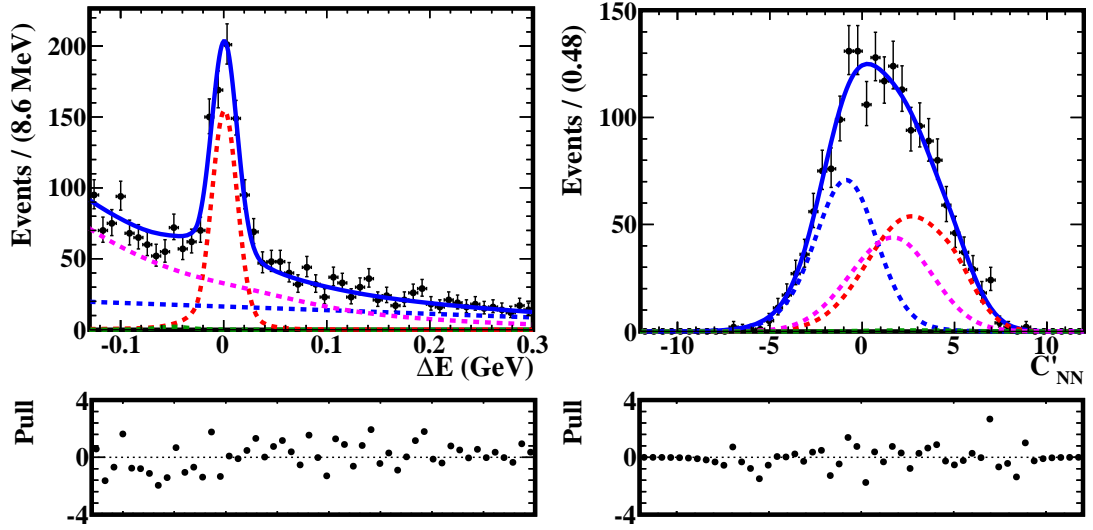


Figure C.5: Signal-enhanced projections of  $\Delta E$  (left) and  $C'_{NN}$  (right) distributions of  $B^\pm \rightarrow D(K_S^0 \pi^+ \pi^- \pi^0) \pi^\pm$  decays in bin 4 from a two-dimensional simultaneous fit to  $B^\pm \rightarrow D\pi^\pm$  and  $B^\pm \rightarrow DK^\pm$  events in generic MC sample with integrated luminosity equivalent to that of data.

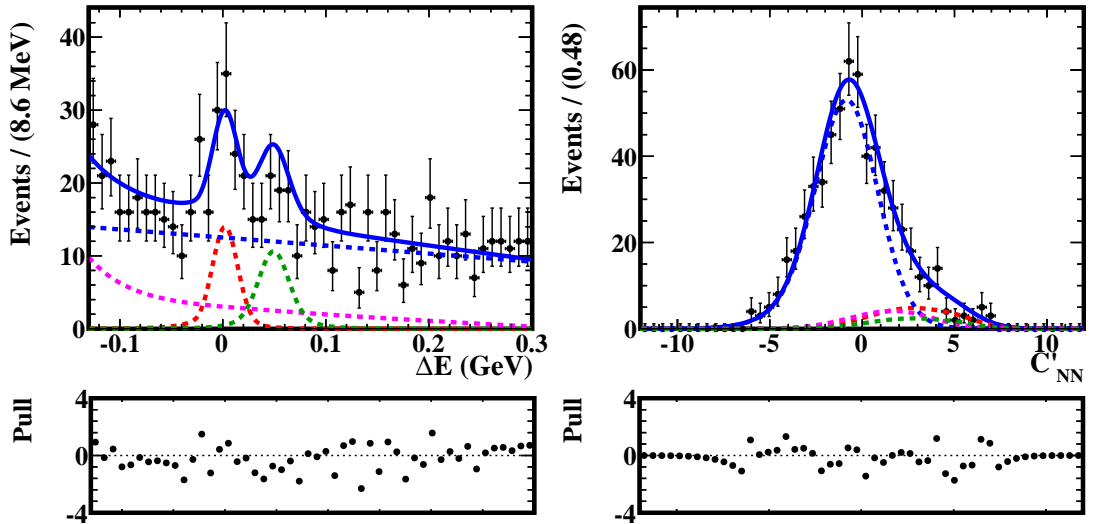


Figure C.6: Signal-enhanced projections of  $\Delta E$  (left) and  $C'_{NN}$  (right) distributions of  $B^\pm \rightarrow D(K_S^0 \pi^+ \pi^- \pi^0) K^\pm$  decays in bin 4 from a two-dimensional simultaneous fit to  $B^\pm \rightarrow D\pi^\pm$  and  $B^\pm \rightarrow DK^\pm$  events in generic MC sample with integrated luminosity equivalent to that of data.

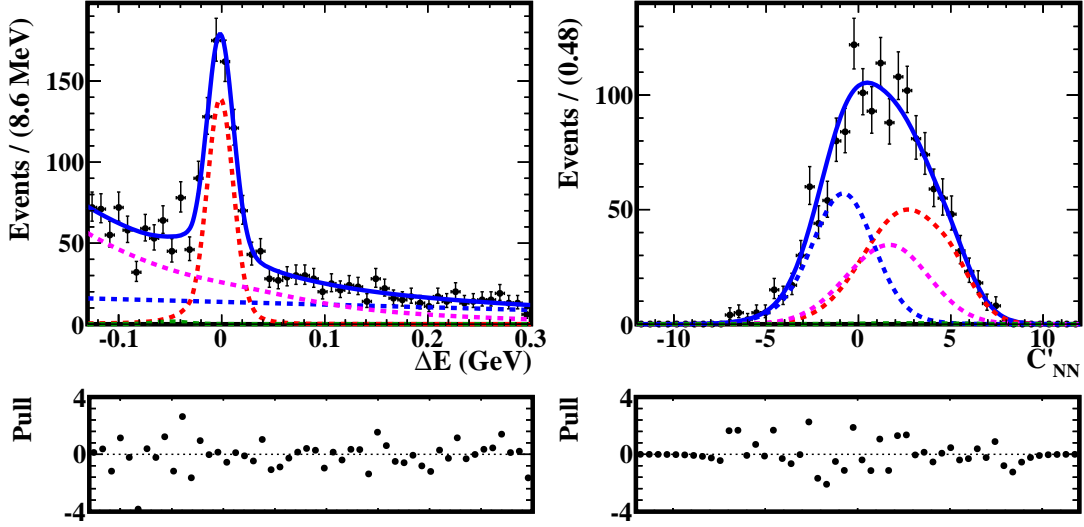


Figure C.7: Signal-enhanced projections of  $\Delta E$  (left) and  $C'_{\text{NN}}$  (right) distributions of  $B^\pm \rightarrow D(K_S^0 \pi^+ \pi^- \pi^0) \pi^\pm$  decays in bin 5 from a two-dimensional simultaneous fit to  $B^\pm \rightarrow D\pi^\pm$  and  $B^\pm \rightarrow DK^\pm$  events in generic MC sample with integrated luminosity equivalent to that of data.

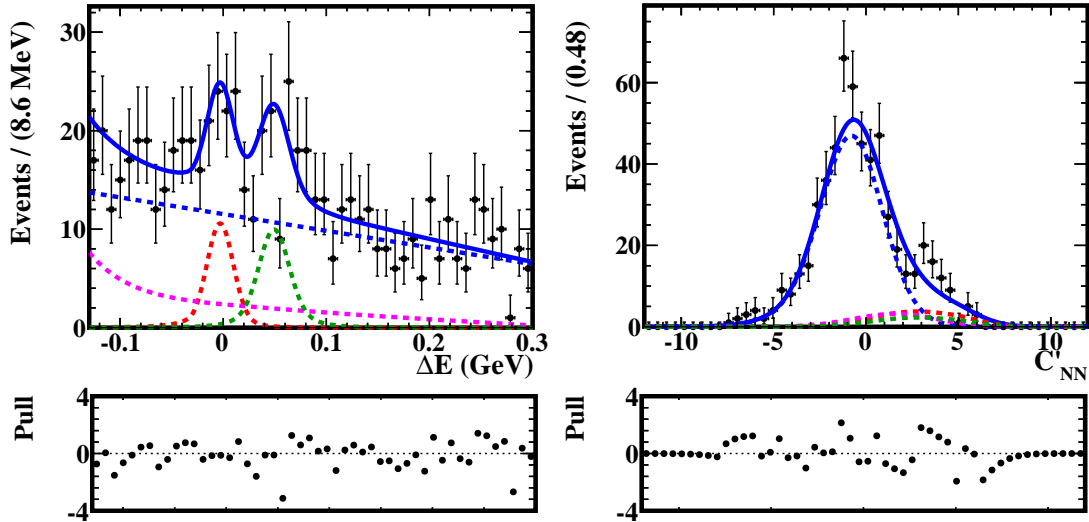


Figure C.8: Signal-enhanced projections of  $\Delta E$  (left) and  $C'_{\text{NN}}$  (right) distributions of  $B^\pm \rightarrow D(K_S^0 \pi^+ \pi^- \pi^0) K^\pm$  decays in bin 5 from a two-dimensional simultaneous fit to  $B^\pm \rightarrow D\pi^\pm$  and  $B^\pm \rightarrow DK^\pm$  events in generic MC sample with integrated luminosity equivalent to that of data.

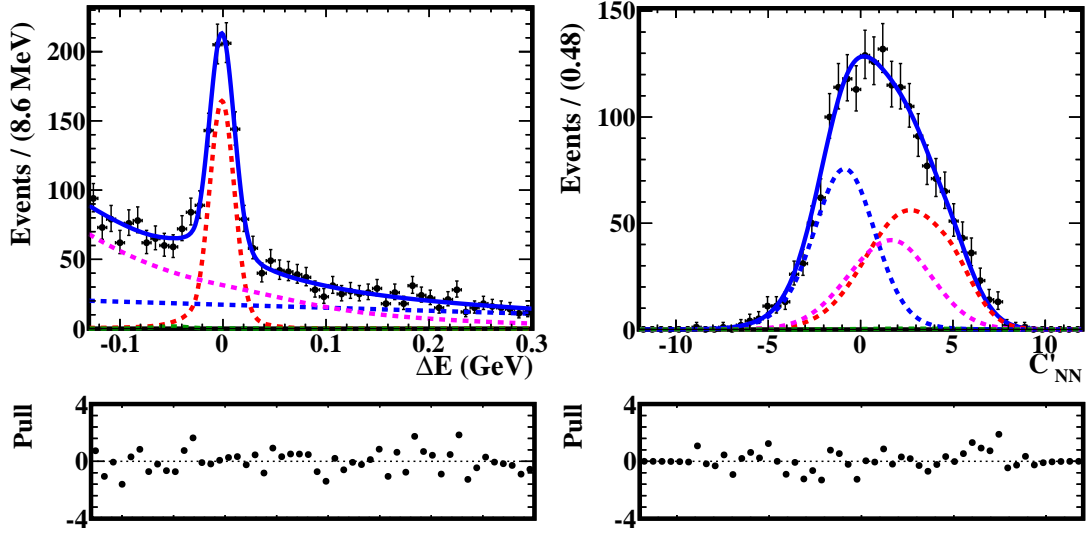


Figure C.9: Signal-enhanced projections of  $\Delta E$  (left) and  $C'_{NN}$  (right) distributions of  $B^\pm \rightarrow D(K_S^0 \pi^+ \pi^- \pi^0) \pi^\pm$  decays in bin 6 from a two-dimensional simultaneous fit to  $B^\pm \rightarrow D\pi^\pm$  and  $B^\pm \rightarrow DK^\pm$  events in generic MC sample with integrated luminosity equivalent to that of data.

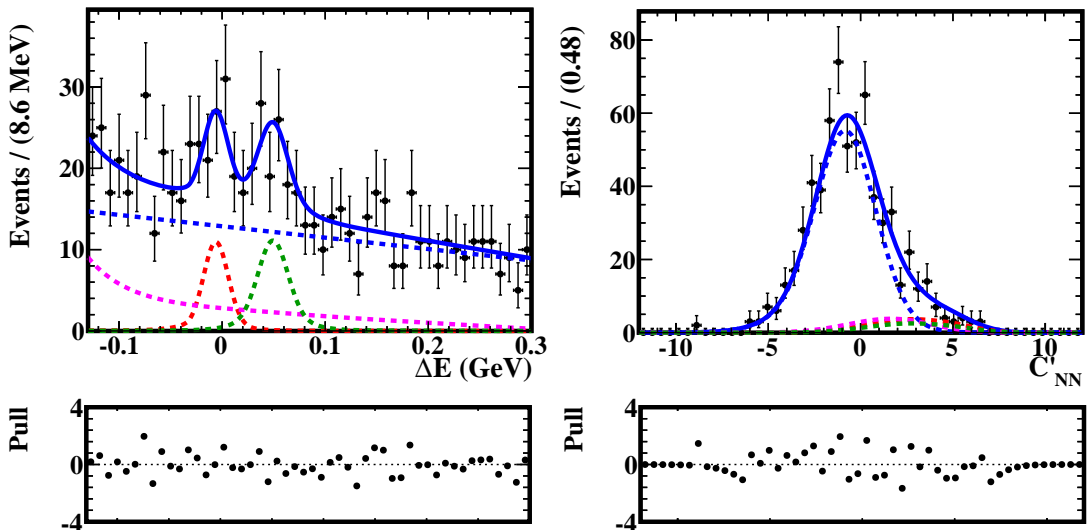


Figure C.10: Signal-enhanced projections of  $\Delta E$  (left) and  $C'_{NN}$  (right) distributions of  $B^\pm \rightarrow D(K_S^0 \pi^+ \pi^- \pi^0) K^\pm$  decays in bin 6 from a two-dimensional simultaneous fit to  $B^\pm \rightarrow D\pi^\pm$  and  $B^\pm \rightarrow DK^\pm$  events in generic MC sample with integrated luminosity equivalent to that of data.

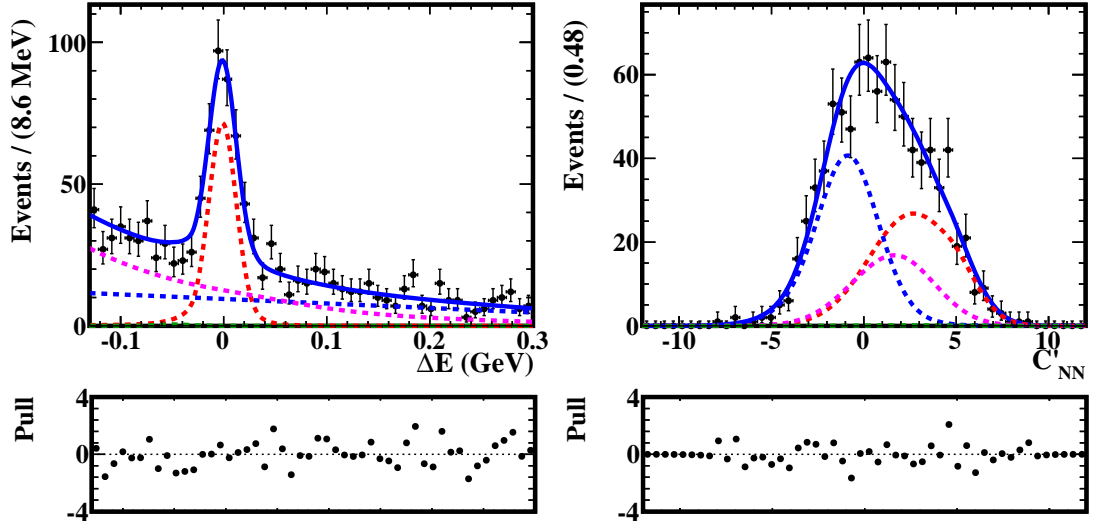


Figure C.11: Signal-enhanced projections of  $\Delta E$  (left) and  $C'_{NN}$  (right) distributions of  $B^\pm \rightarrow D(K_S^0 \pi^+ \pi^- \pi^0) \pi^\pm$  decays in bin 7 from a two-dimensional simultaneous fit to  $B^\pm \rightarrow D\pi^\pm$  and  $B^\pm \rightarrow DK^\pm$  events in generic MC sample with integrated luminosity equivalent to that of data.

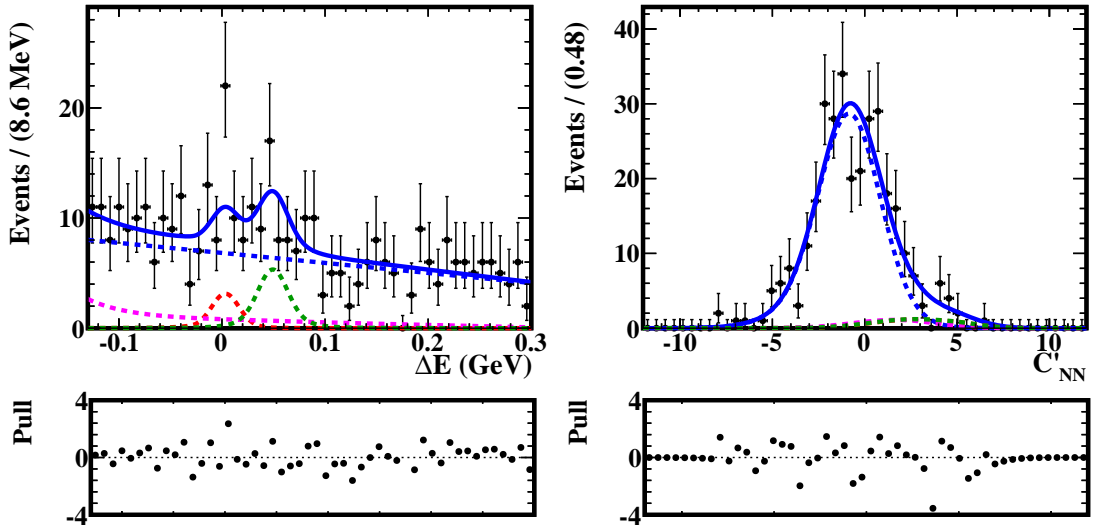


Figure C.12: Signal-enhanced projections of  $\Delta E$  (left) and  $C'_{NN}$  (right) distributions of  $B^\pm \rightarrow D(K_S^0 \pi^+ \pi^- \pi^0) K^\pm$  decays in bin 7 from a two-dimensional simultaneous fit to  $B^\pm \rightarrow D\pi^\pm$  and  $B^\pm \rightarrow DK^\pm$  events in generic MC sample with integrated luminosity equivalent to that of data.

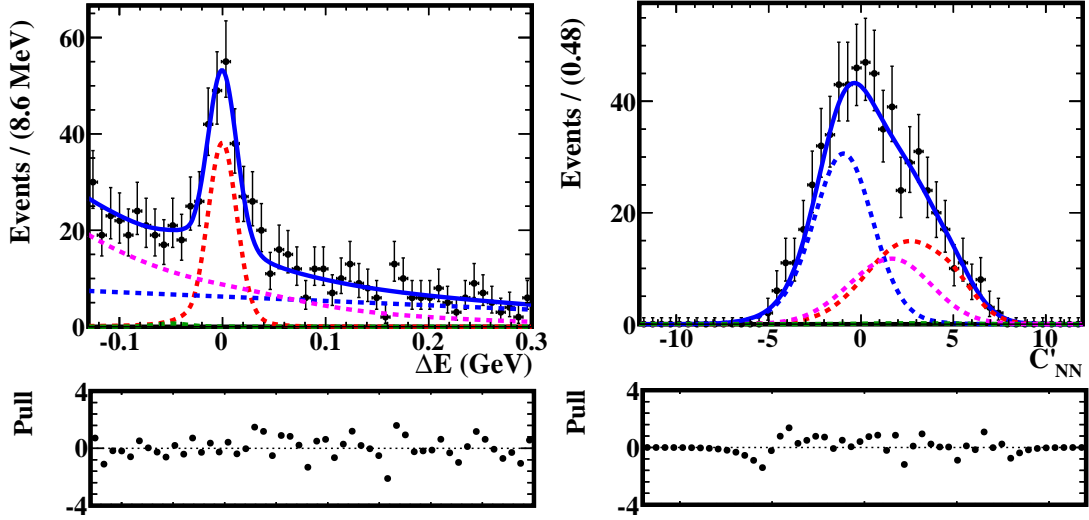


Figure C.13: Signal-enhanced projections of  $\Delta E$  (left) and  $C'_{NN}$  (right) distributions of  $B^\pm \rightarrow D(K_S^0 \pi^+ \pi^- \pi^0) \pi^\pm$  decays in bin 8 from a two-dimensional simultaneous fit to  $B^\pm \rightarrow D\pi^\pm$  and  $B^\pm \rightarrow DK^\pm$  events in generic MC sample with integrated luminosity equivalent to that of data.

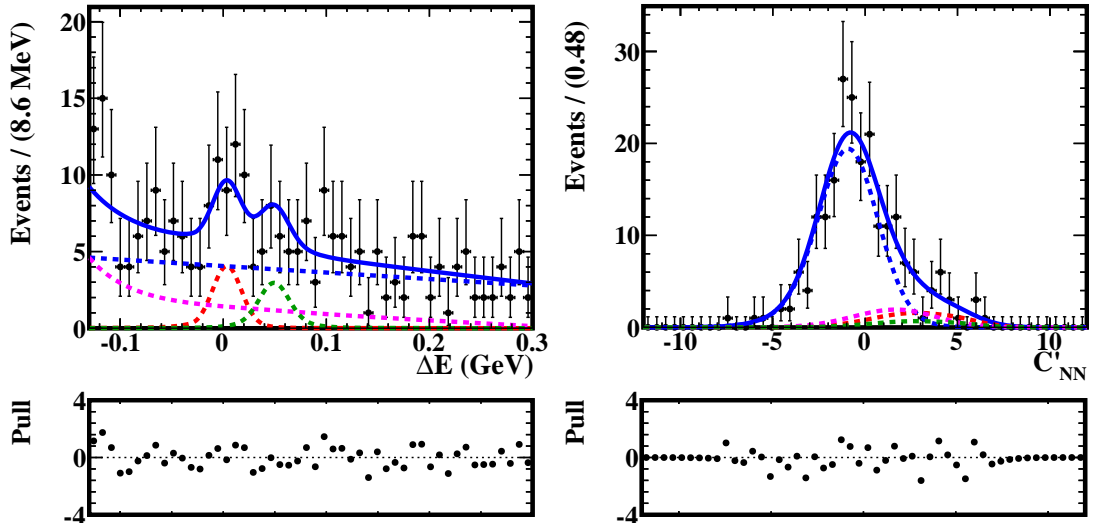


Figure C.14: Signal-enhanced projections of  $\Delta E$  (left) and  $C'_{NN}$  (right) distributions of  $B^\pm \rightarrow D(K_S^0 \pi^+ \pi^- \pi^0) K^\pm$  decays in bin 8 from a two-dimensional simultaneous fit to  $B^\pm \rightarrow D\pi^\pm$  and  $B^\pm \rightarrow DK^\pm$  events in generic MC sample with integrated luminosity equivalent to that of data.

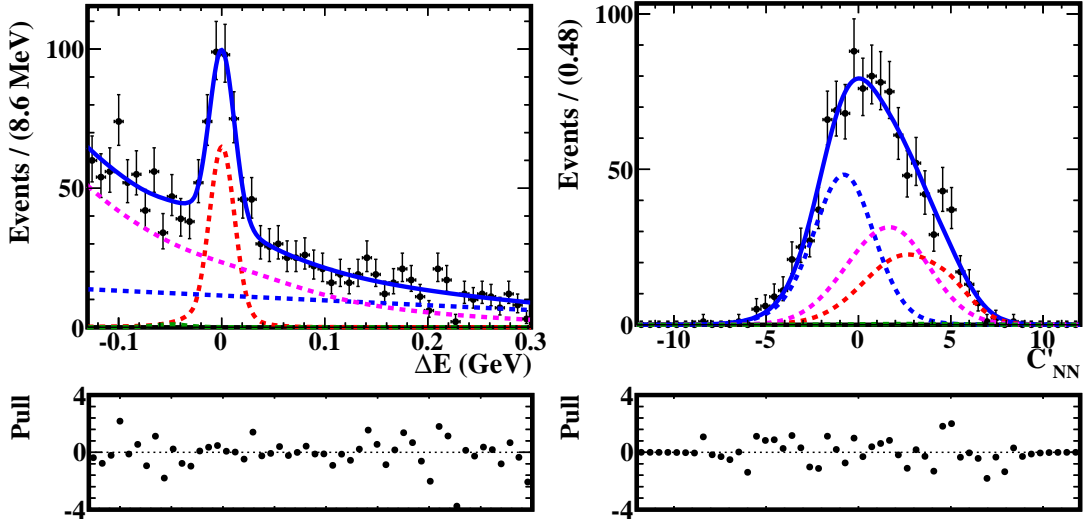


Figure C.15: Signal-enhanced projections of  $\Delta E$  (left) and  $C'_{\text{NN}}$  (right) distributions of  $B^\pm \rightarrow D(K_S^0 \pi^+ \pi^- \pi^0) \pi^\pm$  decays in bin 9 from a two-dimensional simultaneous fit to  $B^\pm \rightarrow D\pi^\pm$  and  $B^\pm \rightarrow DK^\pm$  events in generic MC sample with integrated luminosity equivalent to that of data.

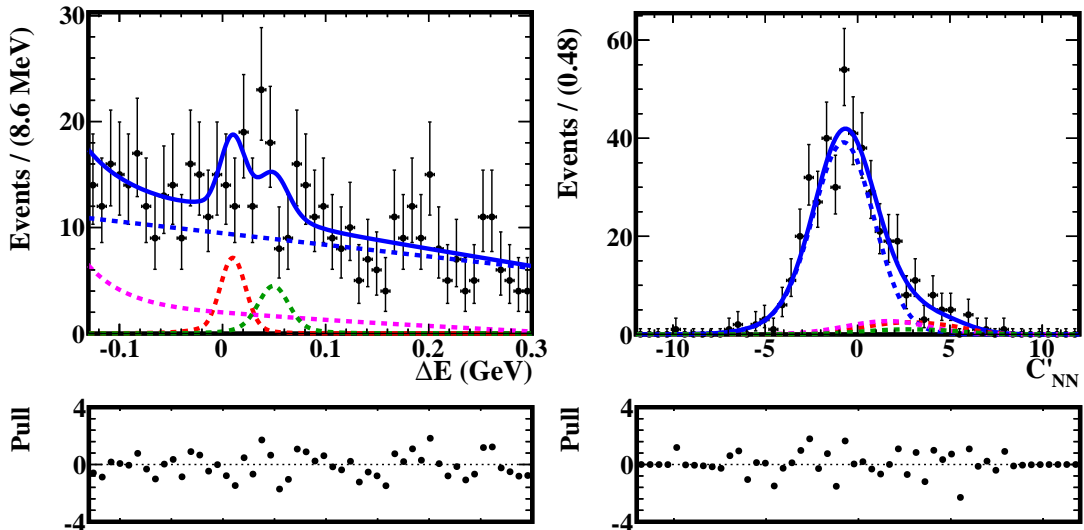


Figure C.16: Signal-enhanced projections of  $\Delta E$  (left) and  $C'_{\text{NN}}$  (right) distributions of  $B^\pm \rightarrow D(K_S^0 \pi^+ \pi^- \pi^0) K^\pm$  decays in bin 9 from a two-dimensional simultaneous fit to  $B^\pm \rightarrow D\pi^\pm$  and  $B^\pm \rightarrow DK^\pm$  events in generic MC sample with integrated luminosity equivalent to that of data.

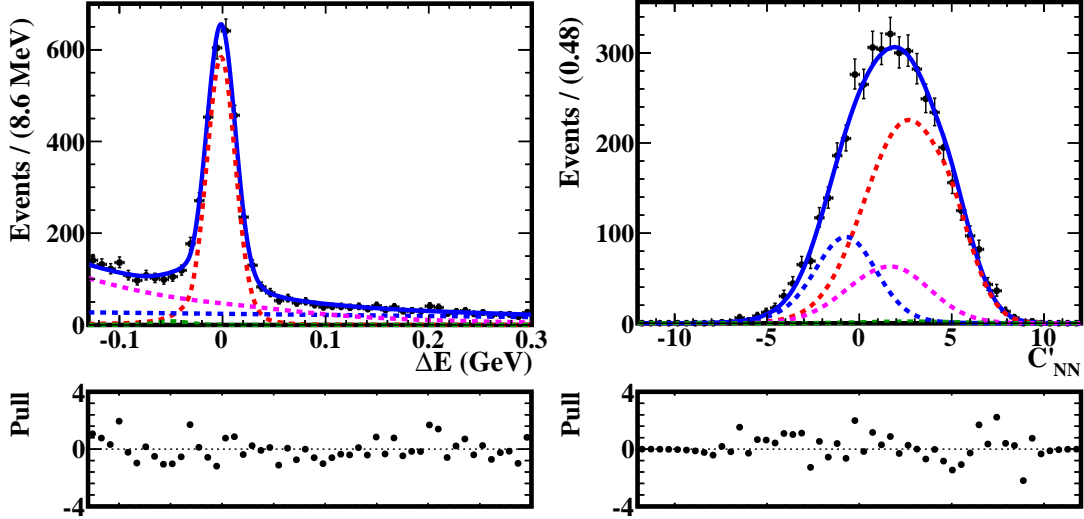


Figure C.17: Signal-enhanced projections of  $\Delta E$  (left) and  $C'_{NN}$  (right) distributions of  $B^\pm \rightarrow D(K_S^0 \pi^+ \pi^- \pi^0) \pi^\pm$  decays in bin 2 from a two-dimensional simultaneous fit to  $B^\pm \rightarrow D\pi^\pm$  and  $B^\pm \rightarrow DK^\pm$  events in data.

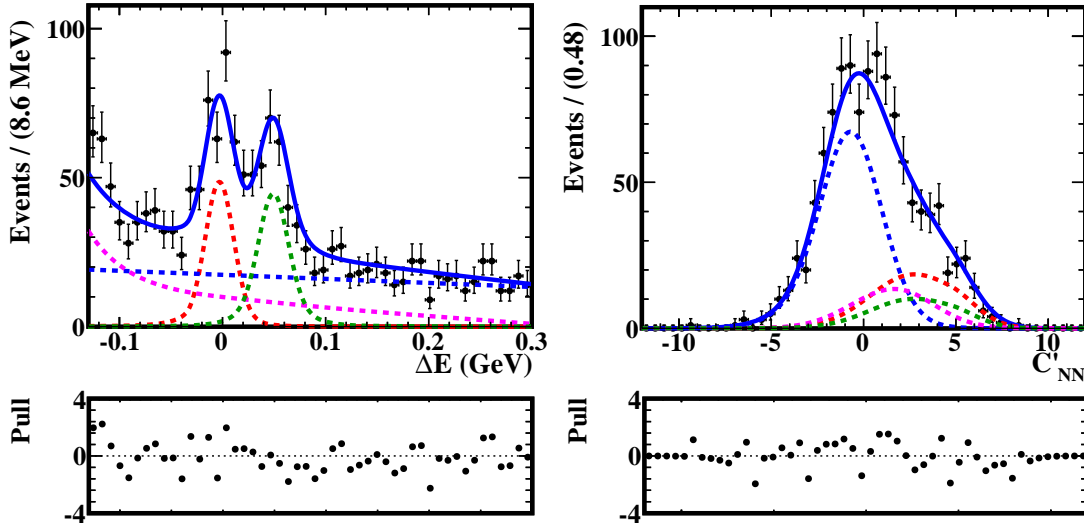


Figure C.18: Signal-enhanced projections of  $\Delta E$  (left) and  $C'_{NN}$  (right) distributions of  $B^\pm \rightarrow D(K_S^0 \pi^+ \pi^- \pi^0) K^\pm$  decays in bin 2 from a two-dimensional simultaneous fit to  $B^\pm \rightarrow D\pi^\pm$  and  $B^\pm \rightarrow DK^\pm$  events in data.

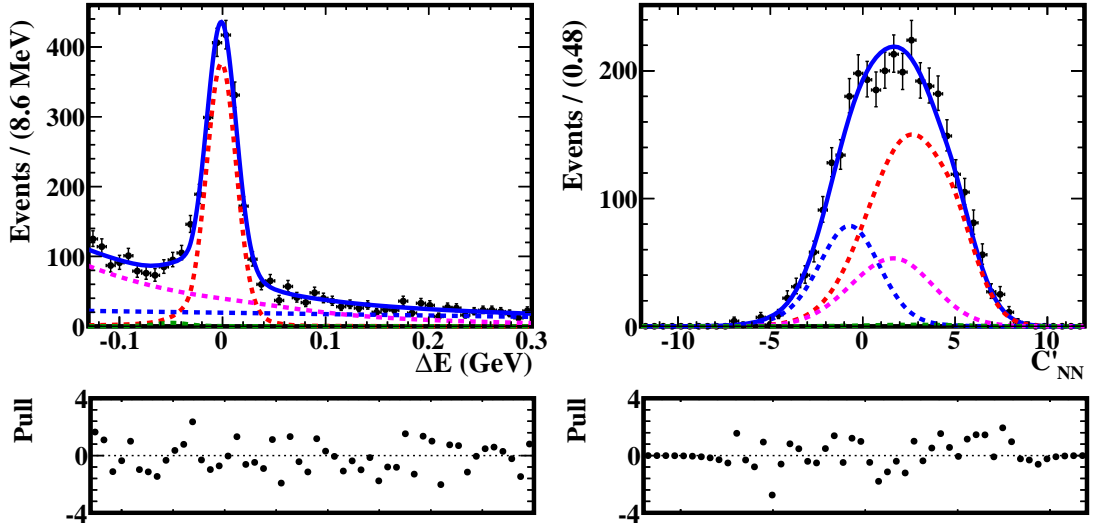


Figure C.19: Signal-enhanced projections of  $\Delta E$  (left) and  $C'_{\text{NN}}$  (right) distributions of  $B^\pm \rightarrow D(K_S^0 \pi^+ \pi^- \pi^0) \pi^\pm$  decays in bin 3 from a two-dimensional simultaneous fit to  $B^\pm \rightarrow D\pi^\pm$  and  $B^\pm \rightarrow DK^\pm$  events in data.

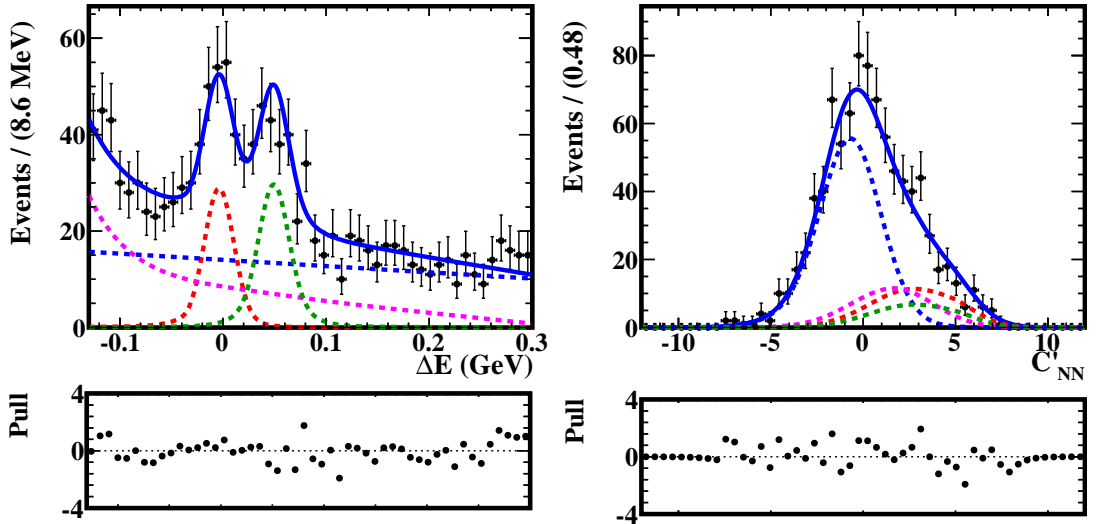


Figure C.20: Signal-enhanced projections of  $\Delta E$  (left) and  $C'_{\text{NN}}$  (right) distributions of  $B^\pm \rightarrow D(K_S^0 \pi^+ \pi^- \pi^0) K^\pm$  decays in bin 3 from a two-dimensional simultaneous fit to  $B^\pm \rightarrow D\pi^\pm$  and  $B^\pm \rightarrow DK^\pm$  events in data.

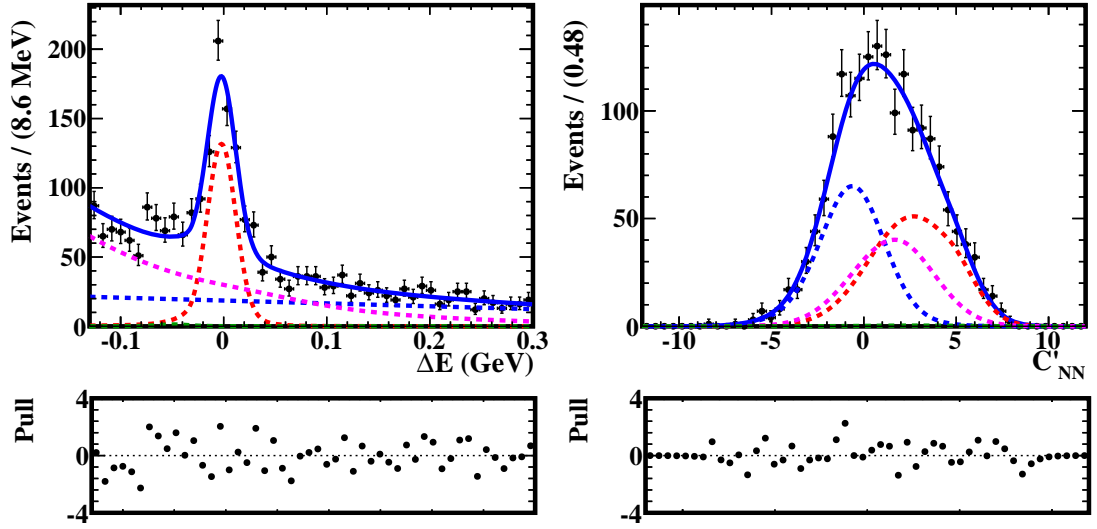


Figure C.21: Signal-enhanced projections of  $\Delta E$  (left) and  $C'_{\text{NN}}$  (right) distributions of  $B^\pm \rightarrow D(K_S^0 \pi^+ \pi^- \pi^0) \pi^\pm$  decays in bin 4 from a two-dimensional simultaneous fit to  $B^\pm \rightarrow D\pi^\pm$  and  $B^\pm \rightarrow DK^\pm$  events in data.

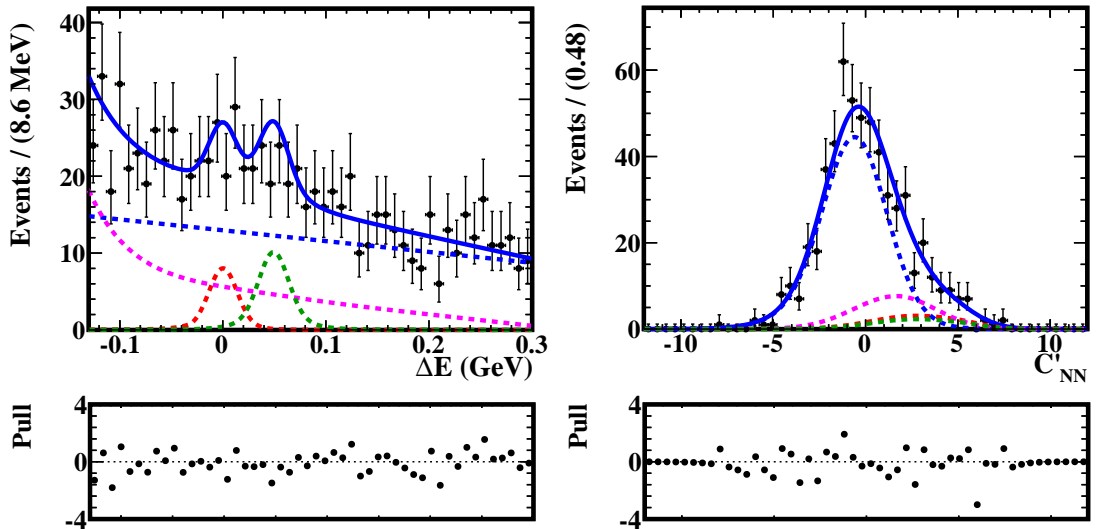


Figure C.22: Signal-enhanced projections of  $\Delta E$  (left) and  $C'_{\text{NN}}$  (right) distributions of  $B^\pm \rightarrow D(K_S^0 \pi^+ \pi^- \pi^0) K^\pm$  decays in bin 4 from a two-dimensional simultaneous fit to  $B^\pm \rightarrow D\pi^\pm$  and  $B^\pm \rightarrow DK^\pm$  events in data.

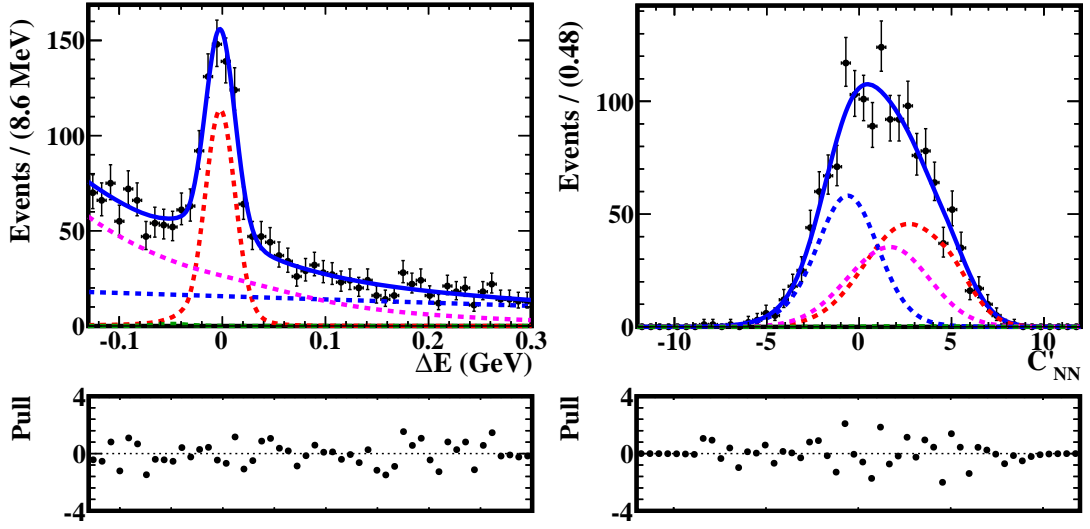


Figure C.23: Signal-enhanced projections of  $\Delta E$  (left) and  $C'_{\text{NN}}$  (right) distributions of  $B^\pm \rightarrow D(K_S^0 \pi^+ \pi^- \pi^0) \pi^\pm$  decays in bin 5 from a two-dimensional simultaneous fit to  $B^\pm \rightarrow D\pi^\pm$  and  $B^\pm \rightarrow DK^\pm$  events in data.

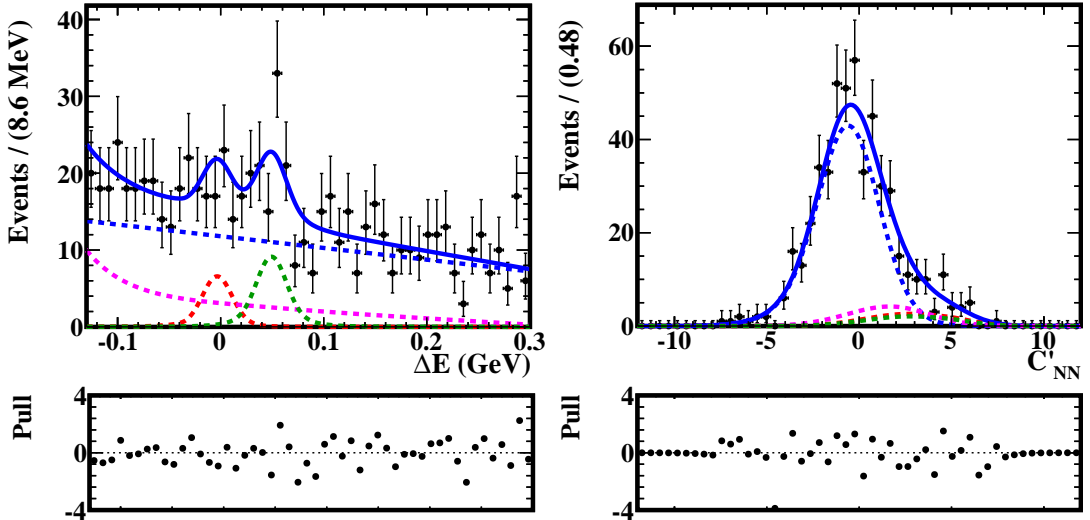


Figure C.24: Signal-enhanced projections of  $\Delta E$  (left) and  $C'_{\text{NN}}$  (right) distributions of  $B^\pm \rightarrow D(K_S^0 \pi^+ \pi^- \pi^0) K^\pm$  decays in bin 5 from a two-dimensional simultaneous fit to  $B^\pm \rightarrow D\pi^\pm$  and  $B^\pm \rightarrow DK^\pm$  events in data.

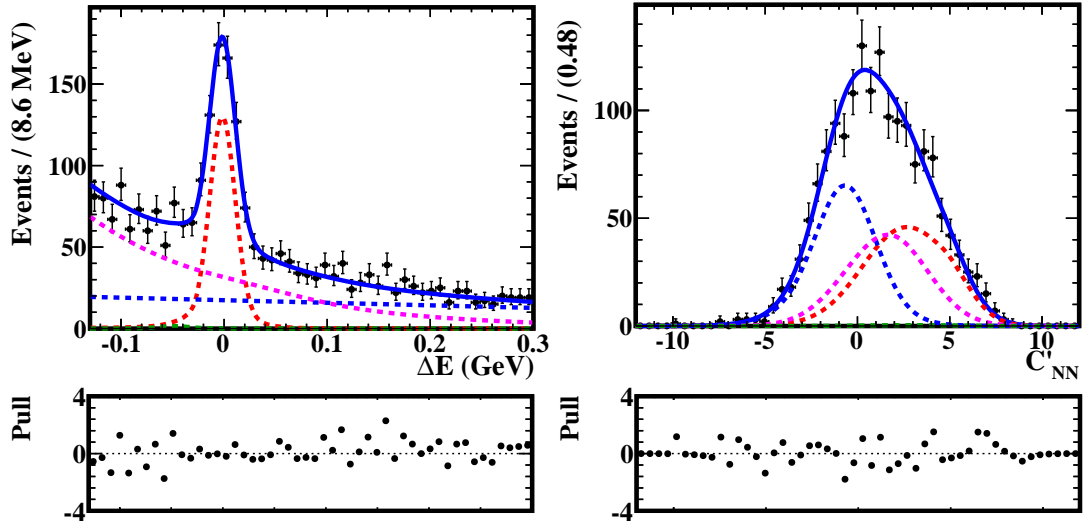


Figure C.25: Signal-enhanced projections of  $\Delta E$  (left) and  $C'_{NN}$  (right) distributions of  $B^\pm \rightarrow D(K_S^0 \pi^+ \pi^- \pi^0) \pi^\pm$  decays in bin 6 from a two-dimensional simultaneous fit to  $B^\pm \rightarrow D\pi^\pm$  and  $B^\pm \rightarrow DK^\pm$  events in data.

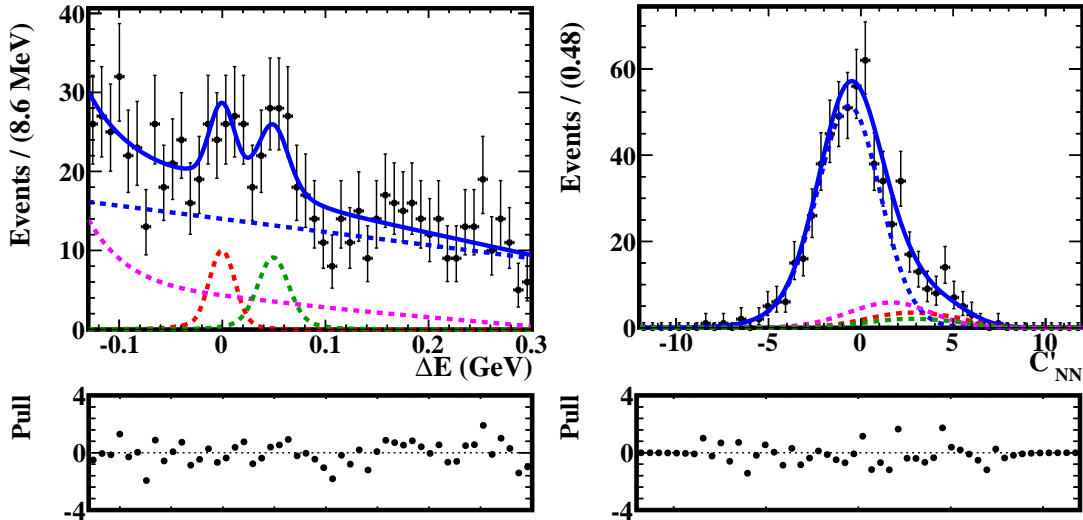


Figure C.26: Signal-enhanced projections of  $\Delta E$  (left) and  $C'_{NN}$  (right) distributions of  $B^\pm \rightarrow D(K_S^0 \pi^+ \pi^- \pi^0) K^\pm$  decays in bin 6 from a two-dimensional simultaneous fit to  $B^\pm \rightarrow D\pi^\pm$  and  $B^\pm \rightarrow DK^\pm$  events in data.

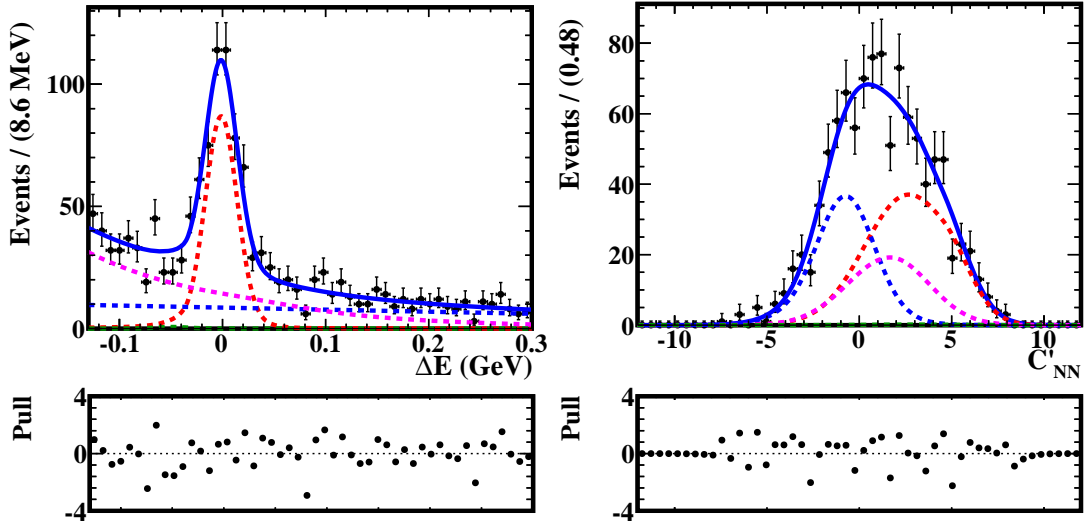


Figure C.27: Signal-enhanced projections of  $\Delta E$  (left) and  $C'_{\text{NN}}$  (right) distributions of  $B^\pm \rightarrow D(K_S^0 \pi^+ \pi^- \pi^0) \pi^\pm$  decays in bin 7 from a two-dimensional simultaneous fit to  $B^\pm \rightarrow D\pi^\pm$  and  $B^\pm \rightarrow DK^\pm$  events in data.

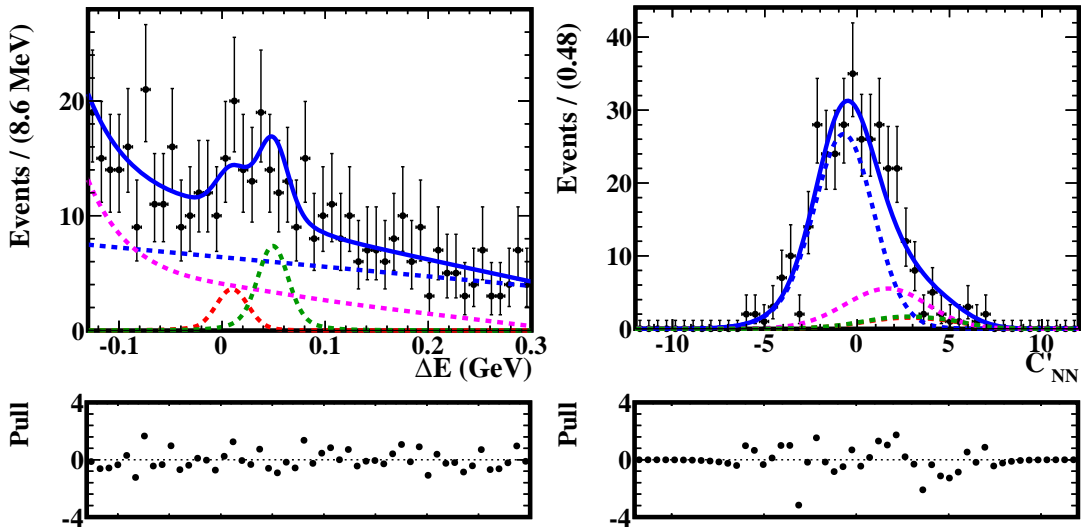


Figure C.28: Signal-enhanced projections of  $\Delta E$  (left) and  $C'_{\text{NN}}$  (right) distributions of  $B^\pm \rightarrow D(K_S^0 \pi^+ \pi^- \pi^0) K^\pm$  decays in bin 7 from a two-dimensional simultaneous fit to  $B^\pm \rightarrow D\pi^\pm$  and  $B^\pm \rightarrow DK^\pm$  events in data.

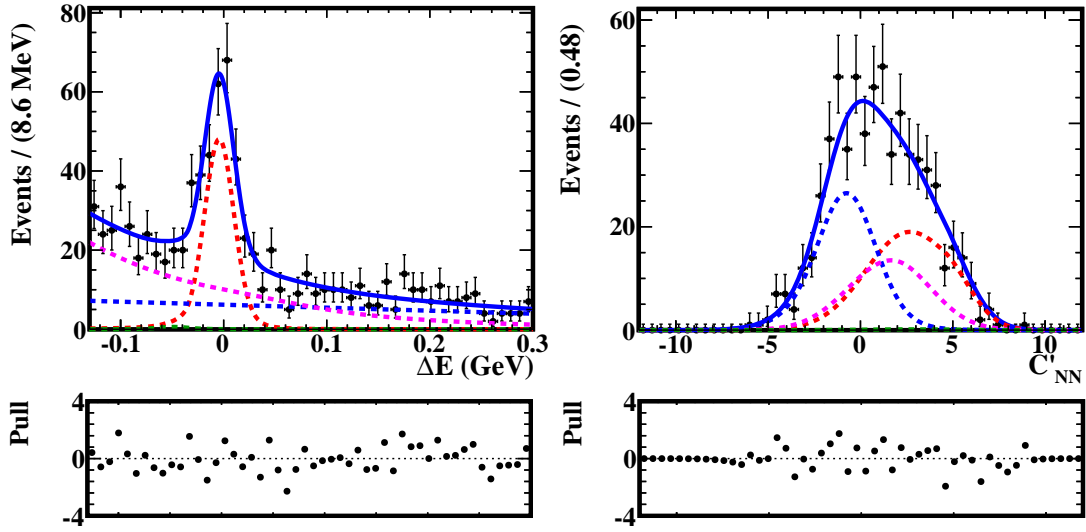


Figure C.29: Signal-enhanced projections of  $\Delta E$  (left) and  $C'_{\text{NN}}$  (right) distributions of  $B^\pm \rightarrow D(K_S^0 \pi^+ \pi^- \pi^0) \pi^\pm$  decays in bin 8 from a two-dimensional simultaneous fit to  $B^\pm \rightarrow D\pi^\pm$  and  $B^\pm \rightarrow DK^\pm$  events in data.

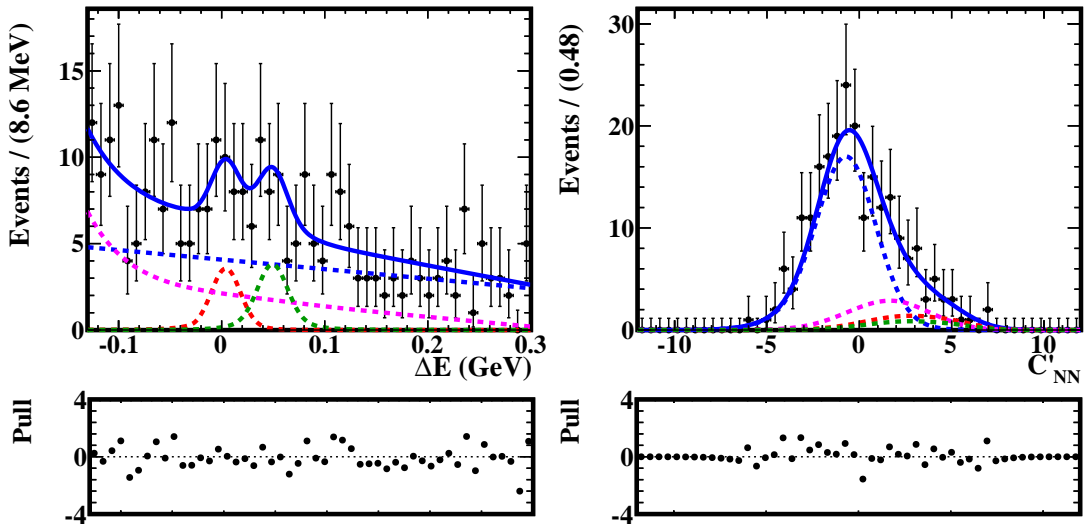


Figure C.30: Signal-enhanced projections of  $\Delta E$  (left) and  $C'_{\text{NN}}$  (right) distributions of  $B^\pm \rightarrow D(K_S^0 \pi^+ \pi^- \pi^0) K^\pm$  decays in bin 8 from a two-dimensional simultaneous fit to  $B^\pm \rightarrow D\pi^\pm$  and  $B^\pm \rightarrow DK^\pm$  events in data.

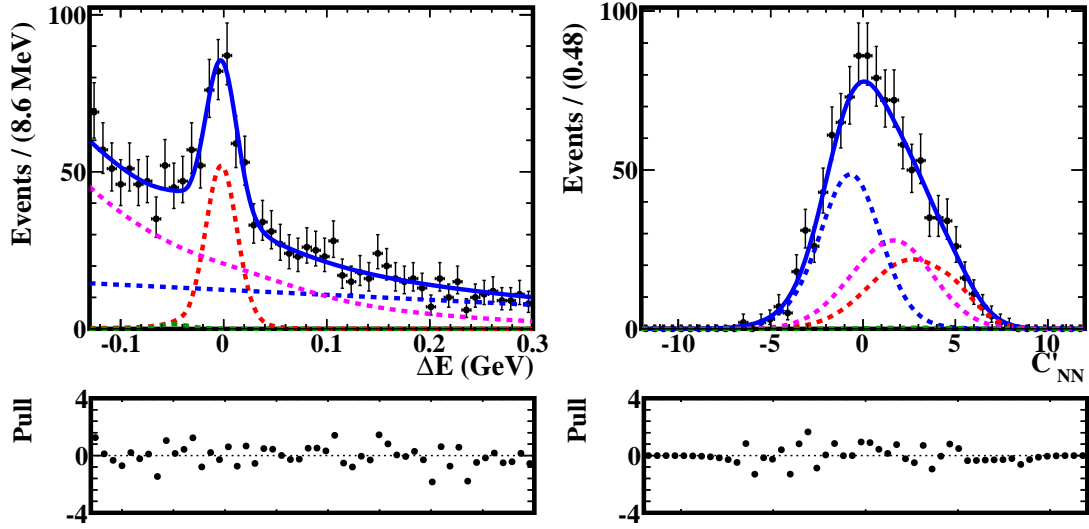


Figure C.31: Signal-enhanced projections of  $\Delta E$  (left) and  $C'_{\text{NN}}$  (right) distributions of  $B^\pm \rightarrow D(K_S^0 \pi^+ \pi^- \pi^0) \pi^\pm$  decays in bin 9 from a two-dimensional simultaneous fit to  $B^\pm \rightarrow D\pi^\pm$  and  $B^\pm \rightarrow DK^\pm$  events in data.

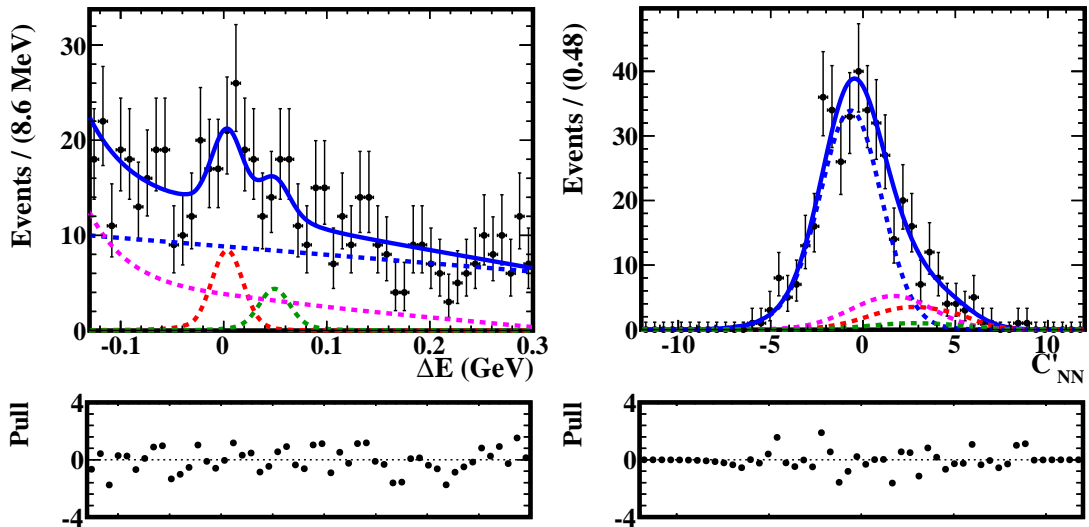


Figure C.32: Signal-enhanced projections of  $\Delta E$  (left) and  $C'_{\text{NN}}$  (right) distributions of  $B^\pm \rightarrow D(K_S^0 \pi^+ \pi^- \pi^0) K^\pm$  decays in bin 9 from a two-dimensional simultaneous fit to  $B^\pm \rightarrow D\pi^\pm$  and  $B^\pm \rightarrow DK^\pm$  events in data.



# APPENDIX D

## Results from pseudo-experiments

The distributions of pull, error and parameter values of  $x_{\pm}$  and  $y_{\pm}$  returned from 250 pseudo-experiments are shown in Fig. D.1–D.8.

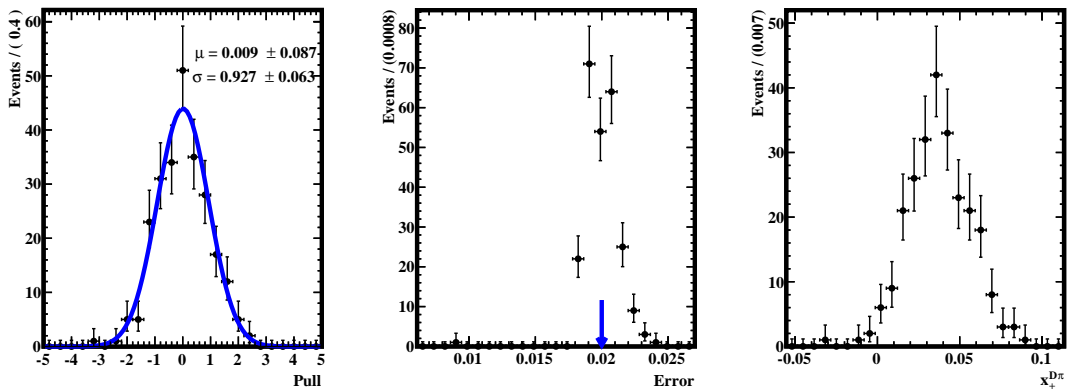


Figure D.1: The pull (left), error (middle) and parameter distributions (right) for  $x_+^{D\pi}$  from 250 pseudo-experiments. The solid blue curve represents the Gaussian fit to the pull distribution. The error obtained from MC sample fit is marked in blue arrow.

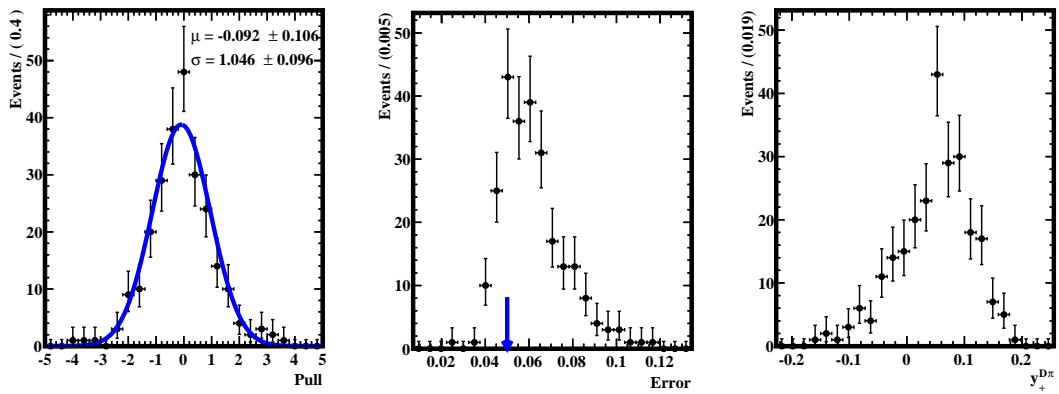


Figure D.2: The pull (left), error (middle) and parameter distributions (right) for  $y_+^{D\pi}$  from 250 pseudo-experiments. The solid blue curve represents the Gaussian fit to the pull distribution. The error obtained from MC sample fit is marked in blue arrow.

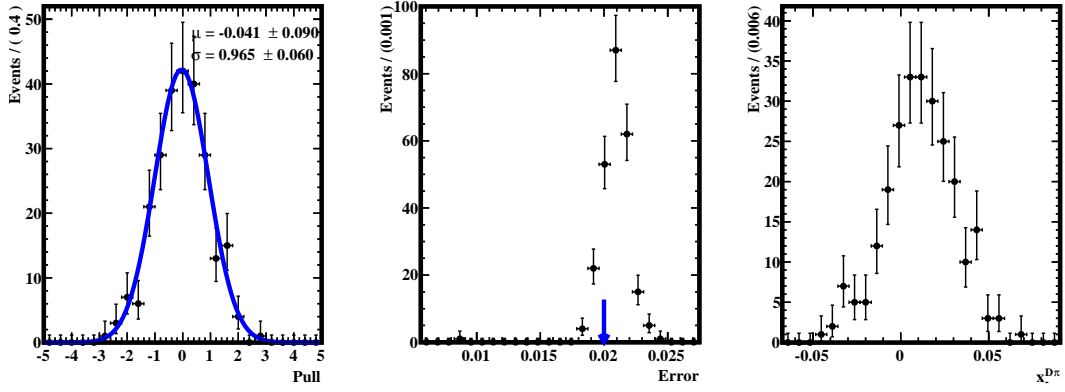


Figure D.3: The pull (left), error (middle) and parameter distributions (right) for  $x_{-}^{D\pi}$  from 250 pseudo-experiments. The solid blue curve represents the Gaussian fit to the pull distribution. The error obtained from MC sample fit is marked in blue arrow.

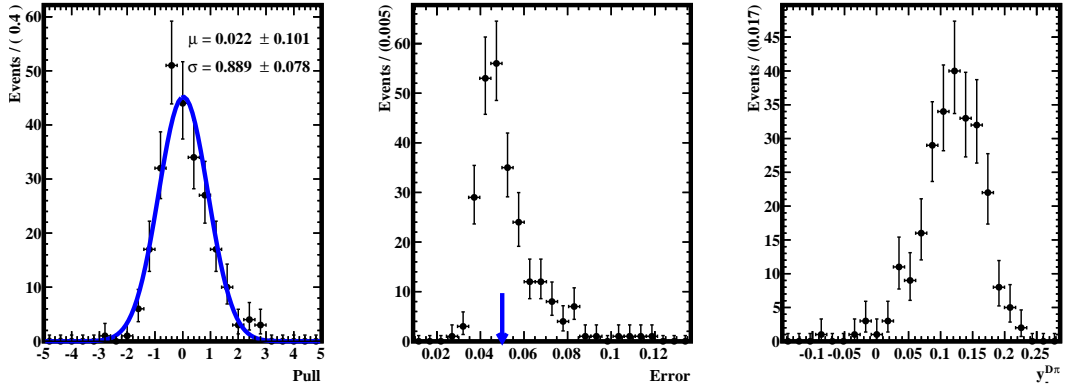


Figure D.4: The pull (left), error (middle) and parameter distributions (right) for  $y_{-}^{D\pi}$  from 250 pseudo-experiments. The solid blue curve represents the Gaussian fit to the pull distribution. The error obtained from MC sample fit is marked in blue arrow.

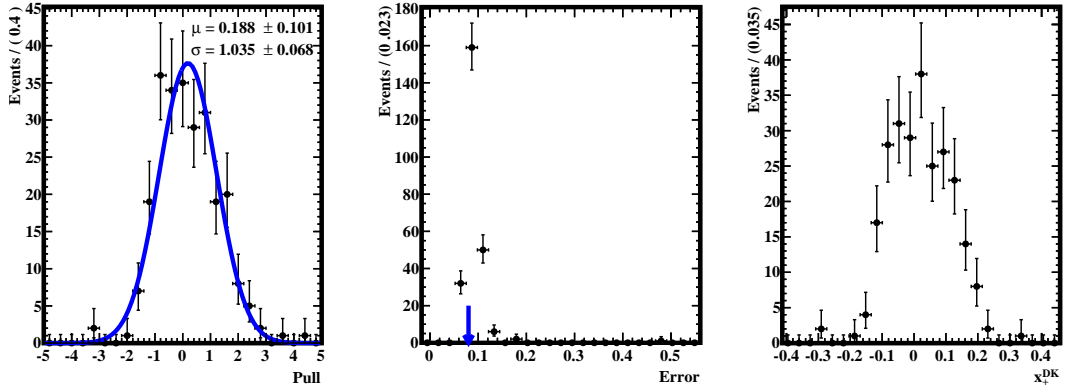


Figure D.5: The pull (left), error (middle) and parameter distributions (right) for  $x_{+}^{DK}$  from 250 pseudo-experiments. The solid blue curve represents the Gaussian fit to the pull distribution. The error obtained from MC sample fit is marked in blue arrow.

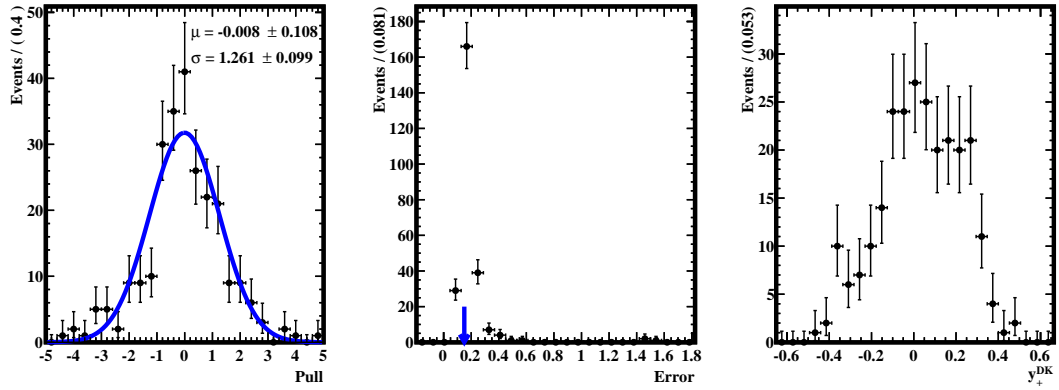


Figure D.6: The pull (left), error (middle) and parameter distributions (right) for  $y_+^{DK}$  from 250 pseudo-experiments. The solid blue curve represents the Gaussian fit to the pull distribution. The error obtained from MC sample fit is marked in blue arrow.

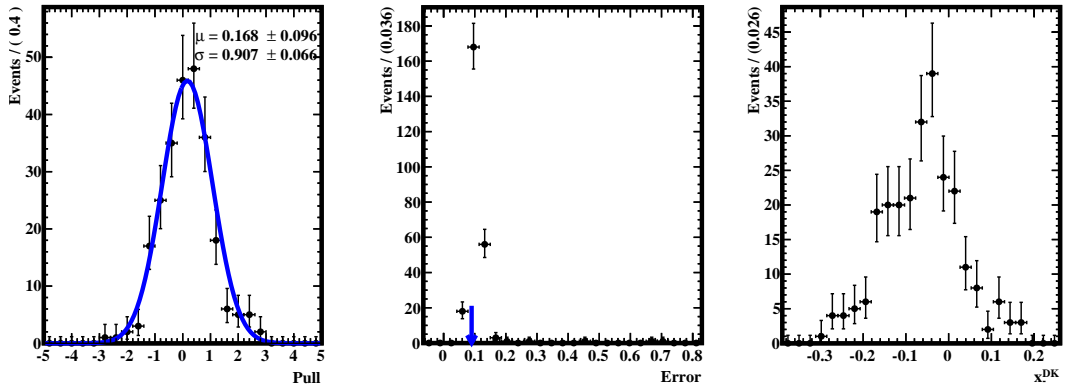


Figure D.7: The pull (left), error (middle) and parameter distributions (right) for  $x_-^{DK}$  from 250 pseudo-experiments. The solid blue curve represents the Gaussian fit to the pull distribution. The error obtained from MC sample fit is marked in blue arrow.

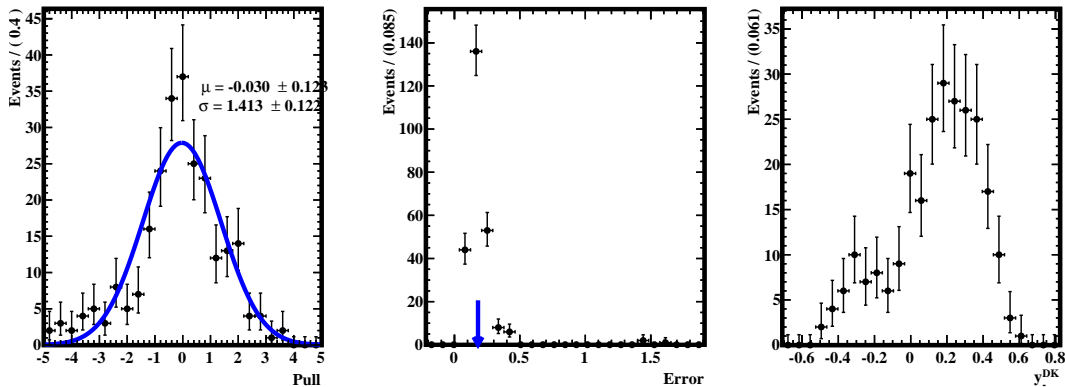


Figure D.8: The pull (left), error (middle) and parameter distributions (right) for  $y_-^{DK}$  from 250 pseudo-experiments. The solid blue curve represents the Gaussian fit to the pull distribution. The error obtained from MC sample fit is marked in blue arrow.



## REFERENCES

- [1] G. L. Glashow, Nucl. Phys. **22**, 579 (1961).
- [2] A. Salam and J. C. Ward, Phys. Lett. **13**, 168 (1964).
- [3] S. Weinberg, Phys. Rev. Lett. **19**, 1264 (1967).
- [4] G. Aad *et al.*, (ATLAS Collaboration), Phys. Lett. B **716**, 1 (2012), [arXiv:1207.7214].
- [5] S. Chatrchyan *et al.*, (CMS Collaboration), Phys. Lett. B **716**, 30 (2012), [arXiv:1207.7235].
- [6] J. Goldstone, A. Salam, and S. Weinberg, Phys. Rev. **127**, 965-970 (1962).
- [7] P. W. Higgs, Phys. Rev. Lett. **12**, 132 (1964); P. W. Higgs, Phys. Rev. Lett. **13**, 508 (1964); F. Englert and R. Brout, Phys. Rev. Lett. **13**, 321 (1964); G.S. Guralnik, C.R. Hagen and T. W. B. Kibble, Phys. Rev. Lett. **13**, 585 (1964).
- [8] E. Noether, Gott. Nachr. **1918**, 235 (1918).
- [9] T. D. Lee and C. N. Yang, Phys. Rev. **104**, 254 (1956).
- [10] C. S. Wu, E. Ambler, R. W. Hayward, D. D. Hoppes, and R. P. Hudson, Phys. Rev. Lett. **105**, 1413 (1957).
- [11] J. H. Christenson, J. W. Cronin, V. L. Fitch, and R. Turlay, Phys. Rev. Lett. **13**, 138 (1964).
- [12] I. I. Bigi and A. I. Sanda, Phys. Rev. D **29**, 1393 (1984).
- [13] G. Lüders, Det. Kong. Danske Videnskabernes Selskab, Mat.-fys. Medd. **28**, 005 (1954).
- [14] M. Tanabashi *et al.*, (Particle Data Group Collaboration), Phys. Rev. D **98**, 030001 (2018).

- [15] A.D. Sakharov, Sov. Phys. JETP Lett. **5**, 24 (1967); A. D. Sakharov, Sov. Phys. JETP **49**, 594 (1979).
- [16] N. Cabibbo, Phys. Rev. Lett. **10**, 531 (1963).
- [17] S. L. Glashow, J. Iliopoulos, and L. Maiani, Phys. Rev. D. **2**, 1285 (1970).
- [18] J.-E. Augustin *et al.*, Phys. Rev. Lett. **33**, 1406 (1974); J. J. Aubert *et al.* Phys. Rev. Lett. **33**, 1404 (1974).
- [19] M. Kobayashi and T. Maskawa, Prog. Theor. Phys. **49**, 652 (1973).
- [20] L. Wolfenstein, Phys. Rev. Lett. **51**, 1945 (1985).
- [21] C. Jarlskog, Phys. Rev. Lett. **55**, 1039 (1985).
- [22] J. Charles *et al.*, (CKMfitter Group), Eur. Phys. J. C **41**, 1-131 (2005) [hep-ph/0406184], updated results and plots available at: <http://ckmfitter.in2p3.fr>
- [23] K. Abe *et al.*, (Belle Collaboration), Phys. Rev. Lett. **87**, 091802 (2001).
- [24] B. Aubert *et al.*, (BABAR Collaboration), Phys. Rev. Lett. **87**, 091801 (2001).
- [25] G. R. Farrar and M. E. Shaposhnikov, Phys. Rev. D **50**, 774 (1994).
- [26] M. B. Gavela *et al.*, Nucl. Phys. B **430**, 382 (1994).
- [27] P. Huet and E. Sather, Phys. Rev. D **51**, 379 (1995).
- [28] J. Brod and J. Zupan, J. High Energ. Phys. **01**, 051 (2014).
- [29] Y. Amhis *et al.*, (Heavy Flavour Averaging Group Collaboration), Eur. Phys. J. C **77**, 895 (2017), [arXiv:1612.07233].
- [30] M. Gronau and D. London, Phys. Lett. B **253**, 483 (1991); M. Gronau and D. Wyler, Phys. Lett. B **265**, 172 (1991).
- [31] M. Nayak *et al.*, Phys. Lett. B **740**, 1 (2015), [arXiv:1410.3964].
- [32] D. Atwood, I. Dunietz and A. Soni, Phys. Rev. Lett. **78**, 3257 (1997).
- [33] D. Atwood and A. Soni, Phys. Rev. D **68**, 033003 (2003), [arXiv:hep-ph/0304085].

- [34] A. Giri, Yu. Grossman, A. Soffer and J. Zupan, Phys. Rev. D **68**, 054018 (2003), [arXiv:hep-ph/0303187].
- [35] A. Bondar, *Proceedings of BINP special analysis meeting on Dalitz analysis*, 2002 (unpublished).
- [36] A. Bondar and A. Poluektov, Eur. Phys. J. C **47**, 347 (2006), [arXiv:hep-ph/0510246].
- [37] A. Bondar and A. Poluektov, Eur. Phys. J. C **55**, 51 (2008), [arXiv:0801.0840].
- [38] R. Aaij *et al.*, (LHCb Collaboration), J. High Energ. Phys. **1808**, 176 (2018); Erratum [JHEP **1810**, 107 (2018)].
- [39] Y. Kubota *et al.*, Nucl. Instrum. Meth. A **320**, 66 (1992).
- [40] D. Peterson *et al.*, Nucl. Instrum. Meth. A **478**, 142 (2002).
- [41] M. Artuso *et al.*, Nucl. Instrum. Meth. A **502**, 91 (2003).
- [42] CLEO-c/CESR-c Taskforces and CLEO-c Collaboration, R.A. Briere *et al.*, Cornell LEPP Report CLNS Report No. 01/1742 (2001).
- [43] <http://www.lepp.cornell.edu/Research/CESR/WebHome.html>.
- [44] <http://www.classe.cornell.edu/Research/CLEO/Detector.html>.
- [45] R. E. Kalman, J. Basic Eng **82**, 35 (1960).
- [46] H. Bethe, Ann. Phys. (Leipzig) **5**, 325 (1930).
- [47] H. Bethe, Z. Phys. **76**, 293 (1932).
- [48] H. Bethe and J. Ashkin, *Experimental Nuclear Physics*, edited by E. Segre (Wiley, New York, 1953).
- [49] S. Kurokawa and E. Kikutani, Nucl. Instrum. Meth. A **499**, 1 (2003), and other papers included in this volume.
- [50] S. Iwata, KEK-PROC-93-19.
- [51] H. Kichimi *et al.*, JINST **5**, P03011 (2010).

- [52] KEKB B-Factory Design Report, KEK Report 95-7, 1995.
- [53] R. B. Palmer, SLAC-PUB 4707, 1988.
- [54] K. Oide and K. Yokoya, Phys. Rev. A **40**, 315 (1989).
- [55] <http://cerncourier.com/cws/article/cern/39147>.
- [56] <https://www.classe.cornell.edu/public/lab-info/upsilon.html>.
- [57] <http://belle.kek.jp/>.
- [58] A. Abashian *et al.*, (Belle Collaboration), Nucl. Instrum. Meth. A **479**, 117 (2002), [arXiv:1710.10086].
- [59] J. Brodzicka *et al.*, (Belle Collaboration), Prog. Theor. Exp. Phys. **2012**, 04D001 (2012), [arXiv:1212.5342].
- [60] G. Alimonti *et al.*, (Belle Collaboration), Nucl. Instr. Meth. A **453**, 71 (2000).
- [61] E. Nygard *et al.*, Nucl. Instrum. Meth. A **301**, 506 (1991) .
- [62] O. Toker *et al.*, Nucl. Instrum. Meth. A **340**, 572 (1994).
- [63] Y. Horii, PhD thesis, Tohoku University (2010).
- [64] H. Hirano *et al.*, Nucl. Instrum. Meth. A **455**, 294 (2000).
- [65] H. Kichimi *et al.*, Nucl. Instrum. Meth. A **453**, 315 (2000).
- [66] <http://sabotin.ung.si/sstanic/belle/nim/total/node65.html>.
- [67] <http://belle.kek.jp/group/trg/>.
- [68] D.J. Lange, Nucl. Instrum. Meth. A **462**, 152 (2001).
- [69] R. Brun *et al.*, CERN Program Library Long Writeup W5013 (unpublished).
- [70] E. Barberio and Z. Was, Comput. Phys. Commun. **79**, 291 (1994).
- [71] Q. He *et al.*, (CLEO Collaboration), Phys. Rev. Lett. **100**, 091801 (2008), [arXiv:0711.1463].
- [72] C. M. Thomas, Ph.D Thesis, <http://cds.cern.ch/record/1427272>.

- [73] W. Verkerke and D. Kirkby, [arXiv:physics/0306116]; root.cern.ch/roofit.
- [74] H. Albrecht *et al.*, (ARGUS Collaboration), Phys. Lett. B **241**, 278 (1990).
- [75] T. Skwarnicki, Ph.D Thesis (Appendix E), DESY F31-86-02 (1986).
- [76] S. Malde *et al.*, Phys. Lett. B **747**, 9 (2015), [arXiv:1509.03858].
- [77] J. Libby *et al.*, (CLEO Collaboration), Phys. Rev. D **82**, 112006 (2010), [arXiv:1010.2817].
- [78] H. Aihara *et al.*, (Belle Collaboration), Phys. Rev. D **85**, 112014 (2012), [arXiv:1204.6561].
- [79] K. Prasanth *et al.*, (Belle Collaboration), Phys. Rev. D **95**, 091101(R) (2017), [arXiv:1703.05721].
- [80] T. Peng *et al.*, (Belle Collaboration), Phys. Rev. D **89**, 091103(R) (2014), [arXiv:1404.2412].
- [81] M. Kenzie, M. Martinelli and N. Tuning, Phys. Rev. D **94**, 054021 (2016), [arXiv:1606.09129].
- [82] R. Itoh, Internal Belle Note # 161.
- [83] E. Nakano, Nucl. Instrum. Methods Phys. Res. Sect. A **494**, 402 (2002).
- [84] Y. Horii *et al.*, (Belle Collaboration), Phys. Rev. Lett. **106**, 231803 (2011), [arXiv:1103.5951].
- [85] M. Feindt and U. Kerzel, Nucl. Instrum. Meth. Phys. Res. A **559**, 190 (2006).
- [86] H. Nakano, Ph.D. Thesis, Tohoku University, 2014, Chap. 4 (unpublished).
- [87] R. A. Fisher, Annals of Eugenics **7**, 179 (1936).
- [88] G. C. Fox and S. Wolfram, Phys. Rev. Lett. **41**, 1581 (1978).
- [89] S. H. Lee *et al.*, (Belle Collaboration), Phys. Rev. Lett. **91**, 261801 (2003).
- [90] H. Tajima *et al.*, Nucl. Instrum. Meth. A **533**, 370 (2004), [arXiv:0301026].
- [91] H. Kakuno *et al.*, Nucl. Instrum. Meth. A **533**, 516 (2004), [arXiv:0403022].

- [92] P. K. Resmi, J. Libby, S. Malde, and G. Wilkinson, *J. High Energ. Phys.* **01**, 82 (2018), [arXiv:1710.10086].
- [93] G. J. Feldman and R. D. Cousins, *Phys. Rev. D* **57**, 3873 (1998).
- [94] K. Negishi *et al.*, (Belle Collaboration), *Prog. Theor. Exp. Phys.* **2016**, 043C01 (2016).
- [95] T. Abe *et al.* (Belle II Collaboration), [arXiv:1011.0352].
- [96] Y. Ohnisi *et al.* *Prog. Theor. Exp. Phys.* 03A011 (2013).
- [97] <https://docs.belle2.org/>.
- [98] <https://www.belle2.org/e21595/e21770/infoboxContent25431/belle2.pdf>.
- [99] <https://web.infn.it/Belle-II/index.php/detector/svd>.
- [100] Z. Natkaniec *et al.* (Belle SVD2 Group), *Nucl. Instrum. Methods Phys. Res., A* **560**, 1 (2006).
- [101] M. French *et al.* *Nucl. Instrum. Meth. Phys. Res., A* **446**, 359 (2001).
- [102] C. Irmeler *et al.* *JINST*, **8** C01014 (2013).
- [103] C. Irmeler *et al.* *JINST*, **11** C01087 (2016).
- [104] M. Friedl *et al.* *JINST* **4** C12005 (2014).
- [105] H. Schroder, (ARGUS Collaboration), *Proc. of the 25<sup>th</sup> International Conference on High Energy Physics, Singapore*, p846 (1990).
- [106] S. Bahinipati *et al.* (Belle Collaboration), *Phys. Rev. D* **84**, 021101 (2011).
- [107] S. E. Csorna *et al.* (CLEO Collaboration), *Phys. Rev. D* **67**, 112002 (2003).
- [108] E. Kou, P. Urquijo, The Belle II collaboration, and The B2TiP theory community, *The Belle II Physics Book*, [arXiv:1808.10567], accepted for publication in PTEP.
- [109] B. Aubert *et al.*, (BaBar Collaboration), *Phys. Rev. D* **78**, 034023 (2008), [arXiv:0804.2089].

## LIST OF PAPERS BASED ON THESIS

1. **P. K. Resmi**, J. Libby, S. Malde and G. Wilkinson, Quantum-correlated measurements of  $D \rightarrow K_S^0 \pi^+ \pi^- \pi^0$  decays and consequences for the determination of the CKM angle  $\gamma$ , *J. High Energ. Phys.* **01**, 82 (2018), [arXiv:1710.10086](https://arxiv.org/abs/1710.10086) [hep-ex].
2. **P. K. Resmi**, J. Libby, K. Trabelsi *et al.*, (Belle Collaboration), First measurement of the CKM angle  $\phi_3$  with  $B^\pm \rightarrow D(K_S^0 \pi^+ \pi^- \pi^0) K^\pm$  decays, *J. High Energ. Phys.* **10**, 178 (2019), [arXiv:1908.09499](https://arxiv.org/abs/1908.09499) [hep-ex].

## PAPERS WITH AUTHORSHIP DUE TO CONTRIBUTIONS TO THE COLLABORATION

1. Ten papers in refereed journals as listed in <http://inspirehep.net/author/profile/P.K.Resmi.1>



## PRESENTATIONS IN CONFERENCES

1. **Asia Europe Pacific School on High Energy Physics (AEPSHEP) 2016**, Beijing, October 2016 : **Poster** presentation titled *Quantum-correlated D decay measurements at CLEO-c*.
2. **9<sup>th</sup> International Workshop on the CKM Unitarity Triangle (CKM) 2016**, TIFR, December 2016 : **Oral** presentation titled *Quantum-correlated measurements of  $D \rightarrow K_S^0 \pi^+ \pi^- \pi^0$  decays and consequences for the determination of  $\gamma$* , [PoS\(CKM2016\)112](#), [arXiv:1703.10317 \[hep-ex\]](#).
3. **3<sup>rd</sup> National Symposium on Particles, Detectors and Instrumentation**, TIFR, October 2017 : **Poster** presentation titled *Quantum-correlated D decay measurements at CLEO-c*.
4. **Belle II General Meeting (B2GM)** held at KEK during June 2018: presented the results from early Belle II data in a parallel session and gave a plenary talk summarising the session.
5. **16<sup>th</sup> Conference on Flavor Physics and CP Violation (FPCP) 2018**, Hyderabad Central University, July 2018 : **Oral** presentation titled *Input from the charm threshold for the measurement of  $\gamma$* , Springer proceedings in Physics [10.1007/978-3-030-29622-3](#), [arXiv:1810.00836 \[hep-ex\]](#).
6. **10<sup>th</sup> International Workshop on the CKM Unitarity Triangle (CKM) 2018**, Heidelberg, September 2018 : **Oral** presentation titled *Latest results on  $B \rightarrow DK/D\pi$  decays from Belle*, [10.5281/zenodo.2411155](#), [arXiv:1812.03440 \[hep-ex\]](#).
7. **27<sup>th</sup> International Workshop on Vertex Detectors (VERTEX) 2018**, Chennai, October 2018 : **Poster** presentation titled *Construction and quality assurance of the Belle II Silicon Vertex Detector*, [PoS\(VERTEX2018\)051](#), [arXiv:1901.09549 \[hep-ex\]](#).
8. **XXIII DAE-BRNS High Energy Physics Symposium 2018**, IIT Madras, December 2018 : **Oral** presentation titled *Measurement of CKM angle  $\phi_3$  using  $B^\pm \rightarrow D(K_S^0 \pi^+ \pi^- \pi^0) K^\pm$  decays at Belle*, Springer proceedings in Physics.
9. **3<sup>rd</sup> Jagiellonian Symposium of Fundamental and Applied Subatomic Physics**, Krakow, June 2019 : **Oral** presentation titled *Measurement of the CKM angle  $\phi_3$  at Belle II*.
10. **European Physical Society Conference on High Energy Physics 2019**, Ghent, July 2019 : **Oral** presentation titled *First measurements of the  $\phi_3$ -sensitive decay  $B^\pm \rightarrow D(K_S^0 \pi^+ \pi^- \pi^0) K^\pm$  with Belle*.